

# SCOOP

## SAR Altimetry Coastal and Open Ocean Performance

### Product Validation Report Phase 2 Test Data Set D2.5

Sentinel 3 For Science – SAR Altimetry Studies  
SEOM Study 2. Coastal Zone and Open Ocean Study  
ESA Contract 4000115382/15/I-BG

Project reference: SCOOP\_ESA\_D2.5b\_01

Issue: 3.3

26<sup>th</sup> July 2019

This page has been intentionally left blank

## Change Record

Date	Issue	Section	Page	Comment
15 <sup>th</sup> April 2019	3.1	Multiple		New Report for Phase 2
26 <sup>th</sup> July 2019	3.2	Multiple		Updates following ESA review

## Control Document

Process	Name	Date
Written by:	D Cotton, T Moreau, E Makhoul-Varona, L Fenoglio-Marc, M Cancet, M Naieje, J Fernandes, A Shaw	
Checked by:	D Cotton	
Approved by:	D Cotton	15/04/19

<b>Subject</b>	SAR Altimetry Coastal and Open Ocean Performance	<b>Project</b>	SCOOP
<b>Author</b>	<b>Organisation</b>	<b>Internal Reference</b>	
D Cotton, T Moreau, E Makhoul-Varona, L Fenoglio-Marc, M Cancet, M Naieje, J Fernandes, A Shaw	SatOC, CLS, isardSAT, U Bonn, Noveltis, TU Delft, U Porto	SCOOP_ESA_D2.5_030	

	Signature	Date
For SCOOP team		
For ESA		

# Table of Contents

<b>TABLE OF CONTENTS</b> .....	<b>4</b>
<b>TABLE OF FIGURES</b> .....	<b>6</b>
<b>1 INTRODUCTION</b> .....	<b>14</b>
1.1 Purpose and scope.....	14
1.2 Document structure .....	14
1.3 References .....	15
<b>2 OPEN OCEAN AND COASTAL ZONE VALIDATION OF THE SCOOP SECOND TEST DATA SET BY CLS</b> <b>18</b>	
2.1 Current state of knowledge and key challenges for SAR altimetry over ocean.....	18
2.2 Summary of Approach.....	20
2.3 Analysis of long-wavelength errors.....	26
2.4 High-frequency analysis .....	39
2.5 Sensitivity to sub-mesoscales .....	41
2.6 Sea Level Anomaly assessment .....	43
2.7 Analysis of the GPD+ Wet Tropospheric Correction .....	45
2.8 Summary of Results .....	54
<b>3 OPEN OCEAN VALIDATION OF THE SCOOP SECOND TEST DATA SET BY ISARDSAT</b> .....	<b>56</b>
3.1 Summary of Approach.....	56
3.2 Results from Validation Test 2.....	58
3.3 Summary of Results .....	71
<b>4 COASTAL ZONE VALIDATION OF THE SCOOP SECOND TEST DATA SET BY SKYMAT</b> .....	<b>72</b>
4.1 Introduction.....	72
4.2 Regions of Interest .....	72
4.3 Data .....	72
4.4 Methodology .....	73
4.5 Results.....	74
4.6 Summary and Main Findings and Recommendations.....	82
<b>5 OPEN OCEAN AND COASTAL ZONE VALIDATION OF THE SCOOP SECOND TEST DATA SET IN THE GERMAN BIGHT BY UBONN</b> .....	<b>83</b>
5.1 Summary of Approach.....	83
5.2 Results from Validation Test 1.....	83
5.3 Results from Validation Test 2.....	87
5.4 Summary of Results .....	90
<b>6 PERFORMANCE ASSESSMENT OF SEA STATE IMPACT ON ALTIMETER RETRIEVED SSH BY NOVELTIS</b> .....	<b>92</b>
6.1 Summary of Approach.....	92
6.2 Results from Validation Test 1: SAR product .....	93
6.3 Results from Validation Test 2: RDSAR product.....	107
6.4 Summary of Results .....	113
<b>7 VALIDATION OF THE WET TROPOSPHERE CORRECTION BY U PORTO (WP7000)</b> .....	<b>114</b>
7.1 Summary of Approach.....	114

7.2	WTC for CryoSat-2 .....	114
7.3	WTC for Sentinel-3A.....	127
<b>8</b>	<b>SUMMARY OF THE PERFORMANCE OF THE SCOOP SECOND TEST DATA SET AND WTC.....</b>	<b>146</b>
8.1	Summary of Results .....	146
8.2	Outstanding Issues .....	150
8.3	Recommendations.....	150
<b>9</b>	<b>LIST OF ACRONYMS.....</b>	<b>152</b>

# Table of Figures

Figure 2.1: Mean power spectral density for LRM, PLRM and SARM sea level anomalies computed as function of the wavenumber over the Agulhas area from March 2013 to December 2013. The spectral slopes (dashed lines) are calculated between 100 km and 200 km wavelength. The 20-Hz noise levels of energy (horizontal dashed lines) are estimated by fitting a plateau for wavelength between 700 m and 1 km. The correlated errors (spectral “bump”) impacting conventional altimetry data are located within the circle for wavelength from 7 km to 30 km [Raynal et al., 2018].	18
Figure 2.2: 20-Hz noise of range for different missions (Jason-2, Saral, Sentinel-3A) and different acquisition modes (LRM, PLRM, SARM) [CLS internal communication].	19
Figure 2.3: Difference of SWH estimates between SAR and PLRM modes for different processing chains: Sentinel-3A ground segment with two different versions of the SAR altimeter retracker (PDGS 2.3 and 2.5), the CNES Sentinel-3 processing prototype (S3PP v1.4) and the CNES Cryosat-2 processing prototype (CPP) [CLS internal communication].	20
Figure 2.4: Map of averages of radial velocity for ascending (left) and descending (right) passes plotted from a 1° x 1° grid computed from January 2012 to December 2013.	23
Figure 2.5: Map of averages of squared mispointing angles for ascending (left) and descending (right) passes plotted from a 1° x 1° grid computed from January 2012 to December 2013.	24
Figure 2.6: Map of averages of pitch (left) and roll (right) angles for ascending (top) and descending (bottom) passes plotted from a 1° x 1° grid computed from January 2012 to December 2013.	24
Figure 2.7: Map of averages of SWH plotted from a 1° x 1° grid computed in January 2013 (top) and December 2013 (bottom).	25
Figure 2.8: Map of SSH difference between TU-Delft RDSAR and CPP PLRM for ascending (top) and descending (bottom) passes plotted from a 1° x 1° grid computed from January 2012 to December 2013.	27
Figure 2.9: SSH difference (m) between TU-Delft RDSAR and CPP PLRM binned per PLRM CPP SWH and radial velocity for ascending (left) and descending (right) passes.	27
Figure 2.10: Map of SWH difference between TU-Delft RDSAR and CPP PLRM plotted from a 1° x 1° grid computed from January 2012 to December 2013.	28
Figure 2.11: Map of averages of SWH plotted from a 1° x 1° grid computed from January 2012 to December 2013.	29
Figure 2.12: Average of SWH difference between TU-Delft RDSAR and CPP PLRM datasets as function of CPP PLRM SWH computed from January 2012 to December 2013.	29
Figure 2.13: Map of SWH difference for ascending (top) and descending (bottom) passes plotted from a 1° x 1° grid computed from January 2012 to December 2013.	30
Figure 2.14: SWH difference (m) between TU-Delft RDSAR and CPP PLRM binned per PLRM CPP SWH and squared mispointing angle for ascending (left) and descending (right) passes.	31
Figure 2.15: SWH difference (m) between TU-Delft RDSAR and CPP PLRM binned per PLRM CPP SWH and radial velocity for ascending (left) and descending (right) passes.	31
Figure 2.16: Map of Sigma-0 difference for ascending (top) and descending (bottom) passes plotted from a 1° x 1° grid computed from January 2012 to December 2013.	32
Figure 2.17: Average of Sigma-0 difference between TU-Delft RDSAR and CPP PLRM datasets as function of CPP PLRM SWH computed from January 2012 to December 2013.	32
Figure 2.18: Map of SSH difference for ascending (top) and descending (bottom) passes plotted from a 1° x 1° grid computed from January 2012 to December 2013.	33
Figure 2.19: Map of SWH difference for ascending (top) and descending (bottom) passes plotted from a 1° x 1° grid computed from January 2012 to December 2013.	33

Figure 2.20: Average of SWH difference between GPOD SARM and CPP SARM datasets as function of CPP PLRM SWH computed from January 2012 to December 2013.....	34
Figure 2.21: Map of Sigma-0 difference for ascending (top) and descending (bottom) passes plotted from a 1° x 1° grid computed from January 2012 to December 2013.....	35
Figure 2.22: Sigma-0 difference (m) between GPOD SARM and CPP SARM binned per orbit and radial velocity for ascending (left) and descending (right) passes. ....	35
Figure 2.23: Average of Sigma-0 difference between GPOD SARM and CPP SARM datasets as function of CPP PLRM SWH computed from January 2012 to December 2013.....	35
Figure 2.24: Map of SSH difference for ascending (top) and descending (bottom) passes plotted from a 1° x 1° grid computed from January 2012 to December 2013. ....	36
Figure 2.25: SSH difference (m) between the innovative SARM and GPOD SARM binned per CPP PLRM SWH and radial velocity for ascending (left) and descending (right) passes.....	37
Figure 2.26: (left) Map of SWH difference plotted from a 1° x 1° grid. (right) SWH differences plotted as function of the CPP PLRM SWH and the radial velocity. Both diagnoses are computed from January 2012 to December 2013. ....	37
Figure 2.27: Average of SWH difference between the innovative SARM and GPOD SARM datasets as function of CPP PLRM SWH computed from January 2012 to December 2013. ....	38
Figure 2.28: (left) Map of Sigma-0 difference plotted from a 1° x 1° grid. (right) Sigma-0 differences plotted as function of the orbit and the radial velocity. Both diagnoses are computed from January 2012 to December 2013. ....	38
Figure 2.29: Plot of the range (top panel), SWH (middle panel) and sigma-0 (bottom panel) 20Hz white noise as a function of SWH for different acquisition modes (PLRM, SARM) and processing chain.....	40
Figure 2.30: Standard deviation of 20-Hz Cryosat-2 range against WW3 SWH estimates for different T02 values. ....	42
Figure 2.31: Standard deviation of 20-Hz Cryosat-2 SWH against WW3 SWH estimates for different T02 values. ....	42
Figure 2.32: Bin-averaged values of Cryosat-2 (SARM minus PLRM) SWH against WW3 SWH estimates for different T02 values.....	43
Figure 2.33: Mean power spectral density for PLRM and SARM sea level anomalies computed as function of the wavenumber over the Agulhas area from January 2013 to December 2013. ....	44
Figure 2.34: Map of the mean along-track GPD+ WTC (top panel) and ECMWF WTC (bottom panel) over SARM areas from January 2012 to December 2013.....	46
Figure 2.35: Map of the mean along-track difference (GPD+ - ECMWF) in meter (top panel) and map of the mean along-track formal error from the GPD+ WTC solution in meter (bottom panel) averaged in 1° by 1° geographical bins over the period of two years. ....	47
Figure 2.36: Map of the mean standard deviation of along-track difference (GPD+ - ECMWF) in meter averaged in 1° by 1° geographical bins over the period of two years (after smoothing). ....	48
Figure 2.37: Mean of the along track WTC differences, GPD+ - ECMWF, as function of the coastal distance (left panel) and latitude (right panel).....	48
Figure 2.38: Time evolution of the mean of the differences between WTC (in centimetre) computed from GPD+ and ECMWF from January 2012 to December 2013. ....	49
Figure 2.39: Map of the mean along track gain of variance between SLA computed with GPD+ and ECMWF WTCs, averaged in 2° by 2° geographical bins over the period of two years. ....	50
Figure 2.40: Mean along track gain of variance between SLA computed using the GPD+ and the ECMWF WTCs as function of the coastal distance (left panel) and the latitude (right panel). ....	50

Figure 2.41: Time evolution of the mean along track gain of variance between SLA computed using the GPD+ and the ECMWF WTCs from January 2012 to December 2013. ....	51
Figure 2.42: (Top panel) Map of the mean difference of variance of SSH crossover difference computed with GPD+ and ECMWF model WTCs, averaged in 4° x 4° geographical bins over the period of two years. (Bottom panel) The reduction or increase of variance in percentage.....	52
Figure 2.43: Time evolution of the mean difference of variance of SSH crossover difference computed with the GPD+ solution and the ECMWF model from January 2012 to December 2013. ....	53
Figure 2.44: (Left panel) Along-track WTCs derived from the ECMWF model (red) and computed by the GPD+ (blue), and the associated GPD+ flag (green) as function of the latitude. (Right panel) Zoom into part of the plot.....	53
Figure 3.1 Geographical masks used in the validation activity over North East Atlantic and Agulhas regions (filter out the land contribution from the analysis).....	56
Figure 3.2 SSH difference maps versus radial velocity and SWH: (left) Difference between Test-1 (GPOD) and Test-2 (Phase-2a) for Agulhas and North East Atlantic regions years 2012-2013; (right) Difference between Test-1 (GPOD) and Phase-2a for Agulhas, Central Pacific and North sea, year 2013.....	58
Figure 3.3 SWH difference maps versus radial velocity and SWH: Difference between Test-1 (GPOD) and Test-2 (Phase-2) for Agulhas and North East Atlantic regions years 2012-2013.....	59
Figure 3.4 SWH difference between Test-1 (GPOD) and Test-2 (Phase-2) as a function of Phase-2 SWH for Agulhas and North East Atlantic regions years 2012-2013.....	59
Figure 3.5 SWH scatter plot Test-2 (Phase-2) versus Test-1 (GPOD) for Agulhas and North East Atlantic regions years 2012-2013. ....	60
Figure 3.6 sigma0 difference maps versus radial velocity and SWH: Difference between Test-1 (GPOD) and Test-2 (Phase-2) for Agulhas and North East Atlantic regions years 2012-2013.....	60
Figure 3.7 sigma0 difference between Test-1 (GPOD) and Test-2 (Phase-2) as a function of Phase-2 SWH for Agulhas and North East Atlantic regions years 2012-2013.....	61
Figure 3.8 SSH precision (std) maps versus radial velocity and SWH: (left) Test-2 data and (right) Test-1 (GPOD) data for Agulhas and North East Atlantic regions years 2012-2013.....	61
Figure 3.9 SSH precision as a function of Test-1 SWH for both Test-1 (GPOD) and Test-2 (Phase-2) data sets (Agulhas and North East Atlantic regions, years 2012-2013). ....	62
Figure 3.10 SWH precision (std) maps versus radial velocity and SWH: (left) Test-2 data and (right) Test-1 (GPOD) data for Agulhas and North East Atlantic regions years 2012-2013.....	63
Figure 3.11 SWH precision as a function of Test-1 SWH for both Test-1 (GPOD) and Test-2 (Phase-2) data sets (Agulhas and North East Atlantic regions, years 2012-2013). ....	63
Figure 3.12 SWH precision as a function of Test-1 SWH for both Test-1 (GPOD) and Phase-2 data sets (Agulhas North Sea and Central Pacific regions, year 2013); different processing baselines considered activating only one processing option per baseline.....	63
Figure 3.13 Sigma0 precision (std) maps versus radial velocity and SWH: (left) Test-2 data and (right) Test-1 (GPOD) data for Agulhas and North East Atlantic regions years 2012-2013.....	64
<b>Figure 3.14 Sigma0 precision as a function of Test-1 SWH for both Test-1 (GPOD) and Test-2 (Phase-2) data sets (Agulhas and North East Atlantic regions, years 2012-2013).....</b>	<b>64</b>
Figure 3.15 SSH difference maps versus radial velocity and SWH: Difference between Test-1 (GPOD) and Test-2 (Phase-2a) for Pacific regions years 2012-2013. ....	65
Figure 3.16 SWH difference maps versus radial velocity and SWH: Difference between Test-1 (GPOD) and Test-2 (Phase-2) for Pacific regions years 2012-2013. ....	65
Figure 3.17 SWH difference between Test-1 (GPOD) and Test-2 (Phase-2) as a function of Phase-2 SWH for Pacific regions years 2012-2013; degradation for SWH larger than 5 meters because there is almost no population of data is available above these SWH values.....	66

Figure 3.18 sigma0 difference maps versus radial velocity and SWH: Difference between Test-1 (GPOD) and Test-2 (Phase-2) for Pacific regions years 2012-2013.....	66
Figure 3.19 sigma0 difference between Test-1 (GPOD) and Test-2 (Phase-2) as a function of Phase-2 SWH for Pacific regions years 2012-2013.....	67
Figure 3.20 SSH precision (std) maps versus radial velocity and SWH: (left) Test-2 data and (right) Test-1 (GPOD) data for Pacific regions years 2012-2013.....	68
Figure 3.21 SSH precision as a function of Test-1 SWH for both Test-1 (GPOD) and Test-2 (Phase-2) data sets (Pacific regions, years 2012-2013).....	68
Figure 3.22 SWH precision (std) maps versus radial velocity and SWH: (left) Test-2 data and (right) Test-1 (GPOD) data for Pacific regions years 2012-2013.....	69
Figure 3.23 SWH precision as a function of Test-1 SWH for both Test-1 (GPOD) and Test-2 (Phase-2) data sets (Pacific regions, years 2012-2013).....	69
Figure 3.24 Sigma0 precision (std) maps versus radial velocity and SWH: (left) Test-2 data and (right) Test-1 (GPOD) data for Pacific regions years 2012-2013.....	70
<b>Figure 3.25 Sigma0 precision as a function of Test-1 SWH for both Test-1 (GPOD) and Test-2 (Phase-2) data sets (Pacific regions, years 2012-2013).</b> .....	70
Figure 4.1 USSH noise as a function of distance to the coast using no misfit .....	74
Figure 4.2 USSH noise as a function of distance to the coast using a misfit filter of less than 3. ....	74
<b>Figure 4.3 USSH noise as a function of distance to the coast using the RDSAR dataset</b> .....	75
Figure 4.4 USSH noise as a function of SWH (top panel) for SAR Phase 2 (isardSAT) dataset in the North East Atlantic Region. The corresponding distribution (bottom panel) is the percentage in the number of the events occurring within a bin interval (i.e., 0.2 m SWH) relative to the maximum number of events occurring as shown. The inshore waters relate to the left plots, the offshore (open ocean) waters represent the right plots. ....	77
Figure 4.5 USSH noise as a function of SWH (top panel) for Phase 1 (G-POD) dataset in the North East Atlantic Region. The corresponding distribution (bottom panel) is the percentage in the number of the events occurring within a bin interval (i.e., 0.2 m SWH) relative to the maximum number of events occurring as shown. The inshore waters relate to the left plots, the offshore (open ocean) waters represent the right plots. ....	77
Figure 4.6 CryoSat SAR Phase 2 USSH and SWH as a function of the angle of approach to the coastline for the North East Atlantic region for 2012 to 2013 where 0° and ± 90° represents normal and parallel to the coast, respectively .....	79
Figure 4.7 CryoSat SAR G-POD Phase 1 USSH and SWH as a function of the angle of approach to the coastline for the North East Atlantic region for 2012 to 2013 where 0° and ± 90° represents normal and parallel to the coast, respectively.....	80
Figure 4.8 The percentage of the CryoSat SAR Phase 2 data rejected when applying a misfit threshold of 3 from USSH and SWH parameter fields as a function of the angle of approach and distance to the coastline for the North East Atlantic region for 2012 to 2013 where 0° and 90° represents normal and parallel to the coast, respectively. ....	81
Figure 4.9 The percentage of CryoSat SAR G-POD (Phase 1) data rejected when applying a misfit threshold of 3 to the USSH and SWH parameter fields as a function of the angle of approach and distance to the coastline for the North East Atlantic region for 2012 to 2013 where 0° and 90° represents normal and parallel to the coast, respectively.....	81
Figure 5.1 SLA (left) and SWH (right) for Test1 SAR Dataset against RDSAR TUDaBo/TALES .....	84
Figure 5.2 Noise and number of observations of Test1 RDSAR (left) and Test1 SAR Dataset (right).....	84
Figure 5.3 Standard deviation of sea level anomalies as function of distance to coast for BSH model, Test 1 Database SAR and RDSAR/TUDaBo .....	85

Figure 5.4 SLA for Test1 SAR Dataset (bottom left) against RDSAR TUDaBo/TALES (top left) and their scatterplot (right). .....	85
Figure 5.5 Scatterplot of Test1 RDSAR/Delft against Test1 SAR Dataset (left) and noise and number of points in RDSAR/TUDaBo-TALES .....	86
Figure 5.6 Scatterplot of sea level anomalies in open ocean (10-20 km) of Helgoland tide gauge against Test1 SAR, Test1 RDSAR and the external SAR/GPOD-SAMOSAS+ and RDSAR/TUDaBo-TALES Dataset.....	86
Figure 5.7 Correlation (left) and standard deviation (right) between tide gauge Helgoland and Test1 SAR, Test1 RDSAR, external SAR/GPOD-SAMOSAS+ and RDSAR/TUDaBo-TALES Dataset. The dashed line gives the number of points, which increases with distance to coast.....	86
Figure 5.8 Comparison of four geophysical parameter (Uncorrected SSH, SWH, wind speed and backscatter) along the selected ground-track of SCOOP Test 1 RDSAR-Delft and in-house RDSAR-BMLE3. ....	87
Figure 5.9 SAR Test 2 dataset: Noise with Hamming (left) and zero-padding (right).....	87
Figure 5.10 SAR Test 2 final dataset: Noise for combined Hamming and zero-padding .....	88
Figure 5.11 Noise and number of data as function of distance to coast for RDSAR Test 1 (left) and Test2 (right) datasets.....	88
Figure 5.12 In-situ validation of Test 2 RDSAR (above) and Test 2 SAR (below) sea level in coastal zone in range 5-10 km (left) and 10-20 km (right) from coast.....	89
Figure 5.13 In-situ validation of Test 2 RDSAR (above) and Test 2 SAR (below) SWH in coastal zone in range 5-10 km (left) and 10-20 km (right) from coast .....	90
Figure 5.14 In-situ validation of RDSAR/TUDaBo-TALES (above) and TEST1 SAR/GOD (below) SWH in coastal zone in range 5-10 km (left) and 10-20 km (right) from coast .....	90
Figure 6.1 Harvest platform location and Cryosat-2 SAR mask Harvest_-00 (since 15/12/2015). The area of the SAR zone is 356 429 km <sup>2</sup> (ocean+land). .....	92
Figure 6.2 Misfit parameter at 20 Hz as a function of the uncorrected sea surface height (altitude – range) at 20 Hz in the Phase 2 SAR dataset (6 months of data) in Harvest. The colours indicate misfit thresholds. ....	94
Figure 6.3 Misfit parameter at 20 Hz as a function of the significant wave height at 20 Hz in the Phase 2 SAR dataset (6 months of data) in Harvest. The colours indicate misfit thresholds. ....	94
Figure 6.4 Number (left) and percentage (right) of altimeter points at 20 Hz as a function of the misfit parameter in the Phase 2 SAR dataset (6 months of data) in Harvest.....	95
Figure 6.5 Statistics on the along-track differences of the uncorrected sea surface height (altitude - range) at 20 Hz (in m) from the SCOOP Phase 1 and Phase 2 SAR datasets in the Harvest region. ....	95
Figure 6.6 Significant wave heights (in m) measured at the Harvest platform calibration site over the period of the SCOOP datasets (mid-Dec. 2015 to end Dec. 2016).....	96
Figure 6.7 Comparison between the significant wave heights (in m) from the IOWAGA model and the buoy located at the Harvest platform calibration site. ....	97
Figure 6.8 Selection of CryoSat altimeter points depending on their distance to the Harvest platform calibration site .....	97
Figure 6.9 Generic diagram of the regional CALVAL method developed by NOVELTIS. ....	98
Figure 6.10 Altimeter SSH absolute bias estimates timeseries (in cm) at the Harvest calibration site, for the SCOOP phase 2 SAR dataset. The colors on the upper plot show the distance (in km) to the tide gauge at the altimetry points considered for the bias computation. The colors on the lower plot show the significant wave height (in m) measured at the Harvest platform at the date of the bias estimates. The grey line shows the mean of the bias estimates. ....	100
Figure 6.11 Comparison between the altimeter SSH and the Harvest in situ SSH (in m) for the SCOOP phase 2 SAR dataset. The colors on the upper plot show the distance (in km) to the tide gauge at the altimetry points	

---

considered for the bias computation. The colors on the lower plot show the significant wave height (in m) measured at the Harvest platform at the date of the bias estimates. ....	101
Figure 6.12 Significant wave heights time series (in m) at the Harvest calibration site, for the SCOOP Phase 1 and Phase 2 SAR datasets and for the in situ buoy. Selection of altimetry points within 20 km off the Harvest calibration site. ....	102
Figure 6.13 Comparison between the SCOOP Phase 1 (blue) and Phase 2 (red) SAR significant wave height observations at 20 Hz and the Harvest in situ significant wave height measurements. ....	103
Figure 6.14 Statistics on the along-track differences of the uncorrected sea surface height (altitude - range) at 20 Hz (in m) from the SCOOP Phase 2 SAR and coastal SAR datasets in the Harvest region. ....	104
Figure 6.15 Difference between the uncorrected sea surface heights (altitude - range) at 20 Hz (in m) from the SCOOP Phase 2 SAR and coastal SAR datasets in the Harvest region. The segment of track encircled in red is shown in more details in Figure 16. ....	105
Figure 6.16 Along-track uncorrected sea surface height (altitude - range) at 20 Hz (in m) from the SCOOP Phase 2 SAR and coastal SAR datasets for a segment of track located close to the coast (cf. Figure 15).....	105
Figure 6.17 Difference between the Pearson correlations at 20 Hz (in %) from the SCOOP Phase 2 SAR and coastal SAR datasets in the Harvest region. The segment of track encircled in red is shown in more details in Figure 18. ....	106
Figure 6.18 Along-track Pearson correlation at 20 Hz (in %) from the SCOOP Phase 2 SAR and coastal SAR datasets for a segment of track (cf. Figure 17).....	106
Figure 6.19 Uncorrected sea surface height (altitude - range) at 20 Hz (in m) from the SCOOP Phase 1 RDSAR dataset in the Harvest region. ....	108
Figure 6.20 Uncorrected sea surface height (altitude - range) at 20 Hz (in m) from the SCOOP Phase 2 RDSAR dataset in the Harvest region. ....	108
Figure 6.21 Statistics on the along-track differences of the uncorrected sea surface height (altitude - range) at 20 Hz (in m) from the SCOOP Phase 1 and Phase 2 RDSAR datasets in the Harvest region.....	109
Figure 6.22 Sea surface height anomaly at 20 Hz (in m) from the SCOOP Phase 1 RDSAR dataset in the Harvest region. ....	110
Figure 6.23 Sea surface height anomaly at 20 Hz (in m) from the SCOOP Phase 2 RDSAR dataset in the Harvest region. ....	110
Figure 6.24 Statistics on the along-track differences of the uncorrected sea surface height (altitude - range) at 20 Hz (in m) from the SCOOP Phase 2 RDSAR MLE3 and MLE4 datasets in the Harvest region. ....	111
Figure 6.25 Comparison between the SCOOP Phase 2 RDSAR MLE3 (blue) and MLE4 (red) significant wave height observations at 20 Hz (left) and at 1 Hz (right), and the Harvest in situ significant wave height measurements.....	112
Figure 7.1 GPD wet tropospheric correction (m) for CryoSat-2, for the various ROI, spanning the year 2012....	116
Figure 7.2 Top left: location of analysed CS2 passes over the Agulhas ROI. Top right: spatial pattern of SLA variance differences at crossovers (difference between SLA computed with GPD+ and SLA computed with ECMWF Op). Bottom left: SLA variance difference at crossovers (mean cycle values), between SLA computed with GPD and that computed with ECMWF-Op. Bottom right: SLA variance differences (GPD-ECMWF-Op), function of distance from coast. ....	116
Figure 7.3 Top left: location of analysed CS2 passes over the Central Pacific ROI. Top right: spatial pattern of SLA variance differences at crossovers (difference between SLA computed with GPD+ and SLA computed with ECMWF Op). Bottom left: SLA variance difference at crossovers (mean cycle values), between SLA computed with GPD and that computed with ECMWF-Op. Bottom right: SLA variance differences (GPD-ECMWF-Op), function of distance from coast. ....	117
Figure 7.4 Top: location of analysed CS2 passes over the East Pacific ROI. Middle: spatial pattern of SLA variance differences at crossovers (GPD- ECMWF Op). Bottom left: SLA variance difference at crossovers	

- (mean cycle values), between SLA computed with GPD and that computed with ECMWF-Op. Bottom right: SLA variance differences (GPD-ECMWF-Op), function of distance from coast..... 118
- Figure 7.5 Top left: location of analysed CS2 passes over the Harvest ROI. Top right: spatial pattern of SLA variance differences at crossovers (GPD- ECMWF Op). Bottom left: SLA variance difference at crossovers (mean cycle values), between SLA computed with GPD and that computed with ECMWF-Op. Bottom right: SLA variance differences (GPD-ECMWF-Op), function of distance from coast..... 119
- Figure 7.6 Top left: location of analysed CS2 passes over the Indonesia ROI. Top right: spatial pattern of SLA variance differences at crossovers (GPD- ECMWF Op). Bottom left: SLA variance difference at crossovers (mean cycle values), between SLA computed with GPD and that computed with ECMWF-Op. Bottom right: SLA variance differences (GPD-ECMWF-Op), function of distance from coast..... 120
- Figure 7.7 Left: location of analysed CS2 passes over the North Indian Coast ROI. Top right: spatial pattern of SLA variance differences at crossovers (GPD- ECMWF Op). Bottom left: SLA variance difference at crossovers (mean cycle values), between SLA computed with GPD and that computed with ECMWF-Op. Bottom right: SLA variance differences (GPD-ECMWF-Op), function of distance from coast. .... 121
- Figure 7.8 Top left: location of analysed CS2 passes over the North Sea ROI. Top right: spatial pattern of SLA variance differences at crossovers (GPD- ECMWF Op). Bottom left: SLA variance difference at crossovers (mean cycle values), between SLA computed with GPD and that computed with ECMWF-Op. Bottom right: SLA variance differences (GPD-ECMWF-Op), function of distance from coast..... 122
- Figure 7.9 Top left: location of analysed CS2 passes over the East Atlantic ROI. Top right: spatial pattern of SLA variance differences at crossovers (GPD- ECMWF Op). Bottom left: SLA variance difference at crossovers (mean cycle values), between SLA computed with GPD and that computed with ECMWF-Op. Bottom right: SLA variance differences (GPD-ECMWF-Op), function of distance from coast..... 123
- Figure 7.10 Top left: location of analysed CS2 passes over the West Pacific ROI. Top right: spatial pattern of SLA variance differences at crossovers (GPD- ECMWF Op). Bottom left: SLA variance difference at crossovers (mean cycle values), between SLA computed with GPD and that computed with ECMWF-Op. Bottom right: SLA variance differences (GPD-ECMWF-Op), function of distance from coast..... 124
- Figure 7.11 WTC variance difference at C2/J2 Xovers with  $\Delta T < 180$  min (GPD-ECMWF-Op), for the various ROI: (1) Agulhas, (2) Central Pacific, (3) East Pacific, (4) Harvest, (5) Indonesia (6) North Indian Coast, (7) North Sea (8) Northeast Atlantic (9) West Pacific. .... 125
- Figure 7.12 RMS differences between WTC from GNSS at coastal stations and those from ECMWF op model (blue) and from GPD+ (red) at nearby altimetric points. From top to bottom and left to right, results for the following ROI are shown (inside brackets the number of stations used for each corresponding ROI): Agulhas (1), Harvest (35), Indonesia (4), North Indian Coast (8), North Sea (57), Northeast Atlantic (41) and West Pacific (3). For the Central pacific and East Pacific, no analyses are shown since these are open ocean regions, without any coastal GNSS station. .... 126
- Figure 7.13 S3A points for cycle 06 with invalid MWR observations: green – land contamination; blue – ice contamination; pink – rain, outliers or additional condition such as all points above latitude  $70^{\circ}$ N or below  $70^{\circ}$ S..... 129
- Figure 7.14 Spatial coverage of match points between S3A and GMI with time difference  $\Delta T < 45$  min and distance  $\Delta D < 50$  km, for S3A cycles 01-26, used in this study (~455000 points). Colour scale indicates WPD differences between the GMI and S3A in cm. .... 130
- Figure 7.15 WPD from S3A versus WPD from GMI (right) and versus WPD GMI - WPD S3A (left). Scale factor: 1.004; Offset: 0.13 cm. .... 130
- Figure 7.16 Top panel: time evolution of the WPD from the GMI (blue) and S3A (pink). Bottom panel: time evolution of WPD differences between GMI and S3A. Colour bars refer to periods when the GMI/S3A match points are all located at high latitudes (green points in Figure 7.3.5) or low latitudes (orange points in Figure 7.3.5) to which correspond smaller or larger WPD variability..... 131
- Figure 7.17 Match points between GMI and S3A. Colours correspond to different time periods, indicated in Figure 7.3.4 by the corresponding colour bars ..... 132
- Figure 7.18 Time evolution of daily and 27-day RMS of the WPD differences between GMI and S3A. .... 132

Figure 7.19 Spatial coverage of crossovers between S3A and J3 with time difference $\Delta T < 45$ min and distance $\Delta D < 50$ km, for S3A cycles 01-26, used in this study (~27500 points). .....	133
Figure 7.20 WPD from S3A versus WPD from J3 (left) and versus WPD J3 - WPD S3A (right). Scale factor: 1.01. ....	133
Figure 7.21 Time evolution of daily and 27-day RMS of the WPD differences between J3 and S3A. RMS $WTC(J3) - WT(S3A) = 1.3$ cm. ....	134
Figure 7.22 WTC (in m) for S3A pass 340, cycle 06: ECMWF, MWR, and GPD (GPD1 in the top plot, GPD2 in the bottom plot) function of latitude. ....	135
Figure 7.23 WTC (in m) for S3A pass 462, cycle 06: ECMWF, MWR, and GPD (GPD1 in the top plot, GPD2 in the bottom plot) function of latitude. ....	136
Figure 7.24 Spatial distribution of the RMS values of the WPD differences (cm) between GPD1 and S3A MWR, for cycles 01 to 26. ....	137
Figure 7.25 Time evolution of the RMS differences between the S3A MWR-based WTC and those from GPD1 and ECMWF. ....	137
Figure 7.26 Top panel: Variance differences at crossovers for each S3A cycle, between GPD1 (no S3A MWR used) and ECMWF and between GPD2 (with S3A MWR) and ECMWF. Bottom panel: SLA variance differences for each S3A cycle, between GPD1 (no S3A MWR used) and ECMWF and between GPD2 (with S3A MWR) and ECMWF. ....	139
Figure 7.27 Top panel: Variance differences at crossovers for each Envisat cycle, between GPD1 (no Envisat MWR used) and ERA Interim and between GPD2 (with Envisat MWR) and ERA Interim. Bottom panel: SLA variance differences for each Envisat cycle, between GPD1 (no Envisat MWR used) and ERA Interim and between GPD2 (with Envisat MWR) and ERA Interim. ....	140
Figure 7.28 Top panel: SLA variance differences function of latitude between GPD1 (no S3A MWR used) and ECMWF and between GPD2 (with S3A MWR) and ECMWF, over the period of S3A cycles 01 to 26, using all points. Bottom panel: SLA variance differences versus distance from coast for datasets computed using the WTC from MWR and ECMWF, GPD1 and ECMWF and GPD2 and ECMWF, over the period of S3A cycles 01 to 26. In the first case, only valid MWR points were selected while in the last two cases all points with valid SLA were used. ....	141
Figure 7.29 From top to bottom and left to right: WTC (in m) for S3A cycle 06 passes 485, 553, 646 and 660, function of latitude. Shown WTC are: ECMWF (blue), MWR (red), GPD1 (black) and Composite (green). .	142
Figure 7.30 Points with Composite WTC out of limits for S3A cycle 06 (24% of the points with valid SLA. ....	143
Figure 7.31 Location of a set of 60 GNSS stations used in this study (adapted from Vieira et al. (2019)). The background map represents the RMS of wet path delay (WPD) in cm. ....	144
Figure 7.32 RMS of differences between WTC from GNSS and WTC from S3A MWR (red), from GPD1 (back dots) and from GPD2 (grey squares) at coastal stations (Baseline 2.27, cycles 1 to 26). Land contamination occurs in the MWR up to 20-25 km from coast. ....	144

# 1 Introduction

## 1.1 Purpose and scope

The ESA Sentinel-3 mission is the second satellite to operate a Delay Doppler mode altimeter based on a CryoSat-2 heritage, but the first one to cover the whole Open Ocean, providing high resolution and high precision of the ocean surface topography, at least along the satellite track direction. Contrarily to CryoSat-2, the Sentinel-3 payload includes a dual frequency altimeter radar (in Ku and C band) (for ionospheric corrections), and a microwave radiometer (for water vapor correction) that will help to reduce range errors and to derive more accurate Sea Surface Height estimations.

The SCOOP project aims to characterize the expected performance of Sentinel-3 SAR-mode altimeter products as generated by the current Sentinel-3 data processing over open ocean, and then to develop, test and evaluate new processing schemes that would provide enhanced performance compared with the baseline (quantifying their skills and drawbacks).

A Cal/Val plan process is established with regard to the different data sets to be considered in the assessment. It includes two phases:

- a) an assessment of the existing Sentinel-3 altimetry processing (in SAR mode and PLRM) over the Open Ocean, and
- b) an analysis of the innovative algorithms by comparison with the reference data sets defined in the preceding phase.

The Product Validation Report (Phase 2) describes the results of the performance assessment of the Phase 2 test data set (CryoSat-2 FBR data with modified processing applied), or the “First Test Data Set”.

## 1.2 Document structure

This document is structured into an introductory chapter followed by seven chapters describing:

- The results of the open ocean and coastal zone validation analysis carried out by CLS in WP 5100, WP5400
- The results of the open ocean validation analysis carried out by isardSAT as part of WP3000 and WP4000
- The results of the coastal zone validation analysis carried out by NOC/SATOC/SKYMAT in WP6200
- The results of the open ocean and coastal zone validation analysis for data in the German Bight carried out by U Bonn in WP5400, and WP6400
- The results of the Performance Assessment of Sea State Impact on Altimeter Retrieved SSH carried out by Noveltis in WP6300
- The results of the WTC validation carried out by U Porto in WP7000.
- Overall Summary of Performance of the Second Test Data Set

## 1.3 References

SCOOP Product Validation Plan: SAR Altimetry Coastal & Open Ocean Performance Exploitation and Roadmap Study. Sentinel 3 For Science – SAR Altimetry Studies Study 2 – Coastal Zone and Open Ocean Study. Project Deliverable D2.4, December 2016.

SCOOP Proposal: SAR Altimetry Coastal & Open Ocean Performance Exploitation and Roadmap Study. Sentinel 3 For Science – SAR Altimetry Studies Study 2 – Coastal Zone and Open Ocean Study. Proposal, January 2015.

Abdalla, S., et al., (2016). "Does Swell Impacts Significant Wave Height Measurements from SAR Altimetry?", SAR Altimetry Workshop, October 31.

Aouf, L., and L. Phalippou, (2015). "On the signature of swell for the Cryosat-2 SAR-mode wave data", Ocean Surface Topography Science Team 2015, October 19-23.

Boy, F., J. D. Desjonquères, N. Picot, T. Moreau, and M. Raynal (2017a). "CryoSat-2 SAR-Mode Over Oceans: Processing Methods, Global Assessment, and Benefits," in IEEE Transactions on Geoscience and Remote Sensing, vol. 55 (1), pp. 148-158.

Boy, F., et al, (2017b). "New stacking method for removing the SAR sensitivity to swell", Ocean Surface Topography Science Team 2017, October 23-27.

Brown, S.; Islam, T. (2017). "Jason-3 GDR calibration stability enabled by the cold sky maneuvers". In Proceedings of the Ocean Surface Topography Science Team Meeting, Miami, FL, USA, 24 October, 2017.

Cipollini, P. (2011). A new parameter to facilitate screening of coastal altimetry data and corrections. Presented at the 5th Coastal Altimetry Workshop, San Diego, USA, available from [http://www.coastalt.eu/sites/default/files/sandiegoworkshop11/poster/P08\\_Cipollini\\_Coastal\\_Proximity.pdf](http://www.coastalt.eu/sites/default/files/sandiegoworkshop11/poster/P08_Cipollini_Coastal_Proximity.pdf)

Cipollini, P. and F.M. Calafat (2016) CP4O – Cryosat Plus 4 Oceans WP4000 Extended evaluation of the CryoSat-2 SAR data in the Coastal Zone. CCN1. ESA AO/1-6827/11/I-NB

CLS (2011). "Surface Topography Mission (STM) SRAL/MWR L2 Algorithms Definition, Accuracy and Specification", 1 June 2011, Ref: S3PAD-RS-CLS-SD03-00017, Iss: 8.0; CLS: Ramonville St-Agne, France.

Cotton, D. et al., (2008). "Development of SAR Altimetry Mode Studies over Ocean, Coastal Zones and Inland Water - State of the Art Assessment", <http://www.satoc.eu/projects/samosa/docs/SAMOSATN01-V1.0full.pdf>

Davis, J.L.; Herring, T.A.; Shapiro, I.I.; Rogers, A.E.E.; Elgered, G. (1985). "Geodesy by radio interferometry—Effects of atmospheric modeling errors on estimates of baseline length". Radio Sci, 20, 1593–1607.

Dibarboure, G., F. Boy, J.D. Desjonqueres, S. Labroue, Y. Lasne, N. Picot, J.C. Poisson, and P. Thibaut (2014). "Investigating short-wavelength correlated errors on low-resolution mode altimetry", J. Atmos. Oceanic Technol., 31 (6), 1337–1362.

Dinardo, S., M. Restano, A. Ambrózio, and J. Benveniste, (2016). "SAR Altimetry Processing On Demand Service for CryoSat-2 and Sentinel-3 at ESA G-POD", Proc. Of the 2016 conference on Big Data from Space (BiDS'16), 312-315.

Dinardo S., Fenoglio-Marc L., Buchhaupt C., Becker M., Scharro R., Fernandez J. Benveniste J. (2018). CryoSat-2 performance along the German coasts, AdSR special Issue CryoSat-2, <https://doi.org/10.1016/j.asr.2017.12.018>, <https://authors.elsevier.com/c/1XXGm~6OiXQOF>

Dinardo, S., L. Fenoglio-Marc, C. Buchhaupt, M. Becker, R. Scharroo, M. Joana Fernandes, and J. Benveniste, (2018). "Coastal SAR and PLRM altimetry in German Bight and West Baltic Sea SAR Altimetry Processing on demand service for CryoSat-2 and Sentinel-3 at ESA G-POD", Adv. Space Res., 62 (6), pp. 1371-1404.

Donlon, C., B. Berruti, A. Buongiorno, M-H. Ferreira, P. Femenias, et al. (2012). "The Global Monitoring for Environment and Security (GMES) Sentinel-3 Mission", Remote Sensing of the Environment, 120, 27-57.

Dufau, C., Orsztynowicz, M., Dibarboure, G., Morrow, R. and P.-Y. Le Traon (2016), "Mesoscale resolution capability of altimetry: present and future", *J. Geophys. Res., Oceans*, 121 (7), pp. 4910-4927.

Dumont et al.: OSTM/Jason-2 Products Handbook, 4.2.6 Range Compression, <http://www.aviso.altimetry.fr/en/data/product-information/aviso-user-handbooks.html>, 2016.

Egido, A., W.H.F. Smith, and E. Leuliette (2017). "Pulse-to-Pulse Correlation Effects on high PRF Low Resolution Mode Altimeters", Ocean Surface Topography Science Team meeting 2017, October 23-27.

EUMETSAT (2017). "Sentinel-3a Product Notice—STM I2 Marine ("Spring Reprocessing Campaign)". Available online: [um/ops-sen3/doc/17/944329](http://um/ops-sen3/doc/17/944329) (accessed on 15 September. 2017).

Fenoglio-Marc, L., Dinardo, S., Scharroo, R., Roland, A., Dutour, M., Lucas, B., Becker, (2019). The German Bight: a validation of CryoSat-2 altimeter data in SAR mode, *Advances in Space Research*, doi: <http://dx.doi.org/10.1016/j.asr.2015.02.014>

Fenoglio L., Dinardo S., Buchhaupt C., Uebbing B., Scharroo R., Kusche J., Becker M. and Benveniste J. (2019). Calibrating CryoSat-2 and Sentinel-3A sea surface heights along the German coast, IAG Proceedings, Springer Verlag

Fernandes, M.J.; Lázaro, C. (2018) "Independent Assessment of Sentinel-3A Wet Tropospheric Correction over the Open and Coastal Ocean". *Remote Sens.*, 10, 484.

Fernandes, M. J., and C. Lázaro, (2016). "GPD+ Wet Tropospheric Corrections for CryoSat-2 and GFO Altimetry Missions", *Remote Sensing*, 8(10), 851; doi:10.3390/rs8100851 (<http://www.mdpi.com/2072-4292/8/10/851>).

Fernandes, M. J., Lázaro, C., Ablain, M., Pires, N. (2015). "Improved wet path delays for all ESA and reference altimetric missions". *Remote Sensing of Environment*, 169, 50-74. doi:10.1016/j.rse.2015.07.023

Fernandes, M.J., Nunes, A. N., & Lázaro, C. (2013a). Analysis and Inter-Calibration of Wet Path Delay Datasets to Compute the Wet Tropospheric Correction for CryoSat-2 over Ocean. *Remote Sensing*, 5(10), 4977-5005. doi:10.3390/rs5104977

Fernandes, M.J.; Pires, N.; Lázaro, C.; Nunes, A.L. (2013b). "Tropospheric delays from GNSS for application in coastal altimetry". *Adv. Space Res.*, 51, 1352–1368.

Gommenginger, C., Cipollini, P. and Snaith. H. CP4O – Cryosat Plus 4 Oceans WP4000 Product Development and Validation - SAR Altimetry over the Open Ocean & the Coastal Zone Product Validation Report (PVR), v 1.0, 23 June 2014, CP4O\_WP4\_SAR\_OpenOceanCoastal\_PVR\_v1.0, available from <http://www.satoc.eu/projects/CP4O/deliverables.html>

Kouba, J. (2008). "Implementation and testing of the gridded vienna mapping function 1 (vmf1)". *J. Geod.*, 82, 193–205.

Labroue, S., M. Raynal, A. Philip, M. Ablain, I. Pujol, T. Moreau, P. Féménias, and F. Boy, (2017). "Characterization of the errors of Sentinel-3A small scale content in SAR mode", Ocean Surface Topography Science Team 2017, October 23-27.

Meissner, T.; Wentz, F.J.; Draper, D. (2012). "GMI Calibration Algorithm and Analysis Theoretical Basis Document", Report Number 041912, 124 pp; Remote Sensing Systems: Santa Rosa, CA, USA.

Mercier, F. (2004). "Amélioration de la Correction de Troposphère Humide en Zone Côtière". Rapport Gocina; CLS-DOS-NT-04-086; 2004, CLS: Ramonville St-Agne, France. (In French)

Moreau, T., et al, (2017). "Investigation of SWH bias in SAR altimetry mode", Ocean Surface Topography Science Team 2017, October 23-27.

Moreau, T., N. Tran, J. Aublanc, C. Tison, S. Le Gac, and F. Boy (2018). "Impact of long ocean waves on wave height retrieval from SAR altimetry data", *Adv. Space Res.*, 62 (6), pp. 1434-1444.

Passaro, M.; Cipollini, P.; Vignudelli, S.; Quartly, G. and H. Snaith (2014) ALES: a multi-mission adaptive subwaveform retracker for coastal and open ocean altimetry. *Remote Sensing of Environment*, 145. 173- 189.10.1016/j.rse.2014.02.008.

Poisson, J. C., F. Piras, P. Thibaut, S. Le Gac, F. Boy, and N. Picot, "New powerful numerical retracker solution accounting for speckle noise statistics," Ocean Surface Topography Science Team 2016, La Rochelle, France, Oct./Nov.

Raney, R.K. (1998). "The delay/Doppler radar altimeter", *IEEE Trans. Geosci. Remote Sens.*, 36, 1578–1588.

Ray, C., C. Martin-Puig, M. P. clarizia, G. Ruffini, S. Dinardo, C. Gommenginger, and J. Benveniste, (2015). "SAR Altimeter Backscattered Waveform Model", *IEEE Trans. GeoSci. And Rem. Sens.*, 53 (2), 911–919.

Ray, C., et A. Egido, (2018). "Waveform model for fully focused SAR altimetry", *Ocean Surface Topography Science Team 2018*, September 27-28.

Raynal, M., S. Labroue, T. Moreau, F. Boy, and N. Picot (2018). "From conventional to delay doppler altimetry: a demonstration of continuity and improvements with Cryosat-2 mission", *Adv. Space Res.*, 62 (6), pp. 1564-1575.

Schall J, Locher A, Kusche J, Rietbroek R, Sudau A (2016) Consistency of Geoid Models, Radar Altimetry, and Hydrodynamic Modelling in the North Sea. *Marine Geodesy* 39(3-4):223{237, DOI 10.1080/01490419.2016.115233

Scharroo, R., E.W. Leuliette, J.L. Lillibridge, D. Byrne, M.C. Naeije, and G.T. Mitchum, (2013). "RADS: consistent multi-mission products", *Proc. of the Symposium on 20 Years of Progress in Radar Altimetry*, ESA SP-710, ESA Publications Division, European Space Agency, Noordwijk, The Netherlands.

Smith, W.H.F., and R. Scharroo (2015). "Waveform Aliasing in Satellite Radar Altimetry", *IEEE Trans. GeoSci. And Rem. Sens.*, 53 (4), 1671–1682.

Stum, J.; Sicard, P.; Carrere, L.; Lambin, J. (2011). "Using objective analysis of scanning radiometer measurements to compute the water vapor path delay for altimetry". *IEEE Trans. Geosci. Remote Sens.*, 49, 3211–3224.

Vieira, T., Fernandes, M. J., Lázaro, C. (2019). "Independent assessment of on-board Microwave Radiometer measurements in coastal zones using tropospheric delays from GNSS". *IEEE Trans. on Geoscience and Remote Sensing.* 57(3), 1804-1816. doi:10.1109/TGRS.2018.2869258.

Wingham, D. J., C. R. Francis, S. Baker, C. Bouzinac, D. Brockley, R. Cullen, P. de Chateau-Thierry, S. Laxon, U. Mallow, C. Mavrocordatos, L. Phalippou, G. Ratier, L. Rey, F. Rostan, P. Viau, and D. Wallis (2006). "Cryosat: A mission to determine the fluctuations in Earth's land and marine ice fields," *Adv. Space Res.*, vol. 37, no. 4, pp. 841–871.

Xu, Y., and L.-L. Fu (2012), "The effects of altimeter instrument noise on the estimation of the wavenumber spectrum of sea surface height", *J. Phys. Oceanogr.*, 42, 2229–2233.

## 2 Open Ocean and Coastal Zone Validation of the SCOOP Second Test Data Set by CLS

### 2.1 Current state of knowledge and key challenges for SAR altimetry over ocean

The Synthetic Aperture Radar (SAR) altimeter is a new generation of radar altimeters providing a better along-track resolution (from few kms to around 300 m) and a higher signal-to-noise ratio (SNR) than that obtainable by conventional pulse-limited altimetry [Raney, 1998; Wingham et al., 2006]. This improvement in performance has been already demonstrated using satellite altimeter data from current missions (i.e. Cryosat-2 and Sentinel-3A/B), all showing at length and in depth the enhanced capabilities of this acquisition mode for monitoring ocean circulation and short oceanic scales [Dibarboure et al., 2014] as depicted in Figure 2.1. Those missions also allowed to underline the potential of SAR altimetry in coastal zones and sea-ice areas.

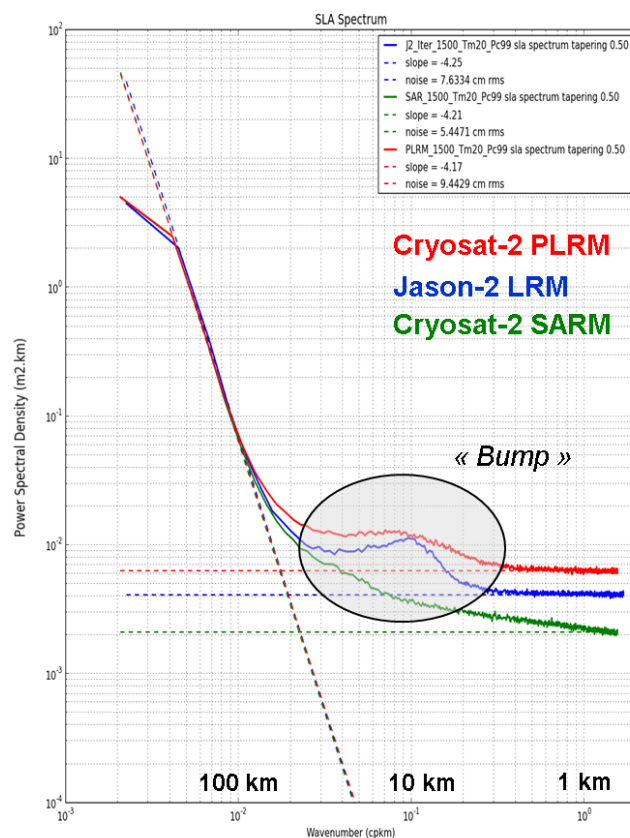


**Figure 2.1: Mean power spectral density for LRM, PLRM and SARM sea level anomalies computed as function of the wavenumber over the Agulhas area from March 2013 to December 2013. The spectral slopes (dashed lines) are calculated between 100 km and 200 km wavelength. The 20-Hz noise levels of energy (horizontal dashed lines) are estimated by fitting a plateau for wavelength between 700 m and 1 km. The correlated errors (spectral “bump”) impacting conventional altimetry data are located within the circle for wavelength from 7 km to 30 km [Raynal et al., 2018].**

The Cryosat-2 satellite, launched into Earth orbit in 2010, offered the first opportunity to gather observational evidence about the altimetric performance of SAR altimeters over ocean, though the amount of data to analyze has been - and still is - rather limited due to the restricted number of ocean and land areas operated in SAR mode, which additionally change dynamically with time (<http://cryosat.mssl.ucl.ac.uk/qa/mode.php>). The Sentinel-3A satellite, and more recently Sentinel-3-B satellite, both carrying a SAR radar altimeter of Cryosat heritage [Donlon et al., 2012], confirmed the benefits brought by SARM in global. So far, the results of the SAR mode have met all expectations, providing more detailed information about properties of the overflown surfaces than those seen from earlier satellite radar altimeters. Today the potential of this technic is unanimously acknowledged in the scientific community. There is now a trend toward more use of SAR altimeter in the future (as is the case for the upcoming Sentinel-3C/D and Sentinel-6 missions), contributing thus increasingly to the time series of ocean topography measurements.

Even if some noteworthy progress was made in SAR altimetry, current performance suggests that there is still room and need for improvement. Much work remains to be done to better exploit the capabilities of the SARM radar altimeter and enable greater benefits to be achieved. Improvements are foreseen in development of new algorithmic methods:

- to improve the precision of SAR-mode measurements, better than we have now (as seen in Figure 2.2), and
- additionally, enhance their spatial resolution (if it is not at maximum) to improve the observations of small-scale ocean structures.

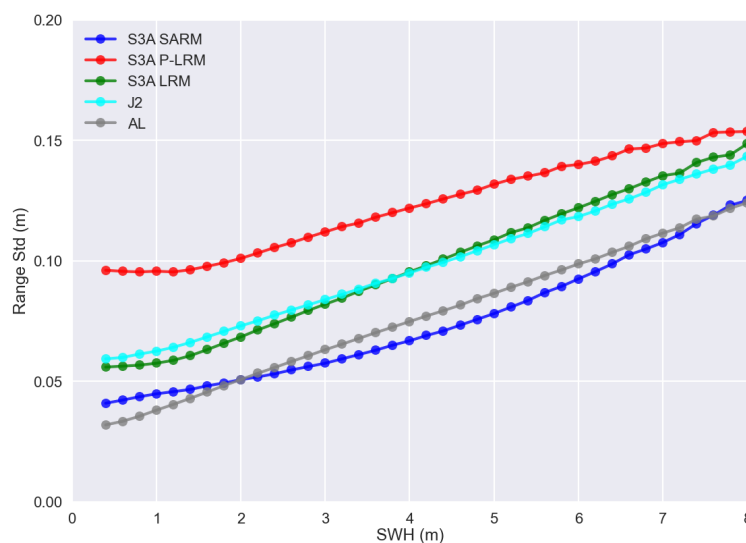


**Figure 2.2: 20-Hz noise of range for different missions (Jason-2, Saral, Sentinel-3A) and different acquisition modes (LRM, PLRM, SARM) [CLS internal communication].**

Further work is also needed to address issues that have been identified on SAR-mode measurements.

The first concern is to improve the accuracy of the significant wave height (SWH) retrieval. A bias of about 10-15 cm remains between SAR and LRM SWH estimates which more importantly depends on SWH (see Figure 2.3) suggesting an inconsistency between data and the retracking model. To date no correction for this bias has been made in SAR altimeter processing, but studies related to this issue are currently underway. Amongst the activities now in progress, mention may be made of those that tend to partially explain the SWH bias between SAR and PLRM, i.e. the correction of the range walk in the unfocused SAR processing [Moreau et al., 2017], the introduction of the vertical wave velocity into echo models [Ray et Egado., 2018], and the use of an exact maximum likelihood estimator [Poisson et al., 2016] in PLRM processing to account for the varying statistical properties over the waveform bins [Egado et Smith, 2017]. Those improvements have been recently presented

in scientific meetings with varying degree of maturity but are not addressed in the frame of this project. It is not yet envisaged to incorporate them in operational data processing either.

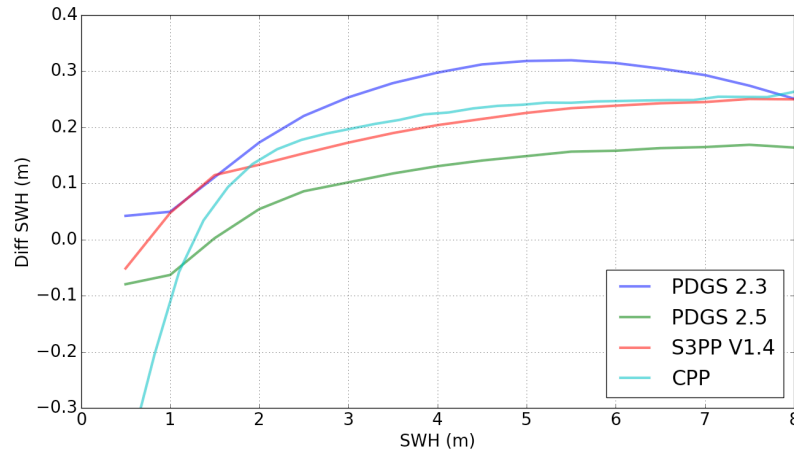


**Figure 2.3: Difference of SWH estimates between SAR and PLRM modes for different processing chains: Sentinel-3A ground segment with two different versions of the SAR altimeter retracker (PDGS 2.3 and 2.5), the CNES Sentinel-3 processing prototype (S3PP v1.4) and the CNES Cryosat-2 processing prototype (CPP) [CLS internal communication].**

The second issue concerns the sensitivity of the unfocused SAR altimeter measurements to long surface waves. Different studies conducted by different groups of the altimetry community converged to say that swell impacts SAR-mode altimetry [Aouf et Phalippou, 2015; Abdalla et al., 2016; Moreau et al., 2018], degrading the precision of SAR-mode measurements and very likely biasing SWH estimates. In spite of these first results, further studies have still to be done in order to gain a better understanding of this sea-state effect at global scales. No less importantly, it is necessary to assess whether such effect introduces or not spurious trends in the altimeter climate record given that altimeter missions increasingly migrate from LRM to SAR mode. This issue has to be carefully examined especially regarding the continuity with measurements obtained by conventional missions in the optic of deriving long term climatic time series.

It was the role of CLS to analyze in-depth the quality and performance of the new processing methodologies developed in the frame of the present study and assess whether they would better take advantage of the SAR-mode capabilities, and potentially overcome the limitation of the nominal processing approach over open ocean. Based upon this assessment, the SCOOP project may recommend to agencies innovative radar altimeter data processing to stimulate the generation of higher-level quality data for the upcoming Sentinel-3 C/D missions.

## 2.2 Summary of Approach

### 2.2.1 Data description

The validation of SARM processing with Cryosat-2 mission is not straightforward because the SAR mode is activated only over a few areas of the ocean. In this respect, the validation has been performed over a long time period, starting from January 2012 to December 2013, to increase and maximize the range of SWH conditions assessed. However, the limited geographical coverage does not account for the different ocean regimes, neither reflects the variability of the satellite orbital parameters. Therefore, risk that results may not be conclusive exists.

The following table lists the different types of data used through this assessment study.

Table 2.1 Data Sets Used in the CLS assessment

Nature	Description	Institution
<b>RDSAR altimeter processing (phase 2)</b>	<p>L1 processing: Similar to RADS RDSAR methodology [Scharroo et al., 2013] for which, unlike the Sentinel-3 baseline processing, a zero-padding of 2 is applied to return pulses to minimise the waveform aliasing [Smith and Scharroo, 2015].</p> <p>L2 processing: MLE3 retracker inherited from Jason-2 mission</p> <p>An enhanced product accounting for updated CAL1 and CAL2 values has been released but was not deemed useful to be evaluated since level-1 and 2 processing have not been changed (only corrected).</p>	<p>TU-Delft based on RADS development</p> <p><a href="http://rads.tudelft.nl">http://rads.tudelft.nl</a></p>
<b>Sentinel-3 SAR altimeter processing (phase 1)</b>	<p>L1B processing: Standard delay-Doppler level-1 processing exploiting Cryosat-2 data but configured as for the operational ocean processing of Sentinel-3 mission data</p> <p>L2 processing: SAR Level-2 retracker prototype with SAMOSA analytical model and Levmar least square estimator developed for the Sentinel-3 Ground Segment [Cotton et al., 2008; Ray et al., 2015] using a LUT to correct for the PTR Gaussian approximation</p>	<p>ESA G-POD SARvatore service [Dinardo et al., 2016]</p> <p><a href="https://gpod.eo.esa.int/services/CRYOSAT_SAR/">https://gpod.eo.esa.int/services/CRYOSAT_SAR/</a></p>
<b>Innovative SARM processing (phase 2)</b>	<p>L1B processing: Along-track Hamming window plus range oversampling by a factor 2 applied to the waveforms</p> <p>L2 processing IsardSAT SAR altimeter ocean retracker (based on Ray et al. [2015]) aligned with L1B processing and configured with fixed PTR setting: <math>\sigma_{al}=0.65</math> and <math>\sigma_{ac}=0.54351</math></p>	<p>Implemented by IsardSAT in a Sentinel-3-like processing prototype</p>
<b>GPD+ Wet Tropospheric Correction</b>	<p>The latest GNSS (Global Navigation Satellite Systems) derived Path Delay Plus (GPD+) algorithm to derive WTC for altimetric missions possessing or not an on-board MWR [Fernandes and Lázaro, 2016]</p>	<p>University of Porto</p>

Additionally, we used data from the Cryosat-2 processing prototype (version 14) from CNES over the 2-year selected period to enable comparison and validation of the reference data sets (phase 1). The processing for the CPP SAR and PLRM is fully described in Boy et al. [2017a] and validation results published in Raynal et al. [2018].

Note that the measurements from the different processing schemes have not been constructed at the same time tag, thus the datasets are not exactly collocated at 20-Hz preventing a direct comparison of their range through simple differences. Instead, we compared sea-level anomaly (SLA) measurements with each other, knowing that the maximum distance between 1-Hz measurements is 3 km which is acceptable for the analysis of large-scale errors but not optimized for detecting very small errors (in the order of centimetres or less) due to possible oceanic signal differences over this gap.

In addition, for the sake of consistency, only uncorrected SLA were considered. Comparing uncorrected (and near-collocated) SLA data from different processing approaches enabled to assess the quality of the altimeter derived parameters, without uncertainty related to possible discrepancies between geophysical corrections used in different data sets that would cast doubt on the results.

## 2.2.2 Methodology

### 2.2.2.1 Round Robin

The SCOOP project aims to characterize the expected performance of Sentinel-3 SAR-mode altimeter products as generated by the current Sentinel-3 data processing over open ocean, and then to develop, test and evaluate new processing schemes that would provide enhanced performance compared with the baseline.

A round robin validation exercise was performed by CLS to quantify skills and drawbacks of the different algorithms under study within the SCOOP project. Particular attention was paid on SAR altimetry measurement and the SARM innovative processing scheme to see whether it outperforms the state-of-art Sentinel-3 baseline or not over open ocean. This is part of the objectives of the project to make concrete and relevant recommendations to Sentinel-3 missions (and Sentinel-6), embarking a SAR radar altimeter, to better exploit the capabilities of this acquisition mode. It is also of importance to ensure that the reduced SAR mode (RDSAR) is fully consistent and valuable for maintaining the data quality continuity between SAR and LRM modes. This condition must be satisfied for enabling RDSAR data to be considered as a low-resolution measurement of reference during SARM observations.

For this study, two types of analysis have been performed, one related to the validation of the phase 1 test data set and the other one to the evaluation of phase 2 test data sets, using in both cases, tools and procedures commonly used for the altimetry product assessment as described in the Product Validation Plan. The first step was to perform stand-alone assessment of the Sentinel-3 baseline processing using SARM data only (phase 1), to check whether it does not present any additional error compared to CPP SARM processing. Then, we evaluated the improvements brought by the newly developed altimeter processing methods (SARM and RDSAR) and models (GPD+WTC) with respect to reference data (assessed in phase 1) through the use of the standard diagnoses established for this study. At the end of this round robin exercise we should be in position to clearly state the benefits of the innovative solutions or not. On that basis, the interest of their implementation into the Sentinel-3 baseline processing are discussed.

Different diagnoses were made to support the following objectives:

- (1) assess the continuity with conventional altimetry missions (by analysing large-scale biases compared to PLRM),
- (2) assess residual errors linked to key parameters for all processing,
- (3) assess the high-frequency improvements brought by the enhanced SARM processing,
- (4) evaluate the spectral content of the different parameters estimated from the waveforms.

To analyse and quantify the improved observational capabilities of the new data processing, diagnoses were conducted over the largest possible number of areas acquired in SARM of the Cryosat-2 mission. The selected areas are the following:

- Central Pacific
- North Atlantic
- Agulhas current
- West Pacific
- Indonesia sea

In this study most of the diagnoses except the spectral analysis were produced using 1-Hz observations (included in data sets) to ease the comparison and limit the impact of 20-Hz noise. On CPP side, the 1-Hz data sets used for comparison were created by using the same compression process as in the Jason-2 ground segment (Dumont et al., 2016).

### 2.2.2.2 Parameters used in the sensitivity study

In order to fully characterize the behaviour and possible errors of an altimeter processing, analyses of their sensitivity to sea state parameters (SWH, Sigma0) and to orbital/platform parameters (radial velocity, off-nadir pointing angles, altitude) have been conducted over the few regions operated in synthetic aperture radar (SAR) mode of the Cryosat-2 mission. Unlike the other parameters, the satellite radial velocity is not a parameter of the retracking model since it is supposed to be corrected appropriately at level-1 processing. However correction error would have a direct impact on the shape of the mean altimeter backscattered waveform making it inconsistent with the model. The analysis of this parameter is thus as important as the other ones.

The following figures (Figure 2.4 to Figure 2.7) illustrate the geographical distribution of those different parameters computed over two years (2012 and 2013) and averaged in 1° by 1° grid. Note that for the platform parameters, data are presented for ascending and descending passes of the satellite separately since parameter values differ over the same area.

Although SAR mode observations are available over a few oceanic regions, a large variation in parameter values is observed allowing to analyze the behavior of the different processing with respect to the different encountered sea state conditions and satellite position and viewing information. However, it may be that this analysis does not lead to clear conclusions particularly in situations where two parameters cannot be separated (caused by incomplete data coverage of the world ocean), preventing from analyzing the dependency with one of the two parameters.

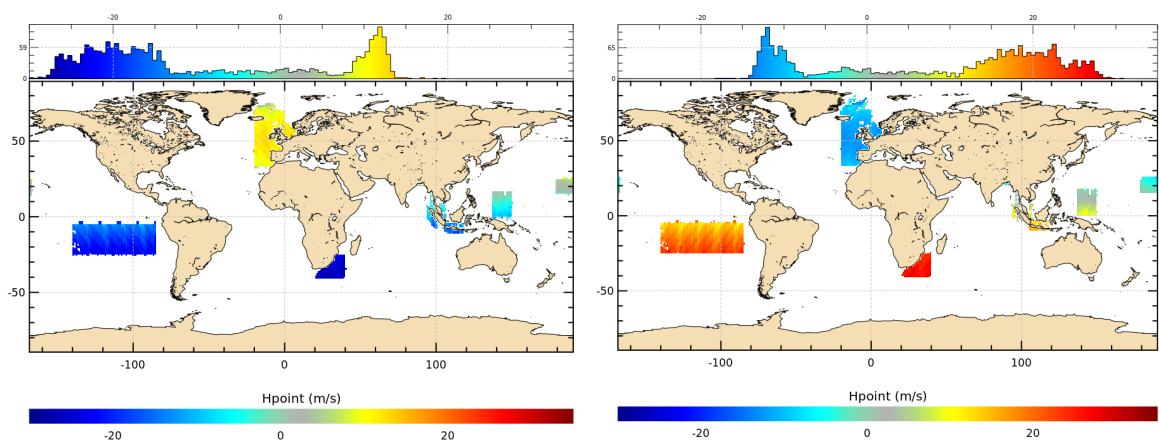


**Figure 2.4:** Map of averages of radial velocity provided by the orbit ephemeris for ascending (left) and descending (right) passes plotted from a 1° x 1° grid computed from January 2012 to December 2013.

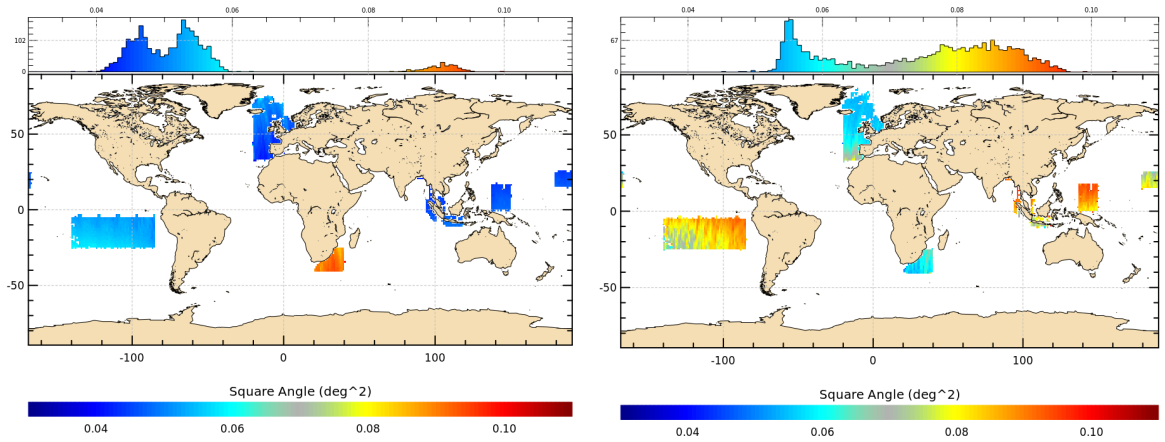


**Figure 2.5: Map of averages of squared mispointing angles for ascending (left) and descending (right) passes plotted from a 1° x 1° grid computed from January 2012 to December 2013.**

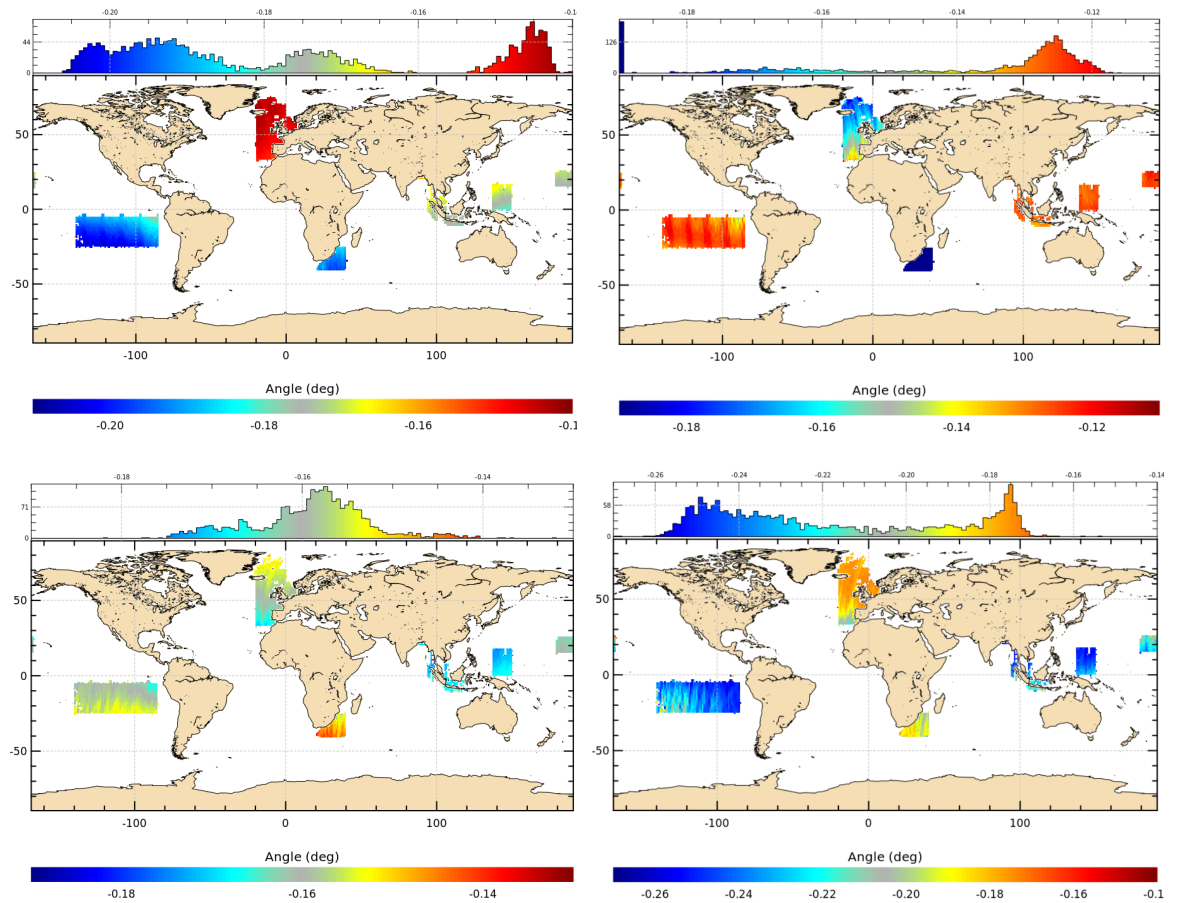


**Figure 2.6: Map of averages of pitch (left) and roll (right) angles for ascending (top) and descending (bottom) passes plotted from a 1° x 1° grid computed from January 2012 to December 2013.**

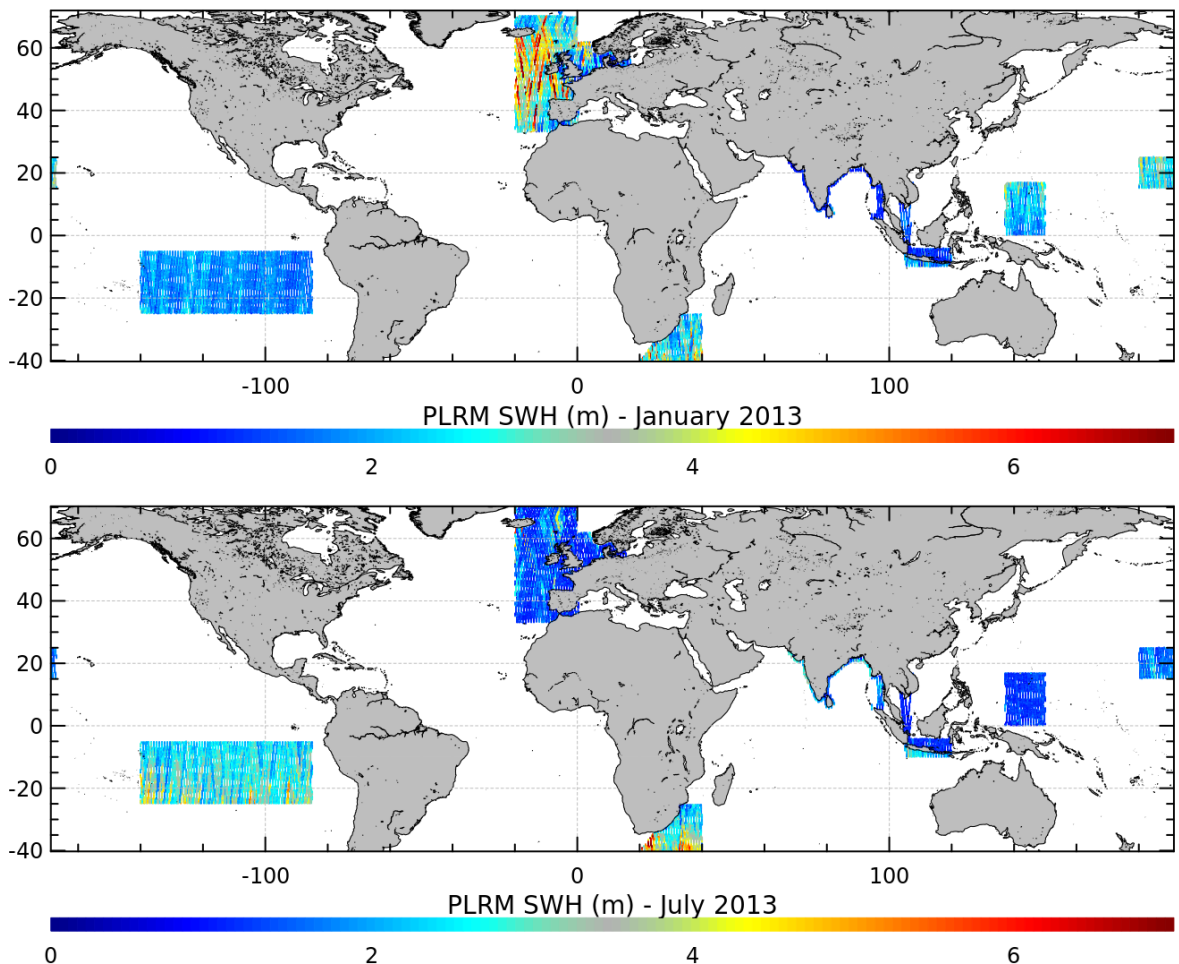


**Figure 2.7: Map of averages of SWH plotted from a 1° x 1° grid computed in January 2013 (top) and December 2013 (bottom).**

### 2.2.2.3 Edited data

Data editing is a methodology commonly used by altimetry users to remove altimeter measurements having lower accuracy in order to provide robust statistics. For this analysis, measurements from high latitudes were removed to avoid sea ice coverage. Furthermore, only data more than 100 km from the shoreline (and the points with a bathymetry lower than -1000 m) were selected to avoid the increased errors in the coastal zone. Additional editing was applied to make sure to filter out all data points for which the SLA value departs from the reference level beyond 1 m. This selection is severe but ensure to eliminate all outliers (that may be related to some spurious observations caused by sea ice, rain, blooms) and to reduce the effect of oceanic variability.

These editing criteria were applied to all data before their analysis.

## 2.3 Analysis of long-wavelength errors

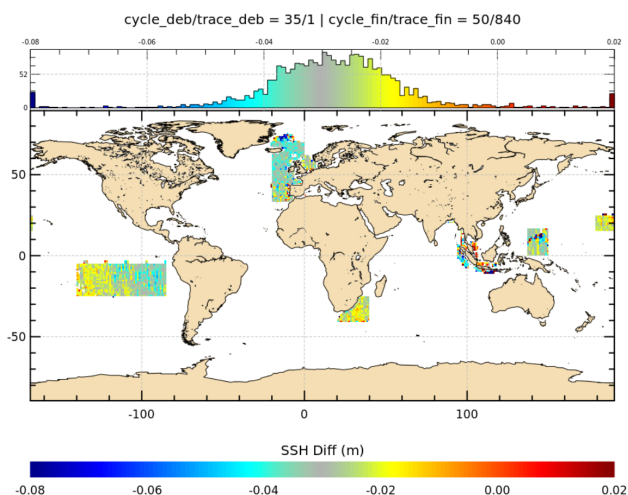
### 2.3.1 Assessment of TU-Delft RDSAR mode over ocean

This section aims at analysing the TU-Delft RDSAR solution in comparison with PLRM outputs of the Cryosat-2 processing prototype from CNES (CPP v14). The TU-Delft RDSAR and CPP PLRM measurements being not exactly collocated (0.5 s apart at maximum which is acceptable for the analysis of small/large scale errors) - preventing to analyze directly their range differences - we thus carried out the assessment of the altimeter-derived measurements through sea surface height (SSH) comparison at quasi-collocated surface locations (SSH being defined as the difference between orbit and range, but no corrections are applied). We also examined the difference of their sea state parameters (SWH and Sigma-0).

#### 2.3.1.1 Sea surface height analysis

The differences between TU-Delft RDSAR and CPP PLRM SSH are computed over two years and averaged in  $1^\circ$  by  $1^\circ$  grid for ascending and descending passes. Figure 2.8 shows the geographical distribution of these differences. Both maps exhibit a good agreement between both processing, showing variations less than 2 cm magnitude. A mean bias close to -3 cm is however observed (TU-Delft range being too long) likely to result from the uncorrected Point Target Response (PTR) approximation (see SWH analysis).

The maps of SSH difference, though low, present geographic pattern of 2 cm magnitude that does not seem to be correlated with the waves. Such residual errors could be linked to other parameters such as squared mispointing angle or radial velocity that are critical parameters in TU-Delft RDSAR processing since they are used as input parameters. In pseudo-low-resolution mode processing, the radial velocity is used to align return echoes within a radar cycle before the average of power is calculated (to obtain a mean 20-Hz waveform). The use of the altitude rate rather than the onboard tracker estimates as in conventional altimetry, allows to avoid blurring the waveform when the onboard tracker is failing to produce the exact rate of change of the range [Scharroo et al., 2013].



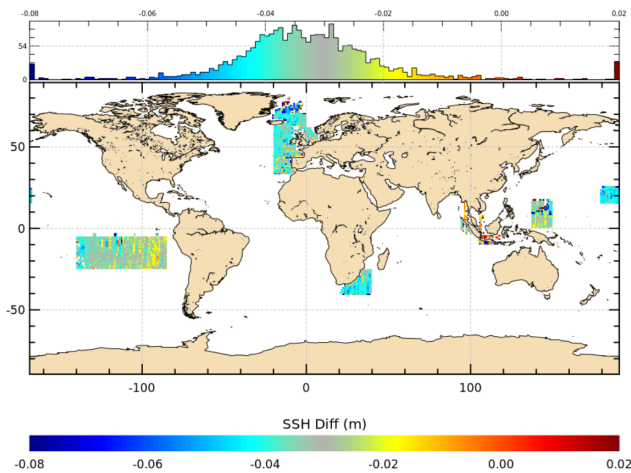


**Figure 2.8: Map of SSH difference between TU-Delft RDSAR and CPP PLRM for ascending (top) and descending (bottom) passes plotted from a 1° x 1° grid computed from January 2012 to December 2013.**

Figure 2.9 shows the SSH differences (in meter) binned per CPP PLRM SWH (x-axis) and radial velocity (y-axis) values. This kind of diagnosis is proved to constitute an important diagnostic tool to better separate the correlations between different parameters, especially when they are alike in some ways. On these plots, a slight dependency of the SSH difference as a function of the radial velocity is observed for ascending passes, but not clearly observed for descending passes. Same diagnosis has been performed with the squared mispointing angle, again without being able to identify any clear dependency. SWH estimates that are more sensitive to antenna mispointing angle would more likely to answer this question.

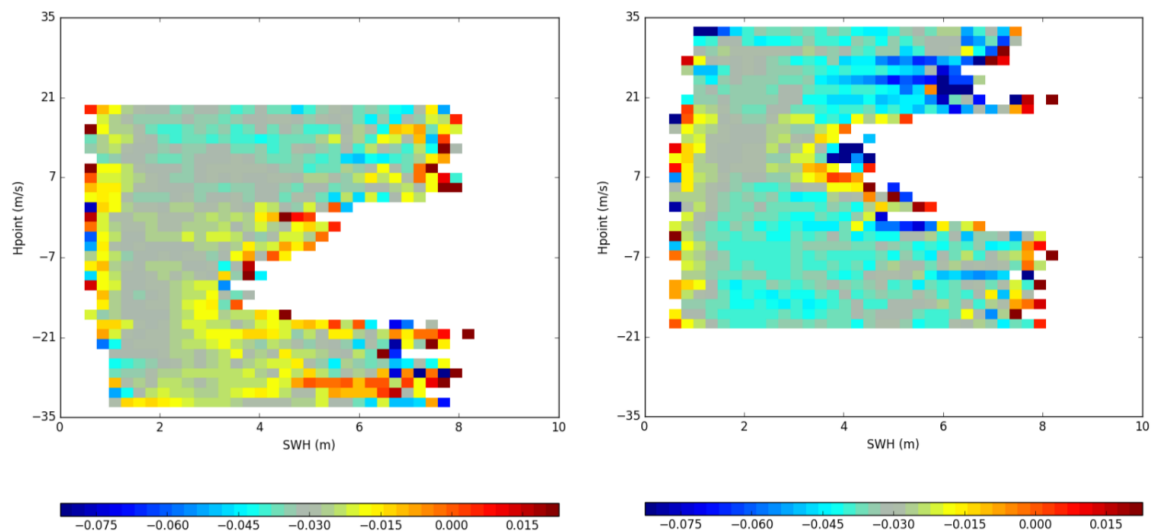
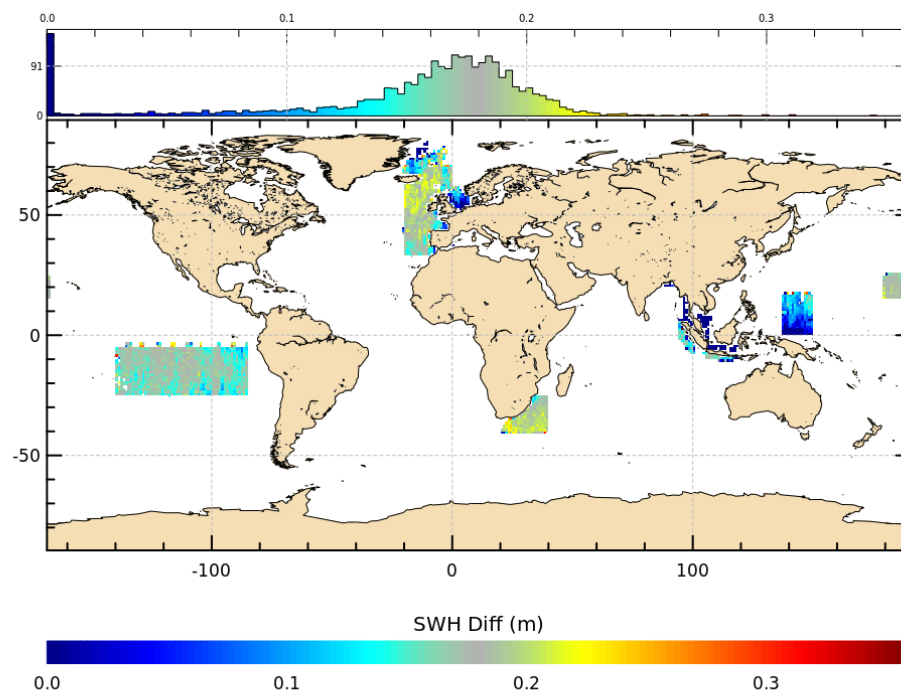


**Figure 2.9: SSH difference (m) between TU-Delft RDSAR and CPP PLRM binned per PLRM CPP SWH and radial velocity for ascending (left) and descending (right) passes.**

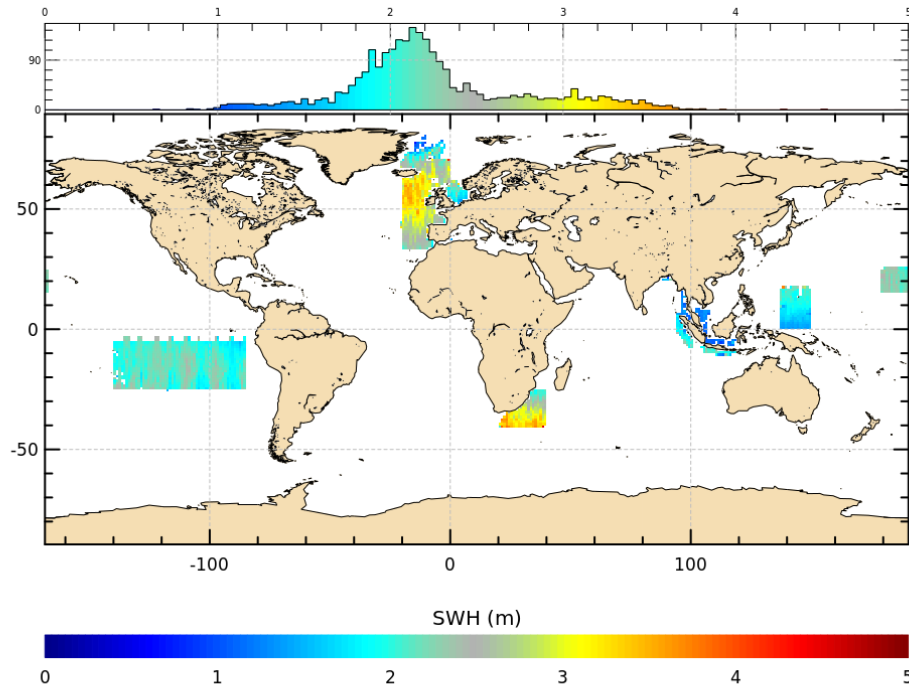
These results show that the TU-Delft RDSAR sea level varies geographically (discrepancy lower than 2 cm) and is biased (a -3 cm global bias) when compared to CPP PLRM outputs. The observed long wavelength errors are however difficult to correlate with parameters such as mispointing angle or radial velocity. More wave situations associated to different mispointing angles and radial velocities are needed to better characterize these discrepancies, and to assess whether this processing ensures a good continuity with conventional altimetry missions.

### 2.3.1.2 SWH analysis

The map of along-track differences between TU-Delft RDSAR and CPP PLRM SWH measurements is plotted from a  $1^\circ$  by  $1^\circ$  grid over the two-year time period (Figure 2.10). The map shows a clear correlation with SWH (plotted in Figure 2.11), with a negative difference for very low waves and close to +20 cm for stronger waves. Note that CPP PLRM waves are found to be too low by 5 cm with respect to Jason-2 waves for not accounting for the varying noise statistic throughout the waveform in the MLE retracker [Egido et al., 2017].

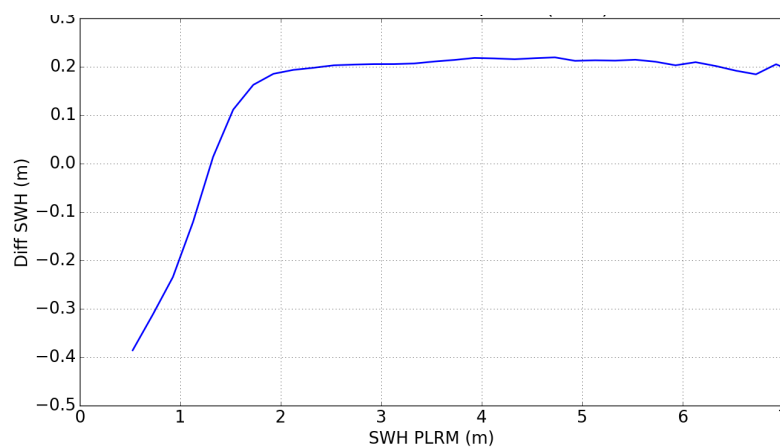


**Figure 2.10: Map of SWH difference between TU-Delft RDSAR and CPP PLRM (from ascending and descending tracks) plotted from a  $1^\circ \times 1^\circ$  grid computed from January 2012 to December 2013.**



**Figure 2.11: Map of averages of CPP PLRM SWH plotted from a 1° x 1° grid computed from January 2012 to December 2013.**

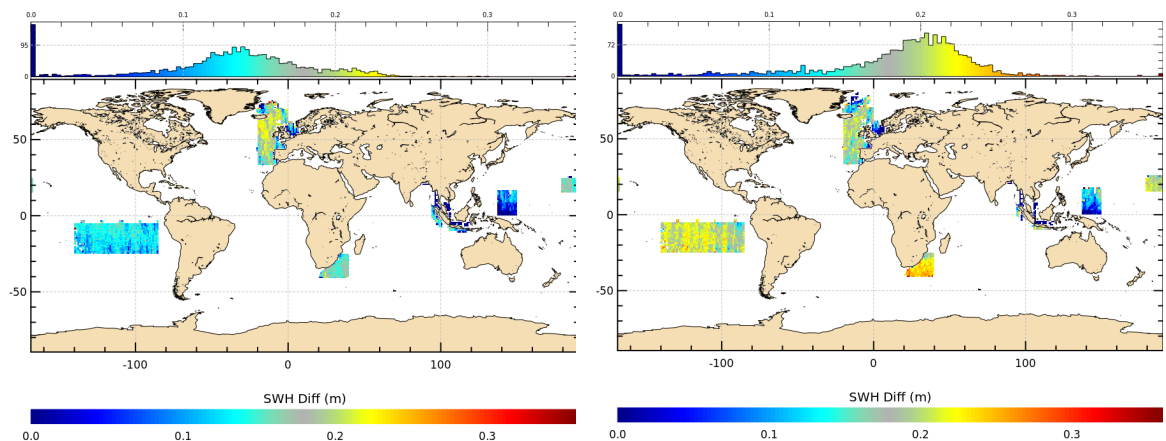
Figure 2.12 shows the SWH difference plotted as function of the PLRM SWH. The result observed is consistent with the previous conclusion derived from the maps. There is a linear error depending on the waves up to 2 m, and for stronger waves the bias saturates at a constant value. Assuming a constant bias of -5cm on the CPP PLRM SWH, this curve shows that the TU-Delft RADS SWH overestimates waves by 15 cm for SWH higher than 2 m. The difference is reduced to zero and then inverted with decreasing SWH. It may be observed that the difference is very similar to the correction Lookup table applied to SWH estimates in conventional altimetry (to account for the Gaussian approximation of the PTR in the analytical Brown ocean retracker). As such, we strongly assume that the TU-Delft RADS SWH estimates and the other retrieved parameters are not corrected from the PTR approximation (the correction is smaller than 2 cm in CPP PLRM range and few hundredths of dB in CPP PLRM sigma-0).



**Figure 2.12: Average of SWH difference between TU-Delft RADSAR and CPP PLRM datasets as function of CPP PLRM SWH computed from January 2012 to December 2013.**

The sensitivity to the other parameters is also analyzed, separating ascending and descending passes for parameters depending on satellite pass (having different values at the same location between ascending and descending). We focused mainly on possible correlation with mispointing angle derived from the star tracker because this is a parameter that can induce errors in the TU-Delft RDSAR retracking since the off-nadir platform angle information is used as input of the RADS RDSAR model. Thereby, any error in this parameter would affect the estimated parameters.

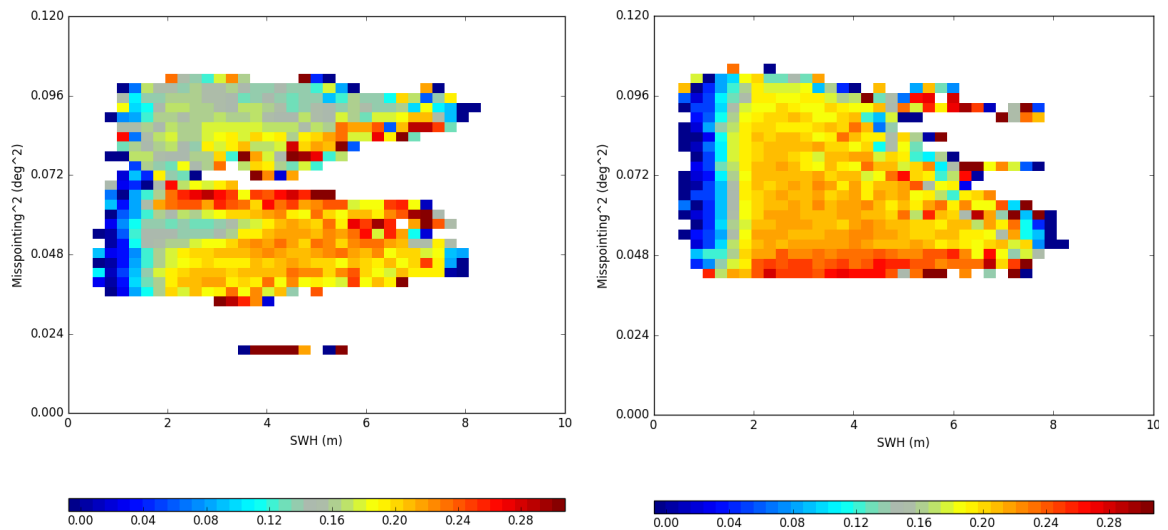
Figure 2.13 Figure 2.12 shows the SWH differences between TU-Delft RDSAR and CPP PLRM for ascending and descending passes over the same period. It appears clearly that the differences depend, in addition to SWH, on non-sea state parameters as the values differ at the same location between ascending and descending passes.



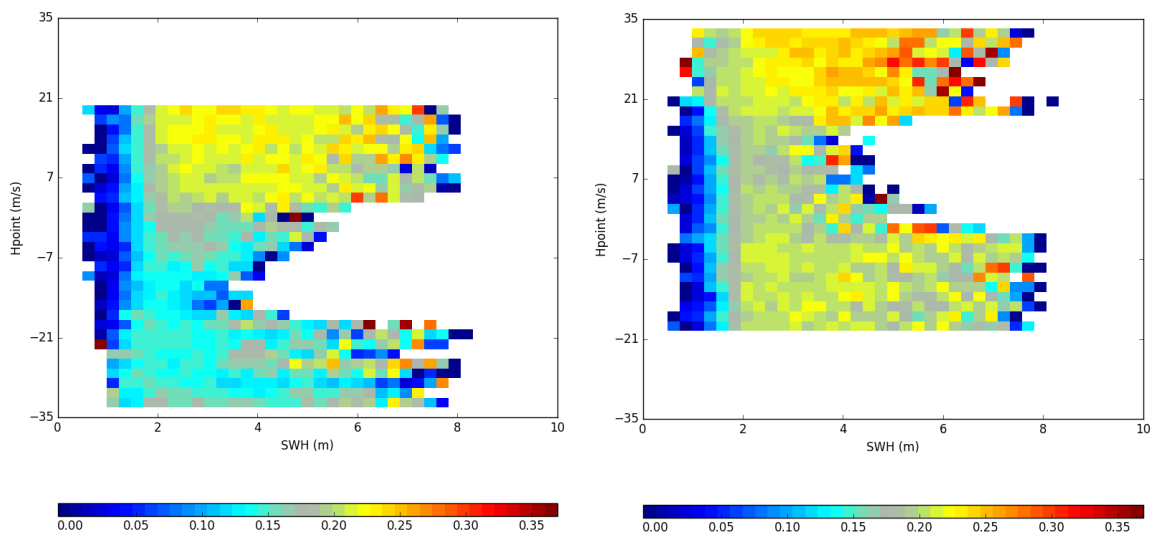
**Figure 2.13: Map of SWH difference for ascending (left) and descending (right) passes plotted from a  $1^\circ \times 1^\circ$  grid computed from January 2012 to December 2013.**

Figure 2.14 shows the SWH differences (in meter) binned per CPP PLRM SWH and squared mispointing values. We can see the correlation with SWH that dominates the plots. At a lesser extent, these figures also exhibit a mispointing dependency. It seems that lower mispointing angle is correlated with higher discrepancies. However, the range scale of mispointing is low and prevents from drawing clear conclusion on the dependency with the platform attitude.

The sensitivity to the radial velocity of the satellite is also analyzed. Figure 2.15 shows the correlation with CPP PLRM SWH and radial velocity. Apart from the correlation with SWH, no other clear correlation is found. The ascending passes exhibit, however, variations wrt radial velocity, but these effects are much less pronounced for the descending passes (with also differing values for the same altitude rate). This analysis should be completed over a wider sea coverage in order to get more wave situations associated to different mispointing angles and radial velocities.



**Figure 2.14: SWH difference (m) between TU-Delft RDSAR and CPP PLRM binned per PLRM CPP SWH and squared mispointing angle for ascending (left) and descending (right) passes.**



**Figure 2.15: SWH difference (m) between TU-Delft RDSAR and CPP PLRM binned per PLRM CPP SWH and radial velocity for ascending (left) and descending (right) passes.**

### 2.3.1.3 Sigma-0 analysis

The quality of the backscattered coefficient (Sigma-0) estimates from the TU-Delft RDSAR processing is analyzed with the same types of diagnoses. Along-track differences between TU-Delft RDSAR and CPP PLRM datasets are computed then averaged in  $1^\circ$  by  $1^\circ$  grid for ascending and descending passes. Figure 2.16 shows the geographical distribution of these differences. Both maps exhibit a mean bias of around  $-5.3$  dB, TU-Delft RDSAR Sigma-0 being lower than CPP PLRM Sigma-0. Figures also show low variations of  $0.2$  dB magnitude that depend on the areas and the type of tracks and are likely to be correlated with the radial velocity of the satellite as well as with the antenna pointing angles derived from the star tracker information (see maps in Figure 2.4 and Figure 2.5) with no evident dominance among these two parameters. Indeed, if the ascending and descending Pacific are perfectly correlated with the radial velocity, the patterns do not match in all regions. In addition, although the ascending and descending maps for the altitude rate shows similar range of variations (but of opposite signs), the spread of the sigma0 difference distributions differs

and is less for ascending passes which is quite homogeneous. The spread seems to reflect more closely the difference of variations in the maps of the squared mispointing angle.

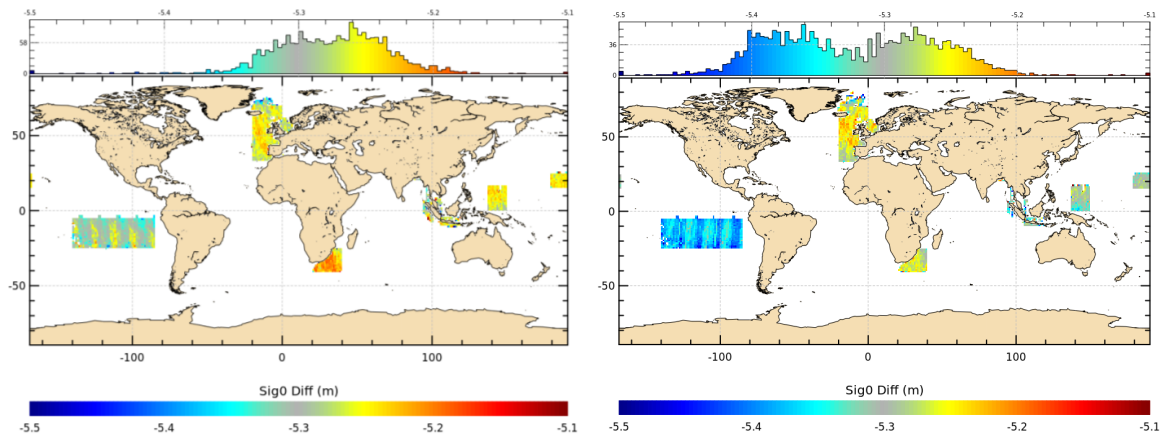


**Figure 2.16: Map of Sigma-0 difference for ascending (left) and descending (right) passes plotted from a 1° x 1° grid computed from January 2012 to December 2013.**

Also note that the sigma-0 bias variation along the segments is linked to the waves as we can see on Figure 2.17 showing the Sigma-0 differences binned per PLRM SWH values. The dependence with respect to the waves is close to 3.3%SWH for waves between 1 m and 4 m. This plot also confirms that the absolute bias between TU-Delft RDSAR and CPP PLRM is close to -5.3 cm, but with different values for ascending and descending passes (higher mean negative value for descending) as already observed on the maps, since the geographical variations depend on the orbit orientation of the satellite.

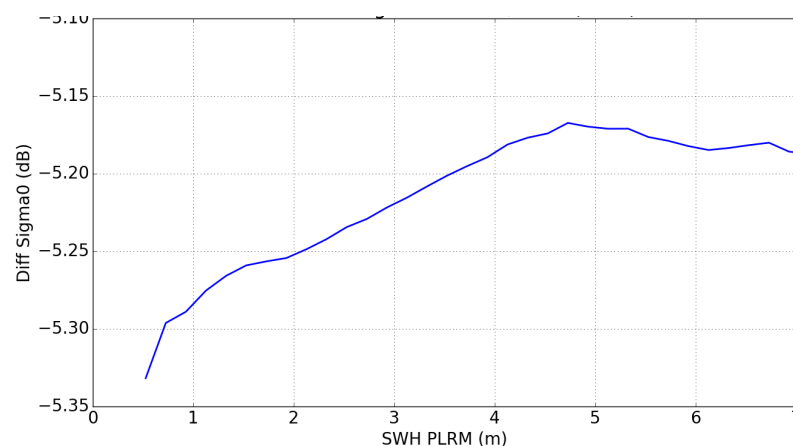


**Figure 2.17: Average of Sigma-0 difference between TU-Delft RDSAR and CPP PLRM datasets as function of CPP PLRM SWH computed from January 2012 to December 2013.**

### 2.3.2 Assessment of GPOD SARM over ocean

This section aims at analysing the GPOD SARM solution in comparison with SARM outputs of the Cryosat-2 processing prototype from CNES (CPP v14). The assessment is performed through SSH, SWH and Sigma-0 comparison at quasi-collocated surface locations.

### 2.3.2.1 Sea surface height analysis

The maps of the difference between GPOD SARM and CPP SARM SSH are given in Figure 2.18 for ascending and descending passes. Both maps exhibit an excellent agreement between both processing, showing variations lower than 1 cm magnitude. This result suggests that GPOD SARM SSH does not exhibit any long wavelength errors, nor present a sea state bias different from the CPP SARM. Note however a mean bias of 2.3 cm (GPOD SARM range being shorter) which is fairly constant from low to high SWH. This value, regardless of how small it is, is not explained and could be due to the many differences in processing approaches. It is not clear if this difference is due to GPOD SARM residual errors or if it comes from both GPOD and CPP processing. But in view of the great consistency between both processing, GPOD SARM sea level can be safely used as a reference to assess the range measurement derived from the innovative SARM processing.

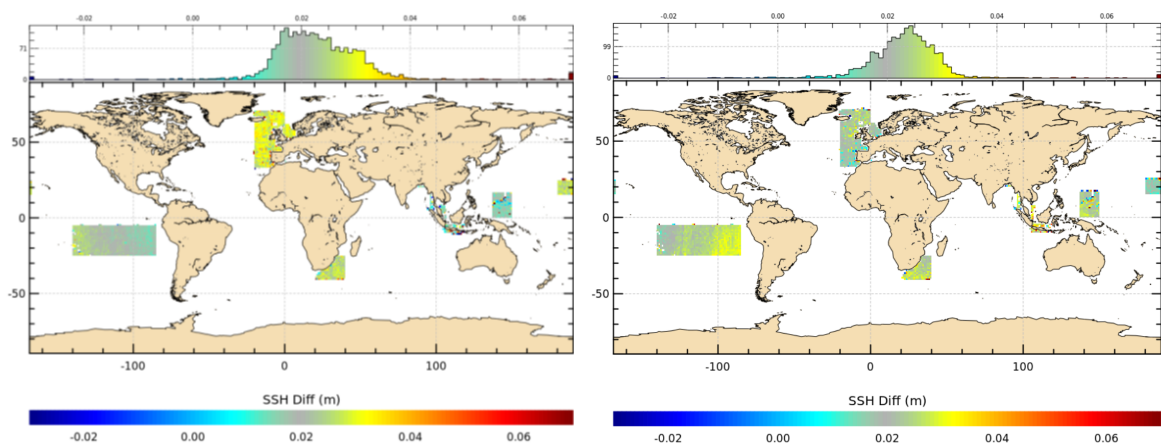


Figure 2.18: Map of SSH difference for ascending (left) and descending (right) passes plotted from a  $1^\circ \times 1^\circ$  grid computed from January 2012 to December 2013.

### 2.3.2.2 SWH analysis

The differences between GPOD SARM and CPP SARM SWH measurements are plotted in Figure 2.19 for ascending and descending passes. The maps show the very good consistency between processing, with differences of only a few cm magnitudes. The two maps also reveal a slight variation of the SWH values that depend on the areas and the type of tracks, but which is not clearly linked to any particular parameters.

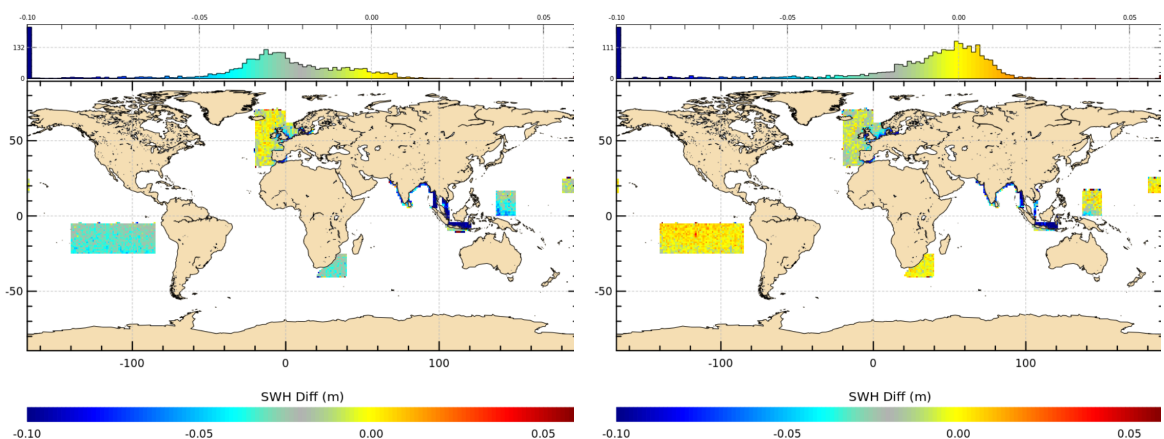
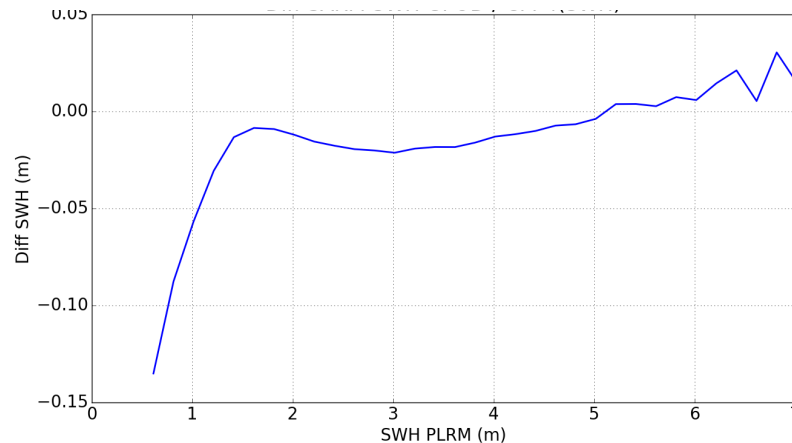


Figure 2.19: Map of SWH difference for ascending (left) and descending (right) passes plotted from a  $1^\circ \times 1^\circ$  grid computed from January 2012 to December 2013.

Figure 2.20 shows the SWH difference plotted as a function of the PLRM SWH. This curve shows the very good agreement between processing, as already observed on the maps. Also note a noticeable SWH difference at very low wave height, GPOD SARM SWH being lower. But we cannot conclude if this difference comes either from GPOD processing or CPP or both of them.

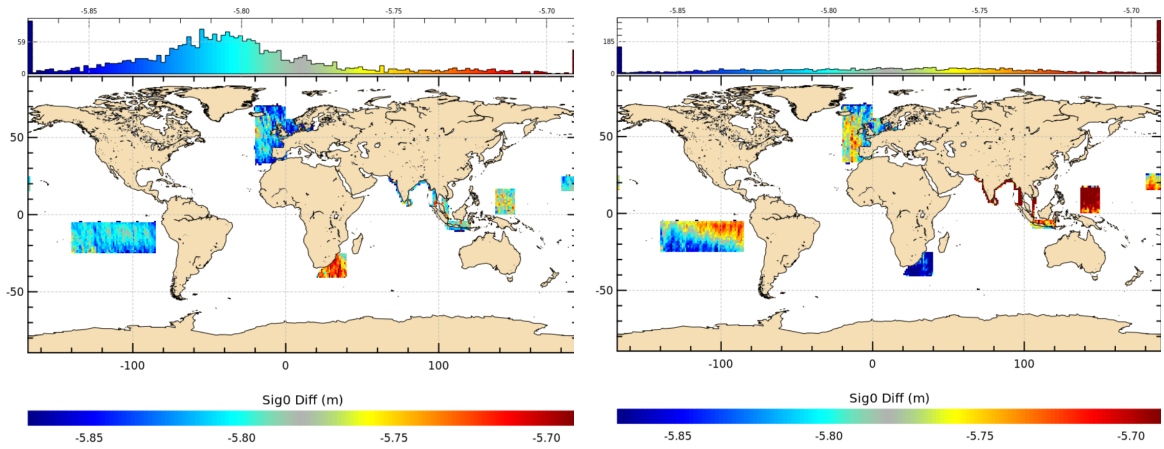


**Figure 2.20: Average of SWH difference between GPOD SARM and CPP SARM datasets as function of CPP PLRM SWH computed from January 2012 to December 2013.**

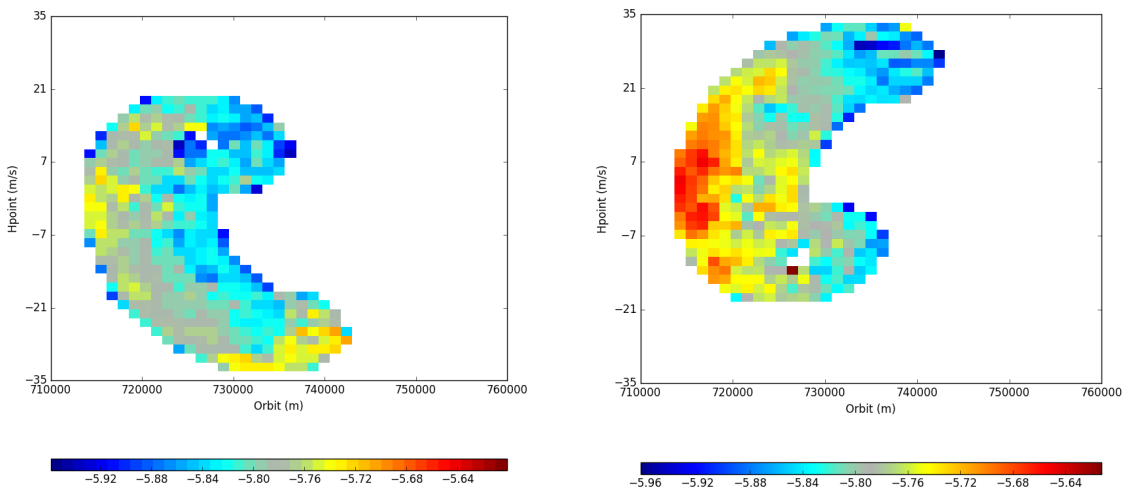
### 2.3.2.3 Sigma-0 analysis

Figure 2.21 shows the difference of Sigma-0 for ascending and descending passes. Both maps exhibit a mean bias close to -5.79 dB, GPOD SARM Sigma-0 being lower than CPP SARM Sigma-0. Note that the CPP SARM Sigma-0 was biased to the Jason-2 mean value but there can still have residual bias of a few tens of dB since SAR-mode acquisition is operated only over few areas that are not representative of the global ocean.

The maps also reveal small geographical variations of the difference. These variations are of only 0.2 dB magnitude and depend on the areas and the type of tracks. The patterns are found to be correlated with the orbit of the satellite as shown in Figure 2.22 (perfectly observed on descending passes but more difficult to detect on ascending passes). Also note a slight dependency of the Sigma-0 differences (less than 0.1 dB) with respect to the waves for SWH higher than 2 m as evidenced in Figure 2.23. On the other side, the Sigma-0 differences binned per orbit and radial velocity values do not exhibit any link to radial velocity. To further understand if this difference is explained by the orbit taken into account in the unfocused SAR-mode processing, a wider data coverage with more wave situations associated to different orbit values are needed. We also have to determine if such an error of 0.2 dB comes either from the GPOD SARM processing or the CPP SARM processing or both of them. At the moment, this difference is within our existing understanding for the SARM Sigma-0 accuracy and thus does not need further investigation.



**Figure 2.21: Map of Sigma-0 difference for ascending (left) and descending (right) passes plotted from a 1° x 1° grid computed from January 2012 to December 2013.**



**Figure 2.22: Sigma-0 difference (m) between GPOD SARM and CPP SARM binned per orbit and radial velocity for ascending (left) and descending (right) passes.**

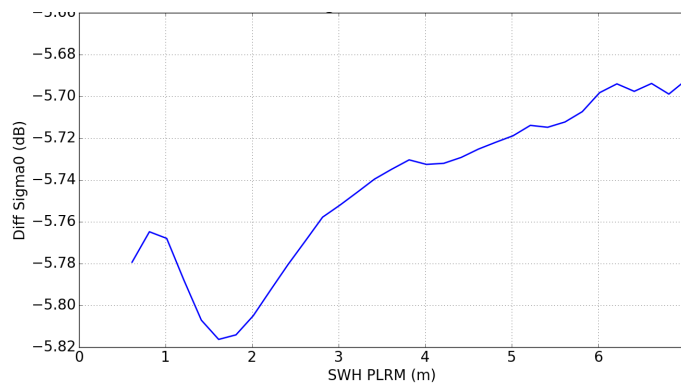


**Figure 2.23: Average of Sigma-0 difference between GPOD SARM and CPP SARM datasets as function of CPP PLRM SWH computed from January 2012 to December 2013.**

## 2.3.3 Assessment of the innovative SARM over ocean

This section aims at analysing the innovative SARM solution from IsardSAT in comparison with GPOD SARM outputs validated previously. The assessment is performed through SSH, SWH and Sigma-0 comparison at quasi-collocated surface locations.

### 2.3.3.1 Sea surface height analysis

The differences between innovative SARM and GPOD SARM SSH are given in Figure 2.24 for ascending and descending passes. Both maps show an excellent agreement between the two SARM processing, without any geographical variations of the difference. We can however notice a mean bias of -1.5 cm, innovative SARM range being longer.

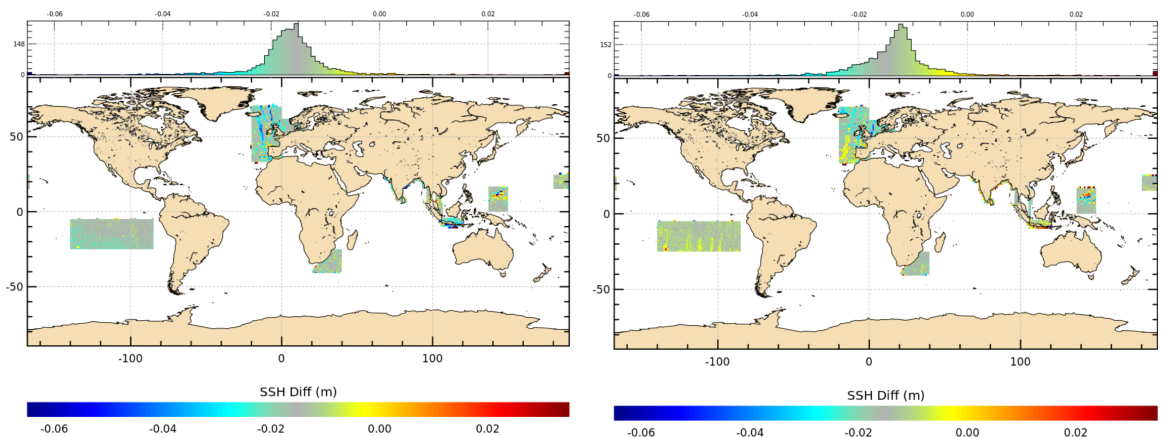


**Figure 2.24: Map of SSH difference for ascending (left) and descending (right) passes plotted from a 1° x 1° grid computed from January 2012 to December 2013.**

The SSH differences were computed for the ascending and descending passes, and binned per CPP PLRM SWH and radial velocity values to better separate the sensitivity of the difference to those two parameters (see Figure 2.25). These plots confirm that there is no specific signature of the SSH difference with respect to the radial velocity, neither significant signal related to the sea state (SWH), as already observed on the maps. Both SARM sea level is perfectly consistent each other.

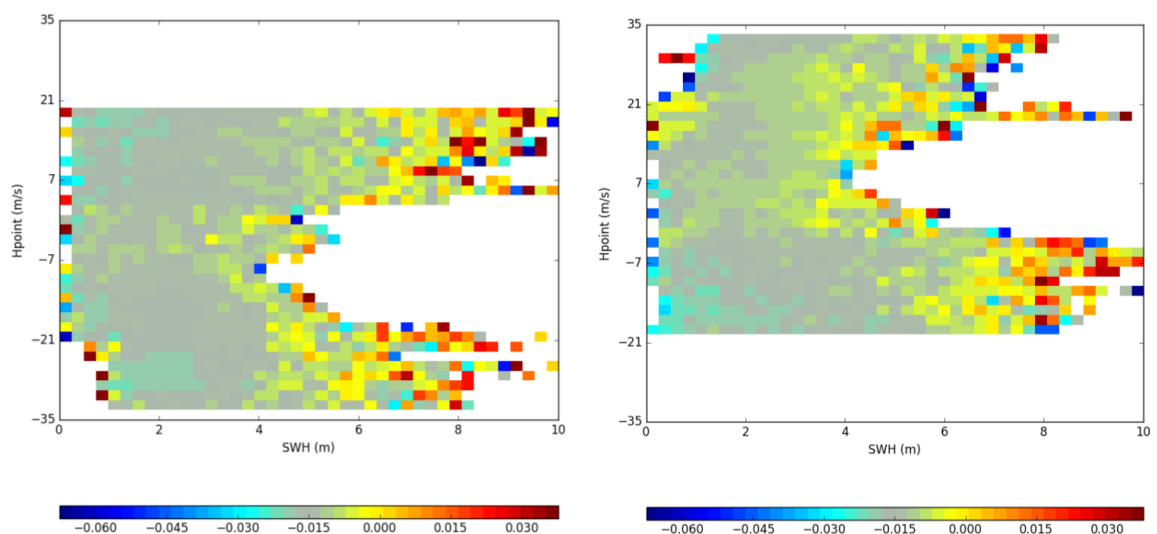


**Figure 2.25: SSH difference (m) between the innovative SARM and GPOD SARM binned per CPP PLRM SWH and radial velocity for ascending (left) and descending (right) passes.**

### 2.3.3.2 SWH analysis

In order to analyze the quality of the innovative SARM processing in SWH the  $1^\circ$  by  $1^\circ$  grid of differences between the innovative SARM and GPOD SARM SWH is plotted over the two-year period (see left panel of Figure 2.26). The map of SWH difference does not show a mean error bias but exhibits geographical variations that are found to be perfectly correlated with the waves as we can see on the right panel of Figure 2.26. Same plot also allows to check that there is no dependency of the difference with respect to radial velocity.

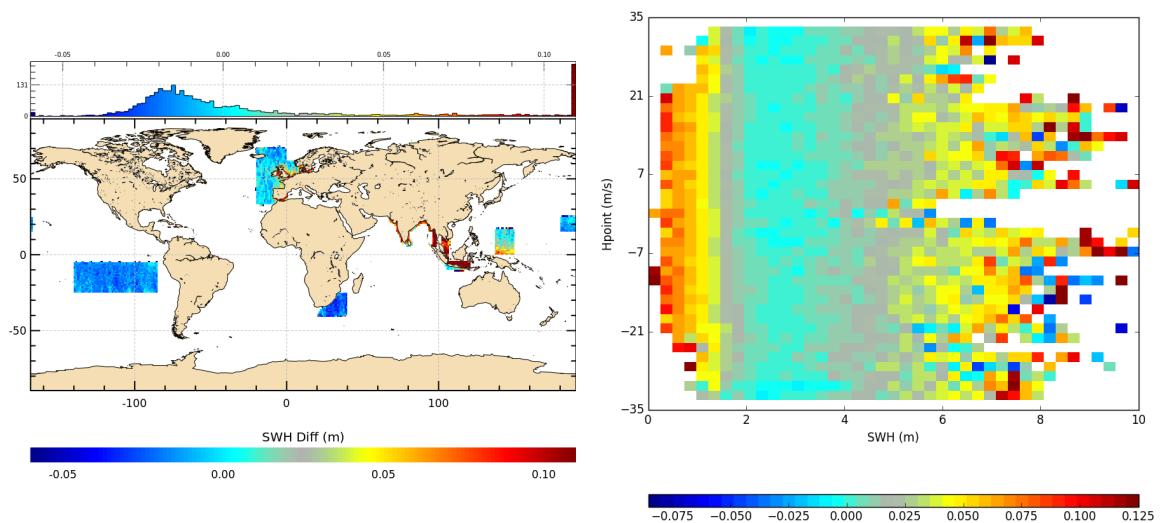


**Figure 2.26: (left) Map of SWH difference plotted from a  $1^\circ \times 1^\circ$  grid. (right) SWH differences plotted as function of the CPP PLRM SWH and the radial velocity. Both diagnoses are computed from January 2012 to December 2013.**

Figure 2.27 shows the SWH difference plotted as a function of the CPP PLRM SWH. We can see from this curve that there is a linear error of the SARM SWH difference depending on the waves (roughly 3% SWH) for SWH higher than 2.25 m. For lower waves large errors are also observed where the innovative SARM processing tends to overestimate waves. Such errors suggest the need to better adjust the PTR setting in the SAMOSA model to correct for the PTR approximation particularly when combined with an along-track Hamming weighting function. As it is, we cannot answer to the main SARM issue on the accuracy of SWH retrieval and of whether the Hamming window (decreasing the contribution of outer pulses of a burst) helps to achieve a better agreement between data and retracking model.

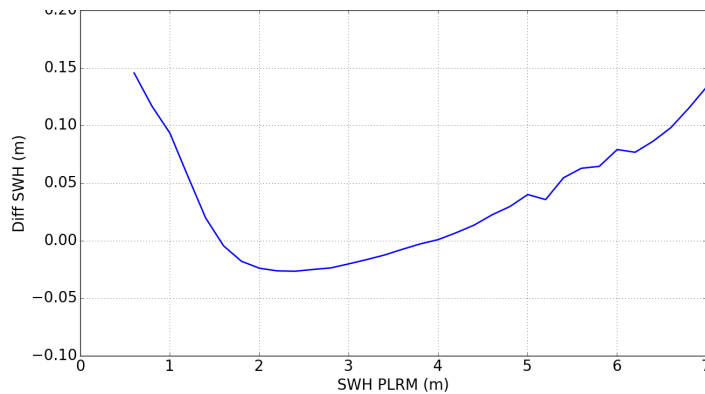


**Figure 2.27: Average of SWH difference between the innovative SARM and GPOD SARM datasets as function of CPP PLRM SWH computed from January 2012 to December 2013.**

### 2.3.3.3 Sigma-0 analysis

The map of the differences between the innovative SARM and GPOD SARM Sigma-0 measurements is plotted in the left panel of Figure 2.28. The map exhibits an excellent agreement between both processing, showing variations of difference lower than 0.1 dB magnitude. These variations clearly depend on latitude suggesting a possible correlation to the orbit of the satellite. On the other hand, there is no mean bias between SARM Sigma-0. Although these discrepancies are negligible, they could be explained by a slight anomaly in the innovative SARM processing to account for the orbit variation in the SARM model. The right panel of Figure 2.28 presents the Sigma-0 difference as a function of the orbit and the radial velocity values. The result observed is consistent with the previous conclusion derived from the map. The variations of the Sigma-0 difference are clearly correlated with the orbit of the satellite. In addition, this plot shows a very slight dependency of a few hundredth of dB with respect to radial velocity.

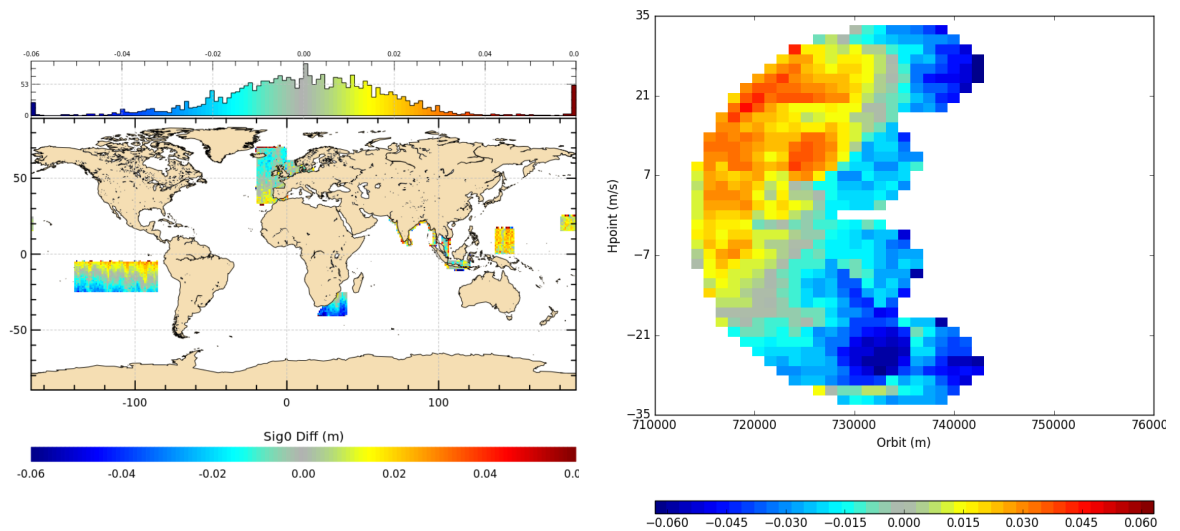


**Figure 2.28: (left) Map of Sigma-0 difference plotted from a 1° x 1° grid. (right) Sigma-0 differences plotted as function of the orbit and the radial velocity. Both diagnoses are computed from January 2012 to December 2013.**

## 2.4 High-frequency analysis

The assessment of the TU-Delft RDSAR and the innovative SARM data sets has revealed some errors at long wavelengths, notably while assessing SWH measurements (more likely due to inappropriate corrections for the PTR approximation used in the backscattered waveform model). Although centimeter scale errors remain in SWH, we can however state that the sea-level data sets are fairly and globally consistent with the references, but also with each other, ensuring a reliable continuity between conventional and Delay Doppler altimetry.

If the innovative SARM is in a very good agreement with the current SARM processing at long wavelengths, now a further question arises: what about the improvements bring by the innovative SARM ?

The innovative SAR mode processing scheme as implemented by isardSAT differs from the Sentinel-3 operational ocean processing in two important ways: (1) it includes a range waveform oversampling by a factor 2 (to avoid signal aliasing for low sea state and produce more accurate retrieval of mainly SWH [Smith and Scharroo, 2015]), and (2) a Hamming weighting window applied in along-track dimension (to mitigate the impact of off-nadir bright targets from land on the retrieved coastal measurements). Those settings were chosen primarily to improve the SAR altimetry performance in coastal zone as suggested by Dinardo et al. [2018]. But no less importantly, this configuration has also to be of some interest in open ocean. (so that improvements are made in both coastal zone and open ocean) to be ultimately recommended for operational use in global ocean. In what follows, we assess its potential capability to improve the detection of ocean topography features, especially at short spatial scales (below 100 km), through noise level analysis.

In theory, since the number of averaged samples used in the multi-looking is unchanged, we did not expect particular precision improvement. The zero-padding process may reduce the noise level at low wave height as already shown by Smith and Scharroo [2015], but the Hamming window should in contrary degrade the noise since the weighting function normally weakens the contribution of off-centered pulses in the burst. The computation of the effective number of looks of SAR altimeter waveforms with and without application of the Hamming function would certainly help to better understand the impact of the Hamming weighting method on the speckle noise reduction.

Figure 2.29 shows the level of the 20Hz white noise as a function of SWH, for range on the top panel, SWH on the middle panel and Sigma0 on the bottom panel. From this figure, we clearly observe the improvement brought by SAR processing (noise reduction in range and SWH) with respect to conventional altimetry (P-LRM mode) in open ocean. Of the SAR altimeter processing studied, the innovative technique gives the best performance, having a much lower standard deviation in SWH (> 35% at 2 m) and a slight noticeable improvement in range for SWH higher than 2 m (but degraded at low SWH). On the other side, no improvement is seen for the Sigma-0 parameter.

Based on these results, we can thus conclude that the precision of SAR altimeter measurements is globally improved (especially in SWH) in open ocean using the innovative SAR approach. We should notice that similar studies were conducted by ESA/CNES/CLS using Sentinel-3A data with the objective to improve the current SAR-mode processing. In this study, the Hamming window and zero-padding methods were assessed. But the results did not come to the same findings, and more importantly showed that the Hamming window configuration leads to a slight degradation of the precision compared to the nominal SAR processing. It is therefore important to make it clear to the altimeter community why the innovative SAR altimeter processing substantially improves the SAR-mode performance in order to fully convince of the reliability of using such settings in Sentinel-3 SAR-mode processing.

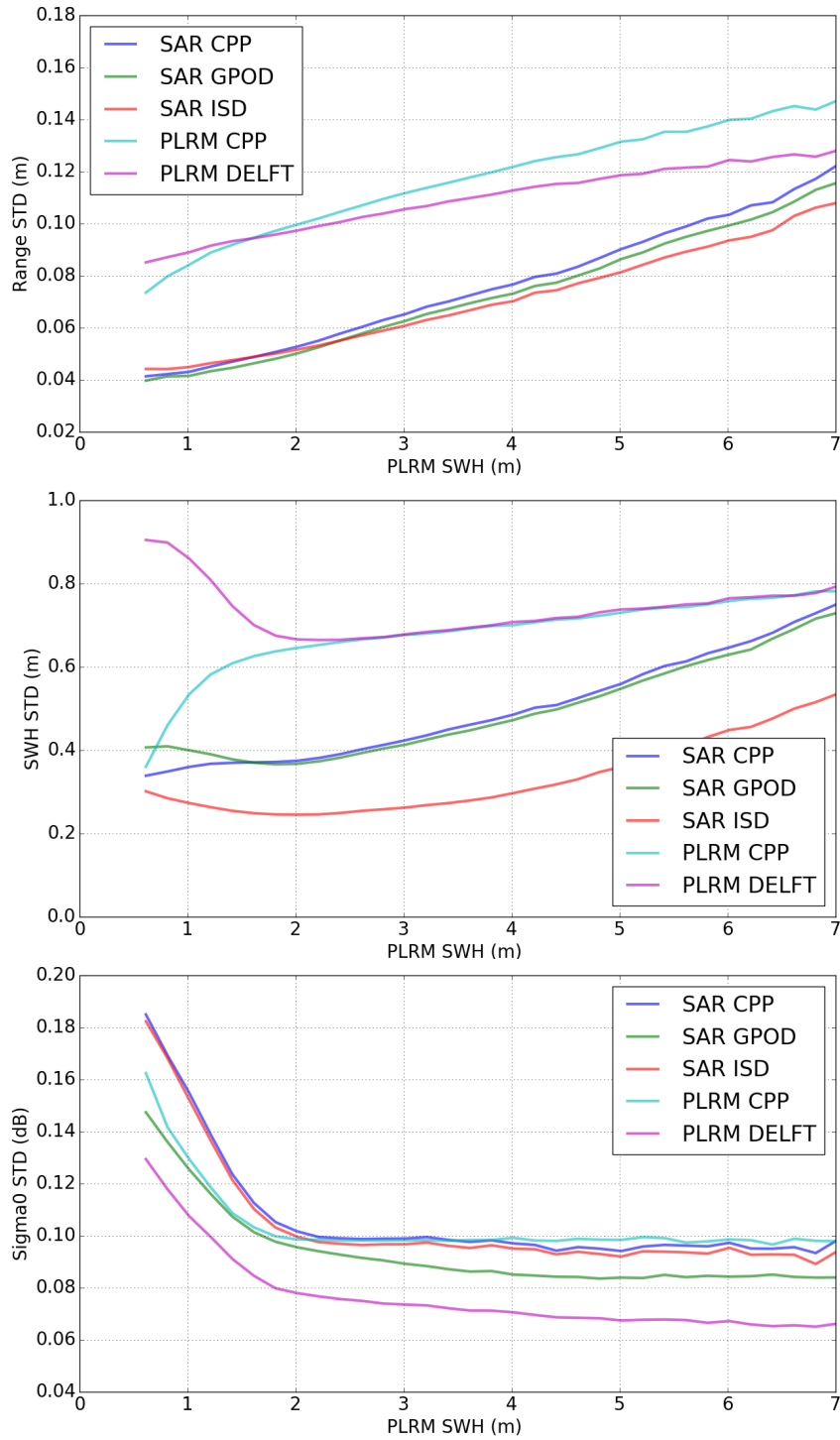


Figure 2.29: Plot of the range (top panel), SWH (middle panel) and sigma-0 (bottom panel) 20Hz white noise as a function of SWH for different acquisition modes (PLRM, SARM) and processing chain.

## 2.5 Sensitivity to sub-mesoscales

Many studies have evidenced the sensitivity of unfocused SAR altimetry measurements to long ocean surface waves [Aouf et Phalippou, 2015; Abdalla et al., 2016; Moreau et al., 2018]. They showed that the noise level of SAR altimeter measurements increases with wavelength of ocean swells (and for particular wave propagation angle with respect to the satellite flight direction), but also that the SWH retrieval is affected by these ocean waves [Moreau et al., 2018]. The observed effects are due to the narrowing view of the SAR altimeter (300 m against a few kms in conventional altimetry) making measurements of only a portion of the long-waves period, that induce variations on the illuminated radar footprint and on the surface height distribution inside this footprint. In such wave conditions, the measured distribution is not predictable and difficult to model, and also depends on which portion of the long-wavelength wave is imaged. It may be thus anticipated that the surface elevations distribution as measured by SAR altimeter departs from the Gaussian sea surface elevation statistic observed within conventional altimeter footprint.

Consequently, the Brown's assumption used in the SAR model for the sea-surface description is no longer held. In cases for which this assumption is not met, the altimeter waveforms cannot be correctly handled by the ocean retracker, causing possible errors in SAR altimeter geophysical retrievals (mainly in SWH estimates as observed by Moreau et al. [2018]). This further rises concern about potential impact of such ocean wave conditions on the sea level time-series when data from the different Sentinel-3 missions but also from the future Sentinel-6 mission, which all have SAR-mode radar altimeter, will be incorporated.

In this section, we examined whether the Doppler beam expansion of the innovative SAR altimeter processing (from 300 to 450 m in along-track dimension) caused by the application of the Hamming window, leads or not to the mitigation of the impacts of long ocean waves. For this, the standard deviation of the 20-Hz measurements in range and SWH of each processing is plotted in Figure 2.30 and Figure 2.31 against the mean wave period (T02) provided by the WaveWatch-III (WW3) wave model from IFREMER ([ftp://ftp.ifremer.fr/ifremer/ww3/HINDCAST/GLOBAL/2015\\_ECMWF](ftp://ftp.ifremer.fr/ifremer/ww3/HINDCAST/GLOBAL/2015_ECMWF)). From these figures, we can observe that the standard deviation of the 20-Hz SAR data depends on SWH and T02, while in the case of PLRM data the standard deviation only depends on SWH. Furthermore, we observe that the estimated parameters from SAR altimetry waveforms (whether for GPOD or the innovative SARM processing) are particularly noisy under long-wave conditions. It has been shown that the SARM noise may come to be even higher than PLRM noise when waves propagate parallel to the satellite flight direction [Moreau et al., 2018]. From these figures, one can also notice a slight less pronounced sensitivity of the innovative SAR processing (brought by the increased along-track resolution), without however reducing significantly the ocean swell impact.

Figure 2.32 shows the SWH differences between SAR (from GPOD and innovative processing) and CPP PLRM estimations for different SWH and T02 values. We observe that the SWH estimates in SAR mode are biased with respect to conventional altimetry data as already reported in large scales analysis. This figure also indicates that the SWH differences between the two modes depend both on SWH and T02, thus suggesting potential inaccuracies in the SWH retrieval for SAR-mode (when compared with PLRM). Furthermore, there is no noticeable improvement brought by the innovative SAR processing. The degradation of the spatial resolution caused by the Hamming window in the innovative SARM processing is not high enough to filter out small sub-mesoscale structures over ocean surfaces (< 1 km). Some studies are currently undertaken to determine a dedicated processing with SAR capabilities enabling to tackle the swell impacts on retrieval performances effectively [Boy et al., 2017b].

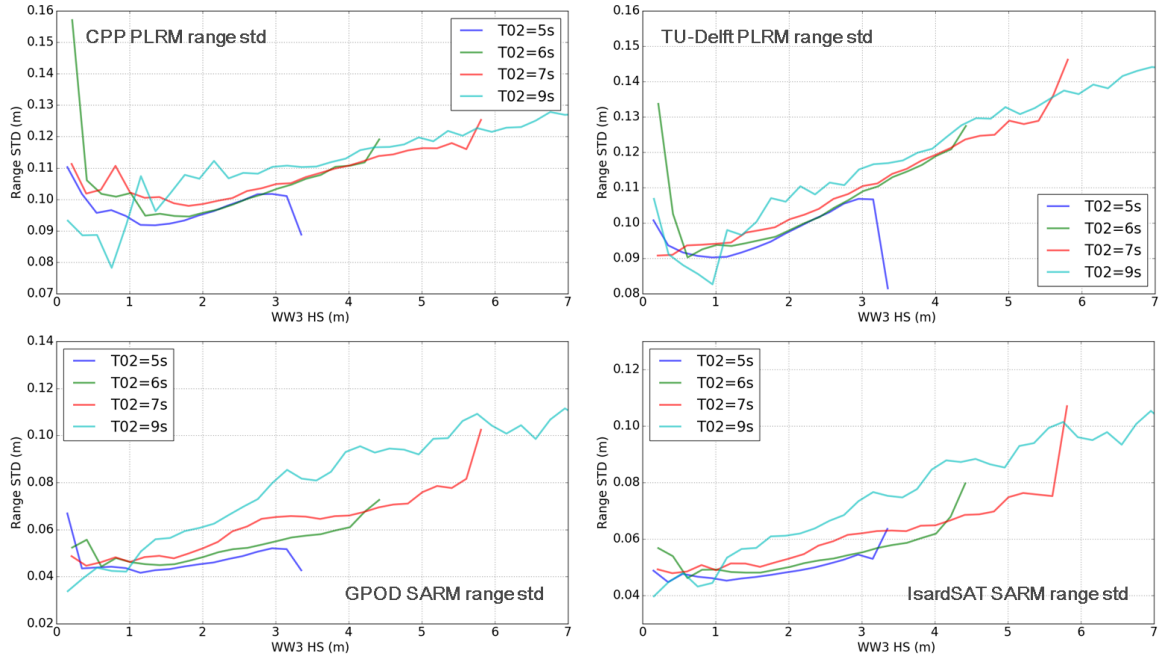


Figure 2.30: Standard deviation of 20-Hz Cryosat-2 range against WW3 SWH estimates for different T02 values.

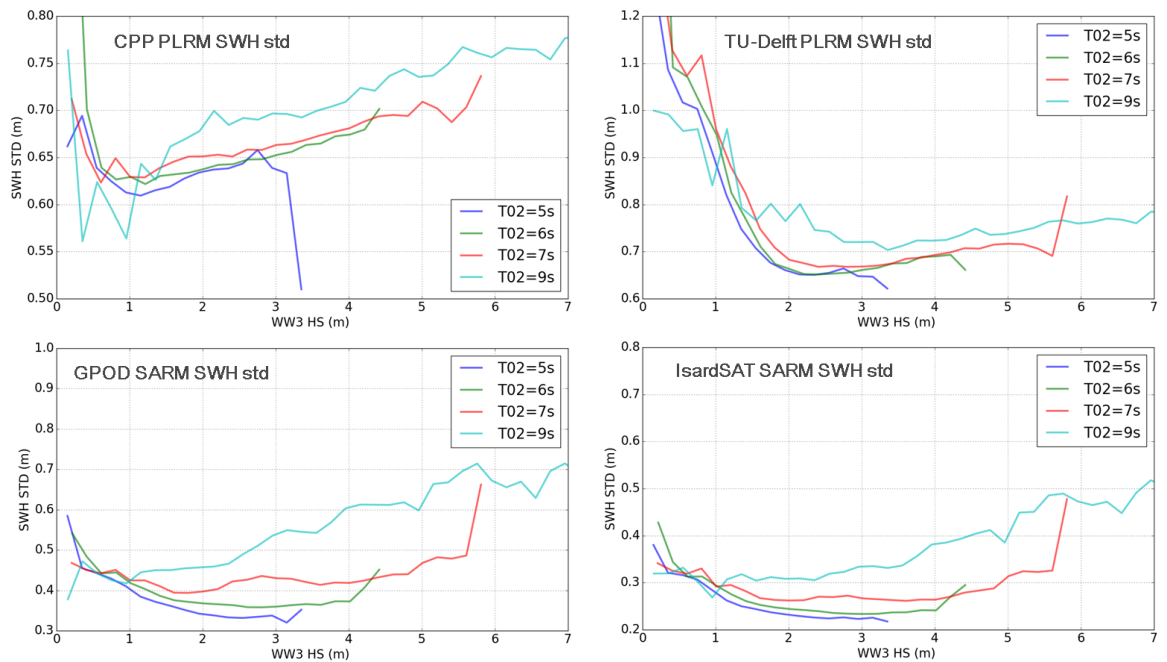
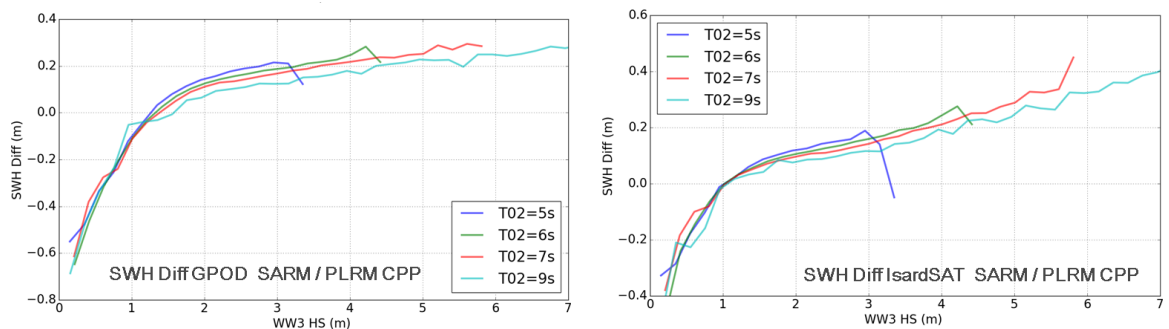


Figure 2.31: Standard deviation of 20-Hz Cryosat-2 SWH against WW3 SWH estimates for different T02 values.



**Figure 2.32: Bin-averaged values of Cryosat-2 (SARM minus PLRM) SWH against WW3 SWH estimates for different T02 values.**

## 2.6 Sea Level Anomaly assessment

Spectral analysis of along-track sea level anomaly was performed to characterize the error of altimetry at different wavelengths. The error estimates are determined as the difference between observations and a theoretical spectrum built as the sum of an oceanic signal energy slope [Xu and Fu, 2012; Dufau et al., 2016] and the 20-Hz noise (calculated for scales between 700 m and 1 km). To allow errors to be characterized from small to large scales, data were selected along segment of 1000 km for different tracks and cycles, then all individual spectra computed were averaged to obtain a visibly smoother spectrum.

We computed the power spectral density (PSD) of the 20-Hz SLA as function of the wavenumber for each altimeter processing under study. Note that the SLA has been calculated using the same model for the mean sea surface (MSS CNES/CLS 2011) and without applying geophysical corrections to make all datasets consistent each other. For this analysis, it has been decided to compute the PSD on the Agulhas current area only, as already performed by Raynal et al. [2018], which exhibits steep ocean slopes and thus more observable oceanic structures than in other SAR mode areas. The PSD obtained for the innovative SAR SLA spectrum is shown in green in Figure 2.33, the reference nominal SAR spectrum is plotted in dark blue and the TU-Delft RDSAR spectrum in red (PSD for both SAR and PLRM CPP are also plotted for comparison).

From this figure, no noticeable difference is observed between processing for wavelength higher than 100 km, showing thus same content at large scales.

At shorter scales, SAR PSD does not show the energetic hump between 10 and 30 km that we observe on PLRM. The so-called spectral “bump” is known to be an artefact affecting conventional altimetry measurements due to errors in estimation that occur over surface heterogeneities (not properly modelled by traditional retracers) and that are smoothed along consecutive 20-Hz observations because of large and overlapped LRM footprints [Dibarboure et al., 2014]. This hump energy coupled with the 20 Hz noise of the PLRM alters the oceanic slope for scales up to 100 km. In SAR mode, the 20-Hz observations do not overlap, preventing hump corruption. The SAR spectra exhibits a cleaner and steeper oceanic slope that should yield more accurate observations of the SLA at small scales.

It can be noticed however a little hump on the innovative SAR PSD for wavelengths ranging from 2 to 10 km, followed by a drop of energy for lower wavelengths. This spectra feature is most likely a consequence of the application of the Hamming window in SAR altimeter processing that creates low spatial correlation between consecutive samples. As already mentioned, the Hamming weighting has the effect of widening the doppler bands (and therefore degrading the along-track resolution). Widening the doppler bands makes contiguous bands to overlap, thereby introducing correlation

between consecutive measurements. Fortunately, the mean sea level spectrum does not seem to be impacted for wavelengths ranging from 30 to 100 km that matters for the community.

Other important feature is the continuous slope from 30 km to smaller scales observed on the SAR SLA PSD, also called “red noise” slope that has been recently evidenced by Labroue et al. [2017] using Sentinel-3A data. There is no yet detailed explanation on the source of such a slope on the SAR-mode spectrum, but observations showing that this slope is very closely related to swells (perfectly correlated with the mean period and propagation angle of waves in swell-dominated regimes). Unfortunately, this signal could not be analysed in this study that is hampered by the limited SARM areas offered by Cryosat-2.

Regarding the high-frequency content, the SAR 20-Hz white noise (calculated from 700 m to 1 km) is as expected much lower than the PLRM white noise, allowing a better observability of small-scale oceanic signals. Note that the noise value corresponds to the noise for the mean SWH over the Agulhas current area (which is close to 2.8 m) and not the 20-Hz noise at 2 m waves which is usually given in altimeter error budget. It should also be noted that the spectral analysis provides a 20-Hz noise level for the innovative SAR processing that does not perfectly match the noise value computed from the 20-Hz to 1-Hz compression (see section 2.4), with 5.1 cm and 5.9 cm respectively at same SWH. This discrepancy may result from the SLA PSD distortion caused by the Hamming function at very short wavelengths, that alters the 20-Hz white noise level estimation from spectrum.

For the PLRM spectral analysis, it can be observed that the TU-Delft RDSAR processing, despite a better noise performance, shows higher correlated errors than CNES PLRM. It is however difficult to link with certainty this result to the use of the range zero-padding algorithm in the RADS processing since the two PLRM processing differs in many other aspects which could explain such difference.

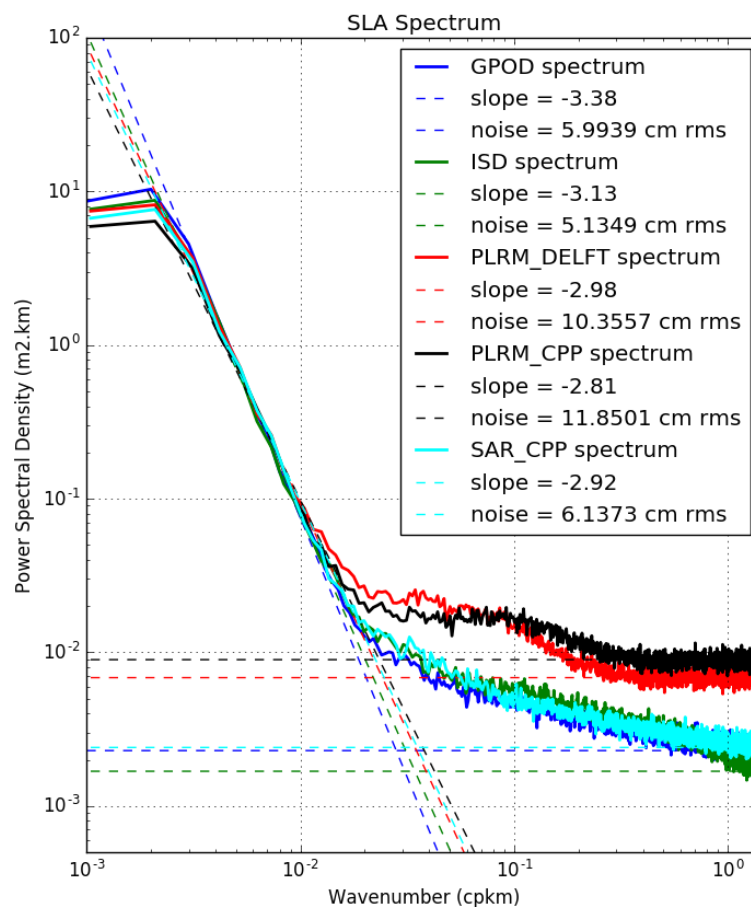


**Figure 2.33: Mean power spectral density for PLRM and SARM sea level anomalies computed as function of the wavenumber over the Agulhas area from January 2013 to December 2013.**

## 2.7 Analysis of the GPD+ Wet Tropospheric Correction

This section reports the results of the analysis done on the Wet Tropospheric Correction (WTC) based on the latest GNSS derived Path Delay Plus (GPD+) methodology by comparison with the WTC derived from the European Centre for Medium Range Weather Forecasts (ECMWF) operational model grids. The overall objective of this validation exercise is to determine whether the GPD+ WTC solution allows to obtain or not a better description of the SLA as it is theoretically expected since it uses MWR measurements from other remote sensing satellites.

### 2.7.1 Data and method overview

For this study, two sets of CryoSat-2 sea level anomalies, one including the GPD+ WTC and the other the ECMWF WTC, have been computed at the same 1-Hz point locations along the CryoSat-2 tracks over SARM areas from January 2012 to December 2013.

#### 2.7.1.1 GPD+ WTC

This method combines several available data sources through an objective analysis (OA) to estimate the WTC values [Fernandes et Lazaro., 2016]:

- WTC derived from Microwave Radiometer (MWR) observations made on-board other remote sensing satellites,
- WTC estimations from Global Navigation Satellite System (GNSS) coastal stations,
- WTC derived from Scanning Imaging Microwave Radiometer (SI-MWR) sensors on board various remote sensing satellites, and
- WTC based on the ECMWF operational model.

The quality of this correction depends on the number of available sensors, the intrinsic sensor errors and the so-called formal error that incorporates various statistical-error components [Fernandes et al., 2015].

#### 2.7.1.2 ECMWF WTC

The ECMWF models run on Gaussian global grids with an approximate resolution of  $0.125^\circ$  and a temporal resolution of 6 hours. The Gaussian ECMWF grids are considered for this comparison exercise since it is likely to be more accurate than the older version based on Cartesian grids.

The WTC model is computed at the altimeter time-tag from the interpolation of two meteorological fields that surround the altimeter time-tag. A WTC must be added (negative value) to the instrument final range to correct this range measurement for wet tropospheric range delays of the radar pulse.

#### 2.7.1.3 Method

A set of dedicated diagnoses has been used to evaluate the quality of the GPD+ WTC correction over open ocean and see if it improves the sea-level anomaly calculation. These diagnoses are the following:

- along track comparison with ECMWF WTC to highlight differences,
- along track and crossover gain of variance of SLA to determine which correction shows the best performances, and

- study of the GPD+ WTC transition where an insufficient number of MWR measurements is available to give an idea of the operational behaviour of this solution.

## 2.7.2 Validation results

The assessment was conducted with robust and standard tools that have already been used in many projects.

### 2.7.2.1 Along-track analysis

Figure 2.34 shows the mean GPD+ and ECMWF WTC values calculated over the two-year period in SARM areas. From this map, it can be seen large spatial variability of this correction with absolute value of a few tens of centimetre, which reflects the importance of this error source in the altimeter sea level computation. It can also be observed that the two WTC corrections exhibit same geophysical patterns at large scales. No statistical analysis (comparison of their mean and standard deviation) could be performed from these maps since the ECMWF model-derived WTC is plotted over a larger geographical coverage (all SAR-mode acquisitions in the period of two years).

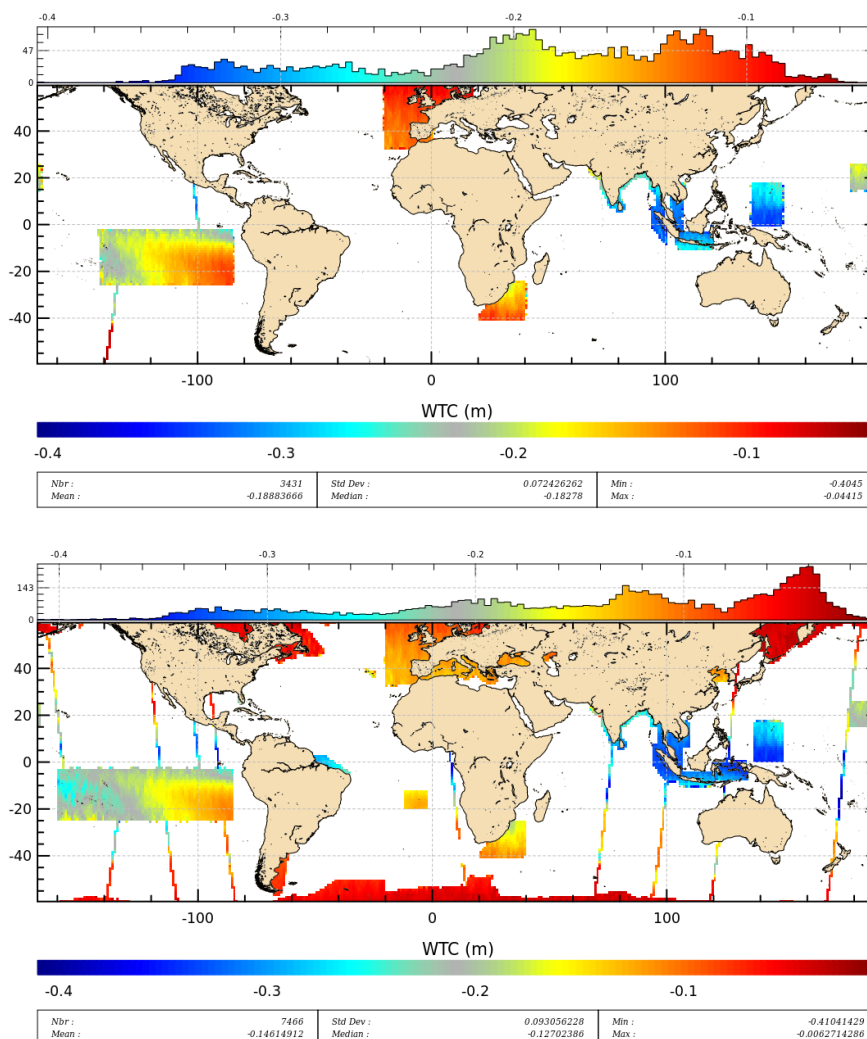
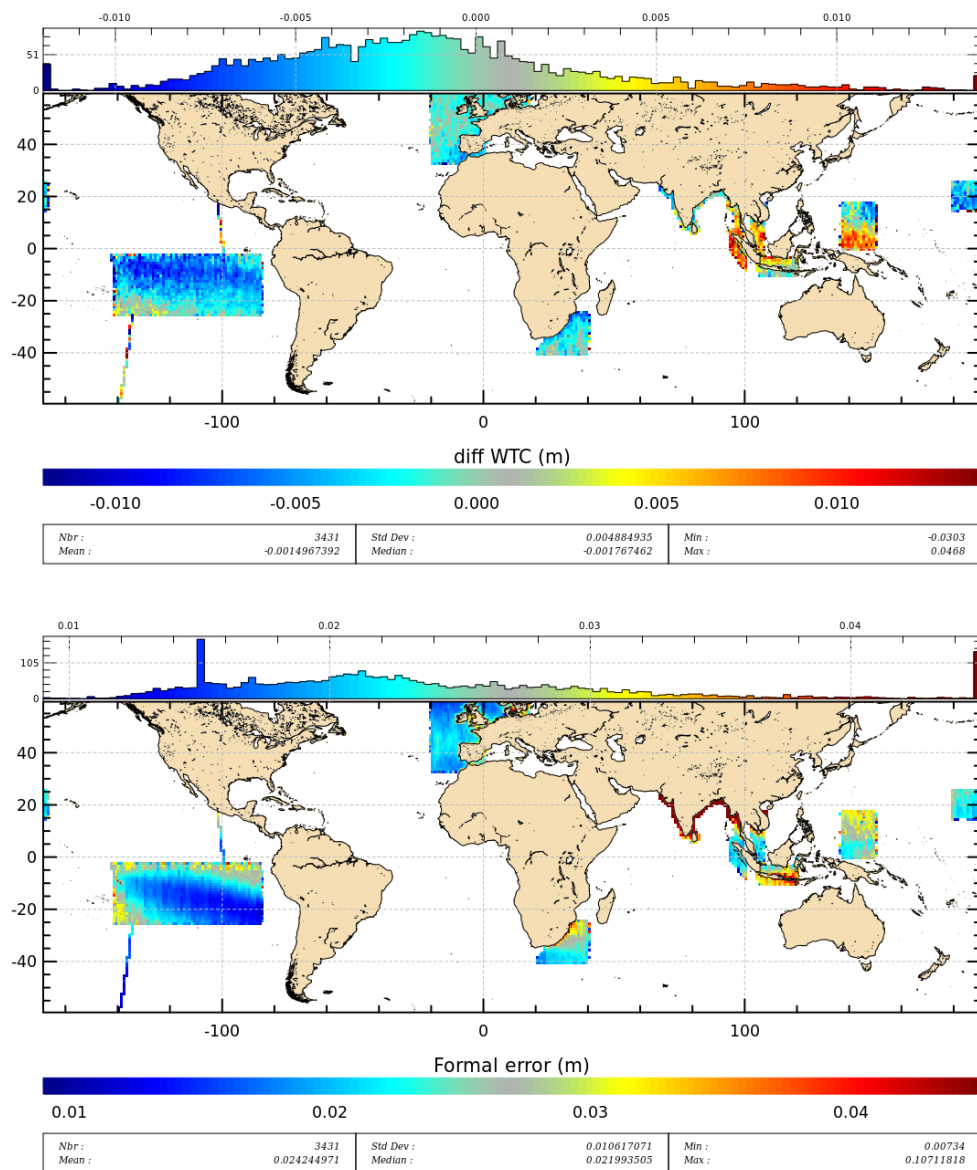


Figure 2.34: Map of the mean along-track GPD+ WTC (top panel) and ECMWF WTC (bottom panel) over SARM areas from January 2012 to December 2013.

Along-track differences between the GPD+ and ECMWF WTCs were computed then averaged in 1° by 1° grid. The top panel of Figure 2.35 shows the map of the mean differences, and the bottom panel the formal error of the GPD+ solution. The map of the standard deviation of the differences is plotted in Figure 2.36. From these maps, one can notice that the differences between GPD+ and ECMWF WTCs are ranged between -1 and 1 cm, where highest differences are observed in low latitudes (mean as high as 1 cm). There is however no clear relation between the WTC differences and the formal error. One can observe situations where WTC differences increase with formal error (in Agulhas current area), and inversely situations where high differences are located in areas of low formal error (for which the GPD+ solution is considered to be more reliable). The map of differences also shows that the GPD+ WTC over estimates the wet situations (warm pool), compared to the model correction. These differences are between 0 and 1 cm for the mid-latitudes in the Indonesia-north Australia area.



**Figure 2.35: Map of the mean along-track difference (GPD+ - ECMWF) in meter (top panel) and map of the mean along-track formal error from the GPD+ WTC solution in meter (bottom panel) averaged in 1° by 1° geographical bins over the period of two years.**

Also note that at higher latitudes where observations from MWR sensors are not available, the standard deviation of the differences is close to zero as the GPD+ WTC uses exclusively ECMWF measurements.

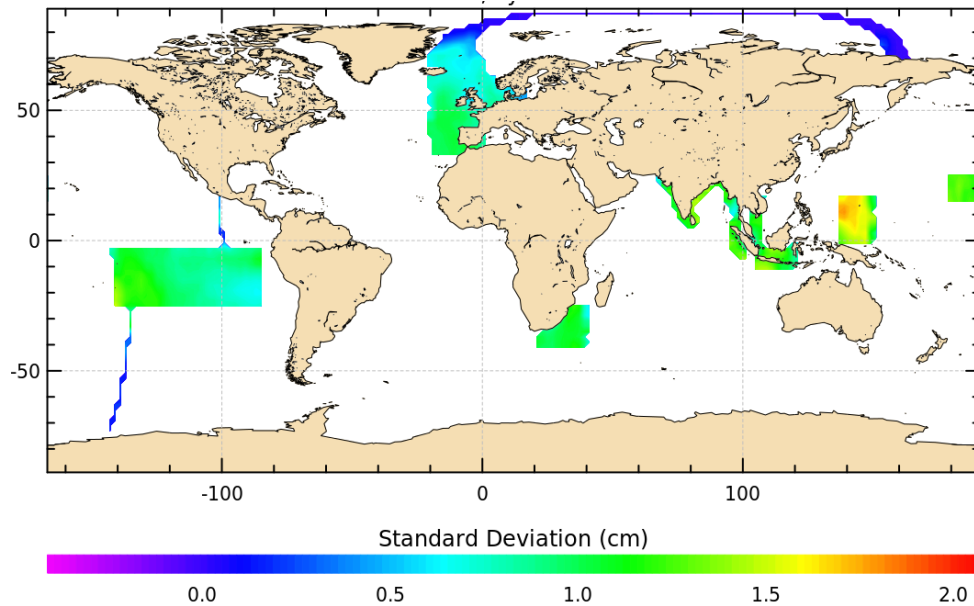


**Figure 2.36: Map of the mean standard deviation of along-track difference (GPD+ - ECMWF) in meter averaged in 1° by 1° geographical bins over the period of two years (after smoothing).**

The Figure 2.37 (right panel) shows that the mean difference (GPD+ - ECMWF) is positive in the equatorial zone and in some areas of the south hemisphere, as already observed in the preceding figure. The left panel of the Figure 2.37 is the mean difference as function of the distance from the coast. These differences are very low near coasts (<10-15km) where radiometer measurements become invalid due to the land contamination in the radiometer footprint. In the coastal strip, the GPD+ WTC is switched to the less accurate ECMWF model-derived WTC interpolated at the altimeter measurement location. For higher distance from the coast the mean difference increases.

This study does not permit to assess accurately the GPD+ WTC behavior in coastal zones given the few coastal areas operated in SARM. A regional analysis focused on GNSS data used in the GPD+ computations would allow to see locally higher differences. However, the impact of the GNSS data in the WTC (notably in Europe coastal zones) is not noticed on the map.

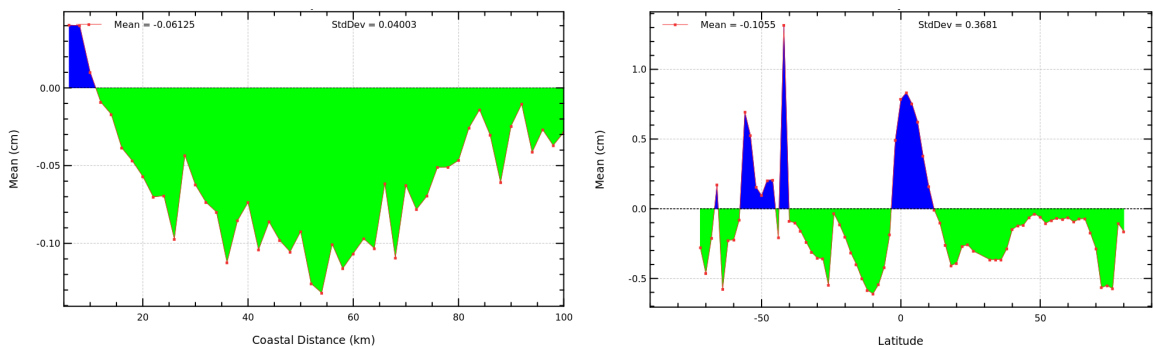


**Figure 2.37: Mean of the along track WTC differences, GPD+ - ECMWF, as function of the coastal distance (left panel) and latitude (right panel).**

In the following figure (Figure 2.38), we plotted the mean of the differences for each cycle of the Cryosat-2 mission in the period ranging from January 2012 to December 2013, with the view to assessing the consistency and the long-term stability of the GPD+ WTC. Although the two-year period is somewhat short to infer any conclusive tendencies, one can observe a trend close to 1 mm/year which must be more closely analysed at global scales and over a longer time period (where interannual signals can be detected). In any case, all radiometers used in the GPD+ corrections have been calibrated against the Special Sensor Microwave Imager (SSM/I), so GPD+ WTC shall have the same long-term evolution of the SSM/I dataset

Also note that the GPD+ WTC values are in average lower by -1.5 mm compared to the ECMWF model-derived WTC values.

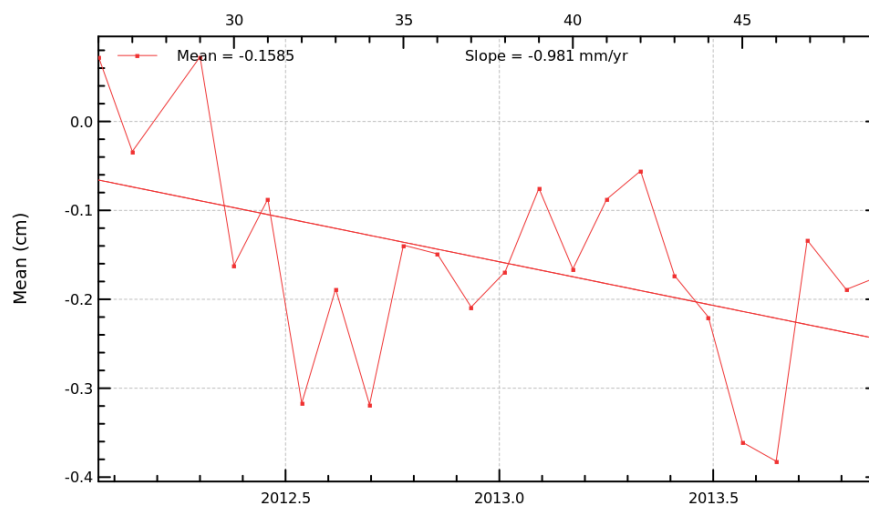


**Figure 2.38: Time evolution of the mean of the differences between WTC (in centimetre) computed from GPD+ and ECMWF from January 2012 to December 2013.**

To conclude this part, low along-track differences (lower than 1 cm) between the GPD+ WTC and the ECMWF WTC are reported which vary in latitude and coastal distance.

### 2.7.2.2 Along-track gain of variance of SLA

After characterizing the differences between each WTC solution, we have determined which one is the most accurate by means of a set of statistical analyses of SLA variance. For this purpose, we computed the difference of variance between SLA with the GPD+ WTC and SLA with the ECMWF model-derived WTC, and checked which one has the lower variance corresponding to a better data quality. The map of the geographical distribution of these differences is plotted in Figure 2.39. From this map, one can see that the mean values of the differences in variance of SLA are quite negative, meaning that the performances are slightly better for the GPD+ solution compared to the ECMWF model. Higher reduction of gain of variance is observed in coastal areas in the Indonesian sea. It could be explained by the fact that the GPD+ solution better detects small scale structures that are smoothed by the ECMWF model. However, in some isolated cases such as the south of the Agulhas current area, the GPD+ WTC slightly degrades the performance for some unexplained reason.

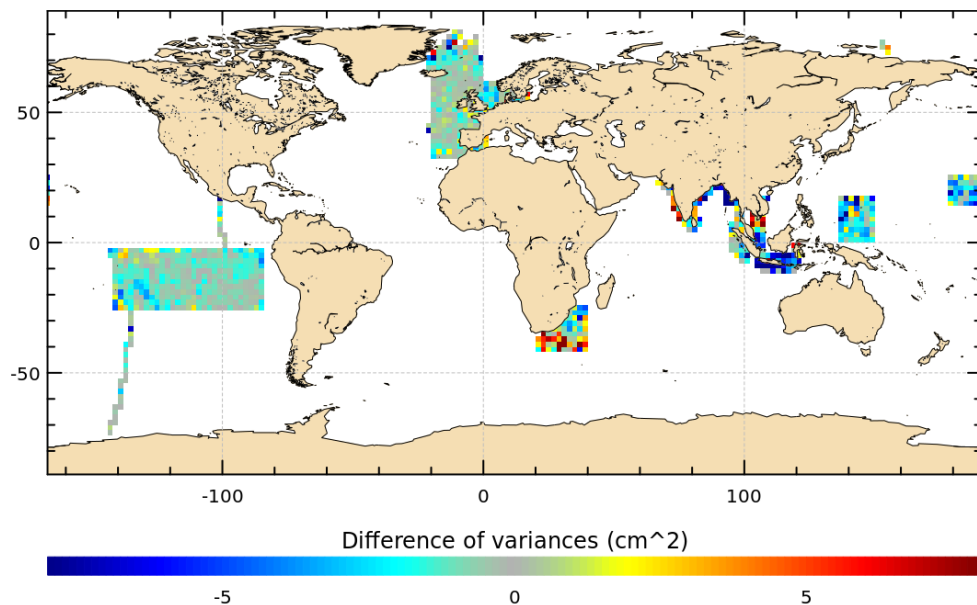


**Figure 2.39: Map of the mean along track gain of variance between SLA computed with GPD+ and ECMWF WTCs, averaged in 2° by 2° geographical bins over the period of two years.**

The reduction of variance computed over the selected SARM areas is also obtained in both open ocean and coastal regions, and particularly for low latitudes and close to the coasts where the differences in variance are clearly negative as shown on the Figure 2.40 (about  $-2.4 \text{ cm}^2$  at distance lower than 100km). The GPD+ solution uses coastal stations of the Global Navigation Satellite System (GNSS) that contributes to the observed improvement of the WTC estimations near the shore.

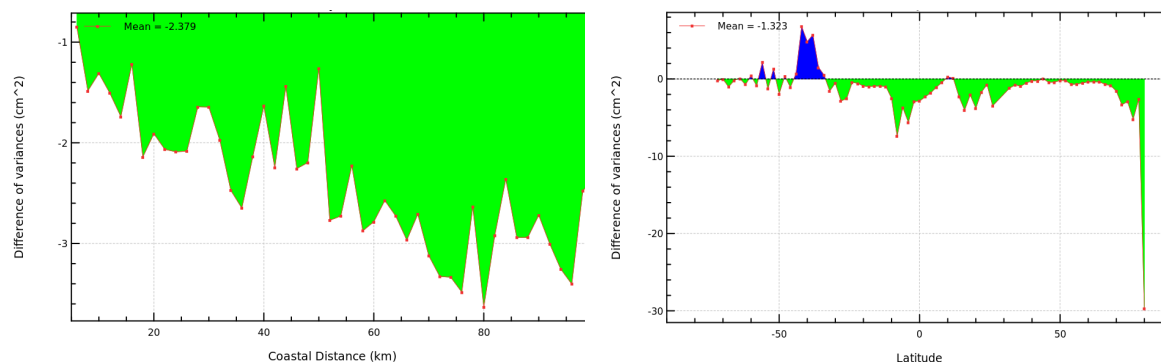


**Figure 2.40: Mean along track gain of variance between SLA computed using the GPD+ and the ECMWF WTCs as function of the coastal distance (left panel) and the latitude (right panel).**

The gain of SLA variance was computed cycle by cycle over the two-year time period and plotted as function of time in Figure 2.41. From this plot, one can see a noticeable reduction of the SLA variance with time (possibly related to an increasing number of MWR observations). The mean value is close to  $-2.5 \text{ cm}^2$  over this period. Note that the first values are not relevant due to the incomplete first cycle, and data missing found in the first few months of the studied period.

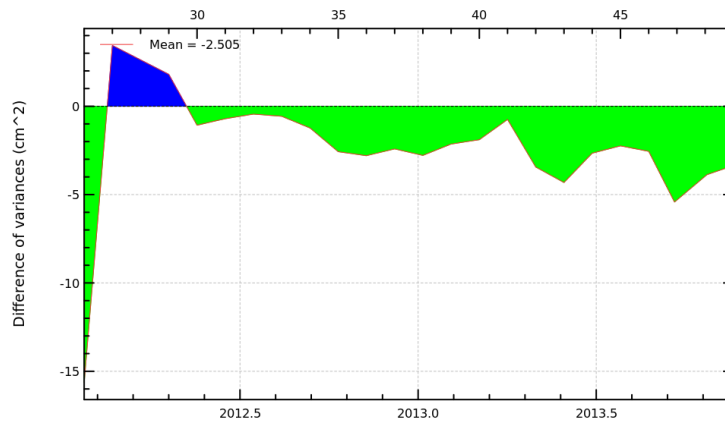


**Figure 2.41: Time evolution of the mean along track gain of variance between SLA computed using the GPD+ and the ECMWF WTCs from January 2012 to December 2013.**

To conclude this part, the along-track gain of variance diagnosis shows that the GPD+ WTC improves the performance between 50S and 50N, at least as far as SARM areas are concerned. This study however did not permit to assess the performance of the GPD+ solution at higher latitudes in polar regions.

### 2.7.2.3 Crossover gain of variance

The difference of SSH variance computed at crossovers is also used as a good indicator for establishing the performance of the WTC solution. Figure 2.42 and Figure 2.43 show the results of the SSH variance analysis on crossovers confirming the improvement of the GPD+ solution seen with along-track SLA gain of variance diagnostic. The map of SSH variance difference at crossovers exhibits a clear SSH variance reduction in most SARM regions (see Figure 2.42) with a reduction by about 1 to 2  $\text{cm}^2$  (corresponding to a reduction by about 2 to 4% of crossover SSH differences). The cycle by cycle monitoring of the gain of variance in Figure 2.43 also shows that the GPD+ solution consistently reduces the SSH variance with respect to the model with values centred on  $-1.3 \text{ cm}^2$ . Data inconsistencies in the first few months may however affect the accuracy of this value.

It should be emphasized that these results are based on crossover points that are located in mid-latitude bands only, due to the particular CryoSat-2 orbit which does not exhibit crossing of ascending and descending arcs in equatorial band and at high latitudes (for 10 days maximum of lag time).

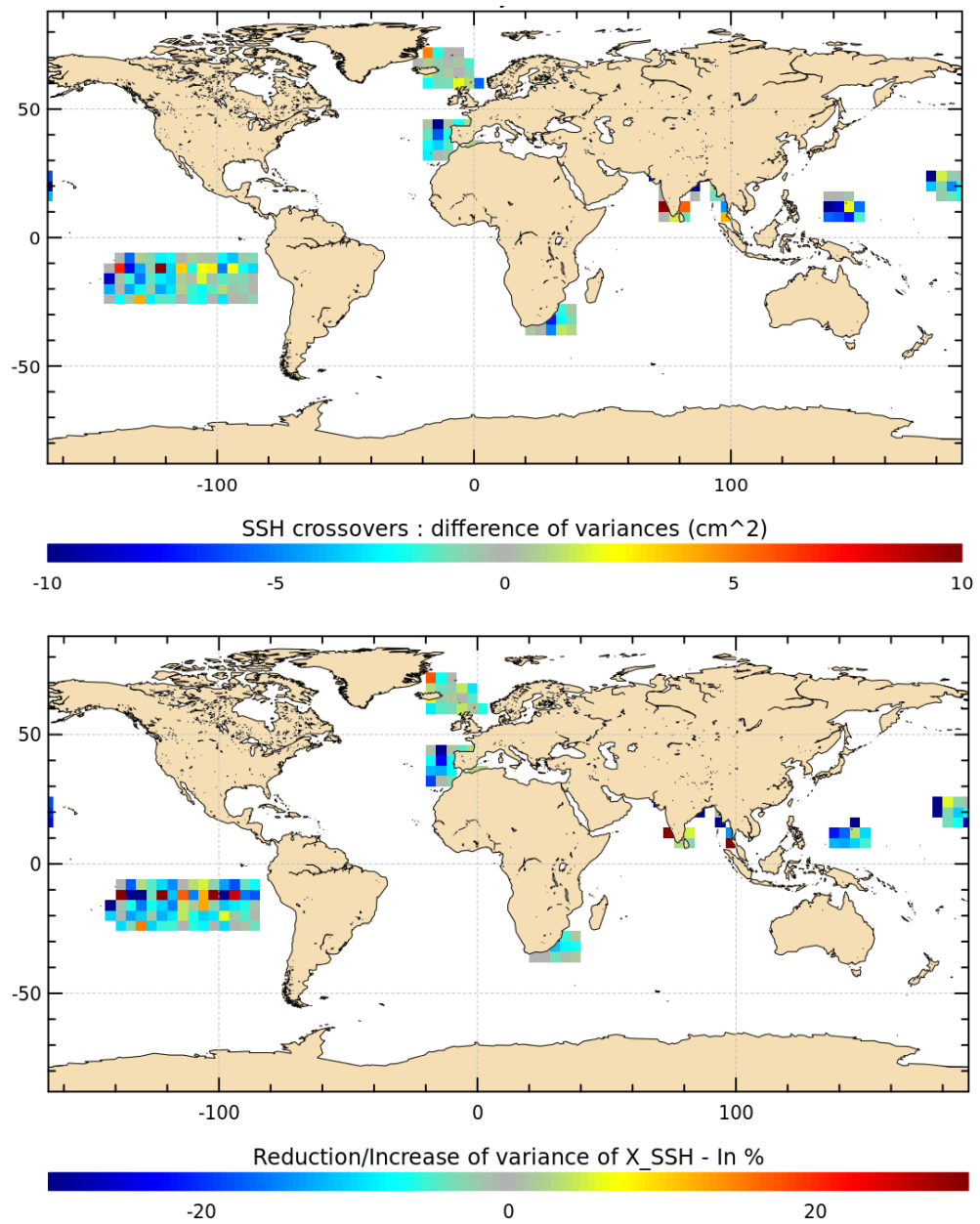


**Figure 2.42: (Top panel) Map of the mean difference of variance of SSH crossover difference computed with GPD+ and ECMWF model WTCs, averaged in 4° x 4° geographical bins over the period of two years. (Bottom panel) The reduction or increase of variance in percentage.**

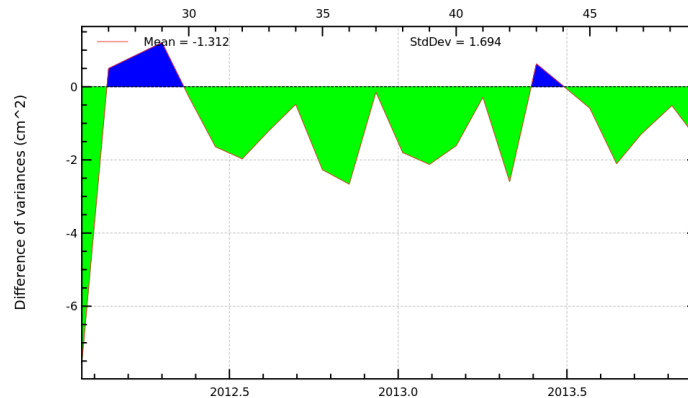


**Figure 2.43: Time evolution of the mean difference of variance of SSH crossover difference computed with the GPD+ solution and the ECMWF model from January 2012 to December 2013.**

### 2.7.2.4 Along-track analysis

A GPD+ WTC flag is provided in the products informing about the data used for computing the wet tropospheric correction. In this part of the assessment we analyse along-track GPD+ WTC values at a GPD+ flag change.

In the example shown in Figure 2.44, one can notice the presence of a little discontinuity of the GPD+ WTC (close to 1 mm) that is likely to be related to a change of the GPD+ flag (moving from the state “1” where WTC estimate is valid to the condition “2” where there are no available observations and for which the ECMWF operational model is used). In practice, when there is an insufficient number of observations, the less accurate ECMWF WTC is used in the AO processing scheme to compute the GPD+ WTC final value, degrading the quality of the WTC at the current point and creating a noticeable discontinuity in WTC that is not physical. As a result, it also impacts the SLA. An interpolation over few kilometres at the discontinuity could be considered to tackle such issue. It may be also envisaged to improve the GPD+ algorithm by propagating the valid WTC estimate up to the change of flag but imposing the ECMWF dynamics to reduce the discontinuity. But, so far, only small jumps of mm height have been observed. Such discontinuities do not have significant physical meaning as the WTC may have large gradients.

Also note that ECMWF model-derived WTC values from CLS differ from values in the GPD+ algorithm of few mm when the GPD+ flag is at “2”.

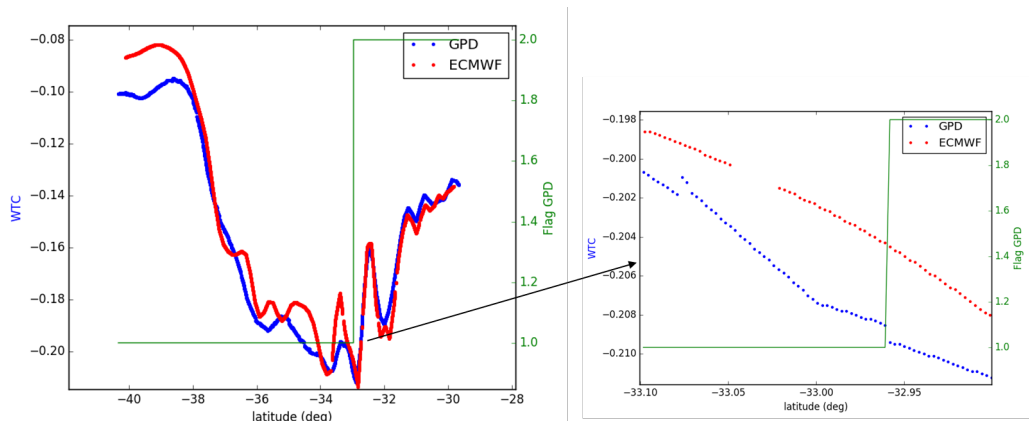


**Figure 2.44: (Left panel) Along-track WTCs derived from the ECMWF model (red) and computed by the GPD+ (blue), and the associated GPD+ flag (green) as function of the latitude. (Right panel) Zoom into part of the plot.**

## 2.8 Summary of Results

This analysis focused on the validation of new altimeter data sets (from the TU-Delft RDSAR and the innovative SARM processing) over ocean, assessing the capability of those processing to be used in operational systems. This analysis also included the assessment of the enhanced wet tropospheric correction (WTC) based on GPD Plus (GPD+) methodology, with the objective to confirm the conclusions drawn by the University of Porto (see the section “Validation of the Wet Tropospheric Correction” in this report) using different diagnostic tools.

Two years of Cryosat-2 data acquired in SAR mode have been used for this assessment. Note that the limited number of ocean areas operated in this radar mode prevents from assessing thoroughly the different processing schemes so that conclusions arising from this study should be confirmed in global.

For the validation of the TU-Delft RDSAR processing, our approach was to check the consistency of its estimated parameters with respect to operational-like PLRM altimeter measurements (from the CNES CPP), and examine whether that processing improves the current PLRM performances and if it is mature enough to be used as a LRM-like reference in comparison with SAR-mode data. The results of this study show first a fairly good agreement when compared with the CNES CPP PLRM, with differences below 2 cm in SLA. Taking a better look at it, at centimeter level, SLA show residual errors likely correlated to mispointing (used as input parameters in RADS but estimated in PLRM MLE4). More wave situations associated to different mispointing angles and radial velocities are needed to better characterize these discrepancies. In addition, absolute biases were found for the different parameters in part explained by the lack of correction for the PTR approximation in the processing. SWH exhibit substantial residual errors correlated with waves that confirm the last point. At a lesser extent, the Sigma0 shows bias of 0.2 dB magnitude depending on waves and possibly correlated with the mispointing angle. On the other hand, some noticeable improvements were found in range and sigma0 measurement precision. But, despite a better noise performance, the TU-Delft processing shows higher correlated errors than CNES PLRM degrading somewhat the content for SLA at scales below 100 km. **On the basis of these results, further work is needed to better understand and correct the long wavelength errors raised in this study. These issues need to be addressed to allow for better continuity with conventional altimetry missions, and ultimately make this processing of interest for the Sentinel-3 mission with its enhanced measurement precision.**

For its part, the innovative SARM processing is of obvious interest to monitor the ocean in coastal areas. There is however less evidence of its ability in improving the quality of open ocean altimetry measurements. The main findings are summarized below.

As for the nominal SAR altimeter processing, the innovative SARM method improves the content of the LRM datasets for wavelengths below 100 km. However, when compared to the nominal Sentinel-3 processing, no improvement in the detection of small-scale oceanic structures was observed, since neither the sea level noise level nor the long ocean wave correlated errors have been reduced. It appears in contrary that the sea level spectrum has slightly more energy for scales from 2 to 10 km due to an overlap between consecutive measurements (resulting from the application of the Hamming function). Fortunately, the mean sea level spectrum does not seem to be impacted for wavelengths ranging from 30 to 100 km that matters for the ocean community. Now, regarding the SWH estimates, results indicate that the innovative SARM provides much-enhanced measurement precision than for the nominal processing (a reduction > 35% at 2 m SWH). On the other hand, no conclusion can be made on the accuracy of SWH estimates, since inappropriate corrections for the PTR approximation were used. Debate remains open on that point. **On the basis of that assessment results (showing substantial reduction of SWH noise and quite-close SLA performance), we advocate the use of the innovative SARM processing for Sentinel-3 mission to improve ocean altimetry products for end-users (more likely in coastal areas). It will be interesting to see if further analyses performed at global scale (using Sentinel-3 data) confirm these results or if different areas provide different conclusions. Such analyses will also need to pay close attention to any sea level changes in the spectrum. Remember that the key issue and challenge for new SARM processing in open ocean is to enhance the altimeter capability**

**in accessing finer scale structures in order to improve our understanding of oceanic (sub)mesoscale processes. Unfortunately, that point has not been adequately addressed in the innovative SARM processing. Last but not least, we strongly recommend to identify the algorithms used in this processing that make the SWH noise improvement and explain the underlying physical principle that allows to make it better than the Sentinel-3 processing. We feel that this is necessary in order to fully convince the altimeter community of the benefit of this processing.**

An assessment analysis of the GPD+ methodology was also performed. Overall, results showed that the GPD+ approach combining various data types leads to a significant improvement of the Cryosat-2 SSH and SLA estimations accuracy. The GPD+ WTC reduces the sea level anomaly variance with respect to the ECMWF operational model correction from both along-track analysis and cross-overs by  $\sim 2 \text{ cm}^2$  (particularly effective in low latitude areas). This approach is also of particular relevance to coastal regions where a reduction of the SLA variance is observed. Unfortunately, this analysis did not permit to assess the GPD+ performance over polar regions due to the relatively small geographical coverage used in this study. It is also important to note that along track discontinuities of a few mm height were observed, without however adverse impact on the SLA accuracy. In case of occurrence of higher discontinuities, a strategy to better handle such discontinuities should be envisaged. **To conclude, the GPD+ correction clearly outperforms the ECMWF operational model-derived correction in both open ocean and coastal areas. This improved solution is of particular interest for altimetry missions which do not possess on-board microwave radiometer. For the Sentinel-3 mission embarking a MWR sensor, such solution is of interest whenever MWR measurements are considered invalid, but could be used as well as independent data for assessing the on-board MWR derived WTC (using GPD+ corrections computed without on-board MWR data). Finally, it should be mentioned that these results were obtained using a two years data set processed over SAR-mode ocean areas only. The global performances/metrics, including LRM areas could differ.**

# 3 Open Ocean Validation of the SCOOP Second Test Data Set by isardSAT

## 3.1 Summary of Approach

The role of isardSAT in the SCOOP project is to test different modifications of the Sentinel-3 SAR L1B processing baseline in order to check the potential improvements that might be achieved (as part of WP3000), providing a test data set for phase-2 (Test-2). During Phase-2 isardSAT is also in charge of retracking this data set with its in-house implementation of the SAR ocean retracker, based on model proposed by Ray et al. 2015.

In order to evaluate the performance of the new processing configuration (Test-2 or Phase-2) against the Test-1 or Phase-1 data test (known also as GPOD data set) and check the consistency of the results a validation has been carried out over a reduced set of areas of interest (AOI). Two differentiated sets of AOIs have been combined in the validation process:

- *North East Atlantic and Agulhas regions (2012-2013)*: in this case specific geographical masks have been used on the validation process to filter out those surfaces close to the coast as shown in Figure 3.1<sup>1</sup>
- *West/Central/East Pacific regions (2012-2013)*

It must be noted that the Phase-2 or Test-2 data set used in the validation corresponds to the data set produced in November 2018, no specific L1B coastal processing was considered.

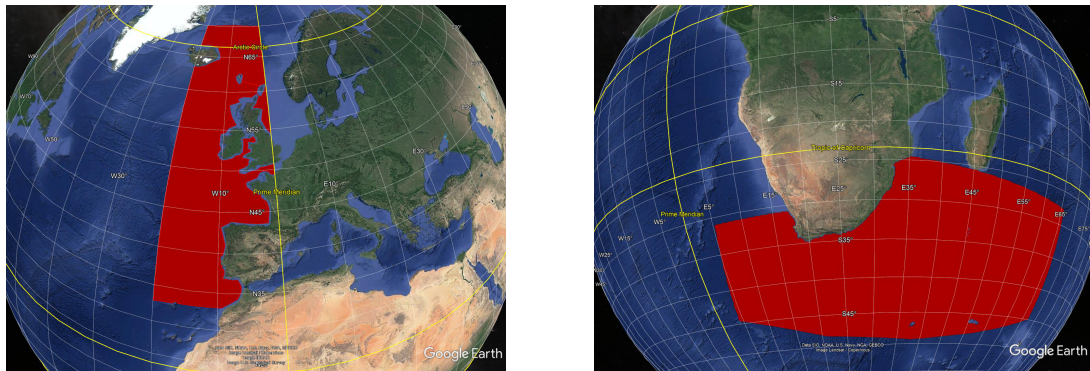


**Figure 3.1 Geographical masks used in the validation activity over North East Atlantic and Agulhas regions (filter out the land contribution from the analysis).**

The validation consists on the performance analysis of Phase-2 (Test-2) against Phase-1 (Test-1) data set both in terms of accuracy and precision on the geophysical retrievals (SSH, SWH and  $\sigma_0$ ): the first one provides information regarding the potential biases in the geophysical parameters w.r.t Test-1 reference baseline; while precision provides information related to the noise performance in the retrieval of the geophysical parameters.

---

<sup>1</sup> The distance to the coast was roughly around 30 Km in case of North East Atlantic and 12 Km for the Agulhas case. These masks are sufficient for the purposes of the validation exercise of the complete processing chain from L1B up to L2.

The large scale analysis of both accuracy (biases) and precision in each individual geophysical parameter are provided as:

- Bi-dimensional distribution maps as a function of the radial velocity and SWH are generated in order to understand whether any unexpected dependencies show up.
- Performance (bias and precision) as a function of the SWH

To build up the previous performance metrics the following procedure is considered:

- For each individual processed track from Test-1 and Test-2:
  - Starting point is to split each individual processed track in consecutive and non-overlapping segments of 20 samples (referred as data block)
  - Standard deviation of each de-trended data block is computed for the different geophysical parameters (SSH, SWH and sigma0)
  - Mean values within each data block are also computed for SSH, SWH and sigma0
  - Mean values of the radial velocity (or height rate) per block are also computed
- Information of all the data blocks of all the tracks corresponding to the different AOIs are combined to produce the different performance metrics with statistical significance:
  - 2-D accuracy maps versus radial speed and SWH:
    - first and for each data block the difference of the mean values between Test-1 and Test-2 data are computed (for SSH, SWH and sigma0);
    - then to generate the 2-D maps, a binning procedure based on the mean radial velocity and mean SWH is considered so that all the data block differences whose associated radial velocity and SWH lie within the limits of a given bidimensional bin are averaged. The binning step considered for the radial velocity is 50 cm/s and for SWH is 50 cm/s
  - 2-D precision maps versus radial speed and SWH<sup>2</sup>:
    - An analogous procedure is followed to construct the 2-D maps, using a bidimensional binning procedure, but in this case the standard deviation of each data block is considered (separately for Test-1 and Test-2 sets). Thus, an average of the different standard deviations of all the data blocks that lie within the limits of a given bidimensional bin (radial) is computed.
  - 1-D accuracy plots versus SWH:
    - Starting point corresponds to all the differences between the mean values of data blocks between Test-1 and Test-2. A binning procedure based only on SWH is considered such that all the data block differences whose associated SWH lies within the limits of a given SWH bin are averaged.
  - 1-D precision plots versus SWH:
    - Starting point corresponds the standard deviations of all the data blocks (separately for Test-1 and Test-2 sets). A binning procedure based only on SWH is considered such that all the data block standard deviation whose associated SWH lies within the limits of a given SWH bin are averaged.

---

<sup>2</sup> To decouple the effect of any SWH bias (between the different data sets Test-1 and Test-2) from the estimation of the corresponding precision (noise performance), the average SWH (mean values per data block) of Test-1 or GPOD data have been assigned to the Test-2 data set in the binning procedure. The same applies for the 1-D precision plots versus SWH. For the accuracy analysis the average value of the SWH of Test-2 (for each block) has been assigned in the binning procedure to the difference block, similar results are obtained for the case of assuming the average value of SWH of Test-1 (or GPOD).

## 3.2 Results from Validation Test 2

### 3.2.1 AOI-1: North East Atlantic + Agulhas areas

#### 3.2.1.1 Accuracy

##### 3.2.1.1.1 SSH

Figure 3.2 (left panel) shows the map of the SSH difference between Test-2 (or Phase-2) data and GPOD (Test-1) as a function of the radial velocity and SWH (of Phase-2 data set). It can be noticed that there is no clear dependency on the radial velocity or SWH; opposed to what was observed in older data during the Phase-2a as shown in Figure 3.2 (right panel), where some radial velocity dependency shows up (specifically when comparing the regions of absolute velocity between 20-30 m/s linked to Agulhas area). It must be noted that the AOIs included in that analysis were Agulhas, Central Pacific and North Sea for the year 2013; while for the Phase-2 Agulhas and North East Atlantic have been considered. Nevertheless, this comparison is fair as the Agulhas region has been included (which is the one related to the critical areas of radial velocity dependency – 20 to 30 m/s) and the North East Atlantic Region has a common latitude span as the North Sea area and so similar span of expected radial velocities.

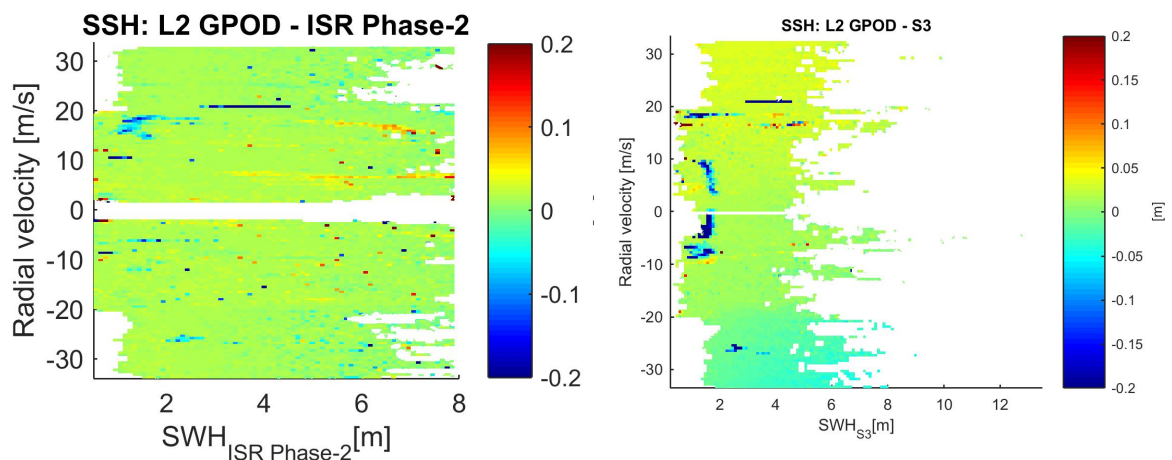


**Figure 3.2 SSH difference maps versus radial velocity and SWH: (left) Difference between Test-1 (GPOD) and Test-2 (Phase-2a) for Agulhas and North East Atlantic regions years 2012-2013; (right) Difference between Test-1 (GPOD) and Phase-2a for Agulhas, Central Pacific and North sea, year 2013.**

##### 3.2.1.1.2 SWH

Analogously the SWH map differences between Test-2 and Test-1 data sets is shown in Figure 3.3. This result doesn't show a dependency on the radial velocity, but there is a slight bias as a function of the SWH as demonstrated by the plot in Figure 3.4, where the dependency is in any case below 20 cm. If we consider the scattering plot of the 20-Hz SWH data without any averaging in data blocks, Figure 3.5, a very good correlation between Test-1 (GPOD) and Test-2 (Phase-2) is obtained.

The shape of bias dependency in Figure 3.4 shows somehow a correlated pattern with the shape of the variable PTR setting as a function of SWH (LUT) used in the retracking process of Test-1 (as shown in SCOOP ATBD, Figure 5.2-2). Such a bias then might be related to the fact that in Test-2 data set the in-house isardSAT retracker uses a fixed PTR setting as the intra-burst Hamming is used, the value of the PTR both along- and across-track has been set to minimize the average error

between Test-2 and Test-1 SWH. From our understanding the differences could be attributed to the fact that the variable PTR LUT setting as a function of SWH has been empirically tuned to the implemented retracker used in GPOD processor (Test-1). A validation with in-situ data would help on properly setting/calibrating the PTR widths, which is out of the scope of the project.

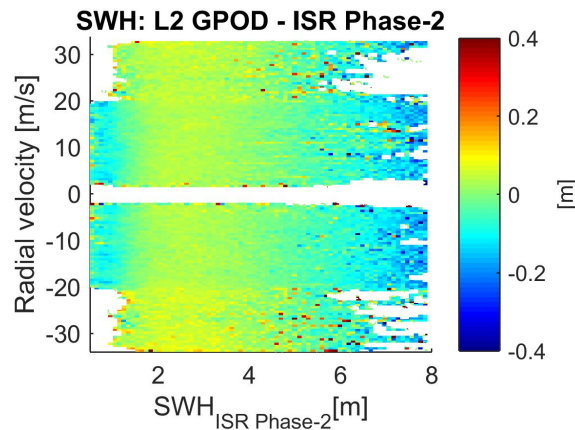


**Figure 3.3 SWH difference maps versus radial velocity and SWH: Difference between Test-1 (GPOD) and Test-2 (Phase-2) for Agulhas and North East Atlantic regions years 2012-2013.**

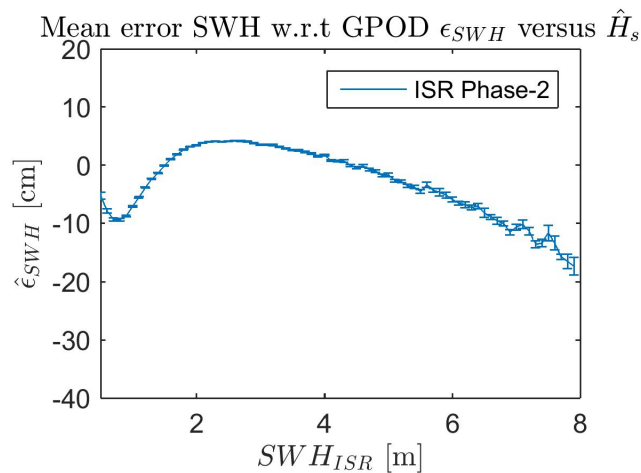


**Figure 3.4 SWH difference between Test-1 (GPOD) and Test-2 (Phase-2) as a function of Phase-2 SWH for Agulhas and North East Atlantic regions years 2012-2013.**

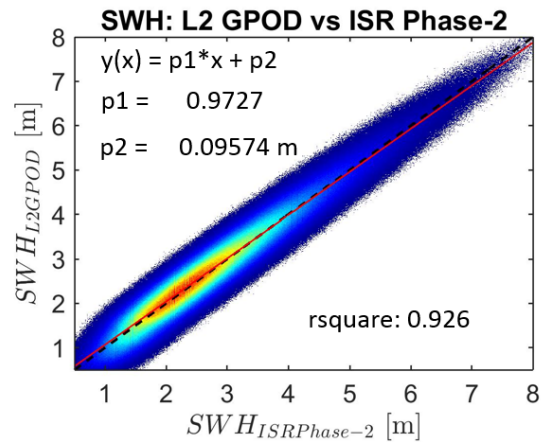


Figure 3.5 SWH scatter plot Test-2 (Phase-2) versus Test-1 (GPOD) for Agulhas and North East Atlantic regions years 2012-2013.

### 3.2.1.1.3 $\sigma_0$

Figure 3.6 depicts the  $\sigma_0$  difference map between Test-1 and Test-2 data sets as a function of the radial velocity and the SWH. No clear pattern as a function of the radial velocity is observed; while a very small dependency of the differences as a function of the SWH is present as shown in Figure 3.7. This dependency can be correlated to the SWH difference as a function of the SWH (shown in Figure 3.4), since the SWH term in the retracker model is a factor in the dilation term that directly modulates the amplitude of each single look waveform.

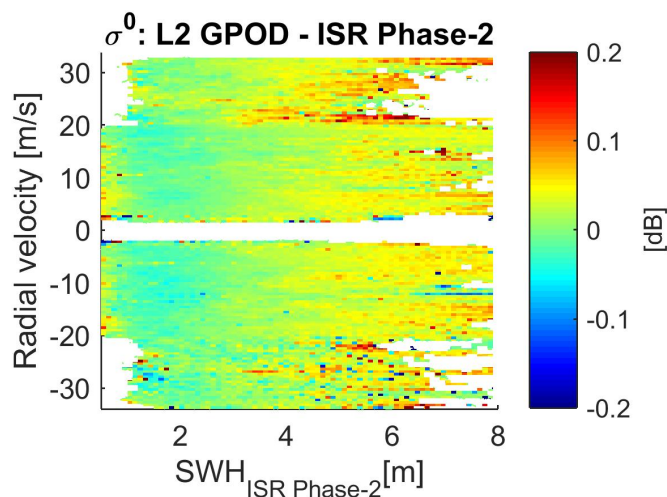
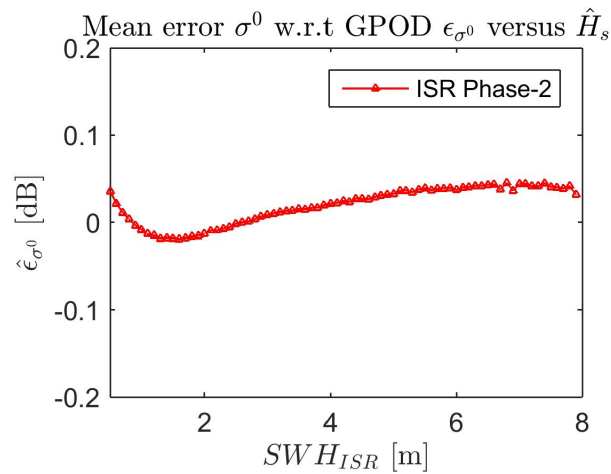


Figure 3.6  $\sigma_0$  difference maps versus radial velocity and SWH: Difference between Test-1 (GPOD) and Test-2 (Phase-2) for Agulhas and North East Atlantic regions years 2012-2013.



**Figure 3.7** sigma0 difference between Test-1 (GPOD) and Test-2 (Phase-2) as a function of Phase-2 SWH for Agulhas and North East Atlantic regions years 2012-2013.

### 3.2.1.2 Precision

#### 3.2.1.2.1 SSH

The precision in the retrieval (measured as standard deviation) of the SSH as a function of the radial velocity and SWH is shown in Figure 3.8 for Test-2 and Test-1, left and right plots, respectively. Very similar noise figures are obtained for both data sets with no radial velocity dependencies and a common expected degradation in noise as SWH increases.

If we consider the precision as a function only of the SWH of Phase-1 as in Figure 3.9, a small degradation for the Phase-2 compared to Test-1 (GPOD) data in the low SWH area is observed. This might be related to the overestimation on SWH of Phase-2 data for the low SWH (as shown in Figure 3.4). An improved precision for Phase-2 data is obtained for SWH above 4m, related to the exploitation of the intra-burst Hamming window.

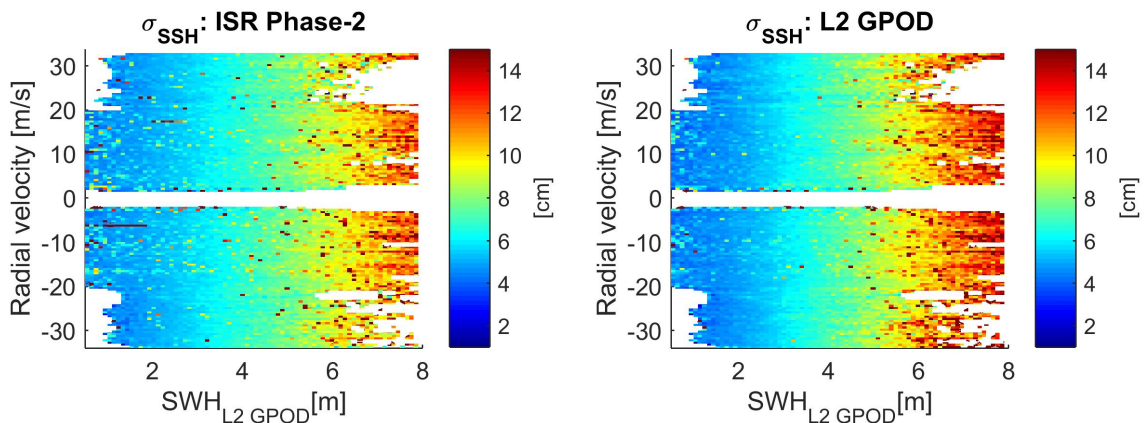


**Figure 3.8** SSH precision (std) maps versus radial velocity and SWH: (left) Test-2 data and (right) Test-1 (GPOD) data for Agulhas and North East Atlantic regions years 2012-2013.

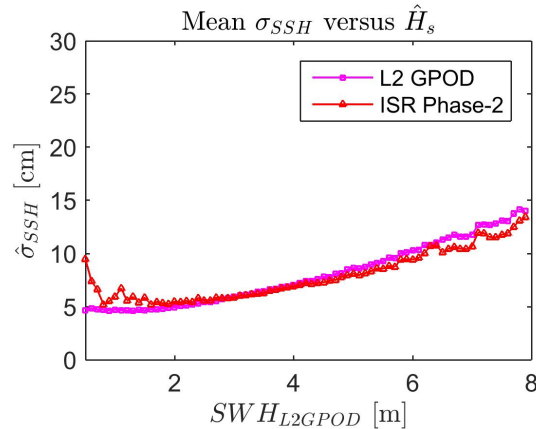


**Figure 3.9** SSH precision as a function of Test-1 SWH for both Test-1 (GPOD) and Test-2 (Phase-2) data sets (Aguhas and North East Atlantic regions, years 2012-2013).

### 3.2.1.2.2 SWH

The precision in the retrieval (measured as standard deviation) of the SWH as a function of the radial velocity and SWH is shown in Figure 3.10 for Test-2 and Test-1, left and right plots, respectively. Test-2 (Phase-2) data shows very good performance compared to Test-1 data, with a consistent improvement of approximately 10 cm throughout the SWH dynamic range. This can be clearly observed in the 1-D precision as a function of the SWH in Figure 3.11.

From one side the improved performance is in part related to the combined exploitation of the intra-burst Hamming and zero-padding in range. From the Phase-2a data analysis considering different processing baselines as reported in Figure 3.12, it was observed that compared to the nominal Sentinel-3 processing baseline the zero-padding only modification was providing improvements in the lower SWH region, while intra-burst Hamming only modification improved the noise for SWH higher than 4 m. It must be noted that the L1B and L2 processor in Phase-2a were not adjusted as in the last version of the Phase-2 data.

In any case, it can be also noticed that the in-house isardSAT retracker was providing in general improved noise performance even for the nominal S-3 processing baseline compared to GPOD (Test-1) for SWH higher than 3-m, Figure 3.12. This can be linked to a much higher stability of the retracker that we suspect can be related to the way the initial SWH seeding for subsequent surfaces has been implemented: it is based on a sliding window approach from previous estimates in order to minimize the impact of potential outliers.

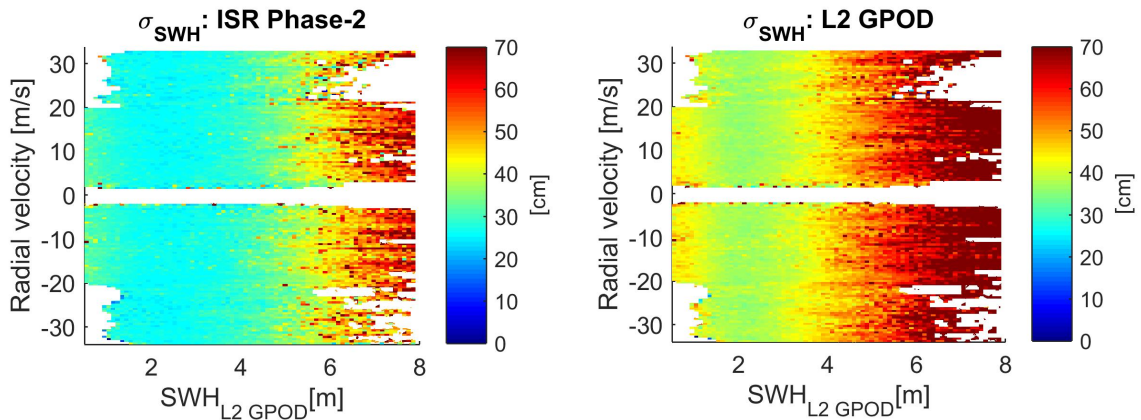


Figure 3.10 SWH precision (std) maps versus radial velocity and SWH: (left) Test-2 data and (right) Test-1 (GPOD) data for Agulhas and North East Atlantic regions years 2012-2013.

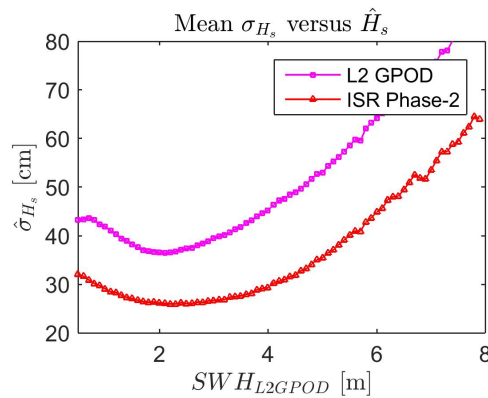


Figure 3.11 SWH precision as a function of Test-1 SWH for both Test-1 (GPOD) and Test-2 (Phase-2) data sets (Agulhas and North East Atlantic regions, years 2012-2013).

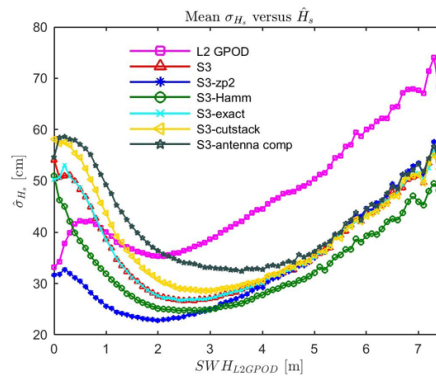


Figure 3.12 SWH precision as a function of Test-1 SWH for both Test-1 (GPOD) and Phase-2 data sets (Agulhas North Sea and Central Pacific regions, year 2013); different processing baselines considered activating only one processing option per baseline.

### 3.2.1.2.3 $\sigma_{\sigma 0}$

The precision in the retrieval (measured as standard deviation) of the  $\sigma_{\sigma 0}$  as a function of the radial velocity and SWH is shown in Figure 3.13 for Test-2 and Test-1, left and right plots, respectively. Very similar noise figures are obtained for both data sets with a slight improvement for the Phase-2 data over the whole SWH range, as shown in Figure 3.14.

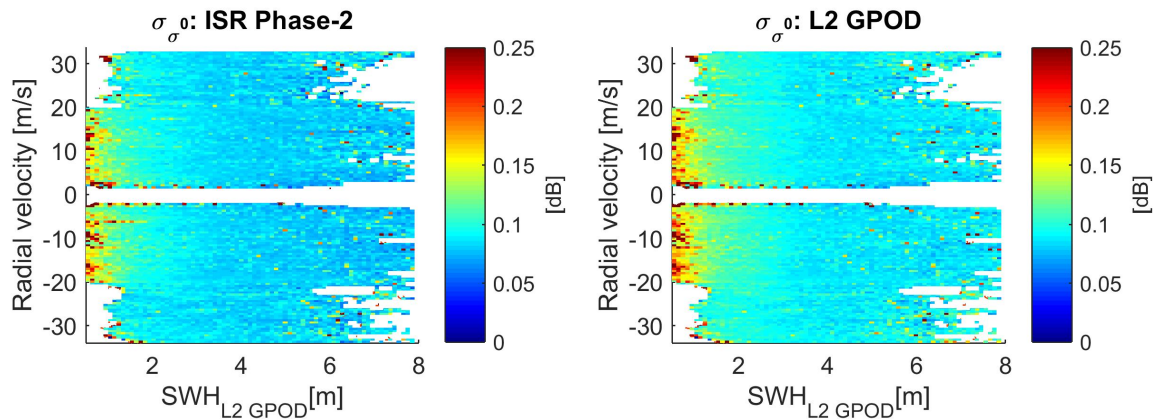


Figure 3.13 Sigma0 precision (std) maps versus radial velocity and SWH: (left) Test-2 data and (right) Test-1 (GPOD) data for Agulhas and North East Atlantic regions, years 2012-2013.

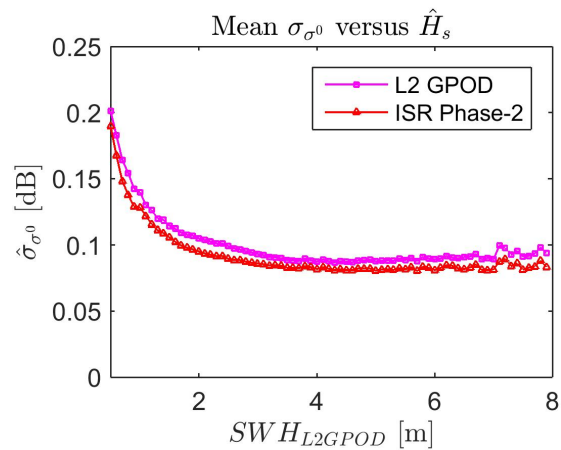


Figure 3.14 Sigma0 precision as a function of Test-1 SWH for both Test-1 (GPOD) and Test-2 (Phase-2) data sets (Agulhas and North East Atlantic regions, years 2012-2013).

## 3.2.2 AOI-1: Pacific (west/central/east) areas

### 3.2.2.1 Accuracy

#### 3.2.2.1.1 SSH

Figure 3.15 shows the map of the SSH difference between Test-2 (or Phase-2) data and GPOD (Test-1) as a function of the radial velocity and SWH (of Phase-2 data set). As in the previous regions no dependency on the radial velocity is observed.

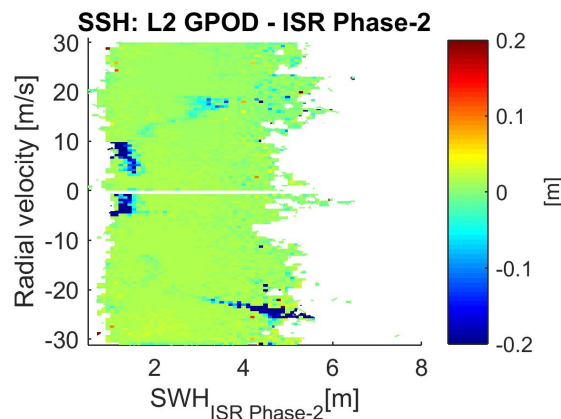


**Figure 3.15 SSH difference maps versus radial velocity and SWH: Difference between Test-1 (GPOD) and Test-2 (Phase-2a) for Pacific regions years 2012-2013.**

#### 3.2.2.1.2 SWH

The SWH map differences between Test-2 and Test-1 data sets is shown in Figure 3.16. This result doesn't show a dependency on the radial velocity, but as in the previous analysed regions there is a slight bias as a function of the SWH as demonstrated by the plot in Figure 3.17, where the dependency is in any case below 20 cm.

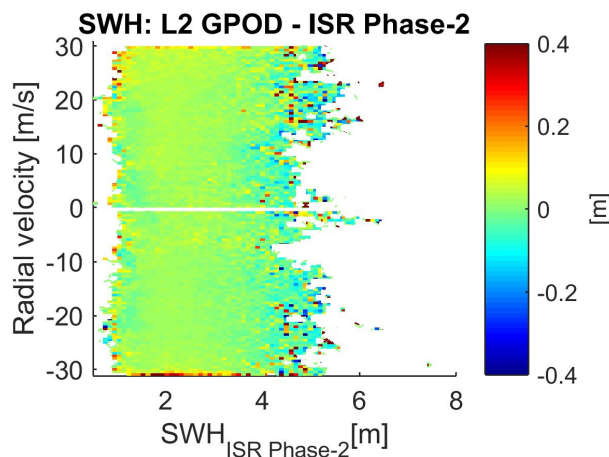


**Figure 3.16 SWH difference maps versus radial velocity and SWH: Difference between Test-1 (GPOD) and Test-2 (Phase-2) for Pacific regions years 2012-2013.**

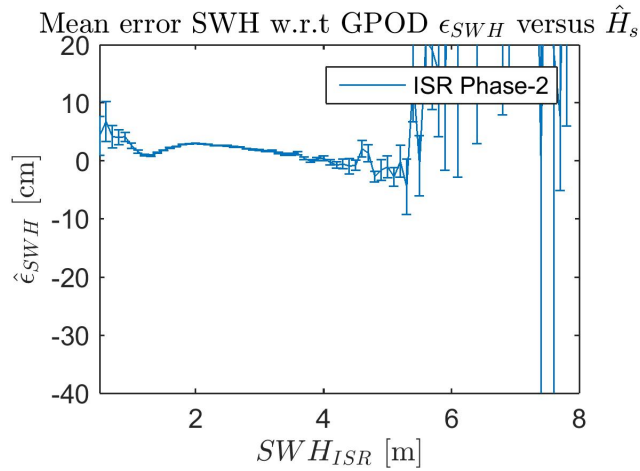


**Figure 3.17 SWH difference between Test-1 (GPOD) and Test-2 (Phase-2) as a function of Phase-2 SWH for Pacific regions years 2012-2013; degradation for SWH larger than 5 meters because there is almost no population of data is available above these SWH values**

3.2.2.1.3 *Sigma0*

Figure 3.18 depicts the sigma0 difference map between Test-1 and Test-2 data sets as a function of the radial velocity and the SWH. Differently from the previous analysed regions a dependency on the radial velocity is observed. CLS analysis on sigma0 differences comparing Test-1 (GPOD) data and CPP data showed also some pattern differences as a function of radial velocity that are likely correlated to the orbit. In any case the differences in sigma0 are below 0.1 dB (Figure 3.19) below the requirement on sigma0 retrieval precision for Sentinel-6 mission.

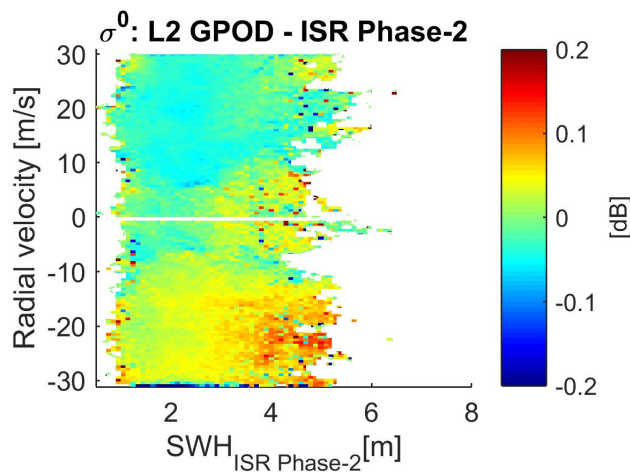


**Figure 3.18 sigma0 difference maps versus radial velocity and SWH: Difference between Test-1 (GPOD) and Test-2 (Phase-2) for Pacific regions years 2012-2013.**

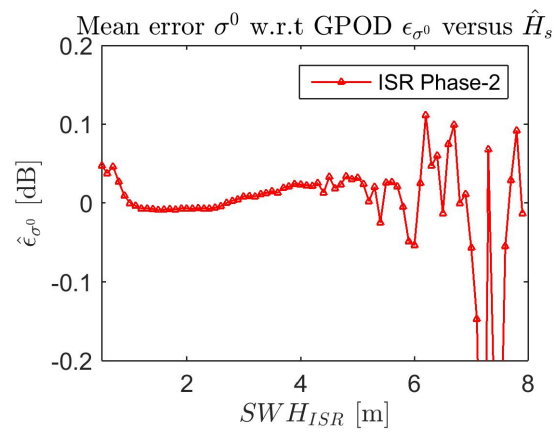


**Figure 3.19 sigma0 difference between Test-1 (GPOD) and Test-2 (Phase-2) as a function of Phase-2 SWH for Pacific regions years 2012-2013.**

### 3.2.2.2 Precision

The results in terms of precision for these regions of interest (Pacific areas) are consistent with the ones obtained for the regions in section 3.2.1.2.

#### 3.2.2.2.1 SSH

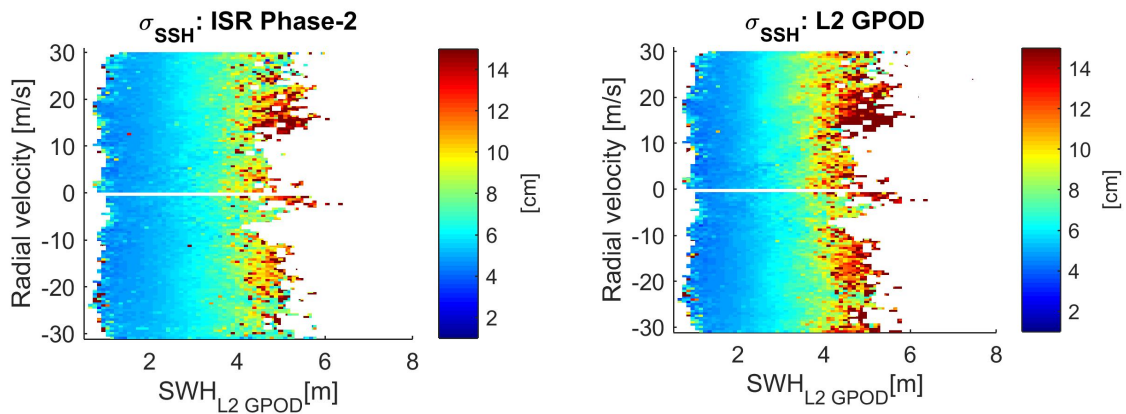


Figure 3.20 SSH precision (std) maps versus radial velocity and SWH: (left) Test-2 data and (right) Test-1 (GPOD) data for Pacific regions years 2012-2013.

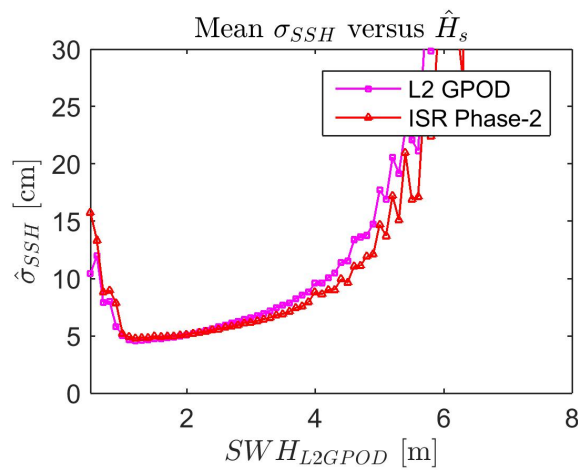


Figure 3.21 SSH precision as a function of Test-1 SWH for both Test-1 (GPOD) and Test-2 (Phase-2) data sets (Pacific regions, years 2012-2013).

3.2.2.2.2 SWH

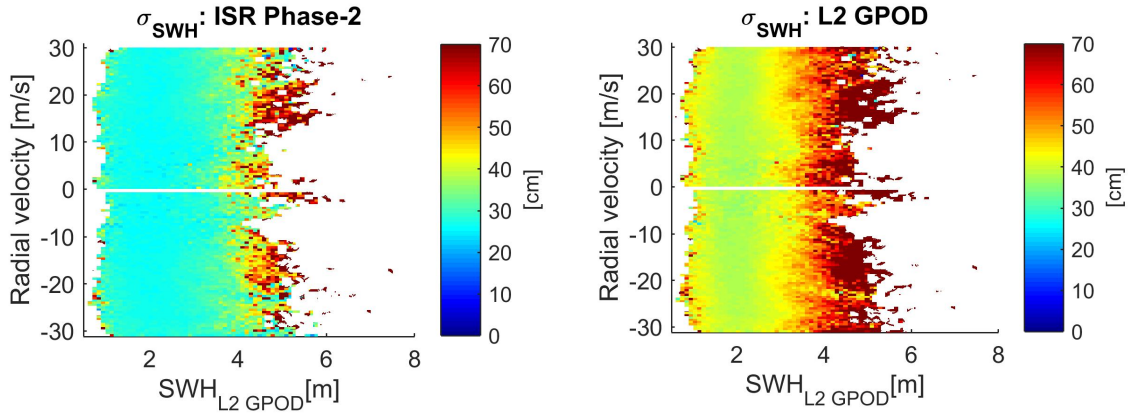


Figure 3.22 SWH precision (std) maps versus radial velocity and SWH: (left) Test-2 data and (right) Test-1 (GPOD) data for Pacific regions years 2012-2013.

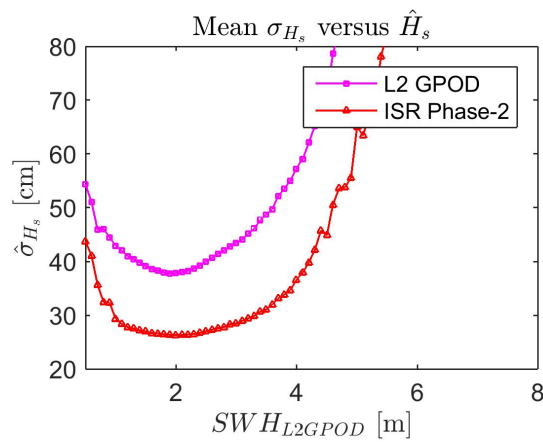
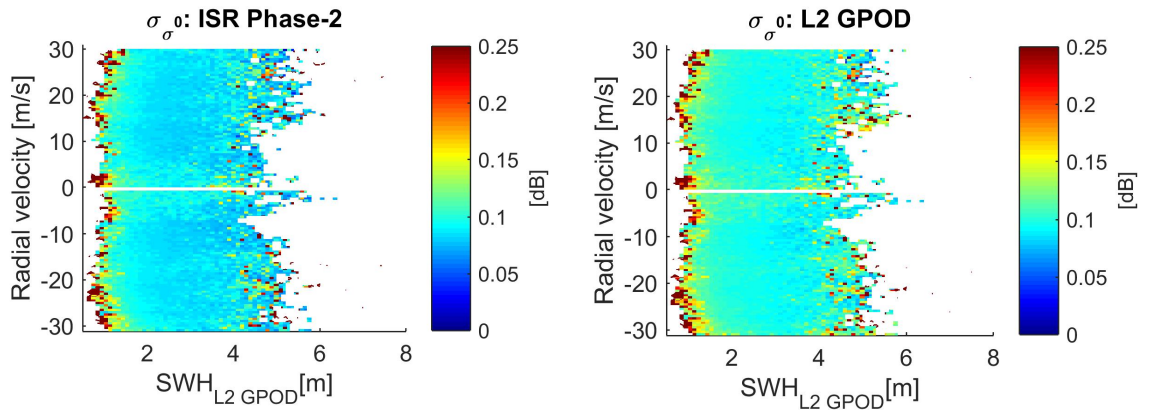
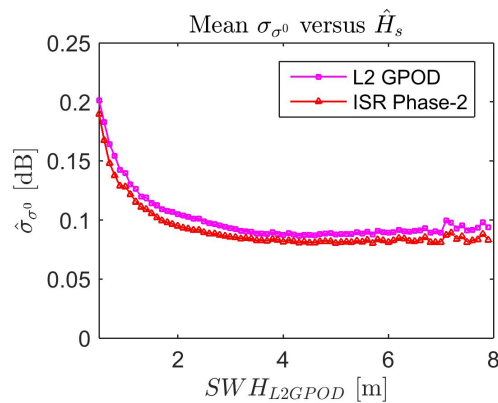


Figure 3.23 SWH precision as a function of Test-1 SWH for both Test-1 (GPOD) and Test-2 (Phase-2) data sets (Pacific regions, years 2012-2013).

### 3.2.2.2.3 $\sigma_{\sigma_0}$



**Figure 3.24** Sigma0 precision (std) maps versus radial velocity and SWH: (left) Test-2 data and (right) Test-1 (GPOD) data for Pacific regions years 2012-2013.



**Figure 3.25** Sigma0 precision as a function of Test-1 SWH for both Test-1 (GPOD) and Test-2 (Phase-2) data sets (Pacific regions, years 2012-2013).

## 3.3 Summary of Results

The main outcomes of the validation exercise are:

- SSH:
  - The global scale analysis over the two sets of regions shows consistency between the SSH of the Test-2 and Test-1 data.
  - No dependency on the radial velocity of the SSH differences between Test-2 and Test-1 data.
  - Very similar noise performance is obtained for both Test-2 and Test-1 data, with a slight improvement on the higher SWH that can be related to the intra-burst Hamming application
- SWH:
  - Small dependency as a function of the SWH of the SWH differences between Test-2 and Test-1 data set, this might be related to the PTR setting: Test-1 uses an variable PTR empirically tuned for the retracker implementation in GPOD (through a LUT), while Test-2 uses isardSAT in-house retracker exploiting a fixed PTR setting; in-situ measurements would be required to fine tune and calibrate the PTR settings.
  - Noise performance improvement around 10 cm throughout the SWH dynamic range (1 to 8-m): part is related to the combined setting of intra-burst Hamming and zero-padding, and another contribution to the improvement can be related to the better stability of the retracker that we suspect can be associated to the way the SWH initial seeding is implemented based on a sliding window of previous estimates
- Sigma0:
  - Global scale analysis over the two sets of regions shows consistency between the Sigma0 of Test-2 and Test-1 data, where a small dependency (below 0.1 dB) as a function of radial velocity is observed on the Pacific regions. This can be linked specifically to some related orbit height dependency as shown by CLS analysis (as such dependency was also observed when comparing Test-1 or GPOD data against CPP data)
  - Similar noise performance are obtained for both data sets (Phase-1 and Phase-2), with a slight improvement for the Test-2 data

# 4 Coastal Zone Validation of the SCOOP Second Test Data Set by SKYMAT

## 4.1 Introduction

The aim of this work package is to characterise the performance of CryoSat-2 SAR mode altimeter product by assessing the uncorrected sea surface height (USSH, Altitude minus Range) and significant wave height (SWH) for both the Phase 1 G-POD dataset and the Phase 2 dataset in nine regions of interest (ROIs). Directional analysis was also carried out over one of the ROIs where the comparison of noise for different directions of approach as a function of distance to the coast was investigated in order to understand how the quality of SAR observations deteriorates close to land.

## 4.2 Regions of Interest

Nine geographical regions were selected for this analysis as they had different sea surface properties providing a realistic sample size of areas to represent the sea surface around the globe.

They are as follows:

- 1) North East Atlantic
- 2) North Sea
- 3) North Indian Coast
- 4) Agulhas
- 5) East Pacific
- 6) Central Pacific
- 7) West Pacific
- 8) Harvest
- 9) Indonesia

## 4.3 Data

### 4.3.1 Phase 1 of the SCOOP project

Altimetry SAR CryoSat-2 data were collected and processed using the G-POD Service, **SARvatore** (**SAR** Versatile **Altimetric** Toolkit for **Ocean** **R**esearch & **E**xploitation). This is a web platform that is used to process the CryoSat-2 data to produce a SAR Level-2 geophysical dataset. The service is based on **SARvatore** Processor Prototype that was developed by EOP-SER Altimetry Team (Salvatore Dinardo, Bruno Manuel Lucas, Jerome Benveniste) in ESA-ESRIN. The SAR datasets generally span the period from 2012 and 2013, with the exception of the Harvest Region (West Coast of USA) which only spans the period from December 2015 to May 2016.

### 4.3.2 Phase 2 of the SCOOP project

A second dataset was produced from the SAR cryostat-2 altimetry data by isardSAT, referred to as SAR Phase 2 in this document. Additionally, this dataset was processed using Zero-Padding in 2 for Range (ZP2) and the HAMM window, both supplied by isardSAT.

A third dataset was produced from TU Delft, and is referred to as RDSAR

## 4.4 Methodology

The performance of the CryoSat-2 SAR mode Level 2 altimeter data is assessed and characterised by firstly investigating the noise along a track as a function of distance to the coastline. The SAR altimetry noise is defined as the successive differences of the uncorrected sea surface height (USSH, i.e. Altitude minus Range) along the track as a function of distance from the coastline (Passaro et al. 2014). The noise is then binned into 1 km intervals where the median value and the upper 75 and lower 25 percentiles are computed. The successive differences technique enables the data to behave statistically like white noise. White noise has a zero mean, a constant variance and is uncorrelated in time. It is a form of pre-whitening, where the "pre" means that the white noise (whitening) occurs first before any analysis takes place. CryoSat-2 SAR Phase 2 is analysed across the nine regions and then compared with the SAR phase 1 (G-POD) dataset. In addition, the RDSAR dataset is briefly examined.

Gommenginger et al. (2014) provided evidence that a misfit parameter applied to the SAR data improves the statistics. The misfit represents the quality of the fit between the L1B waveform and the fitted model (see Equation 1, Gommenginger et al. 2014). Cippolini and Calafat (2016) showed that only using CryoSat-2 SAR observations where the misfit is less than 3 in the SARvatore processor and applying a median bin filter as a function of distance to the coast created a stable USSH noise value of approximately 5 cm very close to the coast. Therefore, in this work package a misfit threshold value of 3 is used as part of the analysis to characterise the performance of the CryoSat-2 SAR mode altimeter products.

The second component of assessing the performance of CryoSat-2 SAR mode Level 2 data is by examining the noise of USSH as a function of Significant Wave Height (SWH) for the inshore region (3 km to 10 km) and an offshore region (43 km to 50 km). This will establish if the SWH influences the USSH noise close to the shore or not. The SWH data are binned in 0.2 m intervals between 0.3 m and 4.9 m to produce the median USSH noise value. A histogram is also calculated representing the SWH distribution in inshore and offshore regions. In order to represent scale, a 100% value is recorded for each histogram reflecting the maximum number of measurements that have occurred within the 0.2 m interval of SWH. Therefore, the integral of the histogram is the total number of altimetry SAR observations. In addition, a small experiment was setup to investigate the effect of applying the Zero Padding 2 in range processor or applying the hamming window is briefly investigated in comparison with the Phase 1 G-POD dataset as a reference frame for USSH noise and SWH.

Finally, the third assessment of the performance of CryoSat-2 is by investigating the angle of approach to the coast line. The angle of approach to the coast is computed by calculating the deviation angle between the direction of the satellite track and the direction of the gradient using the coast proximity parameter (Cipollini, 2011). This *deviation angle* is referred to as the *separation angle* in this document. Once the separation (deviation) angles associated with the USSH observations are computed, they are then binned at 15° intervals. This process is carried out for data within 8 km distance to coast. A separation angle value of 0° represents a satellite track that is normal to the coast, whereas a separation angle of 90° represents a satellite track that is parallel to the coast. Please note that the coastal proximity parameter is a dimensionless measure of the effect of land over altimetric waveforms, where the values have a range between -1 and +1, such that a -1 refers to geographical locations that are unaffected by land (normally offshore) and 1 represents totally affected by land, hence close inshore. The coast proximity parameter is treated as an independent variable and has an advantage over the closest approach to the coast parameter of capturing differences in coastal morphology. In this study, the separation angle dependency is assessed in terms of data lost close to the coast, by computing the percentage of data lost as a function of separation angle and distance to the coast.

## 4.5 Results

### 4.5.1 SAR Altimetry noise (USSH) and distance from the coast for SAR Phase 2 isardSAT and RDSAR

The performance analysis of the USSH observations from the SAR Phase 2 dataset showed similar characteristics over the nine regions where applying no misfit filter gave an USSH noise of 4 cm to within 10 km from the coast. This noise value increased to approximately 5 cm at 5 km from the coast and continued to increase to approximately 7-8 cm at 2 km from the coast. When the misfit filter was applied (i.e. only data with a misfit of less than 3 were valid, rejecting contaminated waveforms due to land echo artefacts) the USSH noise value was generally stable at 4 cm to within 2 km from the coast across all regions. However, the number of retrieved data points was drastically reduced to between 0.3 and 0.5 relative to the number of unfiltered data observations within 5 km of the coast. For example, Figure 4.1 and Figure 4.2 illustrate the USSH (noise) values as a function of distance to the coast with no misfit filter applied, and a misfit filter of less than 3 applied, respectively, for the Agulhas region. It is quite clear that the relatively high USSH noise values within 5 km from the coast are removed from the data using the misfit filter threshold of 3.

In comparison, the Phase 2 RDSAR dataset showed that USSH observations have a larger 10 cm noise value to within 2km of coast for all regions and with some filtering already applied. **Figure 4.3** shows the corresponding RDSAR phase 2 dataset for the Agulhas Region.

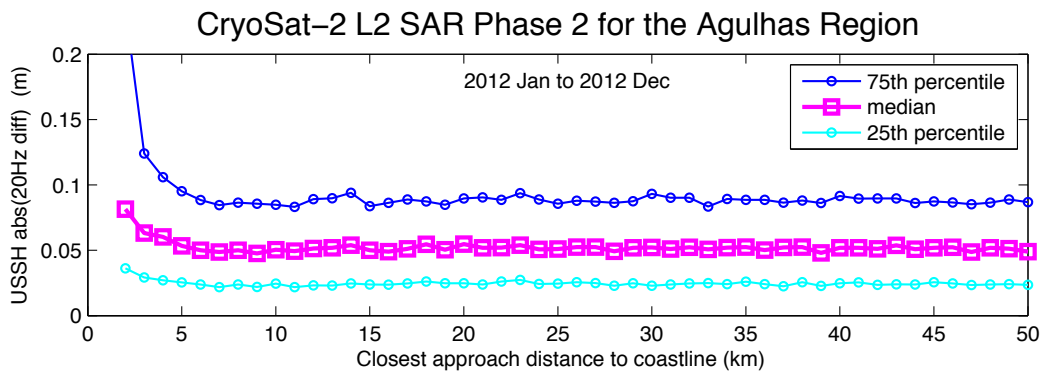


**Figure 4.1** USSH noise as a function of distance to the coast using no misfit

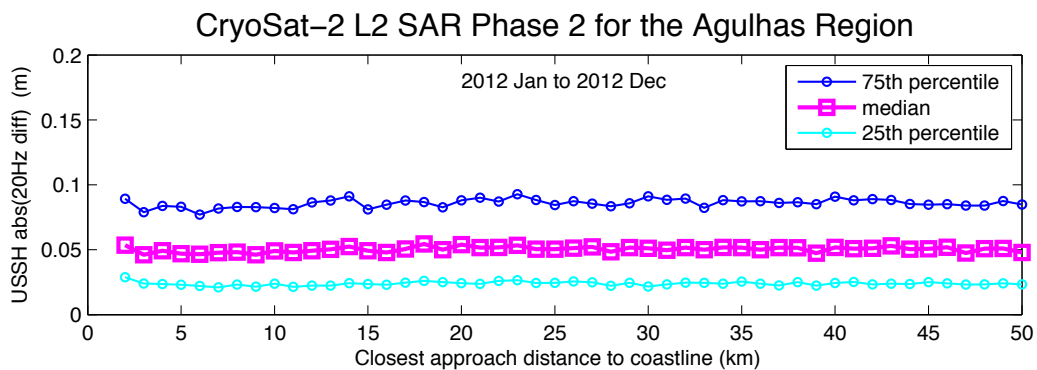


**Figure 4.2** USSH noise as a function of distance to the coast using a misfit filter of less than 3.

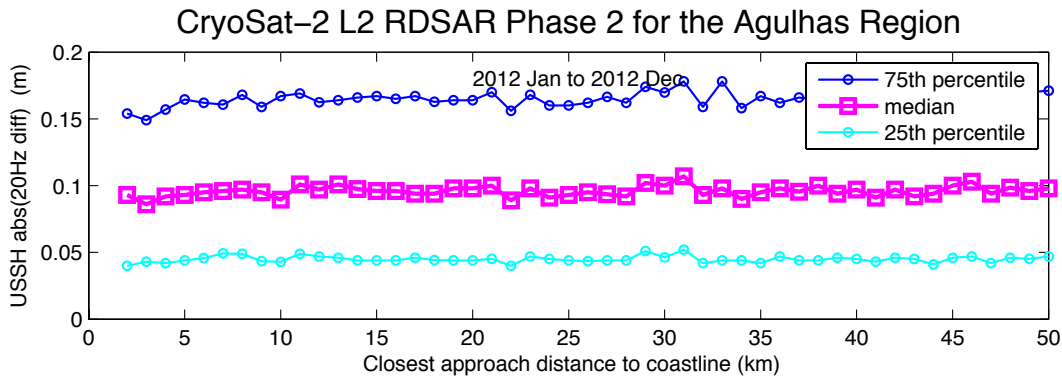


Figure 4.3 USSH noise as a function of distance to the coast using the RDSAR dataset

#### 4.5.2 Comparison between CryoSat SAR Phase 2 (isardSAT) and CryoSat SAR Phase 1 (G-POD)

The analysis of the nine regions reveals that higher noise in USSH in SAR Phase 2 TDS is observed compared with the G-POD Phase 1 for enclosed seas at all distances from the coast when no misfit threshold is applied, but there is an indication that in more open regions, the SAR Phase 2 TDS shows lower noise moving to offshore. For example, Table 4.1 Comparison of SAR Phase 2 (isardSAT) and SAR Phase 1 (G-POD) showing USSH Noise (m) for distances from the coast (km) – before misfit filter applied. shows the median binned USSH value and number of observations in the North East Atlantic region (with no misfit threshold applied) at a given distance to coast. This analysis of the Phase 1 and Phase 2 datasets reveals the need to apply a misfit threshold of 3, as applying this filter shows good consistency in noise from open ocean to inshore waters as well as reducing the difference in noise performance inshore between Phase 2 and Phase 1 (G-POD) to the extent that the differences are not significant (Table 4.2). However, it significantly reduces the number of retrieved “good” USSH data within 10 km of the coastline.

Table 4.1 Comparison of SAR Phase 2 (isardSAT) and SAR Phase 1 (G-POD) showing USSH Noise (m) for distances from the coast (km) – before misfit filter applied.

	Northeast Atlantic 2012						
Distance from the coast (km)	2	3	5	10	20	30	40
SAR Phase2 No. of Observations	26032	25059	23800	21397	19721	18235	16813
G-POD No. of Observations	23347	22527	21328	18915	17628	16389	14809
SAR Phase2 Median Noise value	0.071	0.059	0.051	0.047	0.047	0.047	0.047
G-POD Median Noise value	0.064	0.054	0.047	0.045	0.045	0.047	0.048
Difference	0.007	0.005	0.003	0.002	0.002	0.001	0.000
	Northeast Atlantic 2013						
SAR Phase2 No. of Observations	24665	24659	22273	19591	18334	17163	16513
G-POD No. of Observations	23500	23405	21135	18411	17235	16203	15493
SAR Phase2 Median Noise value	0.075	0.062	0.051	0.048	0.048	0.048	0.049
G-POD Median Noise value	0.066	0.054	0.049	0.047	0.048	0.049	0.049
Difference	0.008	0.008	0.003	0.001	0.000	-0.001	-0.001

**Table 4.2 Comparison of SAR Phase 2 (isardSAT) and SAR Phase 1 (G-POD) showing USSH Noise (m) for distances from the coast (km) – after the misfit threshold of 3 is applied.**

<b>Northeast Atlantic 2012</b>							
<b>Distance from the coast (km)</b>	<b>2</b>	<b>3</b>	<b>5</b>	<b>10</b>	<b>20</b>	<b>30</b>	<b>40</b>
SAR Phase2 No. of Observations	8292	12205	17446	19594	18661	17471	16171
G-POD No. of Observations	7251	10867	15371	16988	16232	15327	13841
SAR Phase2 Median Noise value	0.044	0.045	0.044	0.045	0.046	0.046	0.047
G-POD Median Noise value	0.043	0.044	0.043	0.043	0.043	0.045	0.046
<b>Difference</b>	<b>0.001</b>	<b>0.001</b>	<b>0.001</b>	<b>0.002</b>	<b>0.003</b>	<b>0.001</b>	<b>0.001</b>
<b>Northeast Atlantic 2013</b>							
SAR Phase2 No. of Observations	7224	11260	16241	17685	17266	16297	15846
G-POD No. of Observations	6789	10549	15017	16286	15823	14999	14452
SAR Phase2 Median Noise value	0.046	0.047	0.045	0.046	0.047	0.047	0.048
G-POD Median Noise value	0.043	0.044	0.044	0.045	0.046	0.047	0.048
<b>Difference</b>	<b>0.003</b>	<b>0.003</b>	<b>0.001</b>	<b>0.001</b>	<b>0.001</b>	<b>0.000</b>	<b>0.000</b>

Analysis of the SWH shows that if the misfit threshold of 3 is applied to both Phase 2 and Phase 1 (G-POD) datasets, then generally the SWH for the Phase 2 dataset has a higher value than the G-POD Phase 1 dataset where the SWH is less than 1.6 m (see Table 4.3, North East Atlantic as a regional example).

The difference in SWH between the Phase 1 and Phase 2 datasets increases to approximately 15 cm for smaller wave heights: at around 1.2 m but this value does vary from region to region. In addition, Phase 2 dataset consistently retrieves more data points than G-POD Phase 1, implying that the G-POD processing may be removing more “bad” data compared with that of the isardSAT processing for Phase 2. Please note, that this comparison was not between data at same locations and times.

**Table 4.3 Significant Wave Heights Analysis (m) for CryoSat-2 SAR Phase 2 and G-POD Phase 1 applying a misfit threshold of 3.**

		<b>km to the Coastline</b>						
		<b>2</b>	<b>3</b>	<b>5</b>	<b>10</b>	<b>20</b>	<b>30</b>	<b>40</b>
<b>Northeast Atlantic 2012</b>								
SAR Phase2	No. of Observations	9355	13257	18226	19878	18887	17655	16347
G-POD	No. of Observations	8317	11947	16254	17348	16623	15620	14147
SAR Phase2	Median SWH value	1.322	1.332	1.360	1.483	1.627	1.783	1.804
G-POD	Median SWH value	1.162	1.222	1.277	1.478	1.653	1.834	1.871
	<b>difference</b>	<b>0.160</b>	<b>0.110</b>	<b>0.084</b>	<b>0.005</b>	<b>-0.026</b>	<b>-0.051</b>	<b>-0.067</b>
<b>Northeast Atlantic 2013</b>								
SAR Phase2	No. of Observations	8264	12334	16968	18007	17522	16517	16030
G-POD	No. of Observations	7930	11739	15902	16727	16222	15370	14798
SAR Phase2	Median SWH value	1.353	1.392	1.402	1.574	1.787	1.955	1.977
G-POD	Median SWH value	1.197	1.259	1.292	1.534	1.810	1.995	2.011
	<b>difference</b>	<b>0.156</b>	<b>0.133</b>	<b>0.110</b>	<b>0.040</b>	<b>-0.023</b>	<b>-0.040</b>	<b>-0.034</b>

As part of the investigation of SWH, the distribution of the USSH noise is analysed as a function of SWH for the inshore waters (3 to 10 km from the coastline) and offshore (open ocean) at 43 to 50 km to the coastline, with a misfit threshold of 3 applied to both Phase 1 and Phase 2 datasets. Figure 4.4 and

Figure 4.5 show a typical example of the USSH noise as a function of SWH inshore (left panels) and offshore (right panels) for Phase 2 and Phase 1 (G-POD), respectively, for the North East Atlantic region. No significant differences are observed in the relationship between SWH and USSH noise between inshore and offshore waters. In addition, no significant differences between the two datasets over the nine regions are seen. As previously noted, G-POD (Phase1) appears to extract less data compared with isardSAT Phase 2 dataset. . The USSH noise versus SWH reveal a Gaussian distribution in terms of the number of events occurring for both the inshore and offshore regions. Generally, the SWH shows a general shift in the value of height in terms of the maximum number of events occurring offshore compared with the inshore region throughout most of the regions (Figure 4.4 and Figure 4.5). The USSH noise as a function of SWH shows a similar structure for both inshore and offshore regions. This indicates that that the value of SWH does not have an impact on USSH noise. The high SWH values that correspond to high USSH noise values may be biased because the number of observations that occur at these higher SWHs is very small (see bottom panels in Figure 4.4 and Figure 4.5).

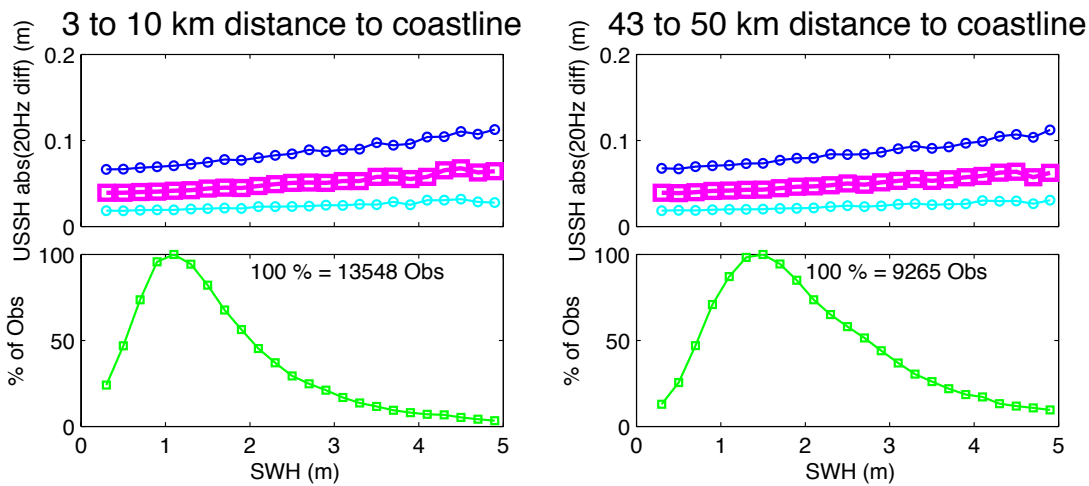


**Figure 4.4** USSH noise as a function of SWH (top panel) for SAR Phase 2 (isardSAT) dataset in the North East Atlantic Region. The corresponding distribution (bottom panel) is the percentage in the number of the events occurring within a bin interval (i.e., 0.2 m SWH) relative to the maximum number of events occurring as shown. The inshore waters relate to the left plots, the offshore (open ocean) waters represent the right plots.

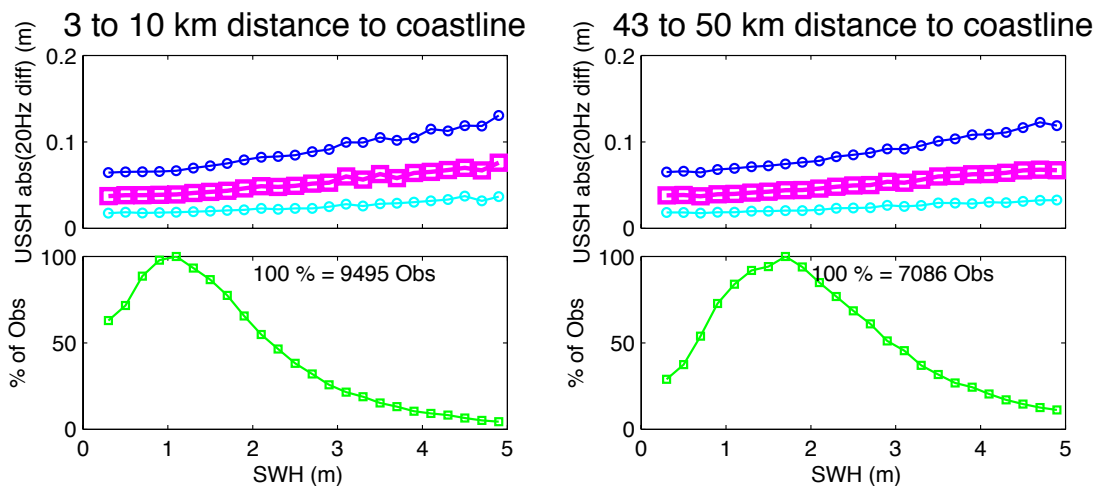


**Figure 4.5** USSH noise as a function of SWH (top panel) for Phase 1 (G-POD) dataset in the North East Atlantic Region. The corresponding distribution (bottom panel) is the percentage in the number of the

events occurring within a bin interval (i.e., 0.2 m SWH) relative to the maximum number of events occurring as shown. The inshore waters relate to the left plots, the offshore (open ocean) waters represent the right plots.

### 4.5.3 Investigation using the Zero Padding 2 in range and Hamming window

An experimental earlier version of the CryoSat-2 SAR data are analysed in order to investigate into the effect of applying the Zero Padding 2 in range processor or applying the Hamming window to the CryoSat dataset is shown in Table 4.4. Here, these two types of processing procedures are compared with the Phase 1 G-POD dataset as a reference frame for USSH noise and SWH in three regions of interest, the North Sea; Central Pacific and Agulhas regions. No misfit threshold is applied to the datasets. The results reveal that the Hamming Window shows consistency in the USSH noise to approximately 5 km from the coast compared with the G-POD and ZP2 datasets but increased in noise inshore. The Hamming Window process also illustrated higher values of SWH at all distances from the coast.

**Table 4.4 Comparison of three regions for SAR Phase 1 (G-POD), Zero Point 2 (ZP2) and Hamming Window (HAMM) for USSH Noise (m) and SWH (m) for distances from the coast (km) in 2013.**

Region	CryoSat-2 SAR Mode Noise (m)						
	km to the Coastline						
	2	3	5	10	20	30	40
North Sea G-POD	0.078	0.059	0.048	0.043	0.043	0.043	0.043
North Sea ZP2	0.086	0.070	0.051	0.043	0.042	0.043	0.042
North Sea HAMM	0.098	0.082	0.060	0.051	0.047	0.048	0.048
Central Pacific G-POD	0.078	0.048	0.046	0.054	0.043	0.050	0.048
Central Pacific ZP2	0.081	0.061	0.054	0.053	0.045	0.051	0.056
Central Pacific HAMM	0.069	0.052	0.044	0.051	0.047	0.049	0.053
Agulhas G-POD	0.075	0.056	0.047	0.049	0.053	0.051	0.054
Agulhas ZP2	0.080	0.062	0.052	0.052	0.053	0.052	0.055
Agulhas HAMM	0.102	0.073	0.059	0.052	0.055	0.051	0.054

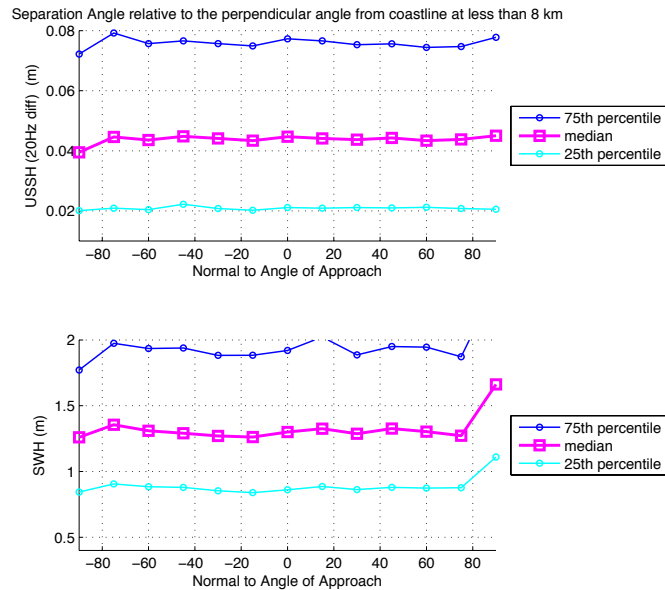
  

Region	CryoSat-2 SAR Mode SWH (m)						
	km to the Coastline						
	2	3	5	10	20	30	40
North Sea G-POD	0.817	0.937	0.974	1.223	1.400	1.461	1.533
North Sea ZP2	1.306	1.353	1.377	1.534	1.630	1.695	1.725
North Sea HAMM	1.976	2.077	2.129	2.237	2.300	2.320	2.326
Central Pacific G-POD	2.122	2.424	2.360	1.958	2.003	2.182	2.064
Central Pacific ZP2	2.061	2.488	2.676	2.107	2.148	2.280	2.226
Central Pacific HAMM	2.591	2.991	3.209	2.636	2.581	2.679	2.685
Agulhas G-POD	1.528	1.668	1.902	1.964	2.311	2.415	2.723
Agulhas ZP2	2.019	2.033	2.251	2.297	2.487	2.611	2.905
Agulhas HAMM	2.283	2.346	2.520	2.606	2.779	2.865	3.202

### 4.5.4 Assessing the performance of CryoSat-2 by Directional Analysis.

Directional analysis is carried out in order to assess the performance of CryoSat data by investigating the angle of approach to the coastline. The North East Atlantic region is chosen to analyse both CryoSat SAR Phase 2 and CryoSat SAR G-POD Phase 1 data sets using a misfit threshold of 3.

The noise (USSH) and SWH parameter fields are used in this assessment and are shown as a function of the deviation (separation) angles at 15° bin intervals within 8 km from the coastline from CryoSat SAR Phase 2 (Figure 4.6) Figure 4.5 USSH noise as a function of SWH (top panel) for Phase 1 (G-POD) dataset in the North East Atlantic Region. The corresponding distribution (bottom panel) is the percentage in the number of the events occurring within a bin interval (i.e., 0.2 m SWH) relative to the maximum number of events occurring as shown. The inshore waters relate to the left plots, the offshore (open ocean) waters represent the right plots.) and the CryoSat SAR G-POD Phase 1 (Figure 4.7). The results show that the noise in USSH and SWH are largely flat across all angles. This is not unexpected



because the misfit threshold of 3 would have removed contaminated waveforms close to the coast, however at the 90° angle (parallel to the coast) there is some deviation, this is most likely related to the smaller number of observations. An offset between SWH Phase 1(GPOD) and Phase 2 can be seen.

**Figure 4.6 CryoSat SAR Phase 2 USSH and SWH as a function of the angle of approach to the coastline for the North East Atlantic region for 2012 to 2013 where 0° and ± 90° represents normal and parallel to the coast, respectively**

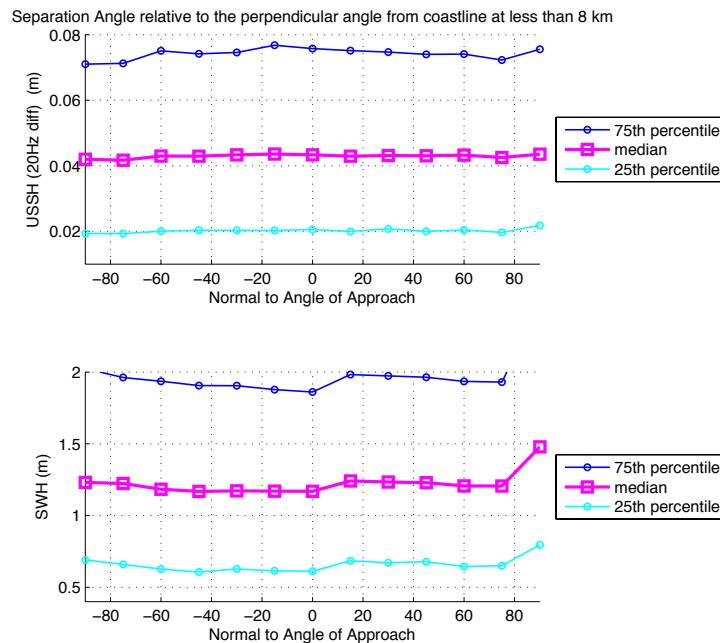


**Figure 4.7 CryoSat SAR G-POD Phase 1 USSH and SWH as a function of the angle of approach to the coastline for the North East Atlantic region for 2012 to 2013 where 0° and ± 90° represents normal and parallel to the coast, respectively.**

As part of this assessment, the percentage of data rejected by applying the misfit threshold of 3 is examined as a function of separation angle and distance to coastline. The USSH and SWH parameters are analysed within the 8 km zone of the coast for the North East Atlantic region for both CryoSat SAR Phase 2 and Phase 1 (GPOD) datasets. The results show no observable differences in the percentage of lost USSH data approaching the coast between Phase 2 data sets (Figure 4.8) and Phase 1 (Figure 4.9). Similarly, very few differences are seen in the percentage of data lost in SWH observations from the Phase 1 and Phase 2 SAR datasets. Generally, the loss of data increases as the tracks approach the coast in all angles of approach. The angles close to normal to the coast have a lower percentage of data lost compared with oblique angles to the normal. For example, the tracks approaching normal to the coast (i.e. 0°) result in data loss of approximately 50% at 2 km, whereas tracks with an oblique angle greater than 60° to the normal lose approximately 80% of data at 2 km from the coast.

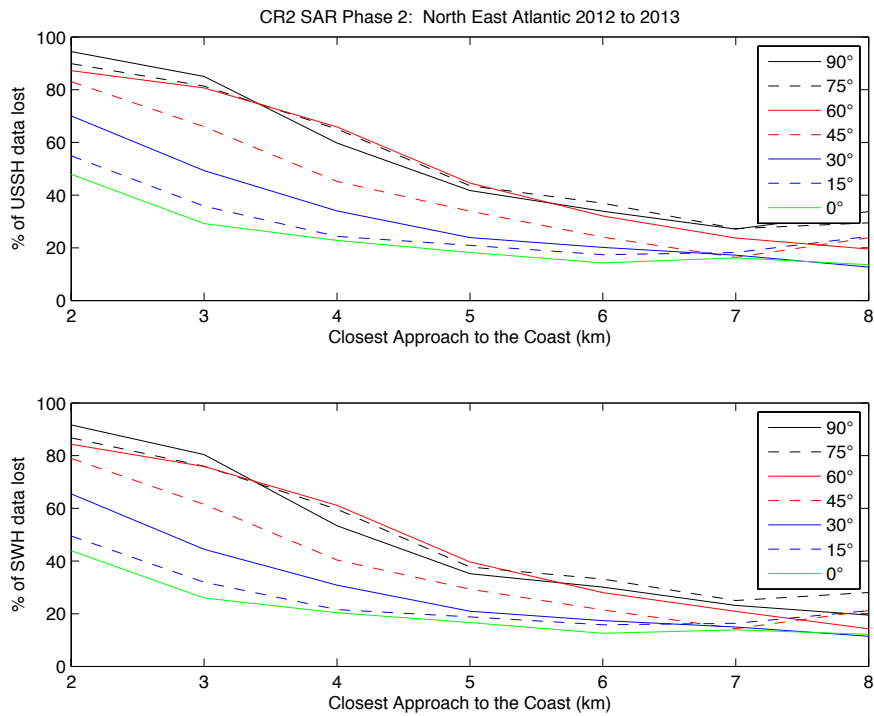


**Figure 4.8** The percentage of the CryoSat SAR Phase 2 data rejected when applying a misfit threshold of 3 from USSH and SWH parameter fields as a function of the angle of approach and distance to the coastline for the North East Atlantic region for 2012 to 2013 where 0° and 90° represents normal and parallel to the coast, respectively.

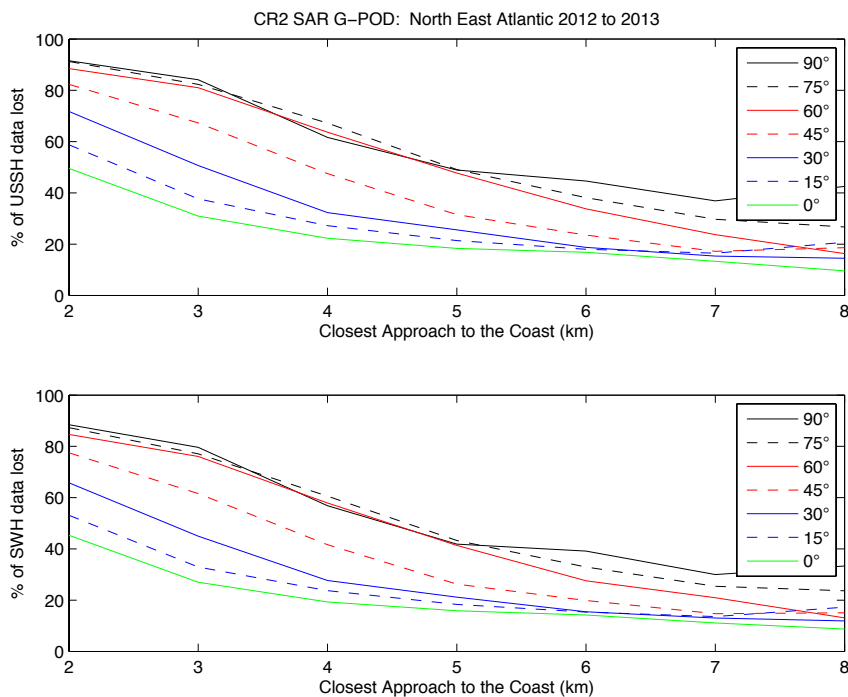


**Figure 4.9** The percentage of CryoSat SAR G-POD (Phase 1) data rejected when applying a misfit threshold of 3 to the USSH and SWH parameter fields as a function of the angle of approach and distance to the coastline for the North East Atlantic region for 2012 to 2013 where 0° and 90° represents normal and parallel to the coast, respectively.

## 4.6 Summary and Main Findings and Recommendations

The effect of the implementation of the misfit threshold of 3 became very evident when applying it to the Phase 1 (G-POD) and Phase2 (isardSAT) TDS datasets, with the two datasets then showing no significant differences between them in terms of USSH noise performance. However, a radical reduction in the number of observations close to the coast is seen when applying the misfit threshold of 3. The reduction in the number of observations close to the coast (i.e. less than 10 km) can be as much as between 50% and 70% compared with not using the misfit threshold. In addition, there appears to be an offset between SWH from Phase 1 and Phase 2 TDS datasets for SWH less than 1.6 m.

No obvious dependency is found in USSH noise or SWH on angle of approach to coast from both Phase 1 (G-POD) and Phase2 (isardSAT) TDS datasets in the North East Atlantic region. Although, there is a significant loss of data up to approximately 90% at 2 km parallel to the coast compared with the same distance of 50% data loss normal to the coast. It is important to note that there is a likelihood that small-scale variability close to the coast in SSH, SWH and  $\sigma_0$  and so higher “noise” close to coast may be demonstrating genuine physical variability as well.

Priority should be given to identify and correct the source of inaccuracy at low wave heights which may be related to the Point Target Response (PTR). Furthermore, this analysis highlighted a caution when using Hamming window such that it should only be applied in the offshore water, or possibly above a particular SWH threshold.

Finally, more independent validation is needed to assess and support the algorithm development for new SAR datasets

# 5 Open Ocean and Coastal Zone Validation of the SCOOP Second Test Data Set in the German Bight by UBonn

## 5.1 Summary of Approach

The University of Bonn has performed an assessment of sea surface height, significant wave height and wind speed for the various SAR and RDSAR datasets produced in the framework of the SCOOP project in the North Sea.

The activities are on local and regional basis and compare the SCOOP datasets with reference datasets, which consist of in-situ and ocean models data and external and in-house altimeter products. Focus is the German Bight. In-situ data have been provided by the German Federal Institute of Hydrology for 16 geo-referenced tide gauge stations for sea level, 4 waverider buoys for wave height and 4 stations for wind measurements. Model data are from the Federal Maritime and Hydrographic Agency (BSH). The SAR “external products” are processed with the SAMOSA2 and SAMOSA+ retrackers and are available through the ESA-ESRIN GPOD platform. The RDSAR “product” is the TALES/ TUDaBo dataset produced in-house in cooperation with the Darmstadt Technical University (Dinardo et al., 2018, Fenoglio et al., 2015, in review).

The validation of SAR against RDSAR, in-situ data and model outputs is made for both open sea (at distances to coast larger than 10 Km) and coastal zone (distances to coast smaller than 10 km). We concentrated on sea level mainly.

Goal is to carry out a characterisation of SAR mode performance and estimation of the data precision and accuracy. The methodology is described in the SCOOP Product Validation Plan (SCOOP\_ESA\_D2.4, section 3.2).

The project has decided to use as Test1 reference dataset the output of the GPOD service, which was one of our two suggested datasets.

The Test 1 (or Phase 1) SAR datasets was produced through GPOD.

The Test 2 (or Phase 2) SAR dataset was produced by isardSAT.

Both Test1 RDSAR and Test2 RDSAR were produced by TUDelft.

## 5.2 Results from Validation Test 1

The Test 1 (or Phase 1) SAR datasets was produced through GPOD. The GPOD settings for the SCOOP baseline Test Data Set has been chosen equivalent to the Sentinel-3 Detail Processing Model (DPM) 2.5. It includes SAMOSA2 as retracker and the Look Up Table (LUT) to correct for sea state correlated biases. The Hamming Weighting, zero padding and antenna pattern compensation are not applied. Data are posted at 20 Hz, approximate beam forming is used and the radar receiving window size is 128 bins.

The Test1 RDSAR dataset was produced by TUDelft based on the RADS processing scheme.

## 5.2.1 SAR Results

The Test1 SAR Dataset has been compared to the RDSAR TUDaBo/TALES dataset in open sea. The standard deviation of differences is 3 cm for SLA and 18 cm for SWH (Figure 5.1). A test ground-track has been selected (20130322T235512\_20130322T235758) for all comparisons.

In coastal zone, the performance of the altimeter data is firstly investigated in terms of noise level as function of the distance to coast. The noise is estimated as the absolute value difference between consecutive sea level anomalies (SLA) at 20 Hz. Figure 5.2 shows the differences between SAR and RDSAR Test1 datasets.

The noise in the coastal zone is investigated following an alternative method by comparing the standard deviations of sea level anomalies (SLA) from altimetry and of model sea level heights, which are here the reference. See in Figure 5.3 the values for the model (green), Test1 SAR Dataset (red) and RDSAR TUDaBo (blue). The adopted ocean model is the BSHcmod ocean model of the German Federal Maritime and Hydrographic Agency (BSH), which has been already used in Fenoglio-Marc et al. (2015), Dinardo et al. (2018) and Schall et al. (2016). Values are still smaller for SAMOSA+, which outperforms SAMOSA2 near coast (Dinardo et al., 2018)

In Figure 5.4 (left) we see a further comparison between SAR and RDSAR TALES/TUDaBo, to confirm the SAR superiority on RDSAR. RDSAR data near coast appear noisier, with standard deviation between SAR and RDSAR in coastal zone of 56 cm, higher compared to the open sea values in Figure 5.1(3 cm). Standard deviation with in-situ tide gauges in open sea between 10 and 20 km from coast is 6 cm for SAR and of 8 cm with RDSAR/TUDaBo (Figure 6).

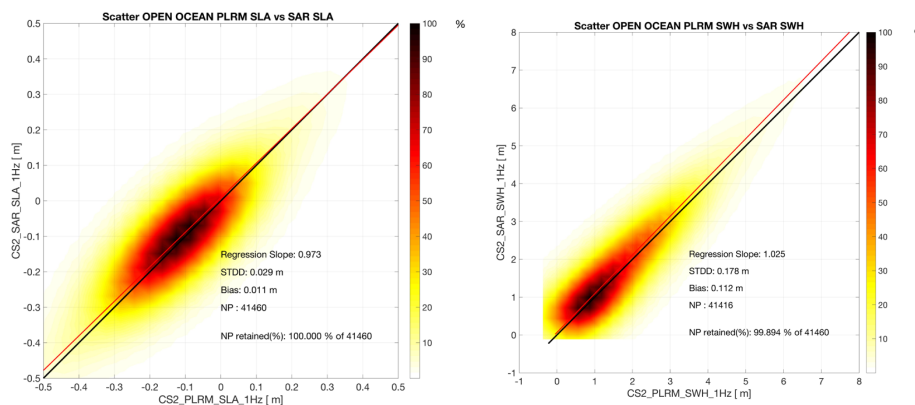


Figure 5.1 SLA (left) and SWH (right) for Test1 SAR Dataset against RDSAR TUDaBo/TALES

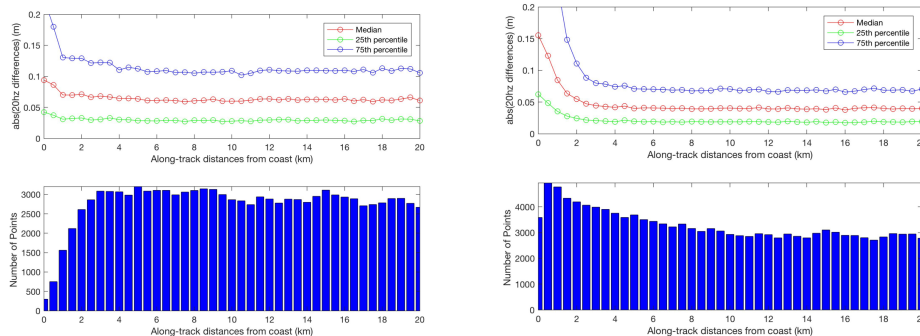


Figure 5.2 Noise and number of observations of Test1 RDSAR (left) and Test1 SAR Dataset (right).

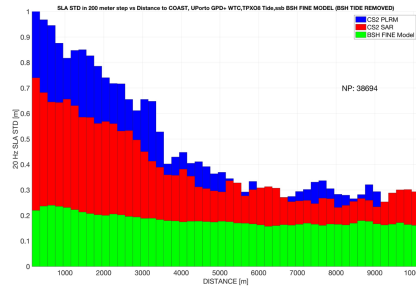


Figure 5.3 Standard deviation of sea level anomalies as function of distance to coast for BSH model, Test 1 Database SAR and RDSAR/TUDaBo

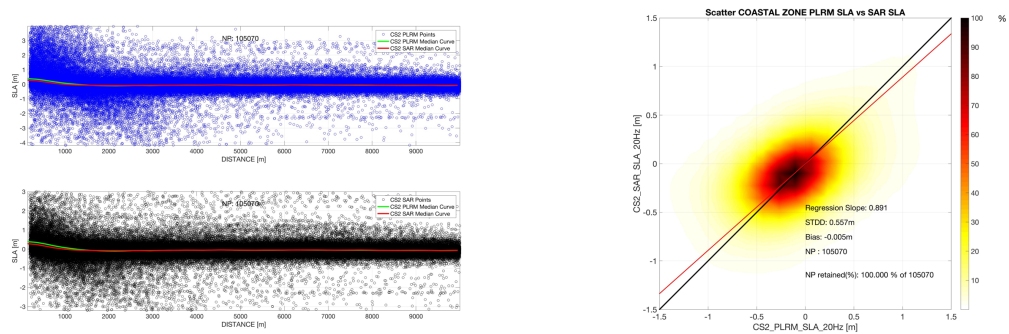
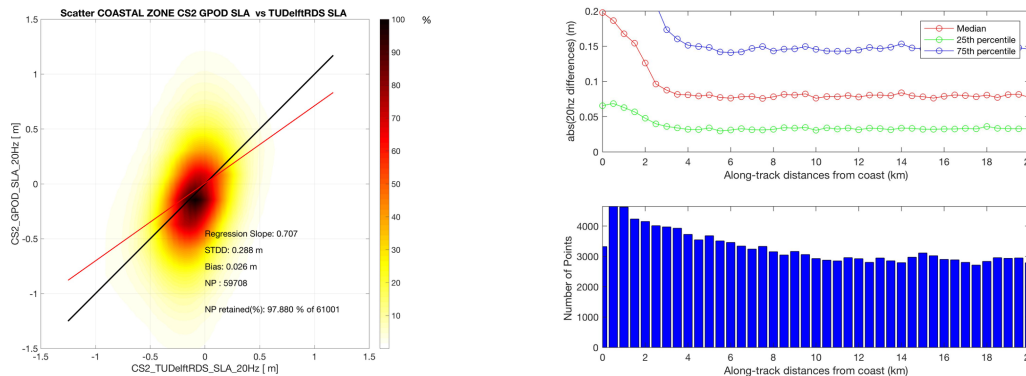


Figure 5.4 SLA for Test1 SAR Dataset (bottom left) against RDSAR TUDaBo/TALES (top left) and their scatterplot (right).

### 5.2.2 RDSAR Results

Along-track analysis shows small differences in altimeter range between SAR and RDSAR in open ocean (< 1 cm, see Figure 5.8). SWH differences are larger. There is a bias in backscatter and in wind speed.

In coastal zone the RDSAR/TUDeft dataset has few data in the first 5 kilometers from coast compared to SAR (Figure 5.2) and RDSAR/TUDaBo (Figure 5.5 right). The missing data mask the low precision of this dataset, leading to a standard deviation of the differences with Test 1 SAR Dataset of 29 cm which is smaller than the RDSAR/TUDaBo value (58 cm). Clearly the MLE3 re-tracker used in RADSAR/TUDeft does not provide a solution for many of the coastal waveforms. The waveforms are available in the product and could be retracked by another re-tracker, as for example TUDaBo/TALES.



**Figure 5.5 Scatterplot of Test1 RDSAR/Delft against Test1 SAR Dataset (left) and noise and number of points in RDSAR/TUDaBo-TALES**

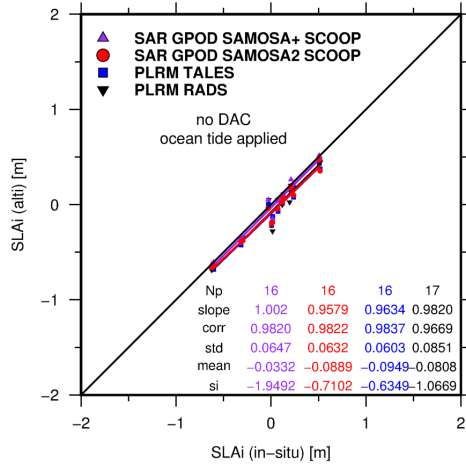


**Figure 5.6 Scatterplot of sea level anomalies in open ocean (10-20 km) of Helgoland tide gauge against Test1 SAR, Test1 RDSAR and the external SAR/GPOD-SAMOS+ and RDSAR/TUDaBo-TALES Dataset**

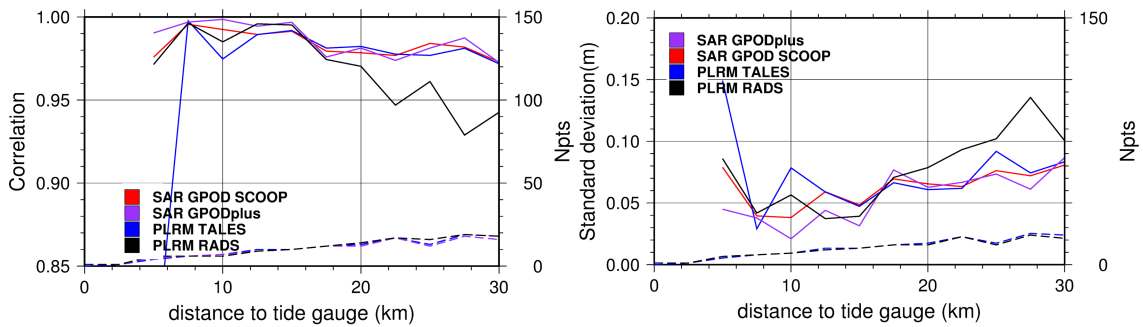


**Figure 5.7 Correlation (left) and standard deviation (right) between tide gauge Helgoland and Test1 SAR, Test1 RDSAR, external SAR/GPOD-SAMOS+ and RDSAR/TUDaBo-TALES Dataset. The dashed line gives the number of points, which increases with distance to coast.**

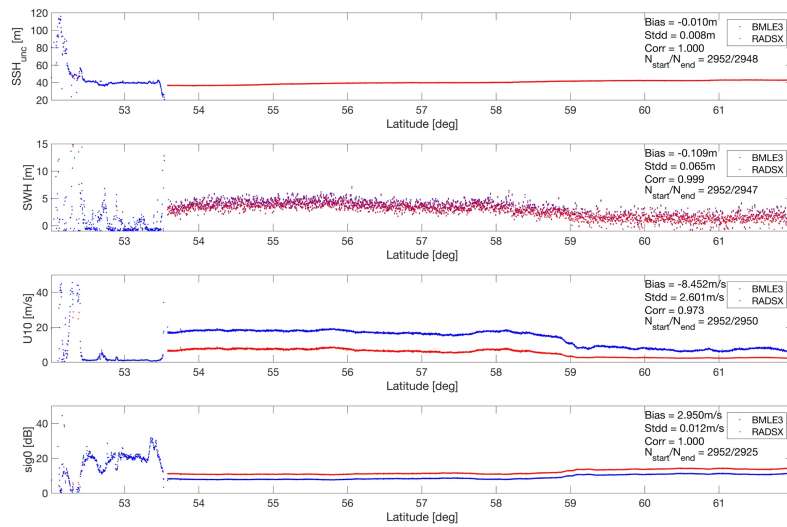


**Figure 5.8 Comparison of four geophysical parameter (Uncorrected SSH, SWH, wind speed and backscatter) along the selected ground-track of SCOOP Test 1 RDSAR-Delft and in-house RDSAR-BMLE3.**

## 5.3 Results from Validation Test 2

### 5.3.1 SAR Results

The Test 2 (or Phase 2) SAR dataset was produced by isardSAT. There were two releases of the Phase 2 isardSAR dataset. The first released in June 2018 and analysed in the PM8 in July 2018 consisted of one zero padding (ZP2) and two Hamming windows (HAMM and HAMM\_noMask) versions, with and without mask. The second released in November 2018 was analysed in the Acceptance Review in December 2018 consisted of two versions, one dedicated to coastal zone and the other to open ocean. UBonn has analysed both.

In coastal zone there very small differences between the noise in coastal zone estimated for the two versions of Hamming. The Zero-Padding alone performed worse than Hamming alone in coastal zone, as seen in Figure 5.9. Both options are used in the final release (see Figure 5.10).

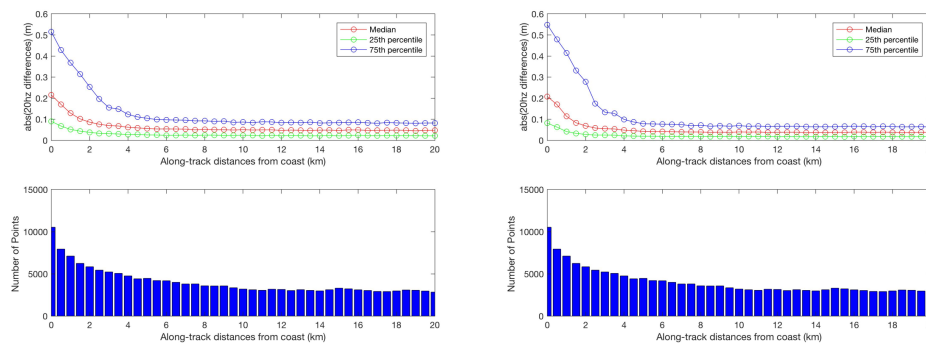


**Figure 5.9 SAR Test 2 dataset: Noise with Hamming (left) and zero-padding (right)**

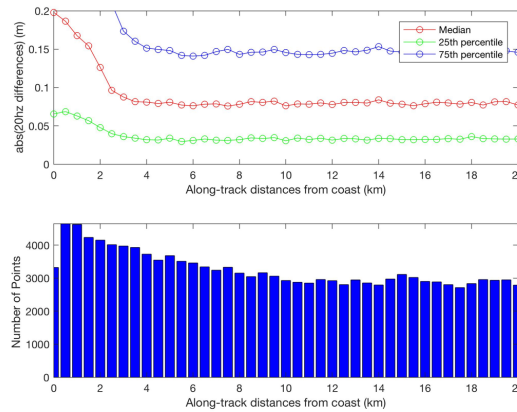


Figure 5.10 SAR Test 2 final dataset: Noise for combined Hamming and zero-padding

### 5.3.2 RDSAR Results

The Test 2 (or Phase 2) RDSAR dataset was produced by TU-Delft. The differences between Test1 and Test2 release are extremely small, as seen in Figure 5.11, therefore the same conclusions found for Test1 RDSAR dataset hold for Test2 RDSAR.

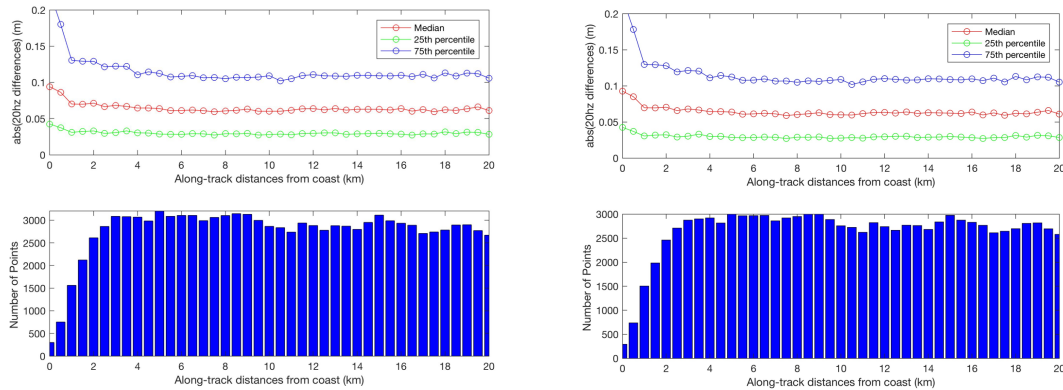


Figure 5.11 Noise and number of data as function of distance to coast for RDSAR Test 1 (left) and Test2 (right) datasets

The in-situ validation has been performed with Test 2 dataset in coastal zone (5-10 km) and open sea (10-20 km) for sea level (Figure 5.12) and significant wave height (Figure 5.13). Test2 SAR data have higher agreement with in-situ data than Test 2 RDSAR. For sea level, correlation and STDD are 0.97 and 9.3 cm for RDSAR and 0.99 and 4.4 cm for SAR in coastal zone. In open sea correlation and STDD are 0.97 and 8.1 cm for RDSAR and 0.97 and 6.7 cm for SAR. The statistics for Test1 SAR data in Figure 5.6 indicate a higher accuracy of the Test1 SAR dataset for sea level. For significant wave height, correlation and STDD are 0.80 and 107 cm for RDSAR and 0.99 and 98 cm for SAR in coastal zone. In open sea correlation and STDD are 0.35 and 45.0 cm for RDSAR and 0.35 and 45.0 cm for SAR. Statistics for Test1 SAR dataset in Figure 5.14 indicates a higher accuracy of the SWH data. Results are summarized in Table 5.1.

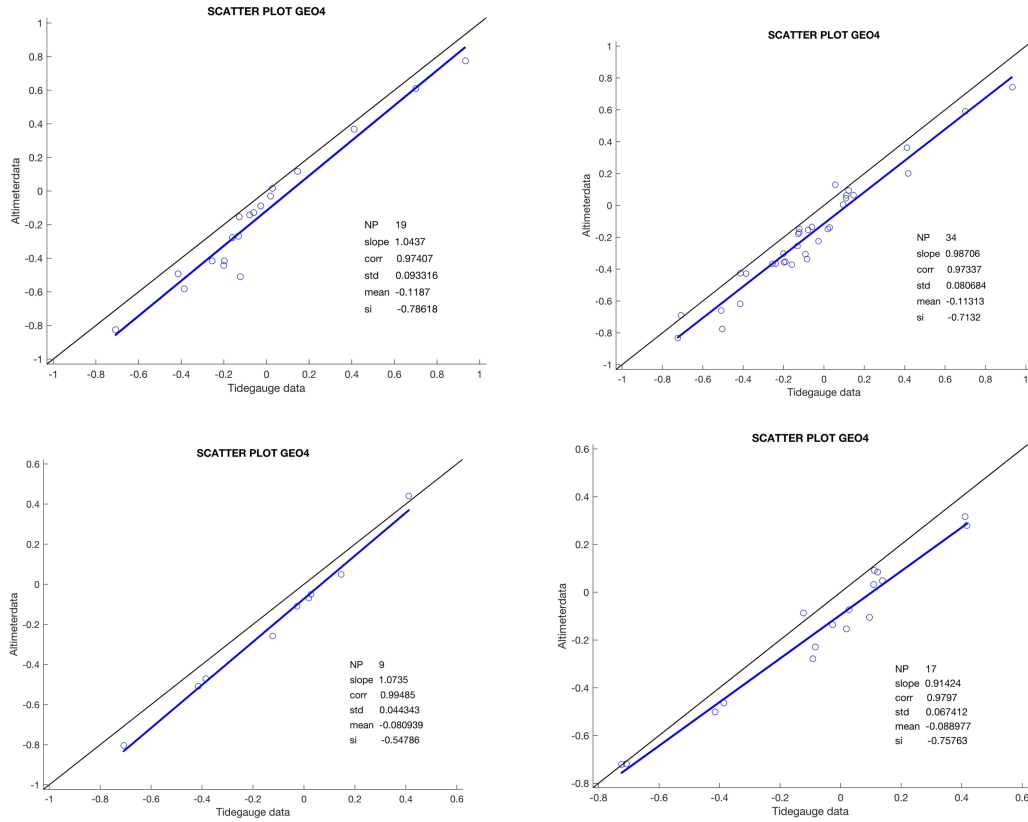
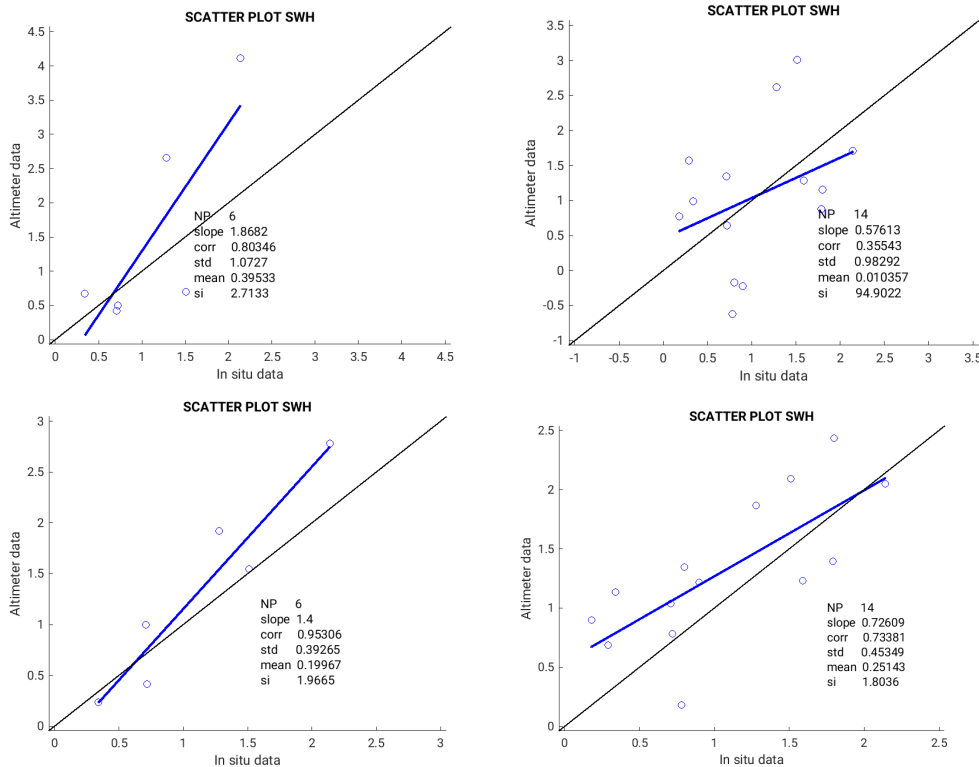
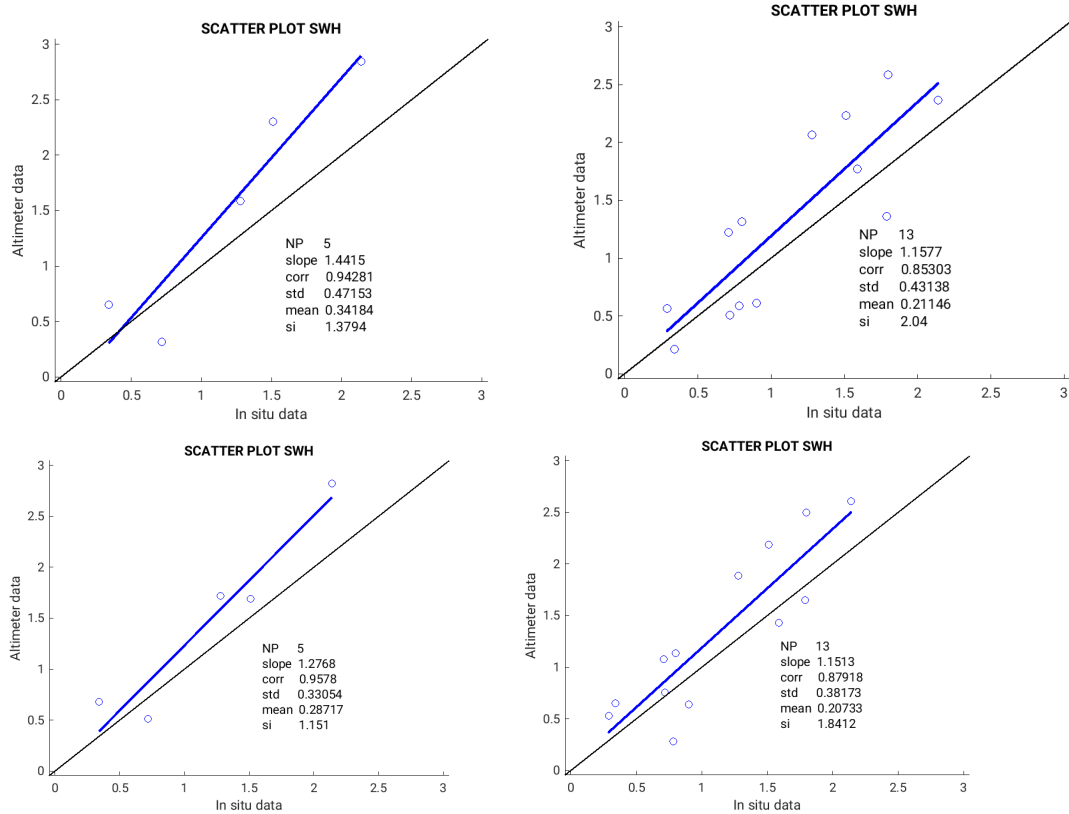


Figure 5.12 In-situ validation of Test 2 RDSAR (above) and Test 2 SAR (below) sea level in coastal zone in range 5-10 km (left) and 10-20 km (right) from coast



**Figure 5.13 In-situ validation of Test 2 RDSAR (above) and Test 2 SAR (below) SWH in coastal zone in range 5-10 km (left) and 10-20 km (right) from coast**



**Figure 5.14 In-situ validation of RDSAR/TUDaBo-TALES (above) and TEST1 SAR/GOD (below) SWH in coastal zone in range 5-10 km (left) and 10-20 km (right) from coast**

		5-10 km	5-10 km	10-20 km	10-20 km
		STDD (cm)	CORR	STDD (cm)	CORR
<i>Test2 RDSAR</i>	SLA	9.3	0.97	8.1	0.99
<i>Test2 SAR</i>	SLA	4.4	0.99	6.7	0.98
<i>RDSAR/TUDaBo</i>	SLA	5.0	0.99	6.9	0.98
<i>Test1 SAR</i>	SLA	4.2	0.99	6.5	0.98
<i>Test2 RDSAR</i>	SWH	107.27	0.80	98.3	0.33
<i>Test2 SAR</i>	SWH	39.26	0.93	45.3	0.73
<i>RDSAR/TUDaBo</i>	SWH	47.2	0.94	43.1	0.85
<i>Test1 SAR</i>	SWH	33.0	0.96	38.2	0.88

**Table 5.1 Statistic of in-situ validation for Test1,Test2 and external/in-house datasets**

## 5.4 Summary of Results

The analysis performed on the SCOOP SAR and RDSAR datasets in the North Sea and in the German Bight can be summarized in the following conclusions:

The Test2 SAR Dataset by IsardSAT is an improvement compared to previous versions. The in-situ validation shows a general agreement in both sea level and significant wave height with in-situ values. Its accuracy is lower than the accuracy of Test1 SAR Dataset (GPOD) larger than the RDSAR datasets.

The Phase 1 and Phase 2 RDSAR MLE3 dataset are not significantly different. The along track analysis show similar sea level in open sea and data missing near coast. Differences are higher for SWH and backscatter coefficient and wind speed. The in-situ validation shows a low agreement in both sea level and significant wave height with in-situ values, differences in SWH are particularly large.

# 6 Performance Assessment of Sea State Impact on Altimeter Retrieved SSH by Noveltis

## 6.1 Summary of Approach

NOVELTIS investigates the various datasets produced in the framework of the SCOOP project, in terms of sea surface height variability, significant wave height accuracy and the impact of sea state on the retrieval of sea surface height.

These activities are performed on local and regional basis, by comparing the SCOOP datasets with the in situ SSH and SWH observations measured at the Harvest platform calibration site.

The analysis of the impact of the sea state on the altimeter SSH is based on the regional absolute calibration method developed by NOVELTIS. The regional absolute calibration of the altimeter range consists in verifying the coherency between the sea surface heights measured by an in situ tide gauge instrument and the sea surface heights measured by the satellite altimeter not only for the track directly flying over the tide gauge station, also called calibration site, but also for tracks located several tens of kilometres off the calibration site. This method is described in the SCOOP Product Validation Plan (SCOOP\_ESA\_D2.4), section 3.4.

Noveltis focuses on Cryosat-2 SAR mode data collected in the new SAR mode region off the Californian coast and over the well-established altimeter calibration site at the Harvest platform (Figure 6.1). This SAR mode region was specifically implemented at the request of the SCOOP study, and so only data collected since this area was included in the Cryosat-2 Mode Mask can be used (i.e. since 15/12/2015).

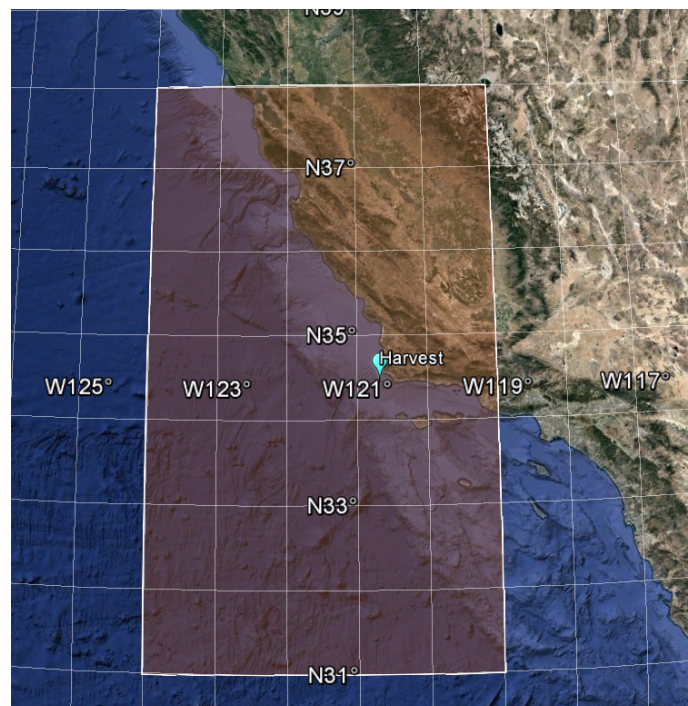


Figure 6.1 Harvest platform location and Cryosat-2 SAR mask Harvest\_-00 (since 15/12/2015). The area of the SAR zone is 356 429 km<sup>2</sup> (ocean+land).

## 6.2 Results from Validation Test 1: SAR product

### 6.2.1 Comparison between Phase 1 and Phase 2 SAR datasets

#### 6.2.1.1 Analysis of the along track sea surface height variability

The Phase 1 and Phase 2 SAR datasets in Harvest cover a 12-month period, from mid-December 2015 to end of December 2016.

The Phase 1 SAR dataset was produced through GPOD. The Phase 2 SAR dataset was produced by isardSAT, considering zero-padding and Hamming Window.

First, the precision of the uncorrected sea surface heights (altitude – range) is assessed for both datasets by computing the median and the standard deviation of the point to point differences of the USSH at 20 Hz in 1-km bins of the distance to the coast. However, it is necessary to filter out the USSH outliers before computing the statistics. To do so, several parameters and flags are available, depending on the products:

- Phase 1 SAR products:
  - Misfit parameter (*Misfit\_20Hz*) ;
- Phase 2 SAR products:
  - Misfit parameter (*Misfit\_analytical\_SWH\_MSSfixed\_20\_ku*) ;
  - Pearson correlation parameter (*Pearson\_corr\_analytical\_SWH\_MSSfixed\_20\_ku*);
  - Validity flag (*Flag\_validity\_L1B\_wvfm\_20\_ku*).

The validity flag, only available in the Phase 2 dataset, indicates whether the L1B waveform is valid or not to be used in the retracking process. In the case of the Harvest region, when considering the first 6 months of the dataset (79 files, from mid-December 2015 to mid-May 2016), only two points over the ocean are flagged because of this validity flag.

The misfit and the Pearson correlation parameters both quantify the fitting between the retracking model and the waveforms. Both datasets contain the misfit parameter but the Pearson correlation parameter, for which the recommendation is to filter out the data with correlation lower than 95%, is only available in the Phase 2 dataset.

As a consequence, the selection of data is based on the misfit parameter value in order to compute the statistics in similar conditions for both datasets. Figure 6.2 (uncorrected sea surface heights) and Figure 6.3 (significant wave heights) show that most of the outliers in the Phase 2 SAR USSH and SWH data are filtered out when considering misfit values lower than 4. With this misfit threshold of 4, 97% of data are used, as shown in Figure 6.4. It should be noticed that the optimal value of the misfit threshold may vary depending on the region. Also, in the Harvest region, the selection based on misfit values lower than 4 is stricter than the selection based on Pearson correlations higher than 95%.

Figure 6.5 shows the noise of the uncorrected sea surface heights at 20 Hz as a function of the distance to the coast for both datasets (Phase 1 in blue and Phase 2 in red), for data with misfit lower than 4. A general improvement can be noticed, from the Phase 1 to the Phase 2 processing. Indeed, the Phase 2 dataset globally shows lower noise and variability (upper and middle plots) than the Phase 1 dataset, except in the first kilometre offshore where an increase is observed in both datasets, a bit larger in the case of the Phase 2 dataset. The Phase 2 processing also enables to retrieve more data whatever the distance to the coast.

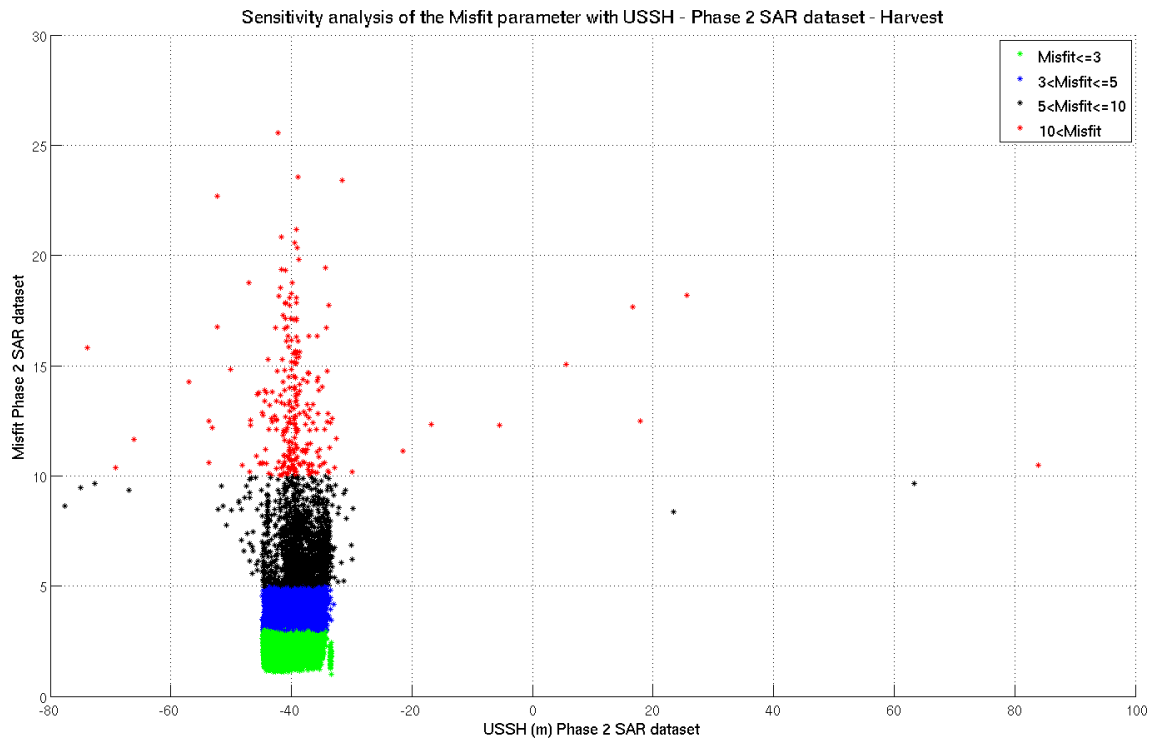


**Figure 6.2 Misfit parameter at 20 Hz as a function of the uncorrected sea surface height (altitude – range) at 20 Hz in the Phase 2 SAR dataset (6 months of data) in Harvest. The colours indicate misfit thresholds.**

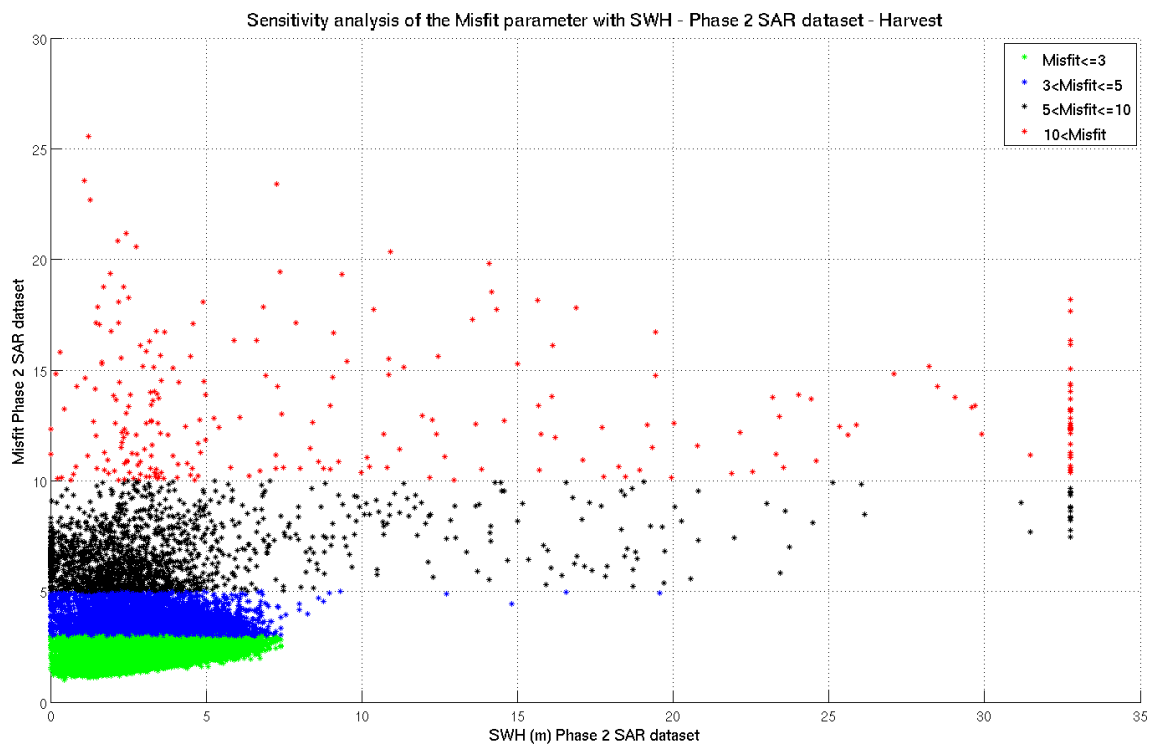


**Figure 6.3 Misfit parameter at 20 Hz as a function of the significant wave height at 20 Hz in the Phase 2 SAR dataset (6 months of data) in Harvest. The colours indicate misfit thresholds.**

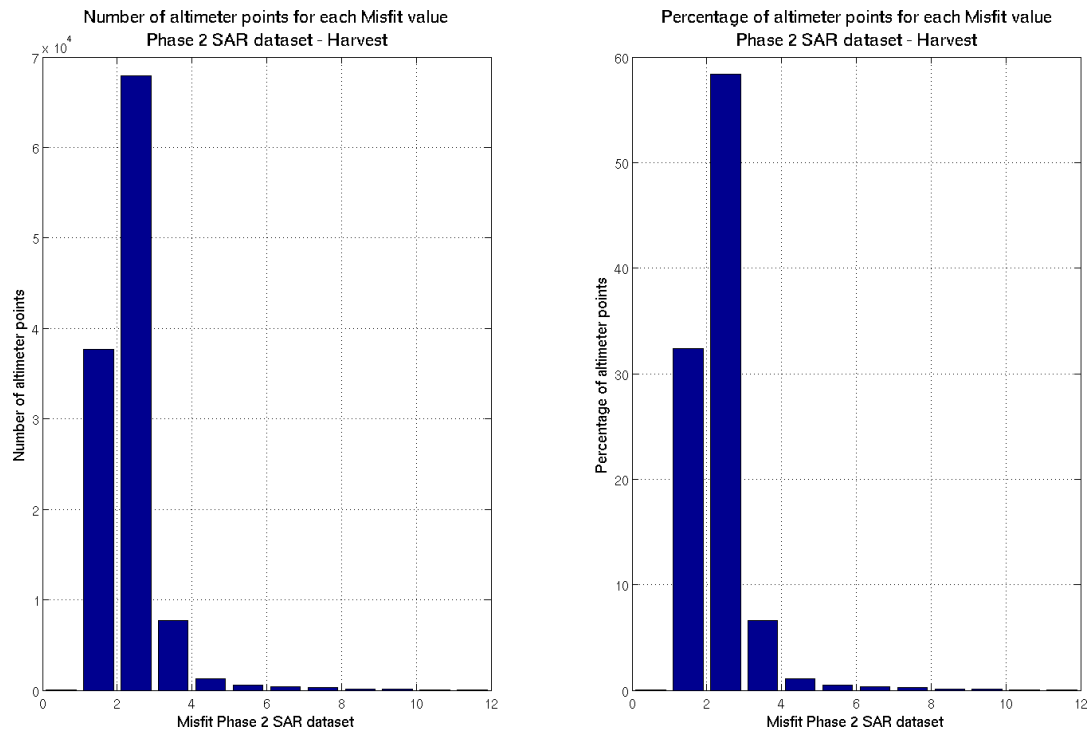


**Figure 6.4** Number (left) and percentage (right) of altimeter points at 20 Hz as a function of the misfit parameter in the Phase 2 SAR dataset (6 months of data) in Harvest.

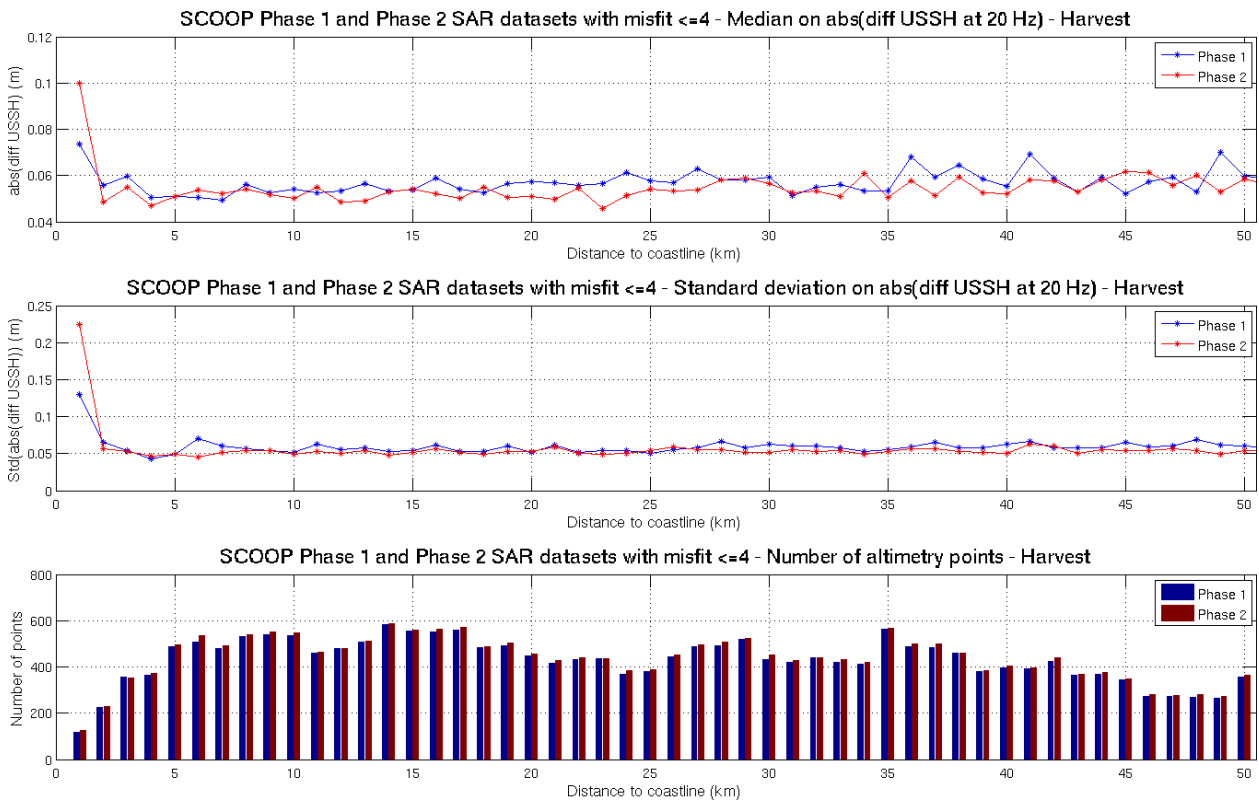


**Figure 6.5** Statistics on the along-track differences of the uncorrected sea surface height (altitude range) at 20 Hz (in m) from the SCOOP Phase 1 and Phase 2 SAR datasets in the Harvest region.

### 6.2.1.2 Sea state impact on the altimeter sea surface height

In order to assess the impact of the sea state on the altimeter SAR sea surface height, the first plan was to analyse the dependency of the altimeter sea surface height absolute bias to the sea state characteristics (Hs, wave period, wave spectrum partitioning, wind...) with a Principal Component Analysis approach, based on the comparison with the IOWAGA regional model outputs provided by IFREMER in the Harvest region.

The Harvest region is of particular interest for such analyses, as it is characterized by rough seas and large wave events, as shown by the time series of significant wave heights measured at the buoy located close to the Harvest platform (Figure 6.6).

However, the comparison between the IOWAGA model and the buoy significant wave heights at Harvest (Figure 6.7) shows that the model generally underestimates the wave heights by several tens of centimetres (and even by more than 1 m for waves > 4m) in this region. As it may introduce some biases when analysing the dependency of the altimeter SSH bias to the model SWH, a different approach was chosen for the assessment of the SCOOP datasets.

The altimeter bias estimates were compared with the significant wave heights measured by the buoy located at Harvest. However, given the relatively short period of time covered by the SCOOP dataset (1 year of data) and the Cryosat-2 long-term repeating orbit (369 days), the number of Cryosat-2 passes that are close enough to be used to estimate the altimeter absolute bias is quite small (12 passes located less than 20 km from the platform, 16 passes located less than 30 km) as shown in Figure 6.8.

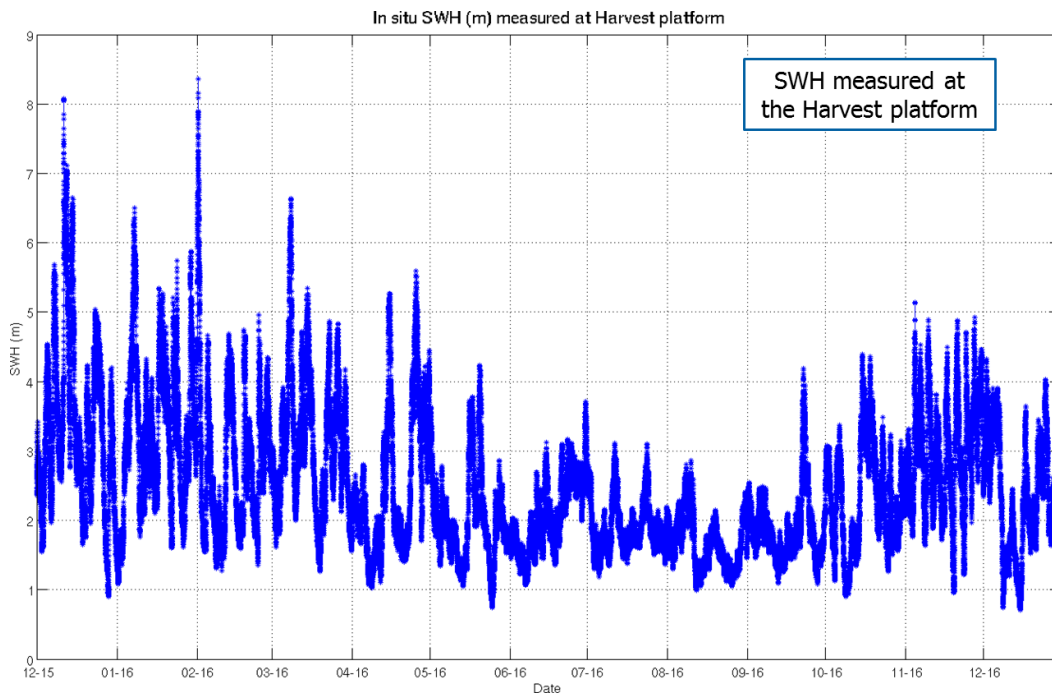


**Figure 6.6 Significant wave heights (in m) measured at the Harvest platform calibration site over the period of the SCOOP datasets (mid-Dec. 2015 to end Dec. 2016).**

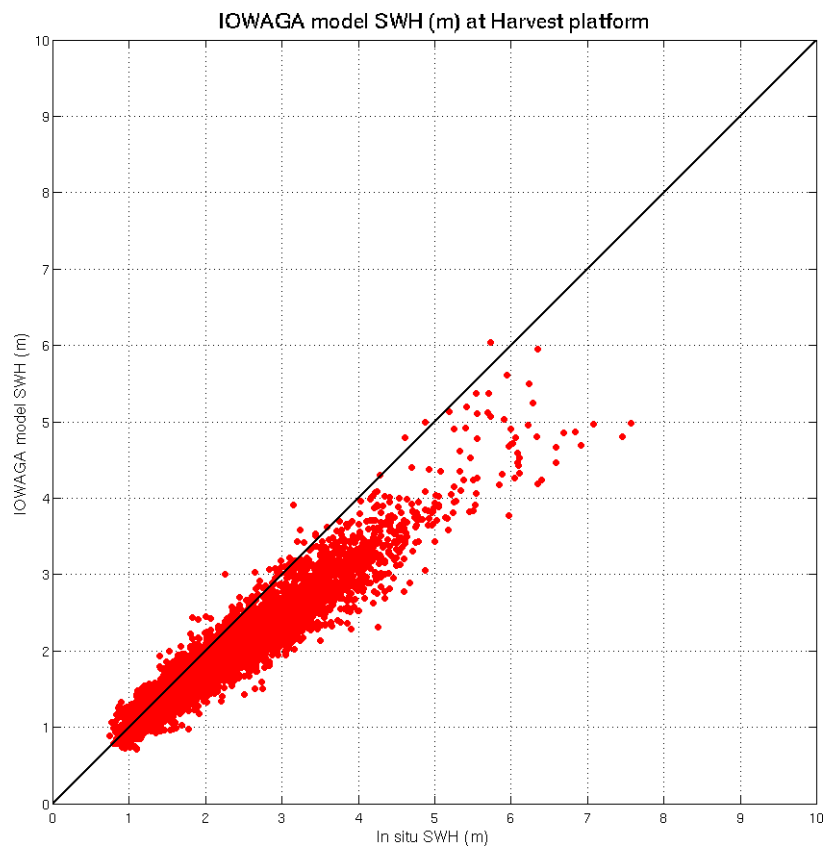


**Figure 6.7 Comparison between the significant wave heights (in m) from the IOWAGA model and the buoy located at the Harvest platform calibration site.**

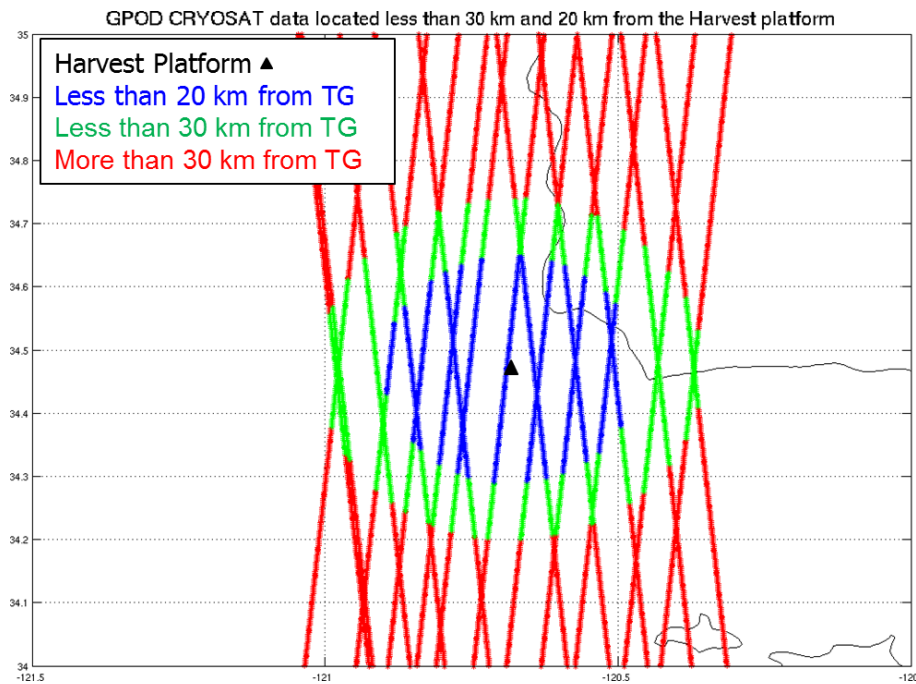


**Figure 6.8 Selection of CryoSat altimeter points depending on their distance to the Harvest platform calibration site**

The altimeter SSH bias estimates were computed using a methodology that is close to the regional CALVAL method developed by NOVELTIS (Figure 6.9) and already used to monitor most of the altimetry missions (Topex/Jason suite missions, Envisat, SARAL/AltiKa, Sentinel-3A&B...).

The altimeter bias estimate is computed as:

$$bias(t) = SSH_{alti}(t) - SSH_{TG}(t) - (MSS_{alti} - MSS_{TG})$$

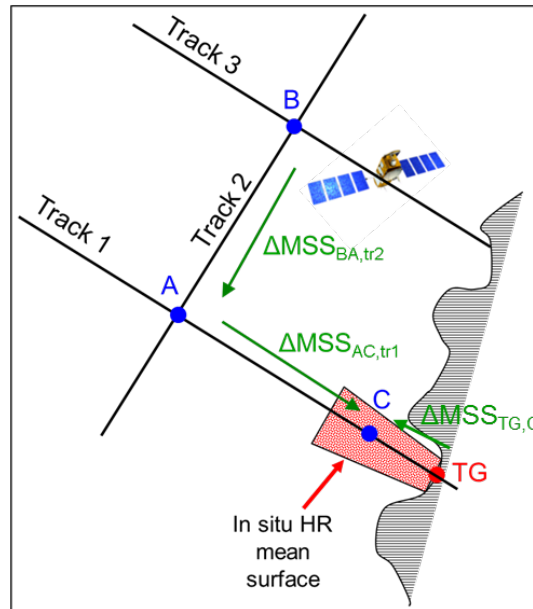


**Figure 6.9** Generic diagram of the regional CALVAL method developed by NOVELTIS.

Compared to the regional CALVAL method, the altimeter bias computation was simplified regarding the processing of the mean sea surface slope between the altimeter point and the Harvest platform. Indeed, in the regional CALVAL method, a succession of mean sea surface profiles from different altimeter missions can be used to compute this MSS slope. Here, given the specific configuration of the Cryosat-2 tracks, the number of MSS profiles to be used would be too complex to manage and would introduce too much error in the processing. The MSS slope was thus computed directly as the DTU10 MSS difference between the altimeter point and the Harvest platform. Using an MSS slope correction is mandatory in this region when considering altimetry observations located more than 2 km from the Harvest calibration site, because of the steep geoid slope.

The altimeter SSH at 20 Hz were corrected for all the propagation and geophysical corrections (ionosphere, dry troposphere, wet troposphere, solid, polar and loading tides). A selection was applied on the data, considering only the altimetry points with misfit parameter value lower than 4.

In addition, the ocean dynamics (tides and effects of the wind and atmospheric pressure) is quite large in the Harvest region and can reach several meters. As the offshore altimetry data and the tide gauge data may not contain the same ocean dynamics signals, it is necessary to remove these signals from both measurements before performing the comparison in order to reduce the variability of the bias estimates. To apply the same corrections to both datasets (in situ and satellite), the following models were used:

- Ocean tides: FES2014 (in-house prediction) ;
- Atmospheric correction: TUGO-m simulation provided by LEGOS.

Finally, the in situ SSH data were corrected with an SSB estimate computed by JPL, given the very large waves that can occur in Harvest (cf. Figure 6.6). Because no SSB correction is available in the SCOOP products, this correction was approximated by 3.5% of the SWH estimated by the SCOOP retracking process at the altimetry points.

All the Cryosat-2 passes within 30 km from the Harvest platform are considered (see Figure 6.8) and the closest altimetry point to the platform is selected for the bias computation. Several tests were done in order to check whether selecting only one point of the 20 Hz altimetry along-track data increases the noise in the bias estimates but it appears that the results are quite close when considering either 1, 10 or 15 altimetry points in this case.

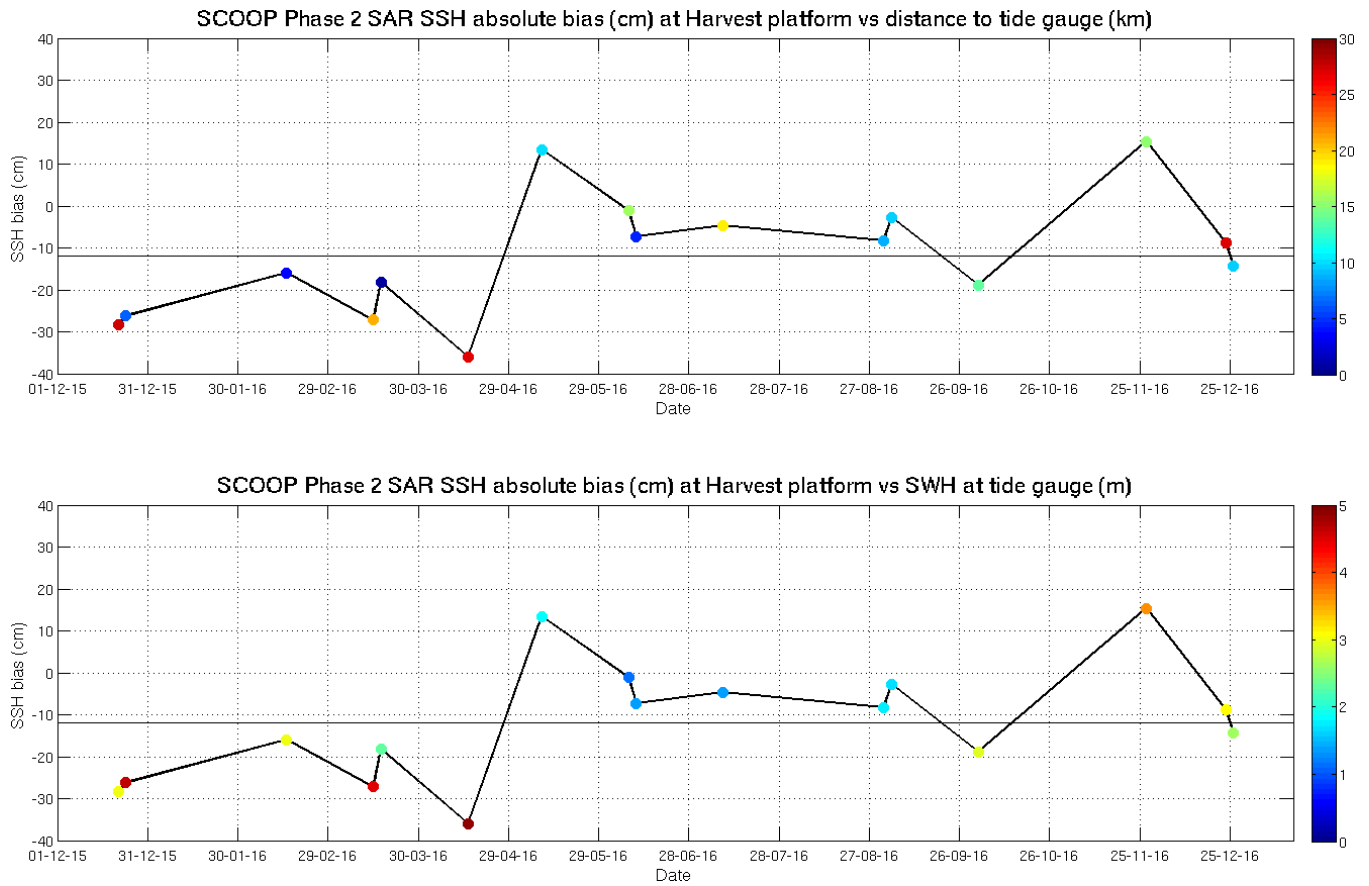
In the end, 16 passes of the SCOOP datasets are used to compute the average SSH bias, as shown in Table 6.1. For both SCOOP SAR datasets (Phase 1 and Phase 2), the mean bias estimate is about -10 cm, with a variability of 14 cm. This seems a bit large, compared to the other altimetry missions for which the variability of the bias estimates is about 2-3 cm in general. Also, the Cryosat-2 SAR SSH are not supposed to be biased by 10 cm.

Figure 6.10 shows the time series of the SSH bias estimates for the SCOOP Phase 2 dataset. On the upper plot, the color at each point gives the distance in km between the altimetry point and the Harvest platform. It appears that there is no clear impact of this distance on the variability of the bias estimates. Figure 6.11 (upper plot) shows the same results in a different way, with a scatterplot of the altimetry SSH (including the MSS slope correction) versus the in situ SSH. Here again, the dispersion in the colors from one point to the other shows that there is no strong link between the bias estimates variability and the distance to the Harvest platform.

On the contrary, the lower plots in Figure 6.10 and Figure 6.11 both highlight the clear dependency of the bias variability with the significant wave heights, shown in colors. Indeed, it appears that the SSH bias estimates are generally larger for waves higher than 3 meters. The mean bias estimates decreases to -4 cm and its variability to 9.5 cm when considering only the 7 points for which the SWH is lower than 2.5 m. These results mean that the approximation of the SSB correction defined as 3.5% of the altimeter SWH is not accurate enough and that an SSB correction dedicated to the SAR SSH should be used.

**Table 6.1 Statistics on the SSH absolute bias of the SCOOP Phase 1 and Phase 2 SAR datasets in Harvest. Selection on 20 Hz SAR data within 30 km off the Harvest platform.**

<b>Comparison to in situ SSH (absolute bias estimates)</b>	<b>Mean bias</b>	<b>Bias Std</b>	<b>Nb of points</b>
<b>SCOOP SAR Datasets</b>			
<b>Phase 1</b>	-10.1 cm	14.1 cm	16
<b>Phase 2</b>	-11.8 cm	14.3 cm	16



**Figure 6.10** Altimeter SSH absolute bias estimates timeseries (in cm) at the Harvest calibration site, for the SCOOP phase 2 SAR dataset. The colors on the upper plot show the distance (in km) to the tide gauge at the altimetry points considered for the bias computation. The colors on the lower plot show the significant wave height (in m) measured at the Harvest platform at the date of the bias estimates. The grey line shows the mean of the bias estimates.

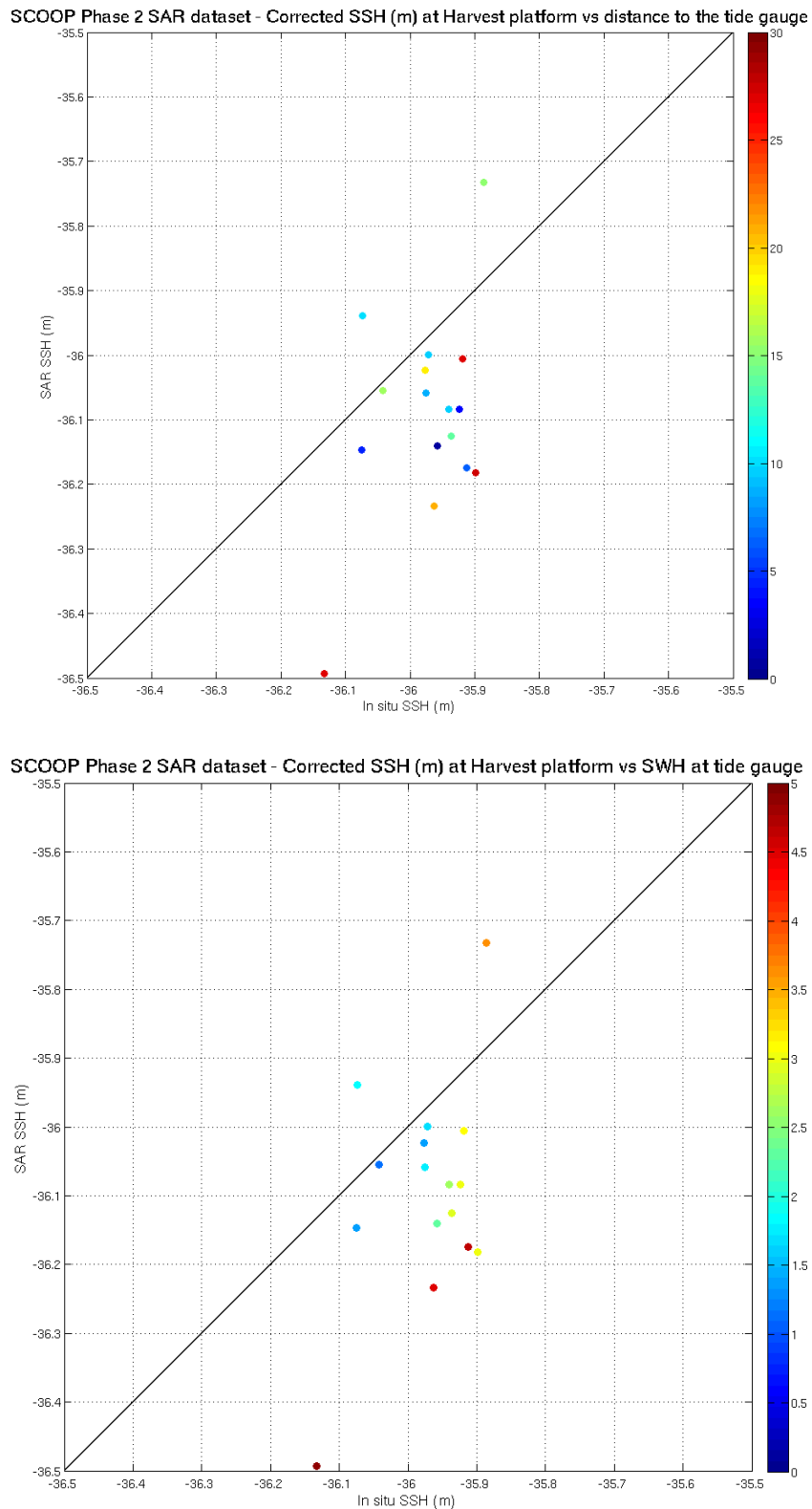


**Figure 6.11 Comparison between the altimeter SSH and the Harvest in situ SSH (in m) for the SCOOP phase 2 SAR dataset. The colors on the upper plot show the distance (in km) to the tide gauge at the altimetry points considered for the bias computation. The colors on the lower plot show the significant wave height (in m) measured at the Harvest platform at the date of the bias estimates.**

### 6.2.1.3 Evaluation of the altimeter retrieved significant wave height

The altimeter retrieved significant wave heights from the SCOOP Phase 1 and Phase 2 SAR datasets were compared with the in situ wave heights measured by the buoy located close to the Harvest platform. All the Cryosat-2 passes within 20 km from the Harvest platform are considered (see Figure 6.8) and the closest altimetry point to the platform is selected for the SWH comparison (12 points). The altimetry data at 20 Hz are used, with a selection on altimetry points with misfit parameter value lower than 4.

Figure 6.12 shows the time series of the significant wave height estimates selected for the comparison. The in situ SWH are interpolated at the Cryosat-2 time of measurements. It appears very clear that the SWH from the Phase 2 dataset are closer to the in situ SWH than the SWH from the Phase 1 dataset.

This is confirmed by the statistics summarized in Table 6.2 and by the scatterplot in Figure 6.13. Even if the number of points for the comparison is small (12 points), the reduction in the variability of the difference between the altimetry and the in situ SWH is significant (-15 cm) for the Phase 2 dataset. The median of the differences is also reduced by 10 cm, which is in agreement with the observations of the other validation groups, who noted a general improvement of 10 cm over the SWH from the Phase 1 GPOD processing to the Phase 2 processing.

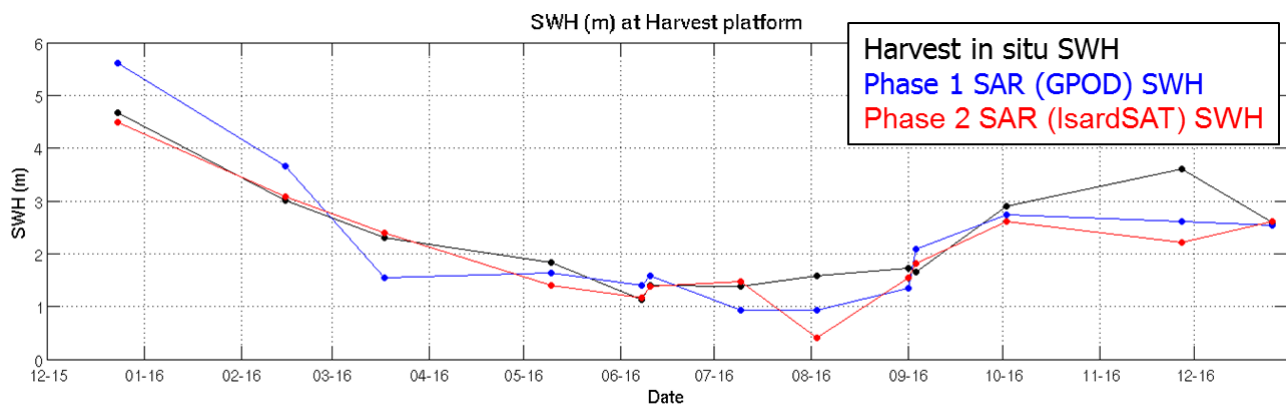


**Figure 6.12 Significant wave heights time series (in m) at the Harvest calibration site, for the SCOOP Phase 1 and Phase 2 SAR datasets and for the in situ buoy. Selection of altimetry points within 20 km off the Harvest calibration site.**

**Table 6.2 Statistics on the comparison between the SCOOP Phase 1 and Phase 2 SAR significant wave height observations at 20 Hz and the Harvest in situ significant wave height data.**

Comparison to in situ SWH SAR Dataset at 20 Hz	Correlation	Std diff	Mean diff	Median diff	Nb of points
Phase 1	0.90	57 cm	-4 cm	-10 cm	12
Phase 2	0.92	42 cm	-17 cm	-0.5 cm	12

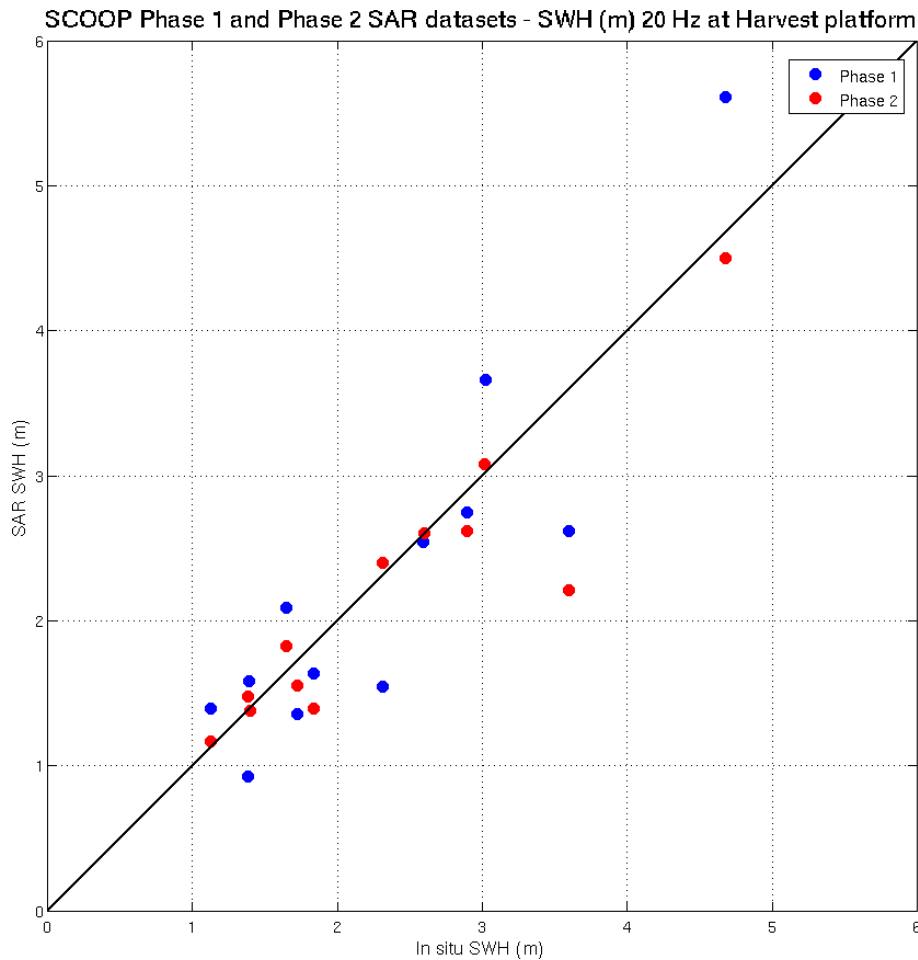


**Figure 6.13 Comparison between the SCOOP Phase 1 (blue) and Phase 2 (red) SAR significant wave height observations at 20 Hz and the Harvest in situ significant wave height measurements.**

## 6.2.2 Comparison between Phase 2 SAR and coastal SAR datasets

In addition to the Phase 2 SAR dataset, a specific coastal SAR dataset was produced by IsardSAT with the aim to improve the coastal SAR sea surface height retrievals.

Figure 6.14 shows the noise of the uncorrected sea surface heights at 20 Hz as a function of the distance to the coast for both datasets (SAR in blue and coastal SAR in red). For both datasets, a selection was applied considering only the altimetry points where the Pearson correlation is higher than 95%, which means that the retracking model fits well the waveform. Unexpectedly, the uncorrected SSH of the coastal SAR dataset show higher variability than the SAR dataset, especially in the first 10 km offshore (middle plot). In addition, one can notice a slight loss of data in the first 10 km offshore in the coastal SAR dataset, which is also unexpected.

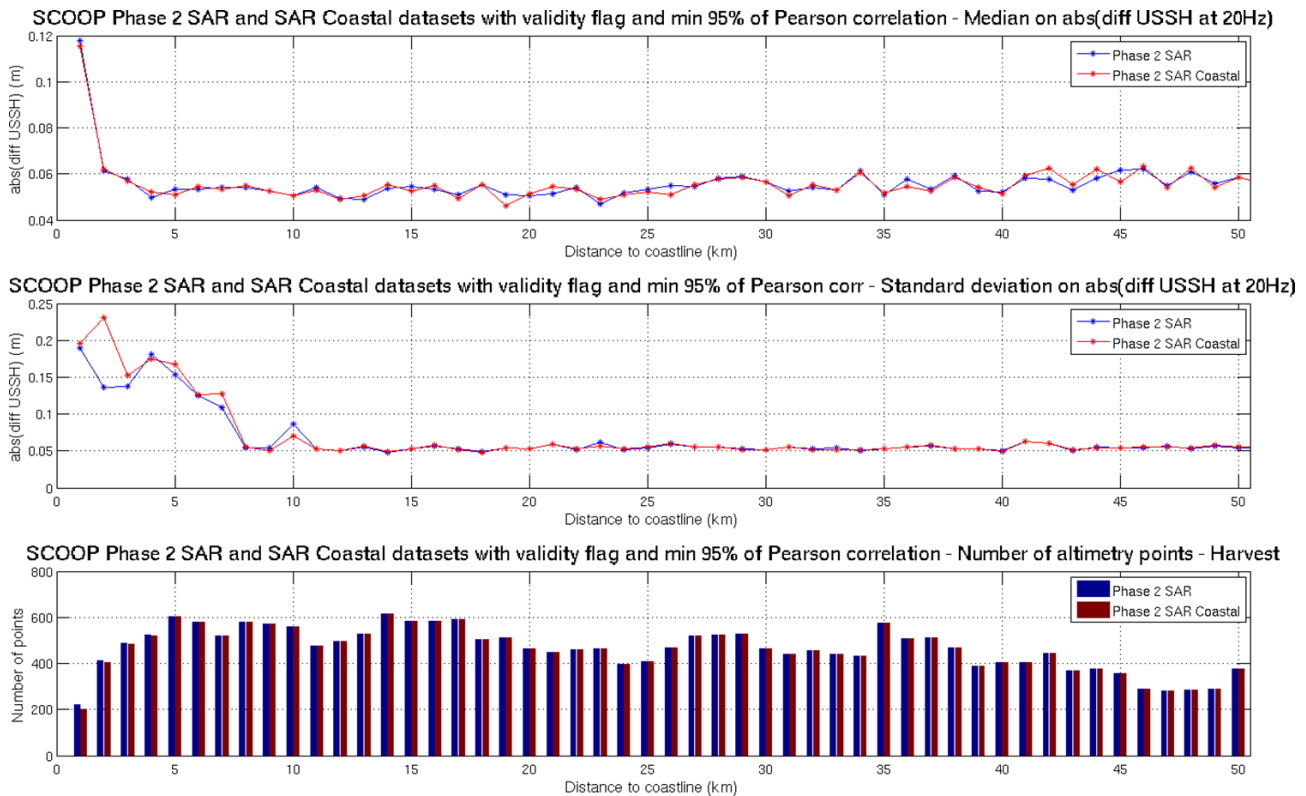


**Figure 6.14 Statistics on the along-track differences of the uncorrected sea surface height (altitude - range) at 20 Hz (in m) from the SCOOP Phase 2 SAR and coastal SAR datasets in the Harvest region.**

The map of the differences between the uncorrected SSH of both datasets highlights the fact that the largest discrepancies are observed close to the coasts, which is expected (Figure 6.15). However, when looking at the uncorrected SSH along a section of a coastal track, encircled in red in Figure 6.15, a large degradation of the USSH can be observed at the most coastal points (North of 37.66°N) in the SAR coastal dataset, while the SAR dataset shows consistent USSH estimates (Figure 6.16). The increase in the variability of the USSH for the coastal SAR dataset observed in Figure 6.14 is thus explained by these coastal problems.

In the comparison in Figure 6.14, the loss of coastal data in the coastal SAR dataset is due to the selection based on the Pearson correlation value. Indeed, the map of the differences of the Pearson correlation at each altimetry point, between the SAR and the coastal SAR datasets, also highlights the fact that the largest discrepancies are located close to the coast (Figure 6.17). When considering the along-track Pearson correlation for one track (encircled in red in Figure 6.17), one can notice a large drop in the correlation in the SAR coastal dataset, when approaching the coast (North of 34.4°N) in Figure 6.18. As the altimetry points with a Pearson correlation lower than 95% are filtered out in the comparison in Figure 6.14, the number of selected coastal points in the coastal SAR dataset is consequently smaller than for the SAR dataset, due to these drops in the correlation close to the coast.

Obviously, this is not the expected behaviour for the coastal SAR dataset and some further investigations are required at IsardsAT to understand why such degradations are observed.

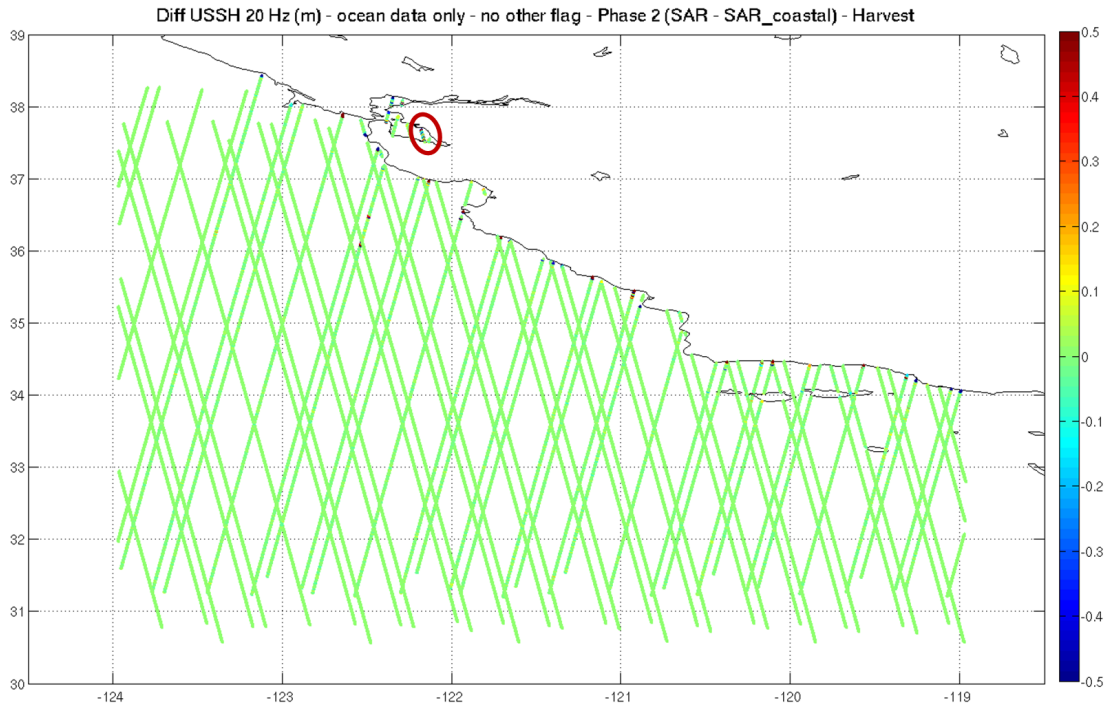


**Figure 6.15** Difference between the uncorrected sea surface heights (altitude - range) at 20 Hz (in m) from the SCOOP Phase 2 SAR and coastal SAR datasets in the Harvest region. The segment of track encircled in red is shown in more details in Figure 6.16.

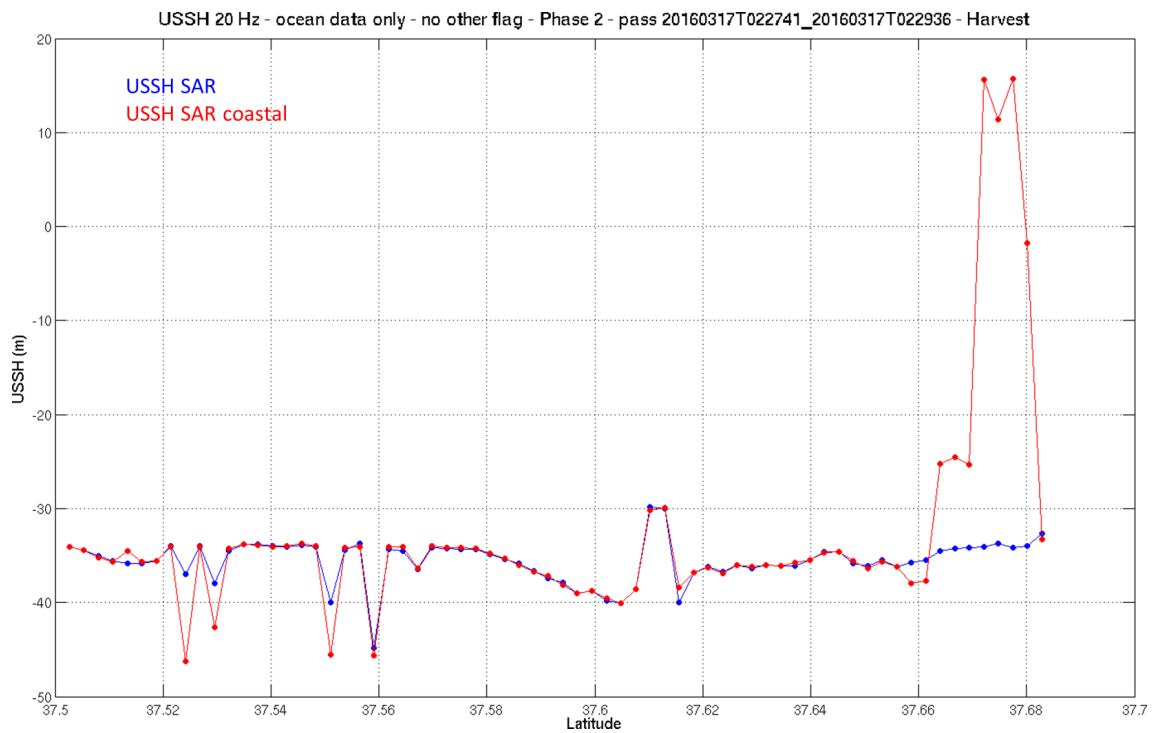


**Figure 6.16** Along-track uncorrected sea surface height (altitude - range) at 20 Hz (in m) from the SCOOP Phase 2 SAR and coastal SAR datasets for a segment of track located close to the coast (cf. Figure 6.15)

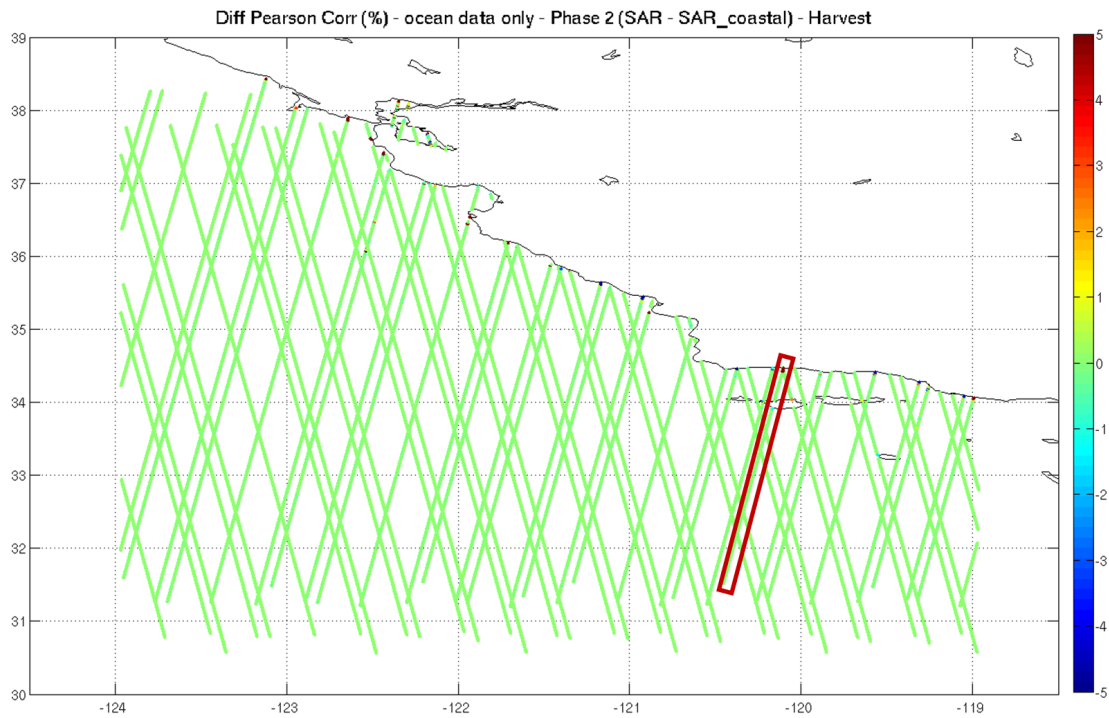


**Figure 6.17** Difference between the Pearson correlations at 20 Hz (in %) from the SCOOP Phase 2 SAR and coastal SAR datasets in the Harvest region. The segment of track encircled in red is shown in more details in Figure 6.18.

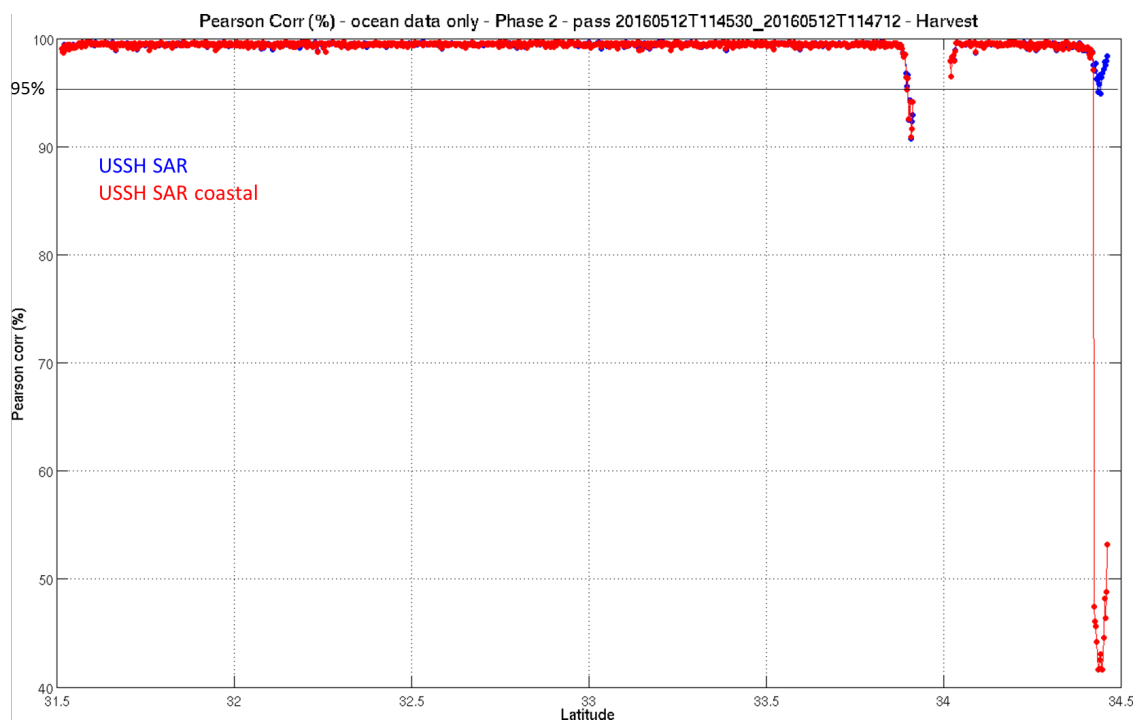


**Figure 6.18** Along-track Pearson correlation at 20 Hz (in %) from the SCOOP Phase 2 SAR and coastal SAR datasets for a segment of track (cf. Figure 6.17)

## 6.3 Results from Validation Test 2: RDSAR product

### 6.3.1 Comparison between Phase 1 and Phase 2 RDSAR MLE3 datasets

The Phase 1 and Phase 2 RDSAR datasets in Harvest cover a 6-month period, from mid-December 2015 to mid-May 2016.

Figure 6.19 and Figure 6.20 show the along-track uncorrected sea surface heights (altitude – range) at 20 Hz for the whole Phase 1 and Phase 2 datasets, respectively. No filter nor selection is applied, which explains why some points are visible on land. Unexpectedly, both maps are similar. This is confirmed by the statistics in Figure 6.21, which show that both datasets (Phase 1 and Phase 2) give exactly the same results in terms of along-track noise, variability and number of points.

The noise and the variability of the uncorrected sea surface heights at 20 Hz for both datasets are shown in Figure 6.21 as a function of the distance to the coast (upper and middle plots, respectively). The lower plot shows the number of points considered for the computation of the statistics in 1-km bins. For both RDSAR datasets, the number of points in the first 10 km offshore appears to be low compared to the SAR datasets, given that no selection was applied on the data. This may be explained by the fact that no coastal tuning was used in the RDSAR processing. The along-track noise of the RDSAR data is globally 50% higher than the noise of the SAR datasets.

Figure 6.22 and Figure 6.23 show the sea surface height anomalies at 20 Hz (pre-computed *ssha\_20Hz* parameter in the RDSAR files) for the whole Phase 1 and Phase 2 datasets, respectively. No filter nor selection was applied on the data, but one can notice the loss of data close to the coasts in the case of the Phase 1 RDSAR dataset (Figure 6.22). The only difference between the two quantities shown in Figure 6.19 (USSH) and Figure 6.22 (SSHA) is the fact that the range corrections were applied and the mean sea surface (MSS) removed in the SSHA parameter. This loss of data is thus potentially linked with one of the corrections applied or with the MSS parameter. For the Phase 2 RDSAR dataset (Figure 6.23), that loss of data close to the coasts is quite reduced compared to the Phase 1 dataset (Figure 6.22). The issue in the computation of the SSHA parameter has been solved for the Phase 2 dataset.

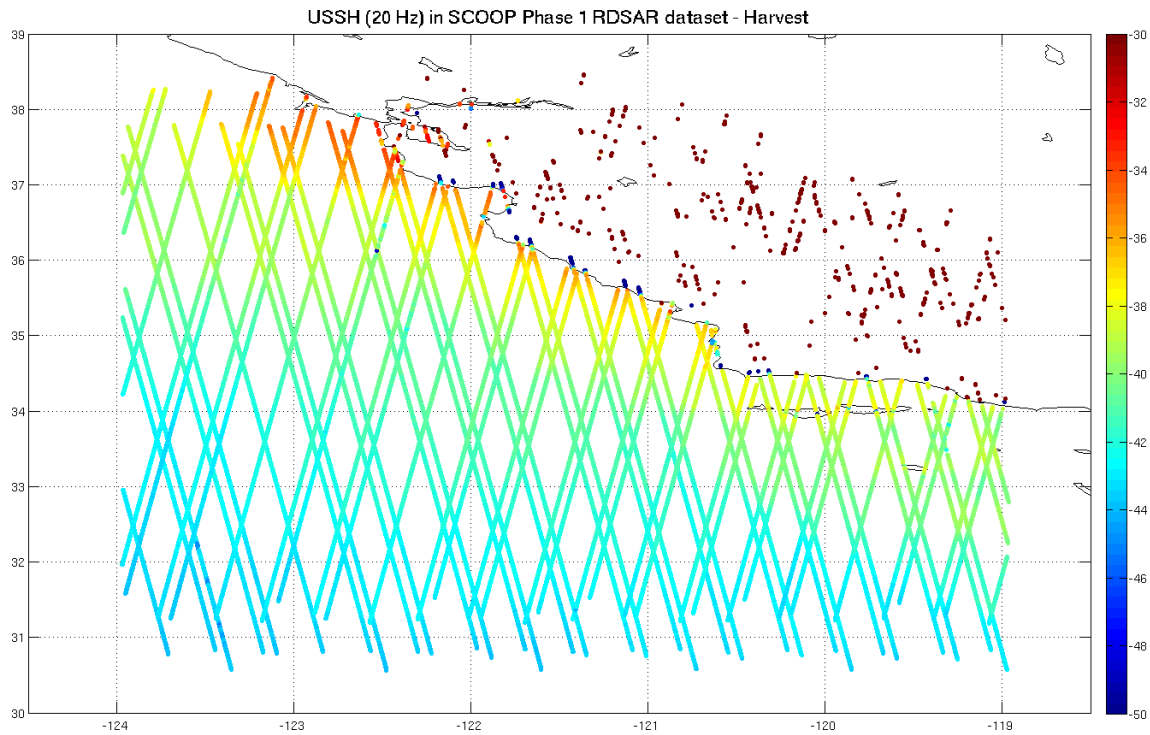


Figure 6.19 Uncorrected sea surface height (altitude - range) at 20 Hz (in m) from the SCOOP Phase 1 RDSAR dataset in the Harvest region.

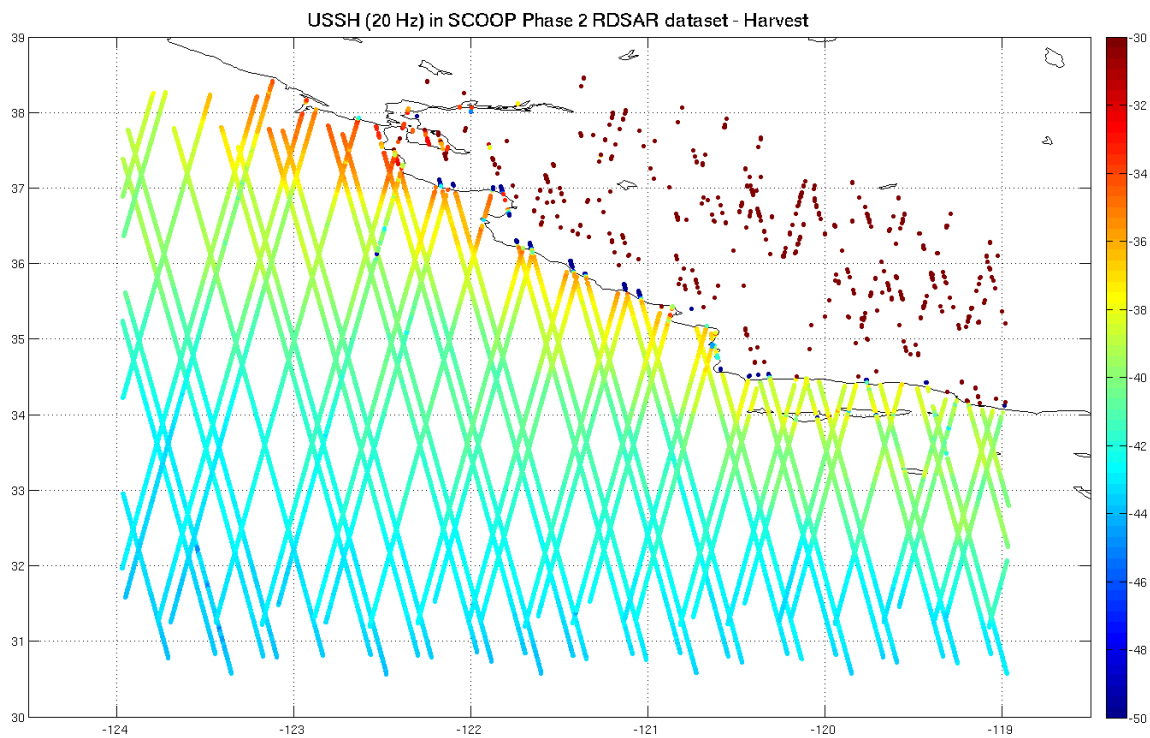
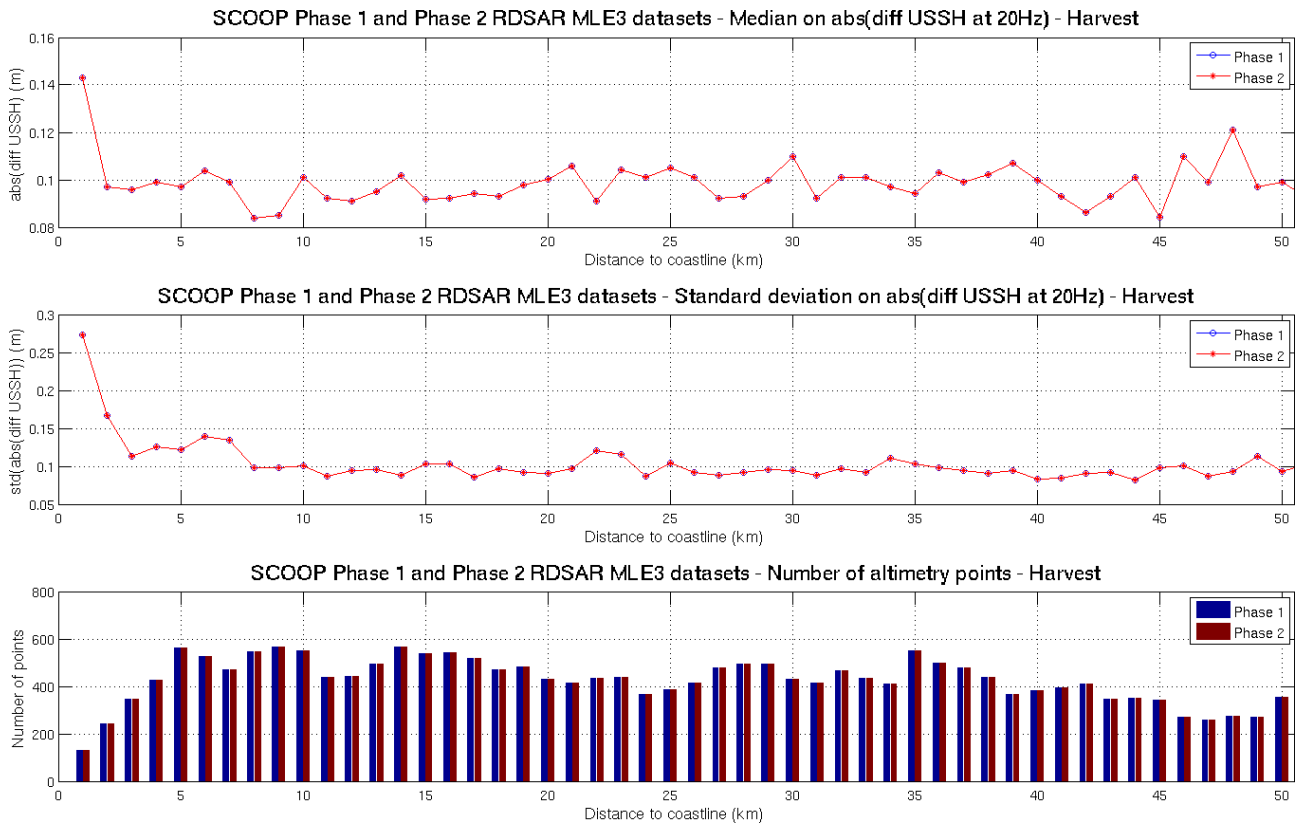


Figure 6.20 Uncorrected sea surface height (altitude - range) at 20 Hz (in m) from the SCOOP Phase 2 RDSAR dataset in the Harvest region.



**Figure 6.21 Statistics on the along-track differences of the uncorrected sea surface height (altitude - range) at 20 Hz (in m) from the SCOOP Phase 1 and Phase 2 RDSAR datasets in the Harvest region.**

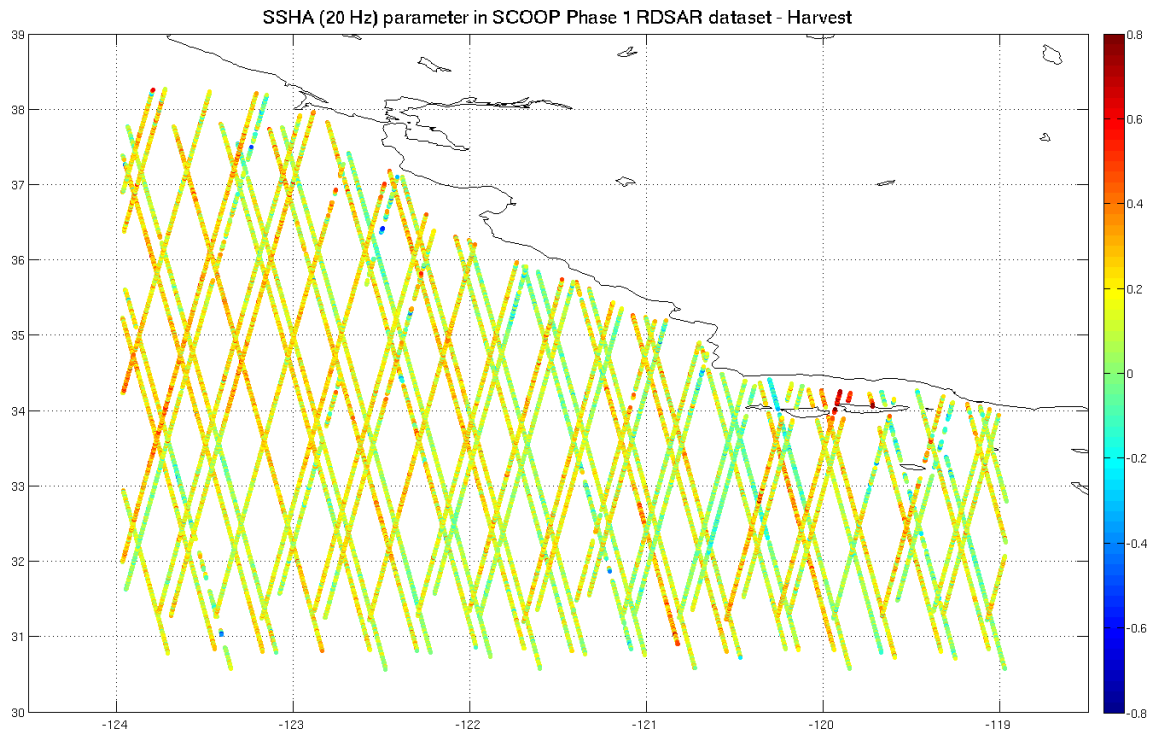


Figure 6.22 Sea surface height anomaly at 20 Hz (in m) from the SCOOP Phase 1 RDSAR dataset in the Harvest region.

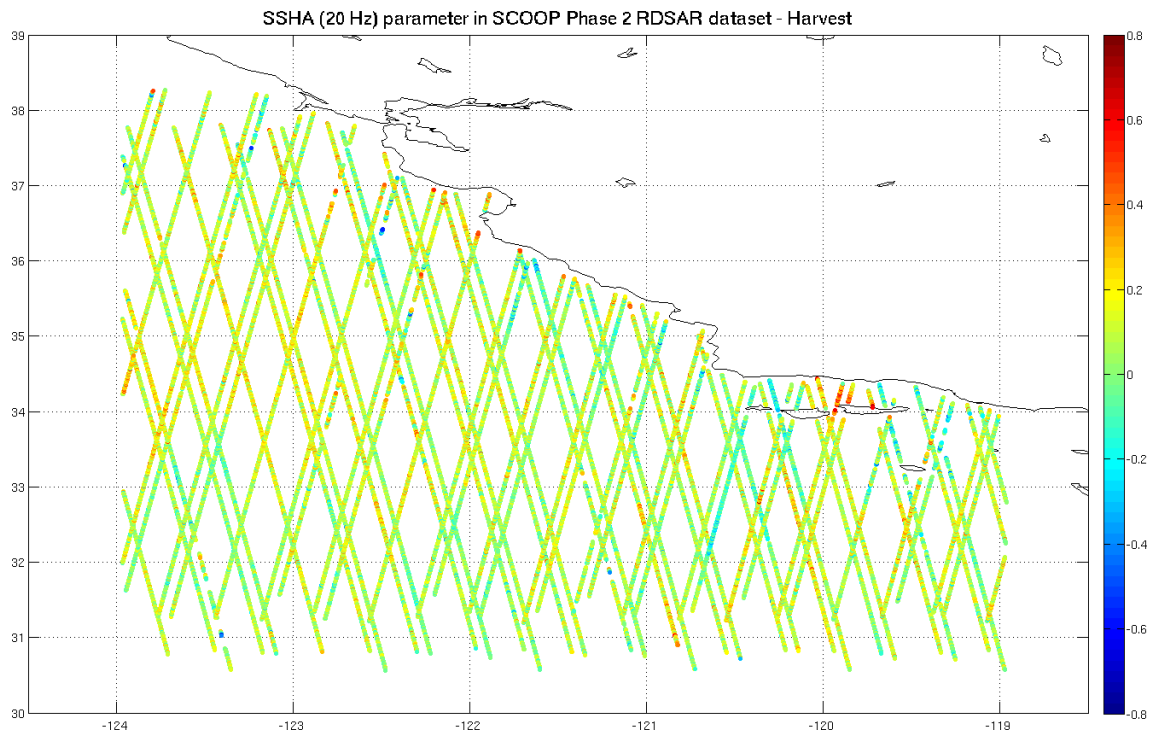


Figure 6.23 Sea surface height anomaly at 20 Hz (in m) from the SCOOP Phase 2 RDSAR dataset in the Harvest region.

### 6.3.2 Comparison between Phase 2 RDSAR MLE3 and MLE4 datasets

A second Phase 2 RDSAR dataset was produced by the Technical University of Delft, using the MLE4 retracking instead of the MLE3 retracking, with the aim to reduce the bias on the significant wave height estimates. The impact on the range is expected to be minor.

Figure 6.24 shows the noise of the uncorrected sea surface heights at 20 Hz as a function of the distance to the coast for both datasets (MLE3 in blue and MLE4 in red). It appears that the uncorrected SSH of the MLE4 dataset are generally noisier than for the MLE3 dataset. In addition, one can observe a slight loss of data in the first 10 km offshore in the MLE4 dataset.

However, the comparison with the in situ significant wave heights measured at the Harvest platform shows an improvement with the MLE4 dataset, compared to the MLE3 dataset, both for the 20 Hz and the 1 Hz SWH estimates (Figure 6.25 and Table 6.3). Obviously, the comparison gives steadier results with the 1 Hz SWH estimates, which are much less noisy than the 20 Hz SWH estimates. However, these statistics in Table 6.3 must be carefully interpreted as they were computed on only 4 points of comparison.

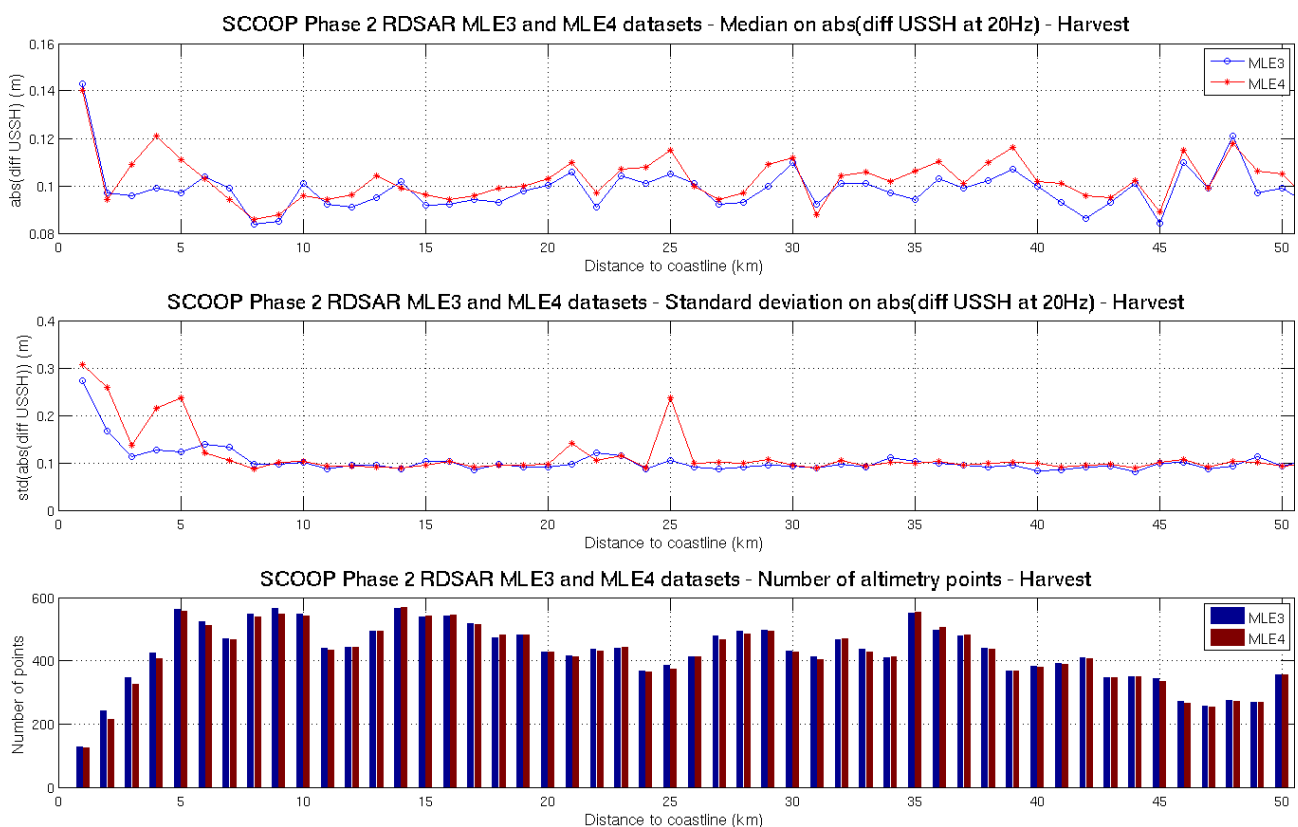


**Figure 6.24** Statistics on the along-track differences of the uncorrected sea surface height (altitude - range) at 20 Hz (in m) from the SCOOP Phase 2 RDSAR MLE3 and MLE4 datasets in the Harvest region.

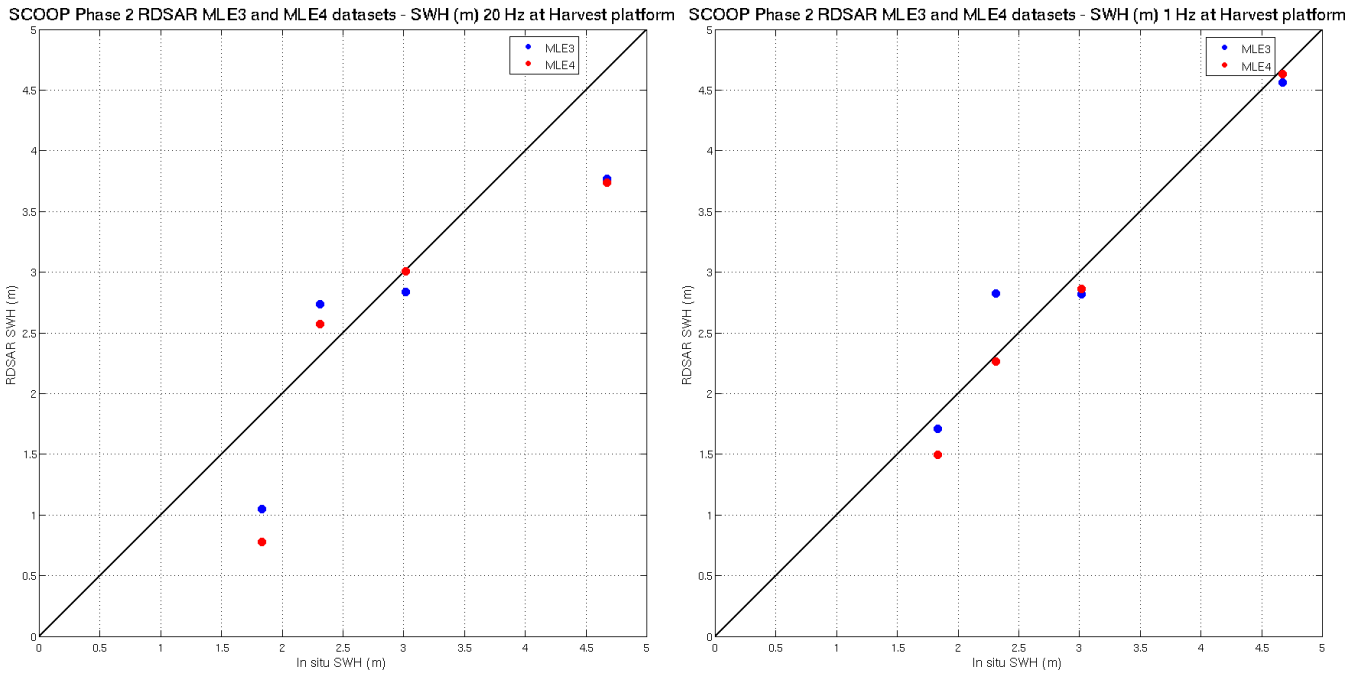


Figure 6.25 Comparison between the SCOOP Phase 2 RDSAR MLE3 (blue) and MLE4 (red) significant wave height observations at 20 Hz (left) and at 1 Hz (right), and the Harvest in situ significant wave height measurements.

Table 6.3 Statistics on the comparison between the SCOOP Phase 2 RDSAR MLE3 and MLE4 significant wave height observations at 20 Hz and at 1 Hz, and the Harvest in situ significant wave height data.

RDSAR Dataset	SWH 20 Hz					SWH 1 Hz				
	Corr	Std diff	Mean diff	Median diff	Nb of points	Corr	Std diff	Mean diff	Median diff	Nb of points
<b>MLE3</b>	0.87	61 cm	-36 cm	-48 cm	4	0.96	33 cm	2 cm	-11 cm	4
<b>MLE4</b>	0.86	65 cm	-43 cm	-47cm	4	0.99	14 cm	-14 cm	-10 cm	4

## 6.4 Summary of Results

The analyses performed on the SCOOP SAR and RDSAR datasets in Harvest can be summarized as follows. However, the number of validation points for comparison with in situ data being very small (4 to 16 depending on the altimetry dataset), these results would need to be confirmed by considering longer altimetry time series (at least two years of CryoSat data).

- **SAR sea surface height noise :**  
A general improvement is noticed from Phase 1 to Phase 2 processing, with lower noise and variability in the Phase 2 dataset (except in the first kilometre offshore) and more data retrieved whatever the distance to the coast.
- **Sea state impact on the SAR sea surface height estimates :**  
The investigation of the SAR SSH absolute bias estimates against the in situ SWH measurements at Harvest shows the clear dependency of the bias variability with the significant wave heights. The increase in the SSH bias variability for large wave conditions highlights the fact that an appropriate SSB correction dedicated to the SAR SSH is needed to compute accurate SSH.
- **SAR significant wave heights accuracy :**  
An improvement of 10 cm is observed in the comparison of the Phase 2 dataset SWH with the in situ SWH at Harvest, compared to the Phase 1 dataset. This is consistent with the observations of the other validation groups in other regions.
- **SAR “coastal” processing :**  
The comparison between along-track SSH processed with the classical Phase 2 SAR processing and with an experimental coastal SAR processing shows some degradations at the coasts in the SSH estimates and in the correlation between the waveforms and the retracking model in the case of the coastal SAR processing, in Harvest. Further investigations are required at IsardSAT to understand why such degradations are observed.
- **RDSAR sea surface height noise:**  
The Phase 1 and Phase 2 MLE3 RDSAR processing give similar results in terms of SSH. The along-track noise of the RDSAR data is globally 50% higher than the noise of the SAR datasets.  
  
The SSHA (anomaly) parameter in the Phase 1 dataset shows an unexpected loss of data close to the coasts, which is corrected in the Phase 2 dataset.  
  
The Phase 2 MLE4 RDSAR SSH retrievals are generally noisier than for the MLE3 dataset and a slight loss of data in the first 10 km offshore. However, the comparison with the in situ significant wave heights at Harvest shows an improvement with the MLE4 dataset, compared to the MLE3 dataset.

# 7 Validation of the Wet Troposphere Correction by U Porto (WP7000)

## 7.1 Summary of Approach

In the scope of WP7000, improved wet tropospheric corrections (WTC) have been computed for CryoSat-2 (CS2) and Sentinel-3A (S3A) using the GPD+ methodology.

Due to the large space-time variability of the WTC, over open-ocean the most accurate way to retrieve this correction is by means of collocated measurements of microwave radiometers (MWR) embarked on the altimetric satellites. However, over non-ocean surfaces, MWR-derived WTC is usually flagged as invalid in the altimetric products. This is due to the fact that: i) the algorithms adopted in the WTC retrieval are tuned for open-ocean conditions; ii) MWR have large footprints (10-40 km, depending on frequency), thus originating bands of invalid measurements around the coastline of 10-40 km width.

Sentinel-3 carries a 2-band MWR, similar to that of Envisat. Therefore, it is expected that S3A MWR-derived WTC exhibits similar performance and problems to those of Envisat, particularly in coastal and polar regions (Fernandes et al., 2015). CryoSat-2, designed as a mission for observing the cryosphere, does not possess an on-board MWR, relying on the WTC derived from the ECMWF model.

The GPD+ algorithm has been developed with the purpose of determining improved WTC for these two types of missions using data combination of all available observations and best atmospheric models. While in case of missions such as Sentinel-3, GPD+ preserves the valid MWR observations over open-ocean, only estimating new values in regions of invalid MWR-derived WTC, in the case of CryoSat-2 estimates are obtained for all along-track points. In the absence of observations, the value of the first guess computed from the ECMWF operational model are adopted. In both cases, the final WTC are continuous, valid over all surface types. The data combination is performed by objective analysis, taking into account the variability of the WTC field and the accuracy of the observations.

Compared with previous GPD versions, GPD+ have the following main characteristics:

- Improved detection of valid/invalid MWR observations, of relevance for all missions except CS2;
- External data sets include scanning imaging MWR (SI-MWR) and GNSS-derived path delays;
- All radiometer data sets have been calibrated with respect to the Special Sensor Microwave Imager (SSM/I) and the Special Sensor Microwave Imager Sounder (SSM/IS) set of sensors, due to their stability and independent calibration.

For these reasons, the studies performed for CryoSat-2 and Sentinel-3 are presented in separate sections. Section 7.2 describes the results for CS2, while in section 7.3 the studies carried out for S3A are presented.

## 7.2 WTC for CryoSat-2

### 7.2.1 Methodology

Following the methodology described in Fernandes and Lázaro (2016), GPD+ WTC have been computed for the following 9 project ROI:

- 1) Agulhas
- 2) Central Pacific

- 3) East Pacific
- 4) Harvest
- 5) Indonesia
- 6) North Indian Coast
- 7) North Sea
- 8) Northeast Atlantic
- 9) West Pacific

Corrections have been computed for CS2 L1B data files made available in the project ftp site, for the years 2012 and 2013. Validation of the WTC has been performed by means of a set of statistical analyses described in this section. Computation and validation encompass the following main tasks:

- Extraction of computation points from L1B data files (20 Hz) and addition of sub-cycle and pass structure using RADS convention;
- Interpolation of WTC from ECMWF operational model for all along-track points;
- Computation of GPD+ WTC for all points (20 Hz) in L1B data files;
- Extraction of sea level anomaly (SLA) fields from CS2 Global Ocean Products (GOP) and RADS (1 Hz data); Interpolation of SLA 1 Hz fields into L1B (20 Hz) points;
- Re-organization of data into sub-cycle files;
- Execution of validation statistical analyses.

For each ROI, a set of statistical analyses has been performed with SLA datasets derived with: i) the GPD+ WTC, ii) the ECMWF-Op WTC:

- Mean cycle values (for each ROI) of weighted SLA variance differences at CS2/Jason-2 (J2) crossovers, weights function of latitude ( $\cos\phi$ ) to account for the increasing number of crossovers at high latitudes;
- Spatial pattern of SLA variance differences at CS2/J2 crossovers with time difference  $\Delta T < 10$  days, to reduce the contribution of mesoscale ocean signals to SLA variability;
- SLA variance differences function of distance from coast.

These analyses are presented for each ROI in sub-sections 7.2.2.1. to 7.3.2.9.

WTC variance difference at C2/J2 Xovers with  $\Delta T < 180$  min (GPD-ECMWF-Op) were also computed using data from all ROI.

In addition, comparisons with GNSS-derived WTC have been performed. For this purpose, the root mean square (RMS) of the differences between WTC from ECMWF or GPD+ at altimeter points and the corresponding GNSS-derived WTC at nearby coastal inland stations, interpolated for the same epochs and binned in classes of distance from coast, have been considered.

## 7.2.2 SLA variance analyses

Figure 7.1 illustrates the GPD+ wet tropospheric correction (m) for CryoSat-2, for the nine project ROI, spanning the year 2012.

Figure 7.2, to Figure 7.10 in the following sub-sections, illustrate the impact of using GPD+ instead of ECMWF WTC in the computation of CS2 SLA for each region of interest. Assuming that SLA variance is due to ocean variability and errors in all involved variables, including those in range corrections such as the WTC, a decrease in SLA variance can be ascertained to more accurate corrections.

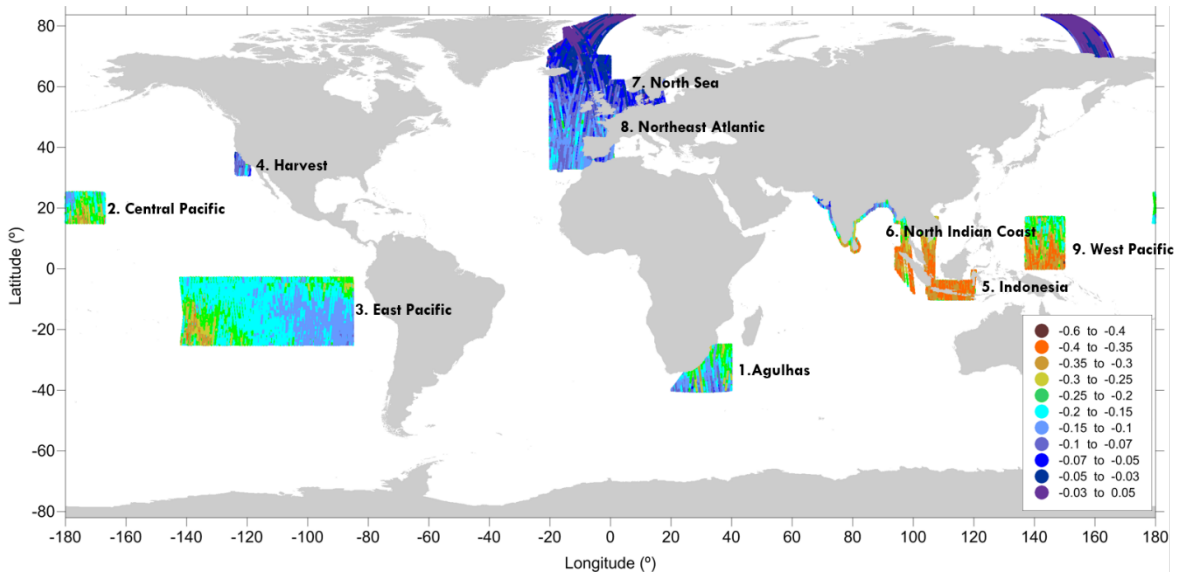


Figure 7.1 GPD+ wet tropospheric correction (m) for CryoSat-2, for the various ROI, spanning the year 2012.

### 7.2.2.1 Agulhas ROI

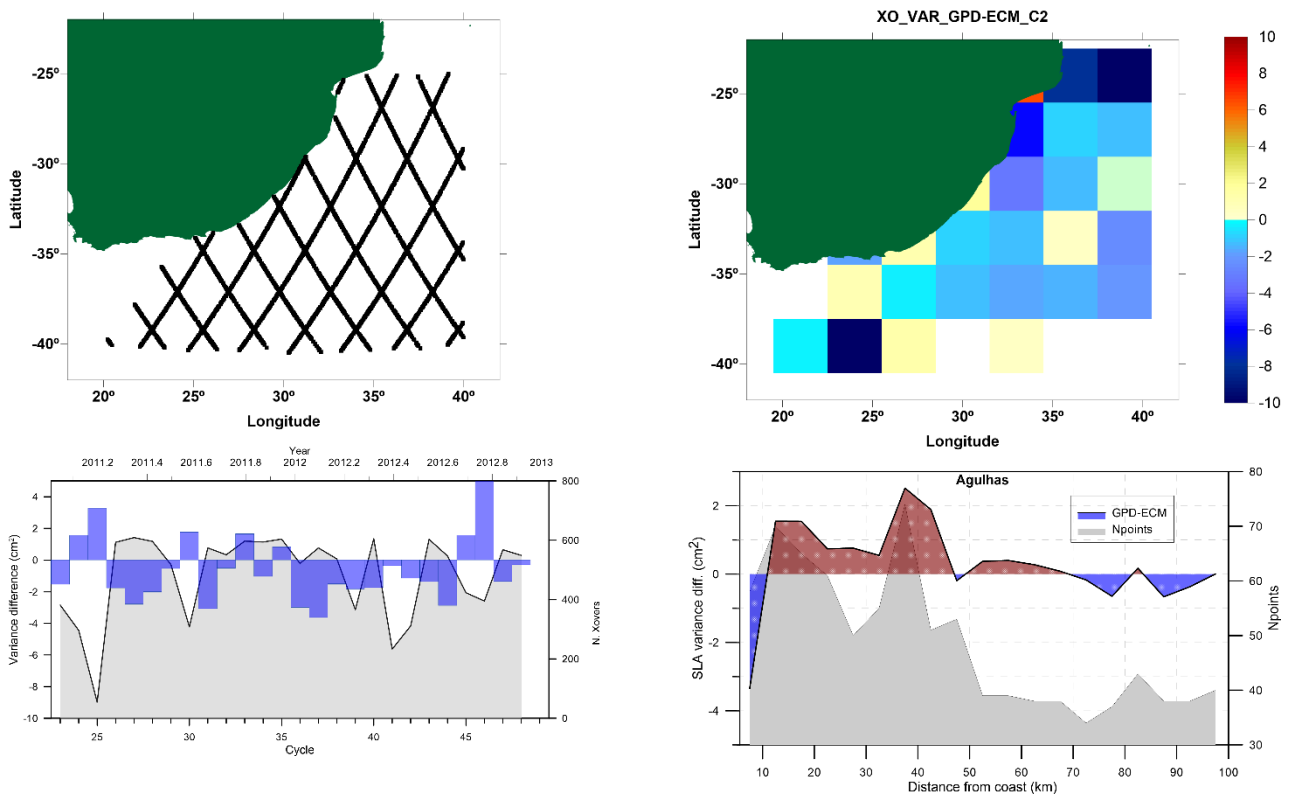
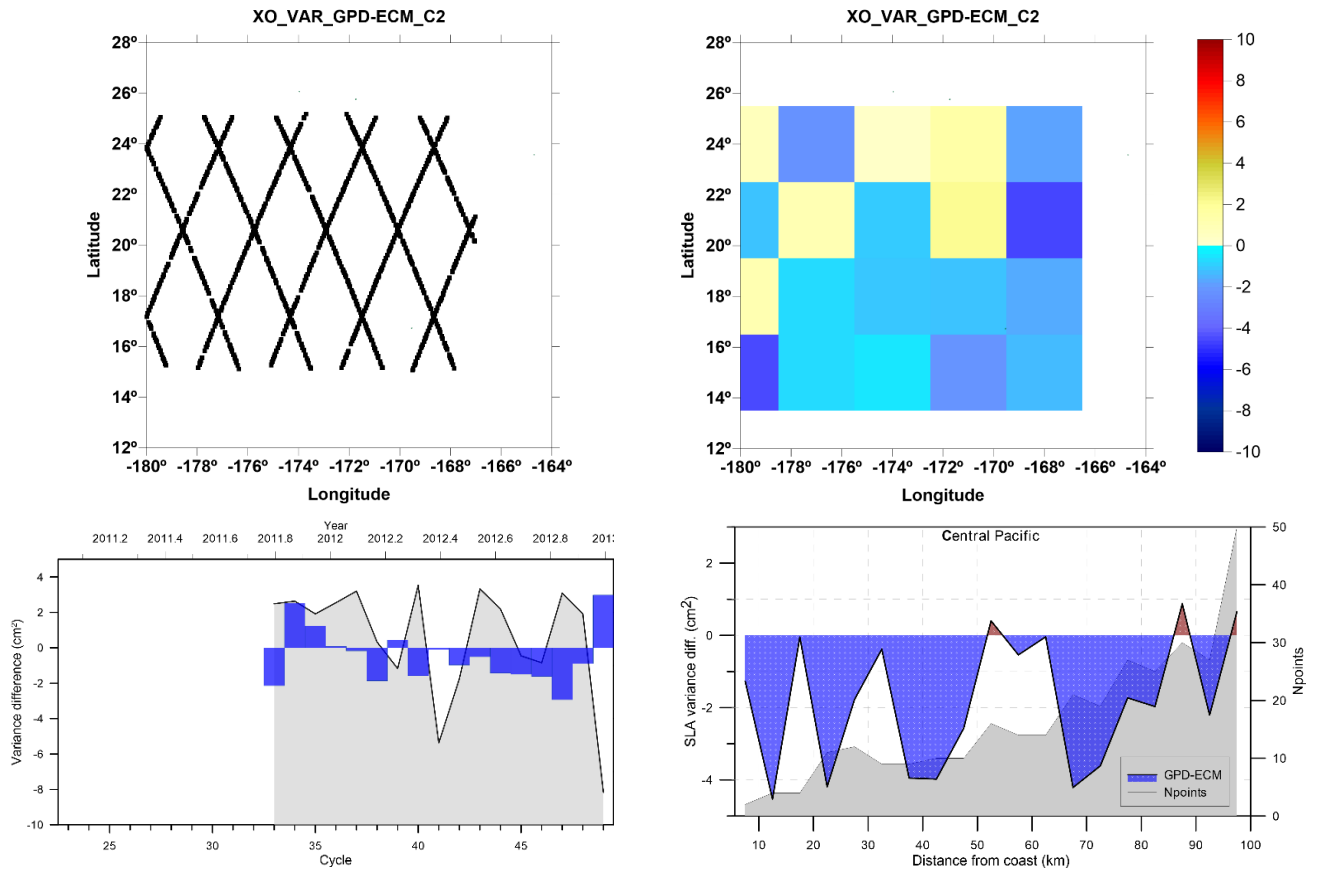


Figure 7.2 Top left: location of analysed CS2 passes over the Agulhas ROI. Top right: spatial pattern of SLA variance differences at crossovers (difference between SLA computed with GPD+ and SLA computed with ECMWF Op). Bottom left: SLA variance difference at crossovers (mean cycle values), between SLA computed with GPD+ and that computed with ECMWF-Op. Bottom right: SLA variance differences (GPD-ECMWF-Op), function of distance from coast.

### 7.2.2.2 Central Pacific ROI



**Figure 7.3** Top left: location of analysed CS2 passes over the Central Pacific ROI. Top right: spatial pattern of SLA variance differences at crossovers (difference between SLA computed with GPD+ and SLA computed with ECMWF Op). Bottom left: SLA variance difference at crossovers (mean cycle values), between SLA computed with GPD+ and that computed with ECMWF-Op. Bottom right: SLA variance differences (GPD-ECMWF-Op), function of distance from coast.

### 7.2.2.3 East Pacific ROI

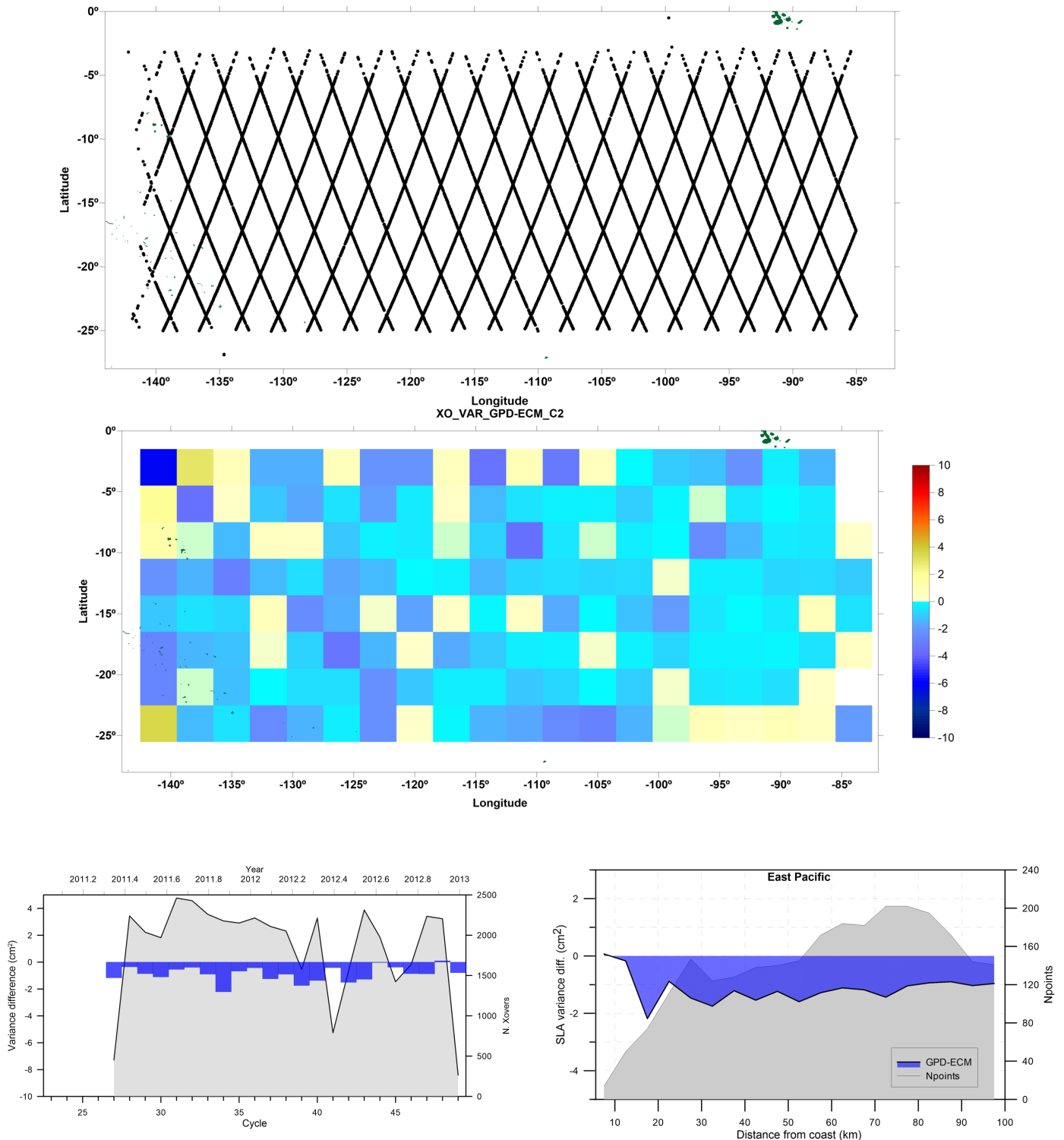


**Figure 7.4 Top: location of analysed CS2 passes over the East Pacific ROI. Middle: spatial pattern of SLA variance differences at crossovers (GPD- ECMWF Op). Bottom left: SLA variance difference at crossovers (mean cycle values), between SLA computed with GPD+ and that computed with ECMWF-Op. Bottom right: SLA variance differences (GPD-ECMWF-Op), function of distance from coast.**

### 7.2.2.4 Harvest ROI

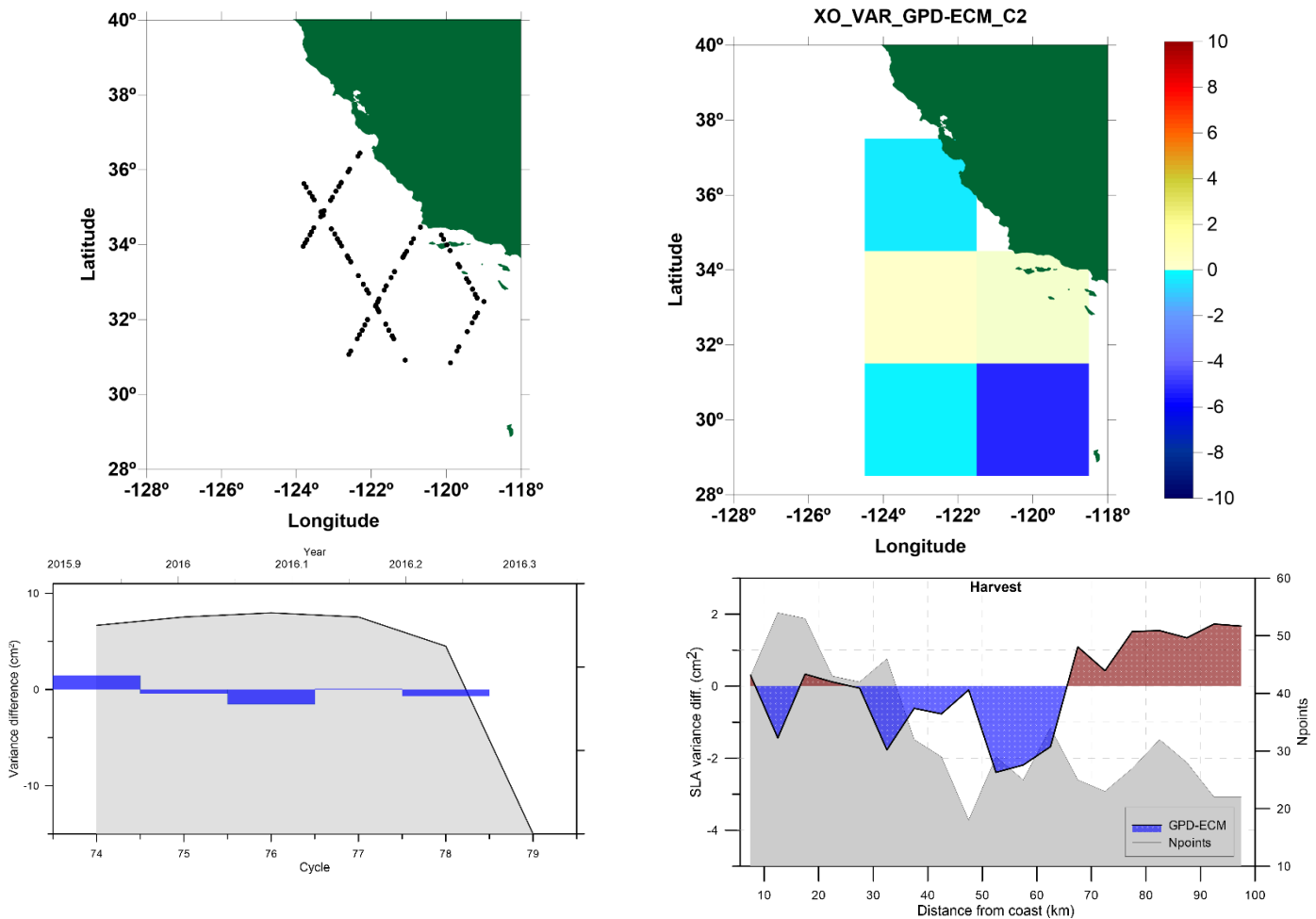


**Figure 7.5** Top left: location of analysed CS2 passes over the Harvest ROI. Top right: spatial pattern of SLA variance differences at crossovers (GPD- ECMWF Op). Bottom left: SLA variance difference at crossovers (mean cycle values), between SLA computed with GPD+ and that computed with ECMWF-Op. Bottom right: SLA variance differences (GPD-ECMWF-Op), function of distance from coast.

### 7.2.2.5 Indonesia ROI

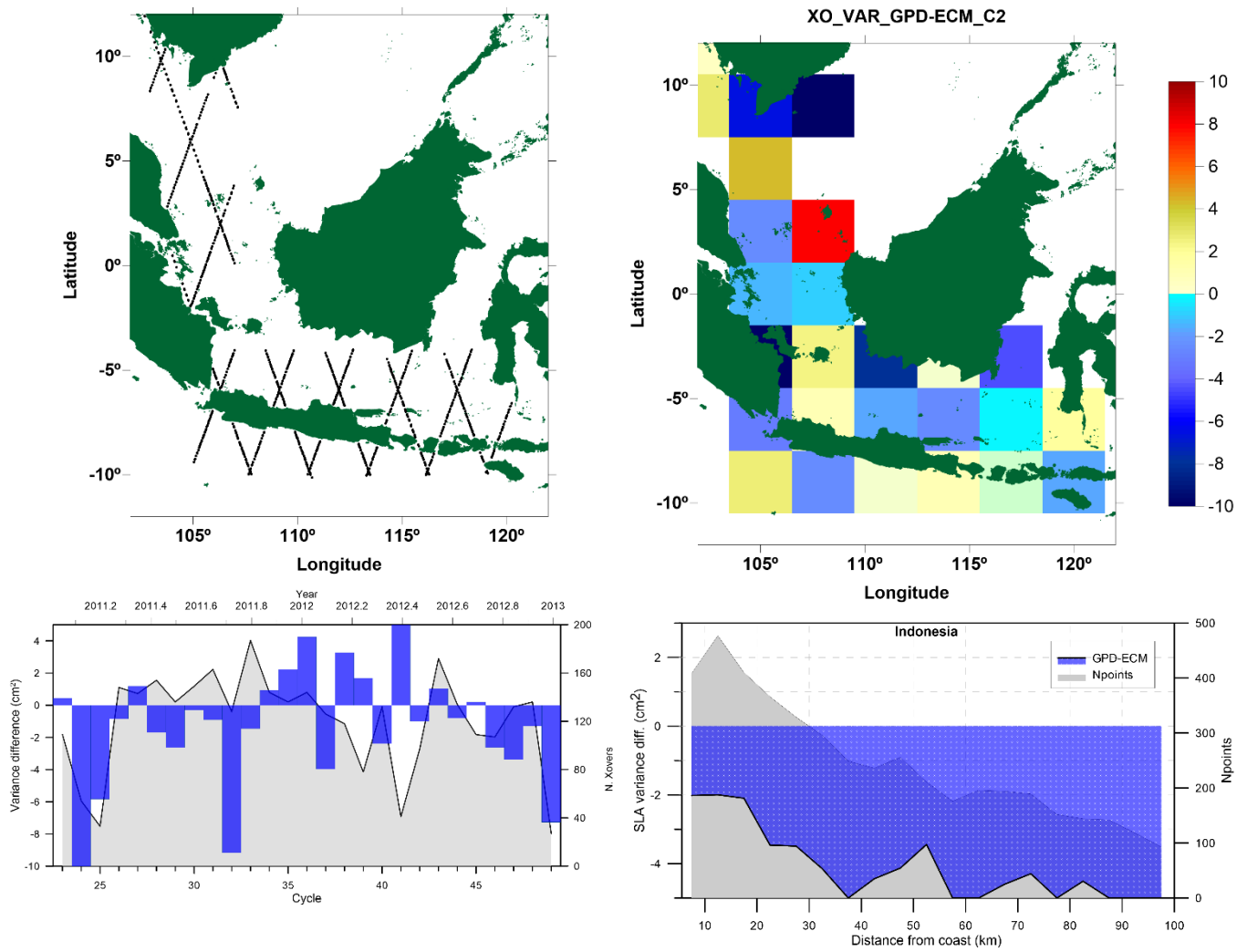


**Figure 7.6** Top left: location of analysed CS2 passes over the Indonesia ROI. Top right: spatial pattern of SLA variance differences at crossovers (GPD- ECMWF Op). Bottom left: SLA variance difference at crossovers (mean cycle values), between SLA computed with GPD+ and that computed with ECMWF-Op. Bottom right: SLA variance differences (GPD-ECMWF-Op), function of distance from coast.

### 7.2.2.6 North Indian Coast ROI

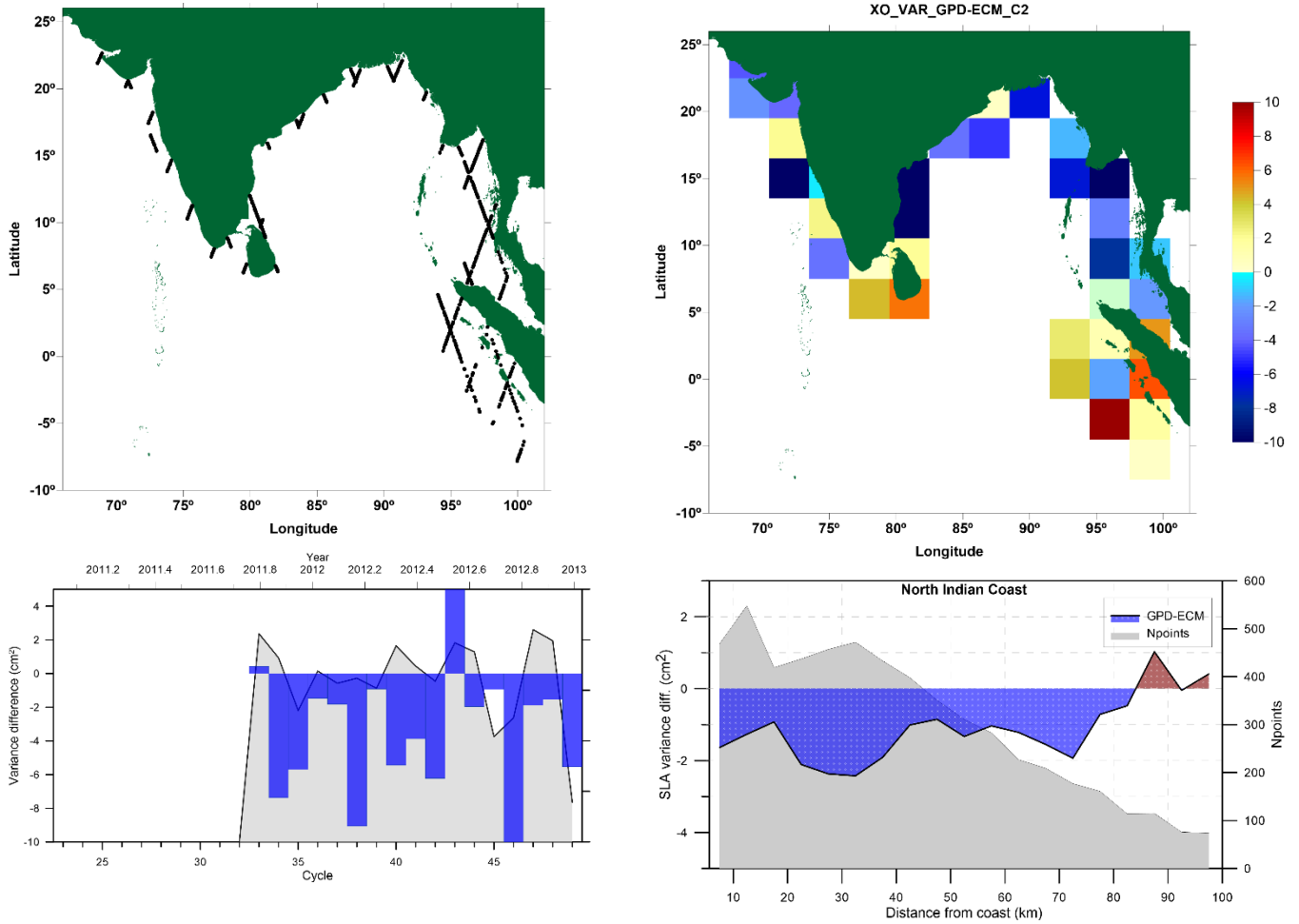


**Figure 7.7** Left: location of analysed CS2 passes over the North Indian Coast ROI. Top right: spatial pattern of SLA variance differences at crossovers (GPD- ECMWF Op). Bottom left: SLA variance difference at crossovers (mean cycle values), between SLA computed with GPD+ and that computed with ECMWF-Op. Bottom right: SLA variance differences (GPD-ECMWF-Op), function of distance from coast.

### 7.2.2.7 North Sea ROI

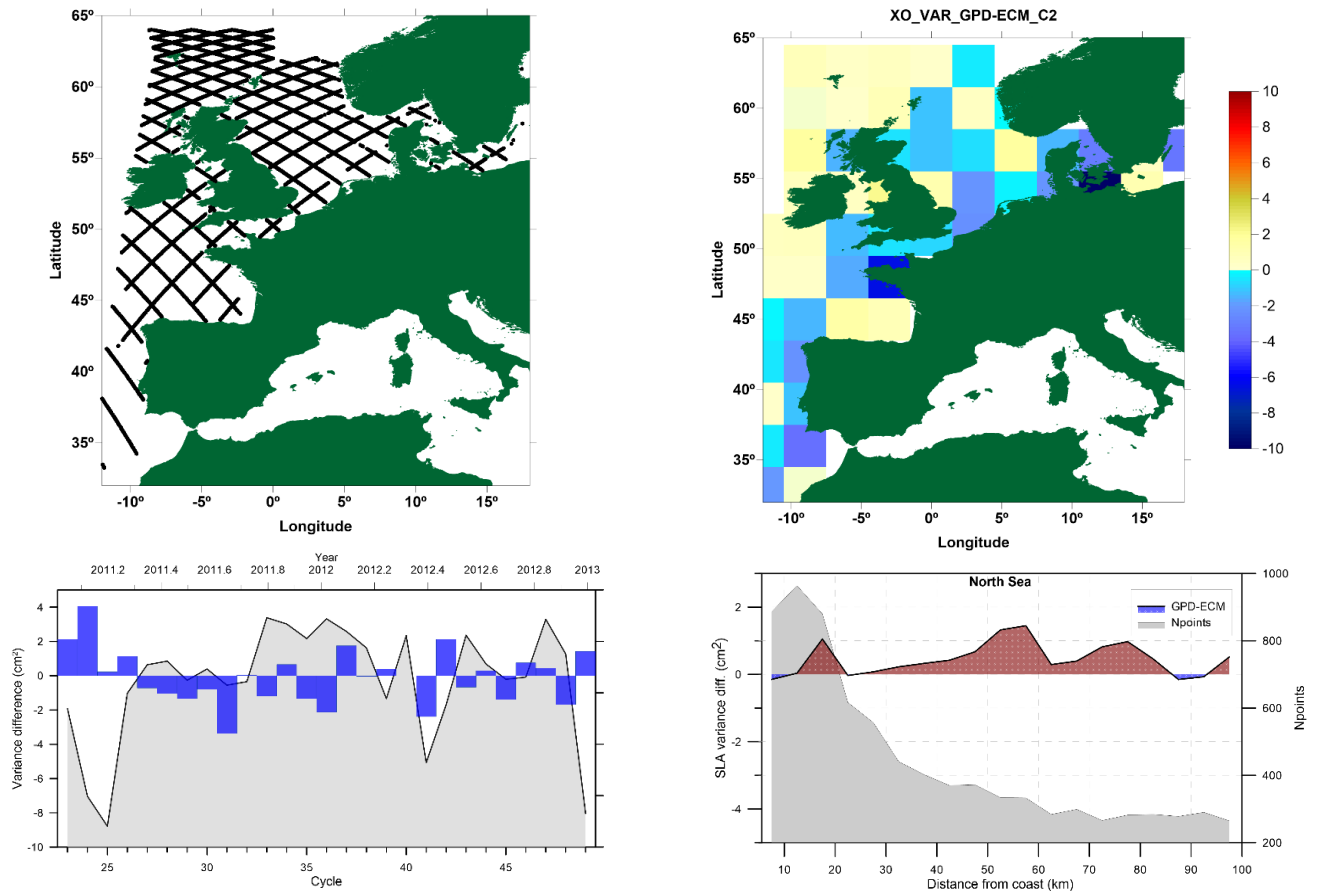


**Figure 7.8** Top left: location of analysed CS2 passes over the North Sea ROI. Top right: spatial pattern of SLA variance differences at crossovers (GPD- ECMWF Op). Bottom left: SLA variance difference at crossovers (mean cycle values), between SLA computed with GPD+ and that computed with ECMWF-Op. Bottom right: SLA variance differences (GPD-ECMWF-Op), function of distance from coast.

### 7.2.2.8 East Atlantic ROI

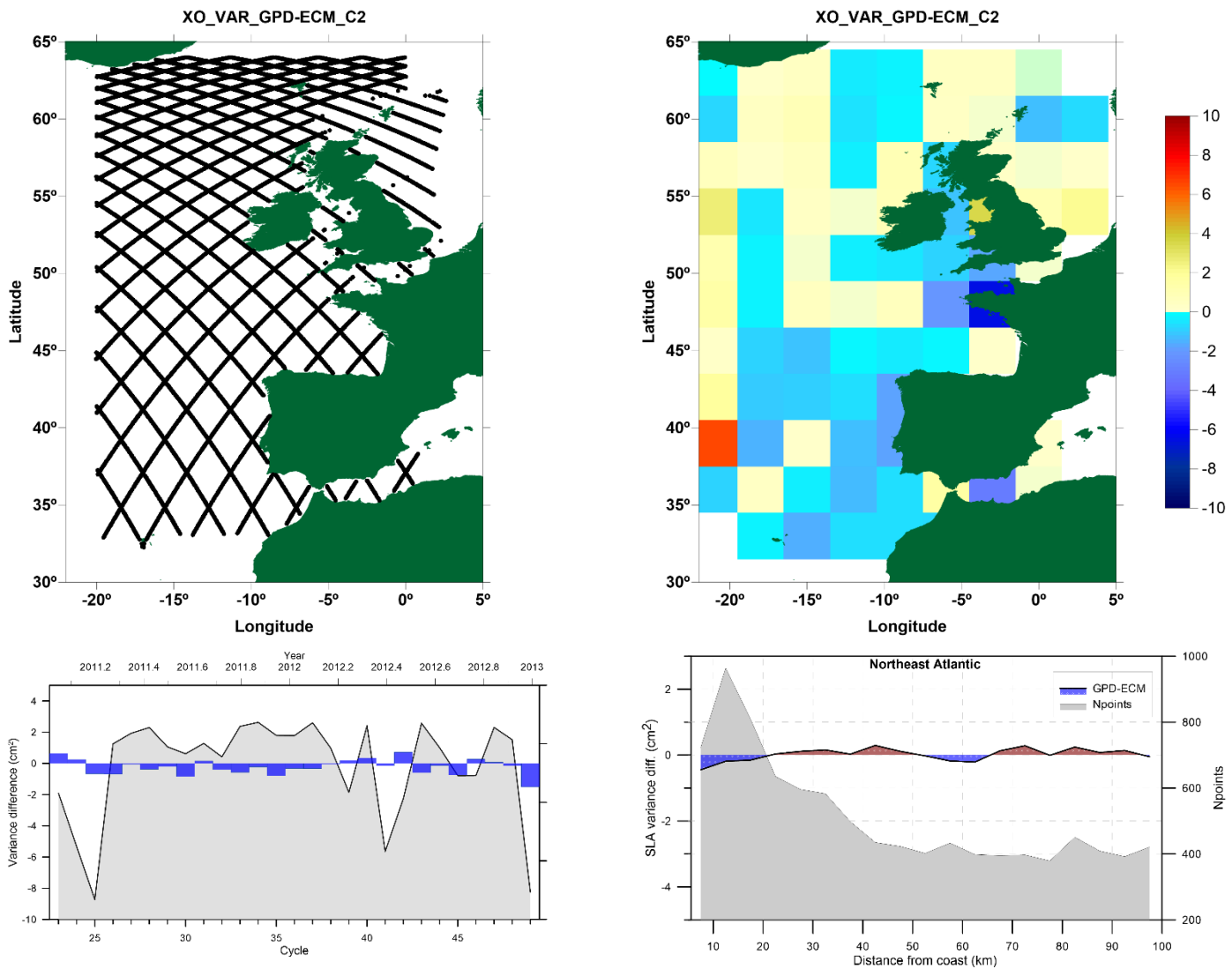


**Figure 7.9** Top left: location of analysed CS2 passes over the East Atlantic ROI. Top right: spatial pattern of SLA variance differences at crossovers (GPD- ECMWF Op). Bottom left: SLA variance difference at crossovers (mean cycle values), between SLA computed with GPD+ and that computed with ECMWF-Op. Bottom right: SLA variance differences (GPD-ECMWF-Op), function of distance from coast.

### 7.2.2.9 West Pacific ROI

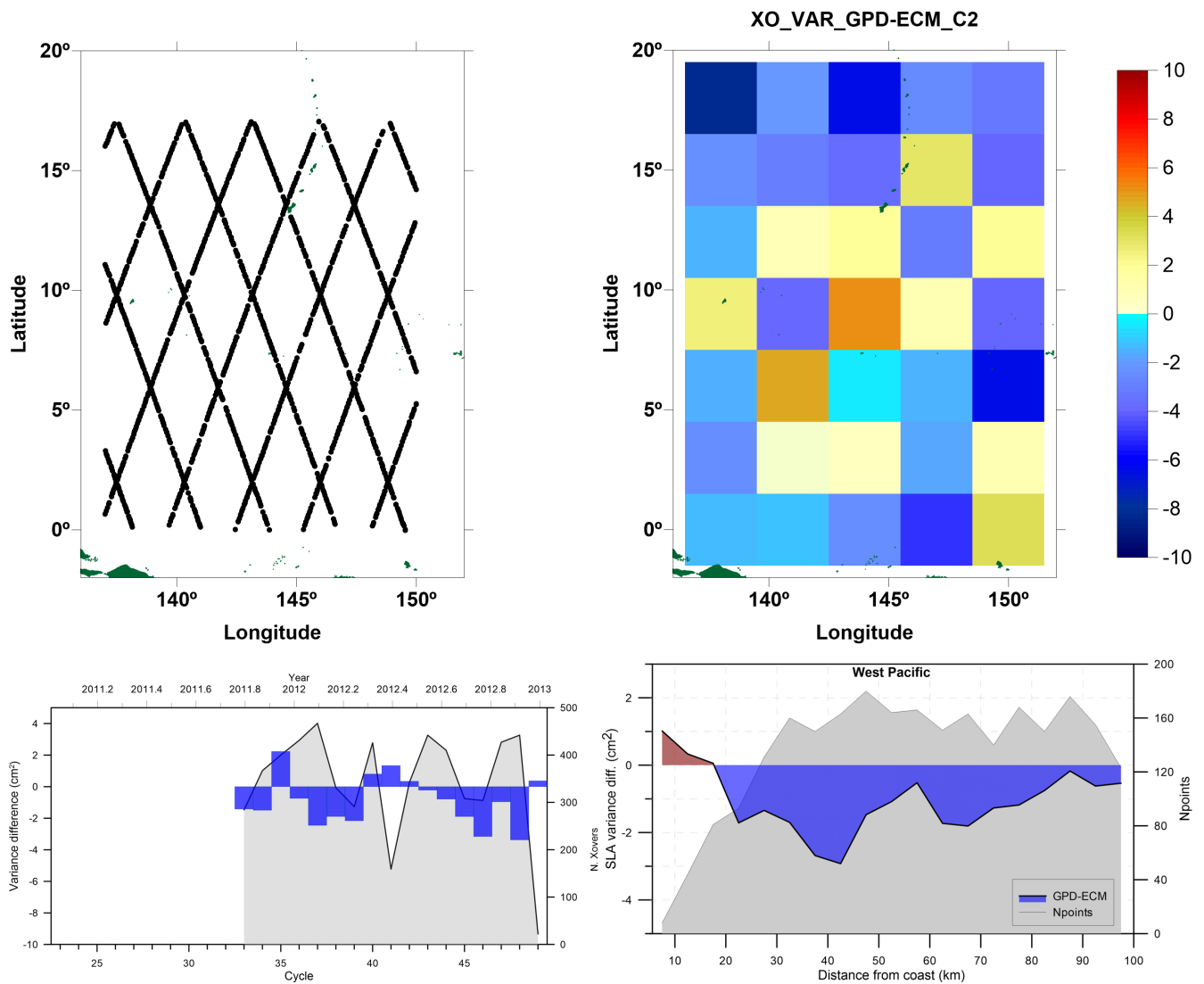


**Figure 7.10** Top left: location of analysed CS2 passes over the West Pacific ROI. Top right: spatial pattern of SLA variance differences at crossovers (GPD- ECMWF Op). Bottom left: SLA variance difference at crossovers (mean cycle values), between SLA computed with GPD+ and that computed with ECMWF-Op. Bottom right: SLA variance differences (GPD-ECMWF-Op), function of distance from coast.

### 7.2.3 WTC differences at crossovers between CS2 and J2

Figure 7.11 illustrates the impact on WTC (GPD+ or ECMWF Op. model) crossover differences with respect to J2 for each region of interest. It can be observed for most ROI that GPD+ leads to a decrease in SLA variance at crossovers when compared with the ECMWF Op. WTC.

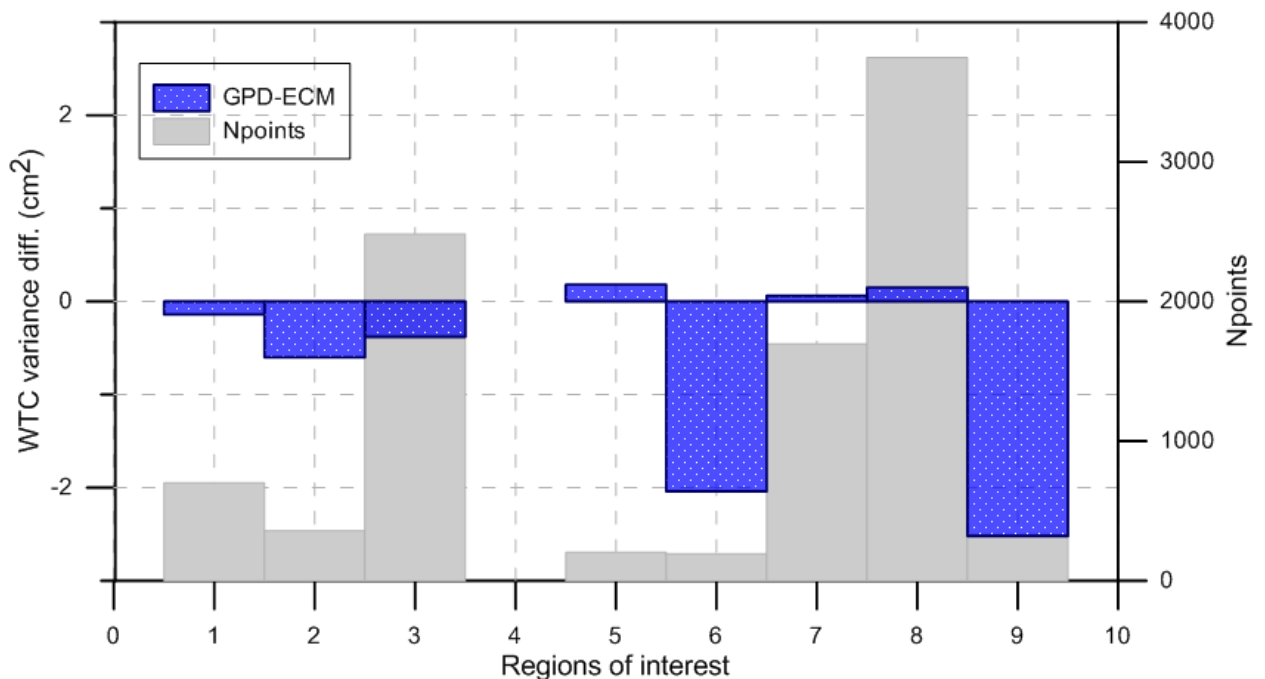


**Figure 7.11 WTC variance difference at C2/J2 Xovers with  $\Delta T < 180$  min (GPD-ECMWF-Op), for the various ROI: (1) Agulhas, (2) Central Pacific, (3) East Pacific, (4) Harvest, (5) Indonesia (6) North Indian Coast, (7) North Sea (8) Northeast Atlantic (9) West Pacific.**

### 7.2.4 Comparison with GNSS

Figure 7.12 shows the RMS differences between WTC from GNSS at coastal stations and those from ECMWF-op model (blue) and from GPD+ (red) at nearby altimetric points for the various ROI are shown. The number of GNSS stations used for each ROI is: Agulhas (1), Harvest (35), Indonesia (4), North Indian Coast (8), North Sea (57), Northeast Atlantic (41) and West Pacific (3). For the Central Pacific and East Pacific, no analyses are shown since these are open ocean regions, without any coastal GNSS station.

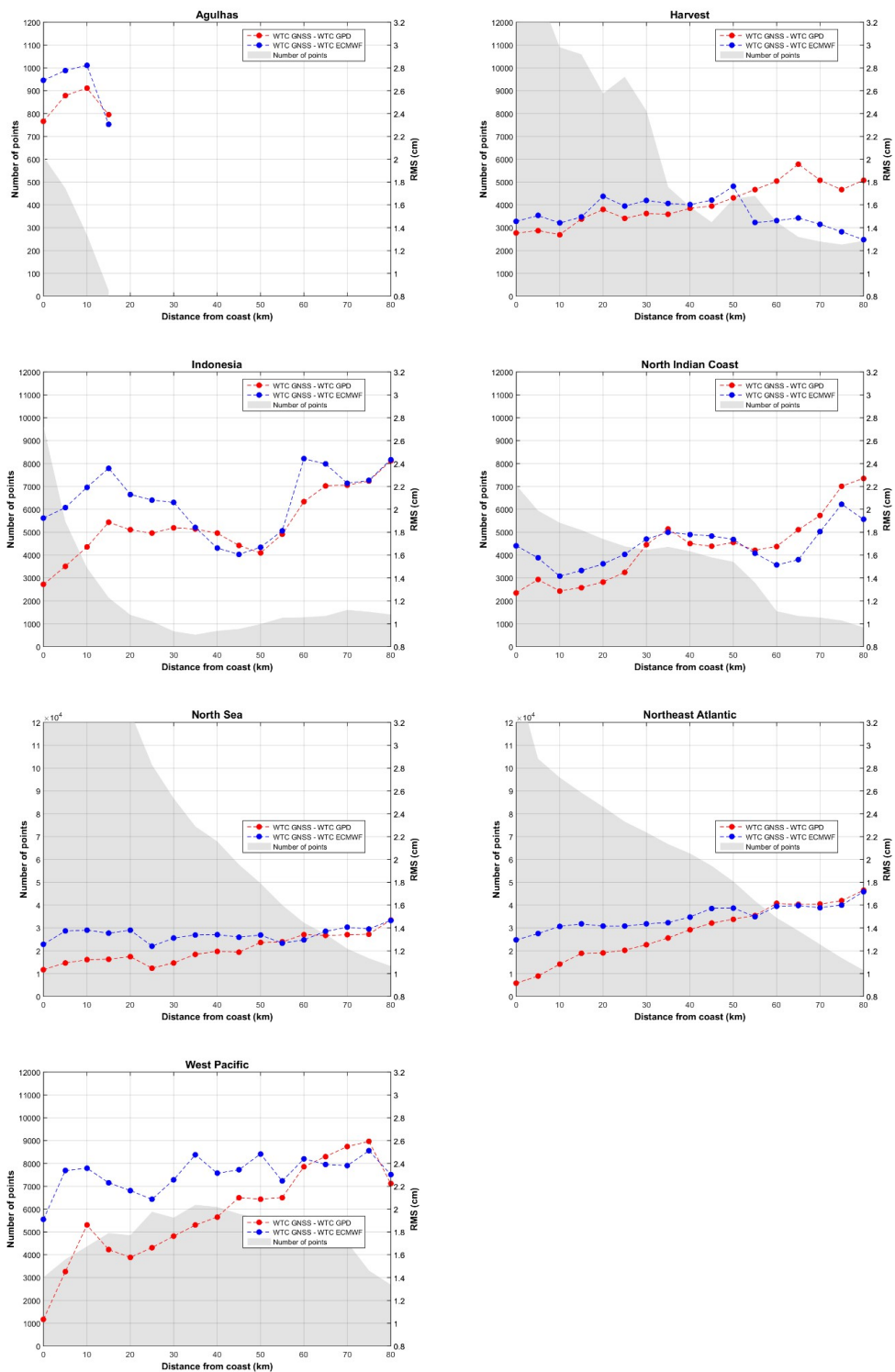


Figure 7.12 RMS differences between WTC from GNSS at coastal stations and those from ECMWF op model (blue) and from GPD+ (red) at nearby altimetric points. From top to bottom and left to right, results for the following ROI are shown (inside brackets the number of stations used for each corresponding ROI): Agulhas (1), Harvest (35), Indonesia (4), North Indian Coast (8), North Sea (57), Northeast Atlantic (41) and West Pacific (3). For the Central pacific and East Pacific, no analyses are shown since these are open ocean regions, without any coastal GNSS station.

## 7.2.5 Summary of Results

This work has been carried out during the first year of the project, a period for which no improved SLA at 20 Hz were available for the CS2 L1B test data set selected for use in the project. As the purpose of WP7000 was to deliver improved WTC for later use in the project, validation was carried out with 1 Hz SLA extracted from RADS and from CS2 COP. Since similar results were obtained in both cases, only those obtained with RADS data have been shown.

It was found difficult to identify robust validation criteria for this analysis as most ROI are small and the period of analysis spans only two years. In regions such as Harvest data are too few for some of the presented results to be significant.

Additional difficulties were found related with the use of 1 Hz SLA interpolated to 20 Hz points to validate the WTC generated at 20 Hz. When using SLA variance analyses, results are sensitive to adopted SLA and SLA editing criteria, as noisy SLA 1 Hz values spread when interpolating data to 20 Hz.

The crossover analysis with respect to J2 is limited by the poor J2 track spacing. In spite of that, GPD+ leads to a consistent decrease in SLA variance at crossovers when compared with the ECMWF Op. WTC for most ROI.

In spite of all limitations, analyses indicate that, as for the global results presented in Fernandes and Lázaro (2016), when compared to the ECMWF Op. model GPD+ leads to SLA variance reduction at crossovers and in particular near the coast (Figure 7.2 to Figure 7.10) for most ROI.

Other diagnostics such as WTC differences with respect to J2 and with respect to GNSS confirm that overall GPD+ is closer to these accurate WTC datasets and therefore an improved correction in comparison with the ECMWF model. The comparison with GNSS also shows no evidence of land contamination in the GPD+ WTC.

These results are in agreement with the independent validation performed by CLS, shown in Section 2.7.

## 7.3 WTC for Sentinel-3A

### 7.3.1 Summary of approach

Launched on February 16, 2016 to a sun-synchronous orbit (inclination 98°.65) at 814 km altitude, 27-days repeat cycle, Sentinel-3A carries a dual channel (23.8 GHz and 36.5 GHz) MWR, similar to that of Envisat, for the retrieval of the wet tropospheric correction. In view to complement the studies carried out for CS2 (Section 7.2), this study aims at: i) contributing to the evaluation of S3A MWR-based WTC through an independent assessment; ii) to derive a first version of a GPD+ WTC for S3A.

S3A data used in this study are the L2 Non Time Critical (NTC) products made available in RADS in February 2018, SRAL/MWR L2 IPF (SM-2) version 06.07 from Processing Baseline 2.27. The S3A baseline MWR WTC is computed from a neural network algorithm based on 5 inputs (CLS, 2011): brightness temperatures at 23.8 GHz and 36.5 GHz, Ku-band ocean backscattering coefficient, sea surface temperature and atmosphere temperature lapse rate.

The data spans 22 months - from cycle 01 (Mar. 01, 2016) to cycle 26 (Jan. 16, 2018). A similar study conducted for a shorter period of 10 months and a previous data version (Baseline 2.15) has been published on Fernandes and Lázaro (2018). In essence, the present study confirms the results of the former, now withdrawn from a larger dataset (22 versus 10 months).

The S3A products also include the Composite wet tropospheric correction (CLS, 2011), based on both radiometer and model-based corrections over areas where the radiometer WTC is missing or

invalid due to the proximity of land (coastal areas and/or radiometer gaps in open oceans) (CLS, 2011, Mercier et al., 2004). A first assessment of this correction is also performed.

The assessment of S3A MWR NTC data has been performed by means of the following analyses:

- Comparison with other MWR: Global Precipitation Measurement (GPM) Microwave Imager (GMI) and Jason-3 (J3) MWR;
- Comparison with WTC from GNSS at coastal stations;
- Comparison with a GPD+ WTC computed only with third party data, with the ECMWF operational model and the Composite WTC;
- Sea level anomaly variance analysis.

GMI is a dual-polarization, multi-channel, conical-scanning, passive microwave radiometer on board the GPM satellite, launched on February 2014. It has been designed with a strict calibration accuracy requirement, enabling the instrument to serve as a microwave radiometric standard. GPM flies on a non sun-synchronous orbit at 407 km altitude and 65° inclination. Its orbit plane completes half (180°) rotation relative to the Sun every 41.1 days. The spacecraft undergoes yaw manoeuvres every 40 days to compensate for the Sun's changing position and prevent the side of the spacecraft facing the Sun from overheating.

The GMI data used in this study are gridded products of total column water vapour (TCWV), in binary format provided by Remote Sensing Systems (RSS, <http://www.remss.com/>). Two 0.25°×0.25° global grids per day are provided, one containing the ascending and the other the descending GPM passes. The RSS products based on the Version-8.2 algorithm and the Radiative Transfer Model have been used (Meissner et al., 2012). The WTC has been computed from these TCWV products using the expression by Stum et al. (2011). Further details can be found in Fernandes and Lázaro (2018).

Jason-3 carries the Advanced Microwave Radiometer 2 (AMR-2), operating at 18.7, 23.8, and 34 GHz. In comparison with the dual-frequency MWR aboard the ESA missions, the additional low frequency channel improves the WTC retrieval, particularly by adding the ability to reduce land effects near the coast. With respect to AMR aboard Jason-2, AMR-2 includes improvements in instrument thermal control and stability. Jason-3 is the first altimeter mission to implement special spacecraft cold sky calibration manoeuvres (CSCM), combined with vicarious on-Earth ocean and land target references, for improving the long-term climate calibration of the radiometer (Brown and Islam, 2017). The J3 data used in this study are those available in RADS.

In the sea level anomaly variance analyses, S3A SRAL data and all required range and geophysical corrections to compute SLA were extracted from RADS.

In the comparisons with other sensors, only S3A points considered valid by the GPD+ algorithm are used, i.e., contamination by e.g. land, ice and rain are removed. Figure 7.13 illustrates invalid points for cycle 06: 28.0% of all points and 10.2% of the points with valid SLA.

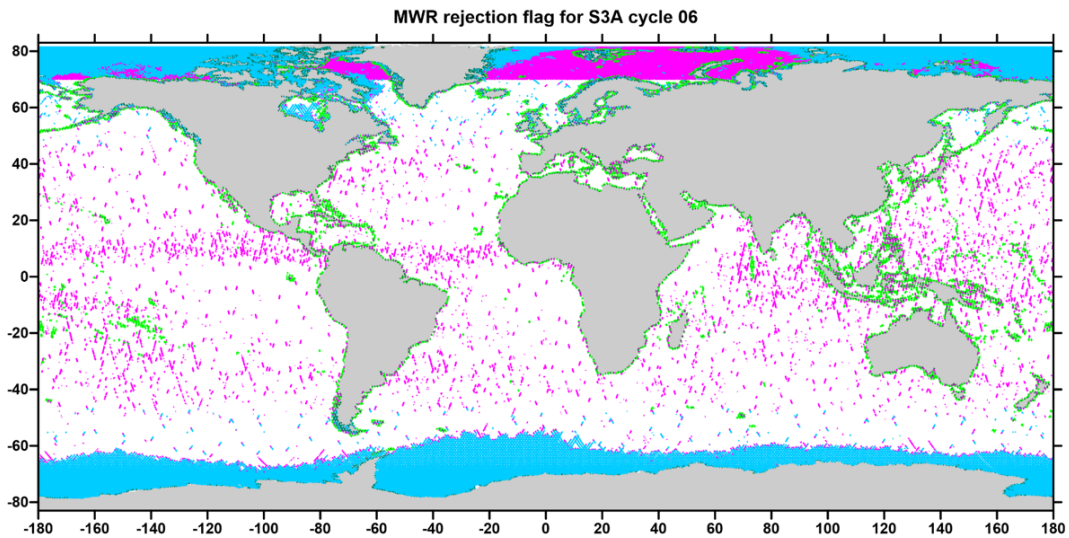


**Figure 7.13 S3A points for cycle 06 with invalid MWR observations: green – land contamination; blue – ice contamination; pink – rain, outliers or additional condition such as all points above latitude 70°N or below 70°S.**

For this study, two types of GPD+ WTC have been computed for S3A: (1) all points are estimated using only external data sources i.e., wet path delays derived from a set of more than 800 GNSS stations and WTC from scanning imaging MWR on board various remote sensing missions, hereafter designated GPD1; and (2) using all data including the S3A MWR measurements, provided they are valid, and only computing new estimates for the invalid MWR points, hereafter named GPD2. GPD2 is the “usual” GPD+ WTC for satellites such as S3A, preserving the valid observations from the on-board MWR, while GPD1, being independent from the S3A MWR, can be used as an additional validation tool for this new instrument. GPD2 required the tuning of the criteria for detecting valid/invalid S3A MWR observations

## 7.3.2 Results

In the comparisons with other sensors presented in this section, the wet path delay (WPD, symmetric of WTC) has been used. All mentioned scale factors, offsets and RMS of differences refer to WPD.

### 7.3.2.1 Comparison with GMI

Figure 7.14 to Figure 7.18 present the results for the comparison between S3A MWR and GMI. This comparison is performed on S3A/GMI match points with a time difference  $\Delta T < 45$  min and distance  $\Delta D < 50$  km (Fernandes et al, 2018). The criteria adopted in the selection of match points is the same as in Fernandes et al. (2013a).

Figure 7.14 illustrates the match points between GPM and S3A for the 22-month period of this study. The colour scale represents WPD differences between GMI and S3A in cm. Red colours mean that GMI measurements indicate wetter conditions than S3A, while blue colours indicate the opposite. The overall mean and RMS of the differences  $WPD(GMI) - WPD(S3A)$  are 0.19 cm and 0.92 cm, respectively.

Figure 7.15 illustrates the scattergram of the WPD from S3A against the WPD from GMI (right) and against WPD difference between the GMI and S3A (left), using the whole set of match points (~455000 points). The scale factor is 1.004 and the offset is 0.13 cm, indicating a very good overall

agreement between the two radiometers, with the GMI measurements indicating slightly wetter conditions than S3A.

The overall pattern of the WPD differences in Figure 7.14 seems to indicate that at the low latitudes, where the WPD is larger, GMI measures wetter than S3A, while at the extreme southern latitudes, corresponding to regions of low WPD values, there is a tendency for GMI to measure drier than S3A. However, the scale factor (1.004) and small offset (0.13 cm) reveal a very good overall match between the two sensors, also demonstrated by the very small scatter of the scatter plot of the two WPDs illustrated in Figure 7.15.

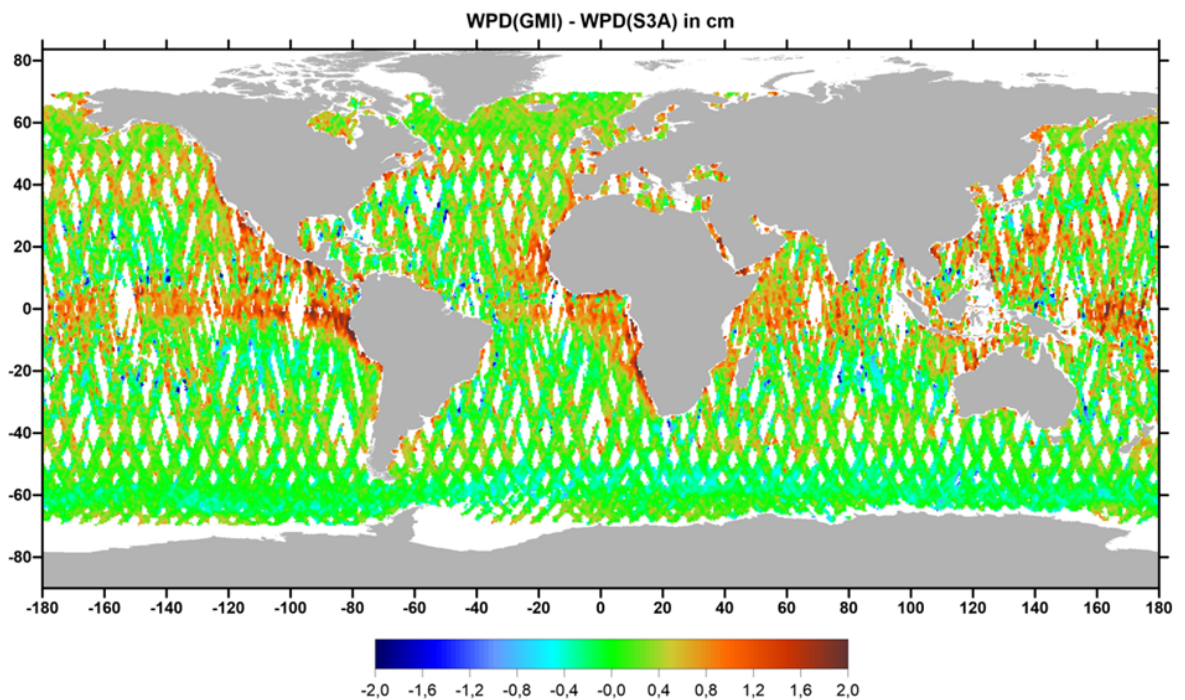


Figure 7.14 Spatial coverage of match points between S3A and GMI with time difference  $\Delta T < 45$  min and distance  $\Delta D < 50$  km, for S3A cycles 01-26, used in this study (~455000 points). Colour scale indicates WPD differences between the GMI and S3A in cm.

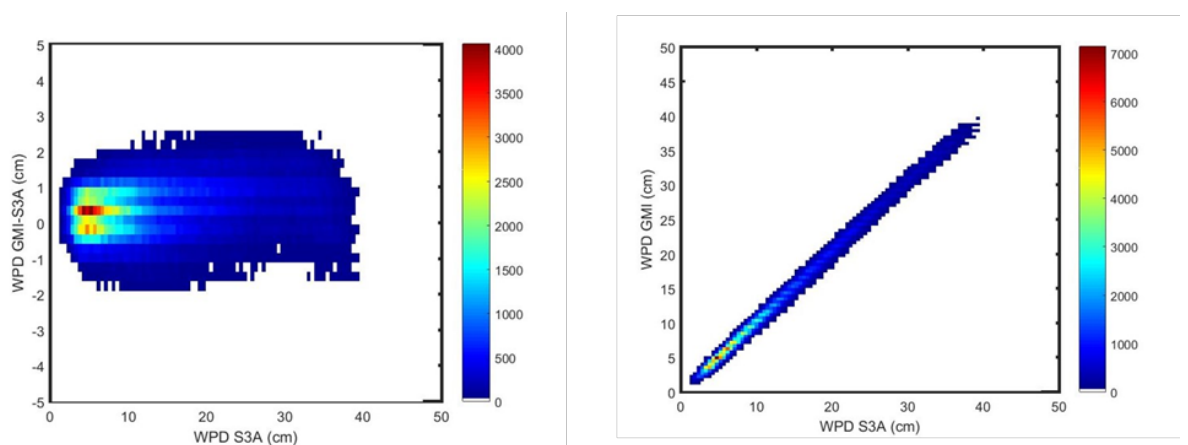
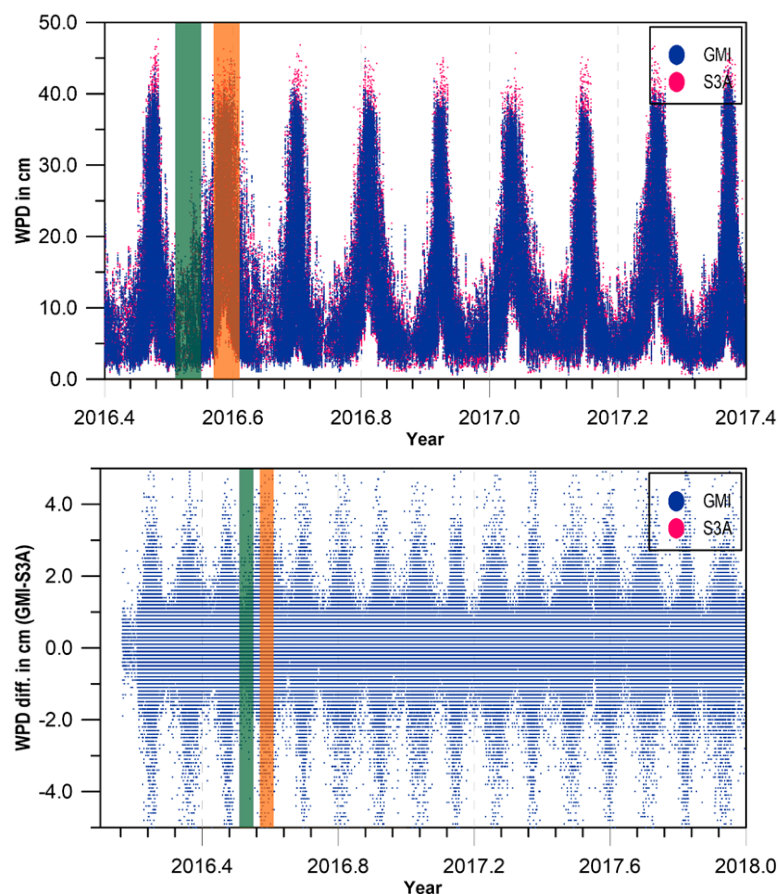


Figure 7.15 WPD from S3A versus WPD from GMI (right) and versus WPD GMI - WPD S3A (left) for the whole set of match points (~455000 points). Scale factor: 1.004; Offset: 0.13 cm.

Figure 7.16 illustrates the time evolution of the WPD from both sensors and the respective differences. The top panel of Figure 5 represents the time evolution of the WPD from GMI (blue) and S3A (pink) while the bottom panel shows the corresponding WPD differences between GMI and S3A.

The observed strong periodic pattern of 41 days is the most curious feature of the comparison between GMI and S3A. When analysing how the spatial pattern of the match points changes with time (Figure 7.17 and Figure 7.18), it can be observed that there are periods for which all match points between the two sensors are located only at high latitudes. An example of these periods is the one corresponding to the green bar in Figure 7.16, to which the points with the same green colour in Figure 7.17 (all above latitude 50°N or below latitude 50°S) correspond. During these periods, since the WPD at high latitudes is low (only a few cm) and with low variability, the differences between the two sensors are very small, with absolute values of less than 1 cm. On the contrary, during periods such as the one corresponding to the orange bar in Figure 7.16 the match points are located at the low latitudes, between  $\pm 50^\circ$  (orange points in Figure 7.17). Over these periods, the WPD reaches higher values (up to 40–50 cm) and has larger variability, inducing larger differences between the two sensors. These results are a clear demonstration of the impact of data sampling in this type of study, which, if not properly accounted for, can lead to misinterpretations.

When daily and 27-day RMS differences are computed (Figure 7.18), the same periodic pattern is shown, now at 82 days, and seem stable. This 82-day periodic pattern occurs due to the fact that S3A orbit is Sun-synchronous, while GPM orbit is not. Due to its orbit characteristics, the GPM orbital plane takes 82 days to complete a full rotation with respect to the Sun and therefore with respect to the S3A orbital plane, explaining the observed periodic signal.



**Figure 7.16 Top panel: time evolution of the WPD from the GMI (blue) and S3A (pink). Bottom panel: time evolution of WPD differences between GMI and S3A. Colour bars refer to periods when the**

GMI/S3A match points are all located at high latitudes (green points in Figure 7.3.5) or low latitudes (orange points in Figure 7.3.5) to which correspond smaller or larger WPD variability.

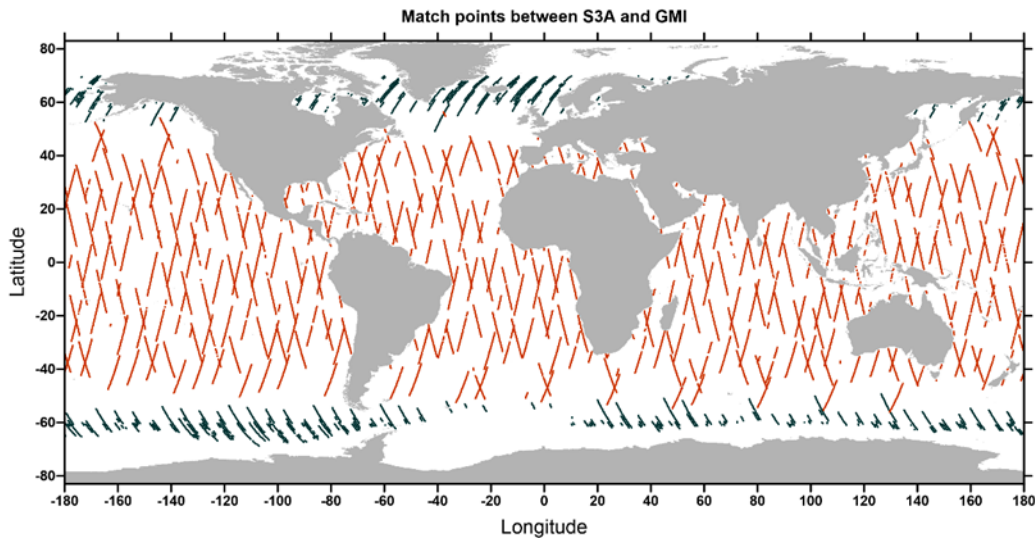


Figure 7.17 Match points between GMI and S3A. Colours correspond to different time periods, indicated in Figure 7.3.4 by the corresponding colour bars

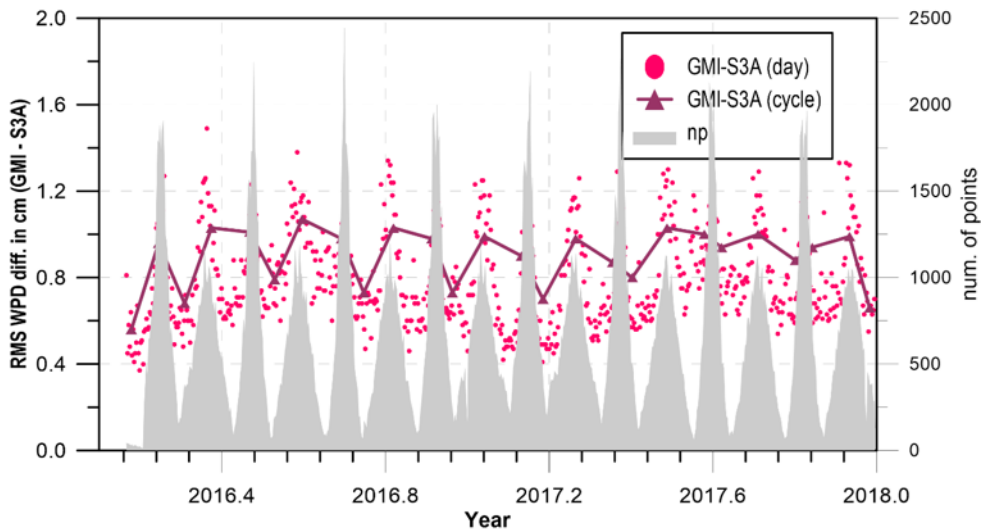


Figure 7.18 Time evolution of daily and 27-day RMS of the WPD differences between GMI and S3A.

### 7.3.2.2 Comparison with J3

To compare the WPD from S3A with that from Jason-3 the differences between the corresponding WPD at the crossovers between these missions have been computed. For this purpose, crossovers between S3A and Jason-3 with time difference  $\Delta T < 180$  min have been computed.

Figure 7.19 illustrates the spatial pattern of the WPD differences between J3 and S3A. The mean and RMS differences between J3 and S3A are  $-0.6$  cm and  $1.3$  cm respectively, indicating that on average J3 measures drier than S3A by about  $0.6$  cm.

Figure 7.20 shows the scattergrams of the WPD from S3A against the WPD from J3 (left panel) as well as against the corresponding WPD differences between J3 and S3A (right panel). The scale factor and offset are 1.01 and  $-0.76$  cm, respectively. Both Figures 7.3.7 and 7.3.8 indicate that J3 measures drier than S3A by about 0.8 cm.

Figure 7.21 depicts the time evolution of the WPD differences between J3 and S3A (daily and 27-day RMS values in centimetres). These results indicate that in spite of the small span of the data, there is an overall agreement between these two sensors.

The statistical parameters of the comparisons between S3A and J3 MWR are in agreement with the results presented in Fernandes and Lázaro (2016) and further work by these authors (Fernandes and Lázaro, 2018), comparing the same sensors with the SSM/I and SSM/IS sensors, which also indicate that Jason-2 and J3 measures drier than the latter sensors by about 0.6 cm and 1 cm, respectively.

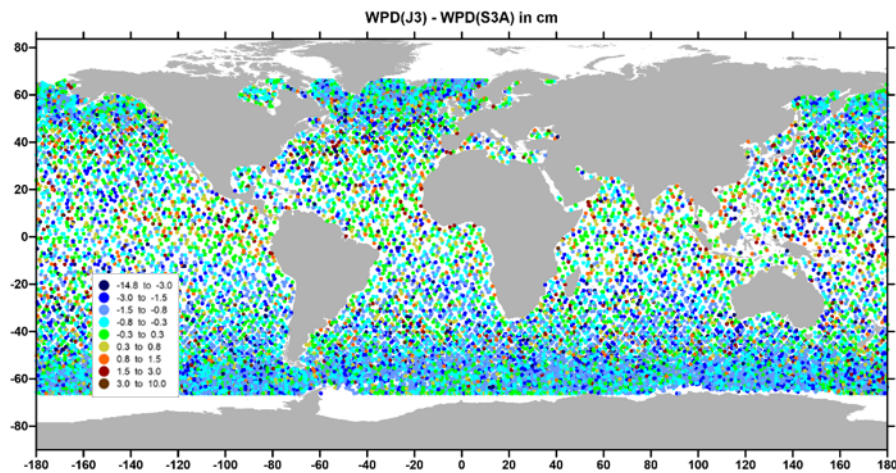


Figure 7.19 Spatial coverage of crossovers between S3A and J3 with time difference  $\Delta T < 45$  min and distance  $\Delta D < 50$  km, for S3A cycles 01-26, used in this study (~27500 points).

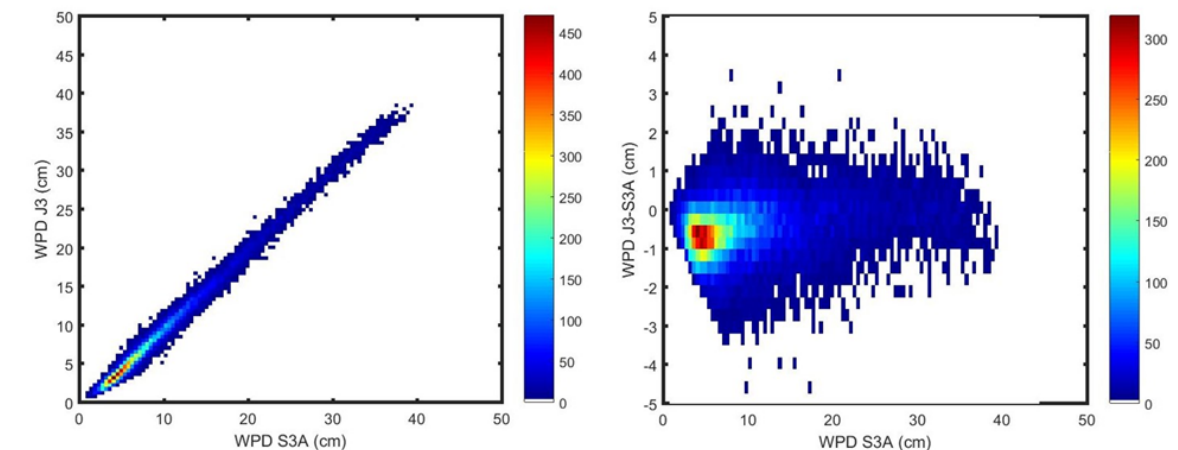


Figure 7.20 WPD from S3A versus WPD from J3 (left) and versus WPD J3 - WPD S3A (right). Scale factor: 1.01.

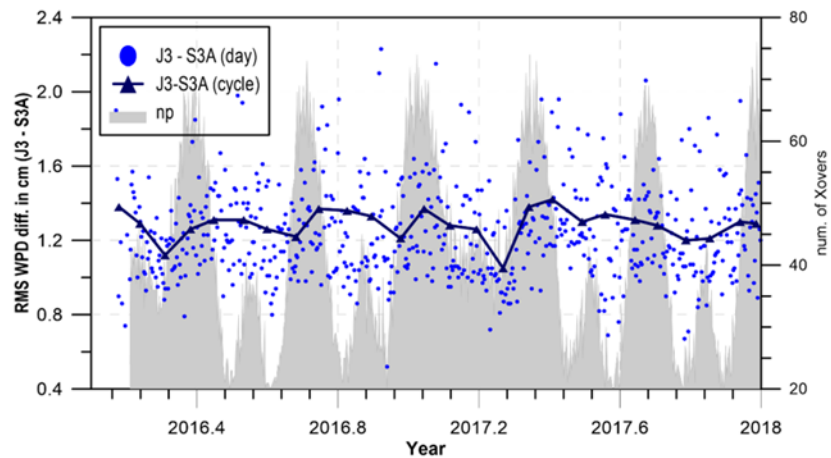


Figure 7.21 Time evolution of daily and 27-day RMS of the WPD differences between J3 and S3A. RMS  $WTC(J3) - WT(S3A) = 1.3$  cm.

### 7.3.2.3 Comparison with an Independent GPD+ WTC, ECMWF Operational Model and the Composite WTC

As mentioned above, two types of GPD+ WTC have been computed for S3A cycles 04 to 26: (1) GPD1, using only third-party data; and (2) GPD2, using all data including the S3A MWR. GPD1 WTC can be used as an external dataset, allowing an independent assessment of the S3A MWR WTC. In the second case, GPD2 preserves the S3A MWR-derived WTC, whenever flagged as valid. Only new estimates are computed for the invalid points, using all available observations. The comparison between these two WTC and between them and the S3A MWR-derived WTC (the latter comparison being performed only at valid MWR observations) gives further insight into the quality of the MWR observations, since it is performed using all S3A points and not only a subset (match points), as is the case of the comparison with the other MWR sensors.

Figure 7.22 shows an example where the different WTC from S3A MWR, ECMWF operational model, GPD1 (top) and GPD2 (bottom) are compared for S3A pass 340, cycle 06. Figure 7.23 shows the corresponding plots for pass 462, same cycle. In these plots, only points with valid SLA are shown. Ice, land, and rain contamination can be observed in the MWR-derived WTC, more pronounced in pass 462 than in pass 340.

In these figures, it can be observed that GPD1 and GPD2 are very similar, in spite of the fact that GPD1 does not use any observations from the S3A on-board MWR. It can also be concluded that, in regions with a valid MWR, the ECMWF operational model values are also very close, the main difference being that some, though important, small scale features are missing. These figures are a clear illustration of typical S3A MWR-derived WTC, where invalid observations can be observed near the coast, at high latitudes and at low latitudes, associated with heavy rain events.

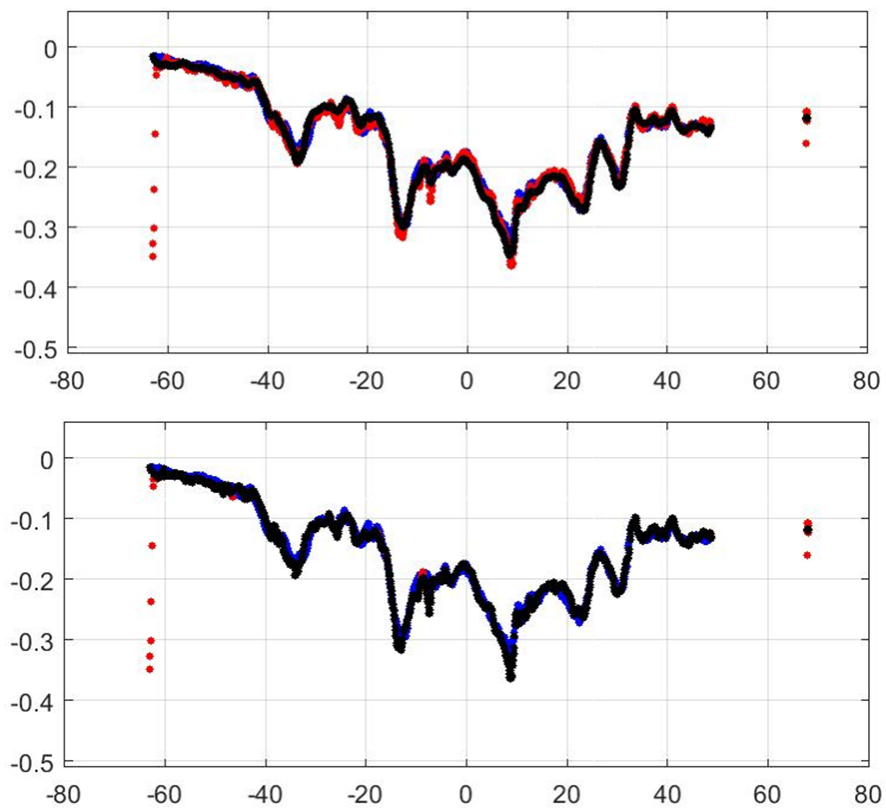
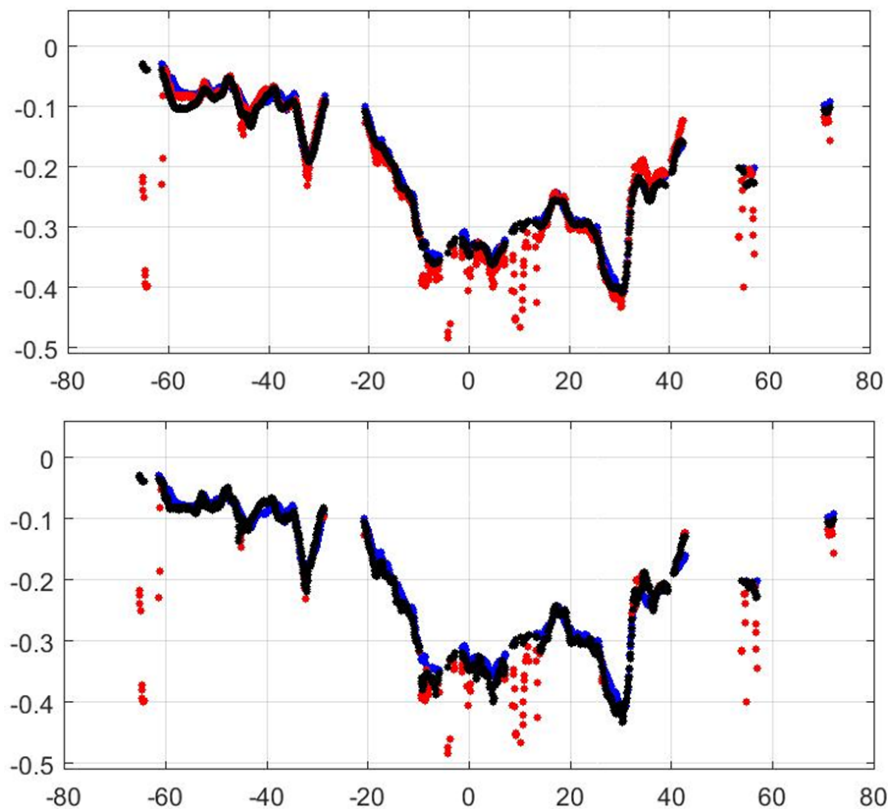


Figure 7.22 WTC (in m) for S3A pass 340, cycle 06: ECMWF (blue dots), MWR, (red dots) and GPD+ (black dots), GPD1 in the top plot, GPD2 in the bottom plot, function of latitude.



**Figure 7.23 WTC (in m) for S3A pass 462, cycle 06: ECMWF (blue dots), MWR (red dots), and GPD+ (black dots), GPD1 in the top plot, GPD2 in the bottom plot, function of latitude.**

Figure 7.24 illustrates the spatial distribution of the RMS of the WPD differences (cm) between GPD1 and S3A MWR for the whole period of study (cycles 01 to 26). This indicates that the largest differences between these two WTC are associated with regions with the largest WTC variability and ocean circulation patterns. Large differences also occur in some coastal regions, a possible indicator that some noisy MWR observations may still be present, in spite of the fact that all MWR measurements at distances from coast less than 30 km have been removed.

Figure 7.25 shows the time evolution of the RMS of the differences between the S3A MWR WTC and those from GPD1 and ECMWF, only for the valid MWR points. Note that for these points, GPD2 is equal to the MWR, so these differences are not shown. This evidences that the S3A WPD is closer to GPD1 (RMS difference less than 1 cm) than to the ECMWF model (RMS difference 1.3 cm). The time evolution of these differences, shown as 27-day RMS values in Figure 7.25, is stable, with an expected small seasonal signal.

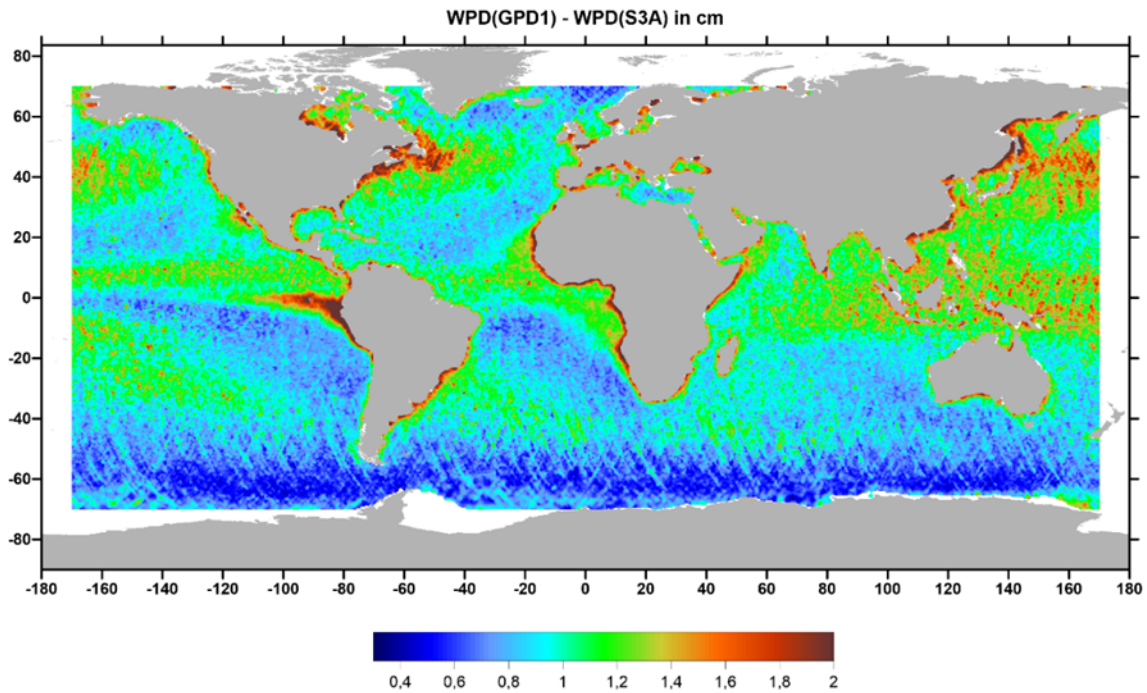


Figure 7.24 Spatial distribution of the RMS values of the WPD differences (cm) between GPD1 and S3A MWR, for cycles 01 to 26.

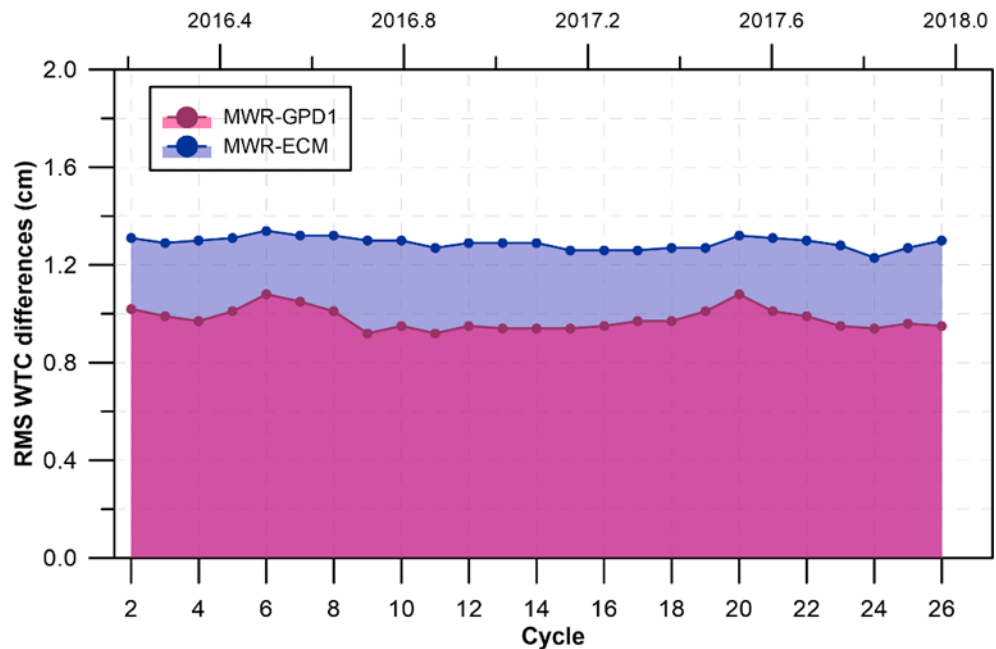


Figure 7.25 Time evolution of the RMS differences between the S3A MWR-based WTC and those from GPD1 and ECMWF.

Aiming at inspecting the impact of the S3A WTC on the computation of SRAL-derived sea level anomalies in comparison with other WTC such as ECMWF, GPD1, and GPD2, various SLA variance analyses have been performed that can be divided into: (1) SLA along-track variance differences (weighted mean values per cycle and at collocated points, function of distance from coast and function of latitude); and (2) SLA analysis at crossovers (weighted mean cycle values and spatial pattern). The results are shown in Figure 7.26 to Figure 7.28.

The SLA variance analyses at crossovers presented in Figure 7.26 (top panel) indicate that the S3A MWR reduces the variance both with respect to ECMWF and GPD1, the first reduction being significant (mean cycle values of 1.1–1.5 cm<sup>2</sup>), while the latter (not shown, inferred from the same figure) is quite small (mean cycle values of 0.1–0.3 cm<sup>2</sup>).

While the results from the variance analysis at crossovers indicate that the S3A MWR consistently reduces the SLA variance with respect to the WTC that only incorporates non-collocated radiometers (GPD1) and that the latter increases the variance with respect to the GPD+ WTC that makes use of the S3A MWR (GPD2), the same does not happen in along-track SLA variance analysis. In the along-track SLA variance differences, computed cycle by cycle (Figure 7.28, bottom panel), GPD1 leads, in most cycles, to a slightly larger SLA variance reduction with respect to ECMWF than the GPD+ WTC that incorporates the S3A MWR (GPD2). This is also demonstrated in Figure 7.29, which presents the along-track variance differences function of latitude and distance from coast. This figure shows that, in comparison with GPD2, apart from some high latitude bands, GPD1 leads to a slightly larger SLA variance reduction with respect to ECMWF. In this comparison, all points with valid SLA have been analysed. This result is more evident in the SLA variance analysis function of distance from coast (Figure 7.28, bottom panel), where GPD1 consistently reduces the variance with respect to both MWR and GPD2.

This result is not expected since, in all previous analyses performed by the authors, the WTC derived from observations of the on-board MWR always reduced the SLA variance with respect to the WTC that only uses non-collocated observations, in all types of diagnoses and when only valid MWR points are selected. As an example, Figure 7.27 illustrates for Envisat the same variance analysis shown in Figure 7.26 for S3A, proving that, contrary to S3A, the GPD+ WTC that incorporates the valid observations from the Envisat radiometer consistently reduces the SLA variance with respect to the correction that only uses third party observations. Figure 7.27 also evidences the strong impact the increasing number of observations with time used in the GPD+ estimations has on the quality of these corrections, in particular on GPD1.

Similar analysis has been presented in Fernandes and Lázaro (2018) for J3 using the same period of observations analysed for S3A. These results indicate that although the overall performance of the S3A MWR seems good, improvements are still required to retrieve a WTC with the quality of that for Envisat or J3.

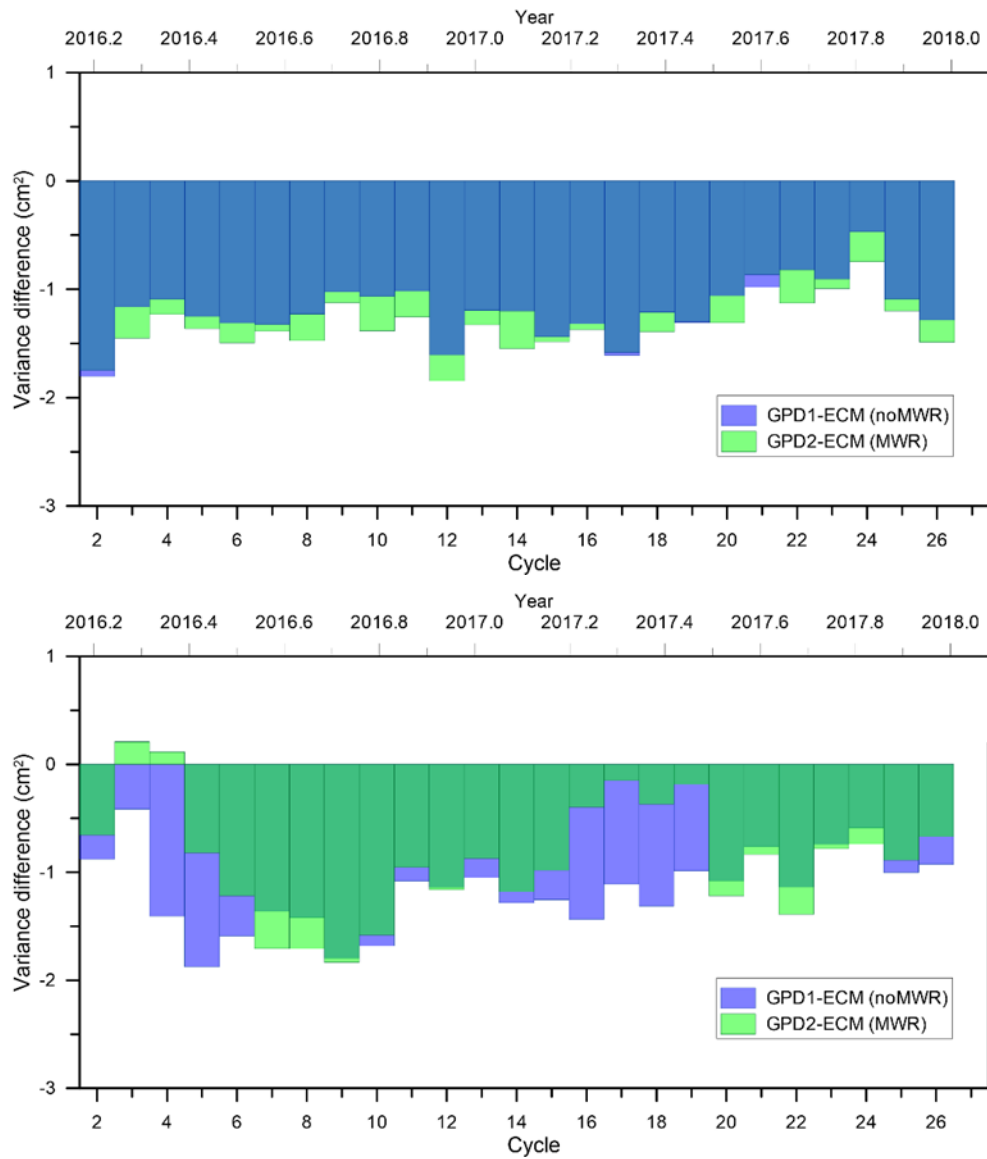


**Figure 7.26 Top panel: Variance differences at crossovers for each S3A cycle, between GPD1 (no S3A MWR used) and ECMWF and between GPD2 (with S3A MWR) and ECMWF. Bottom panel: SLA variance differences for each S3A cycle, between GPD1 (no S3A MWR used) and ECMWF and between GPD2 (with S3A MWR) and ECMWF.**

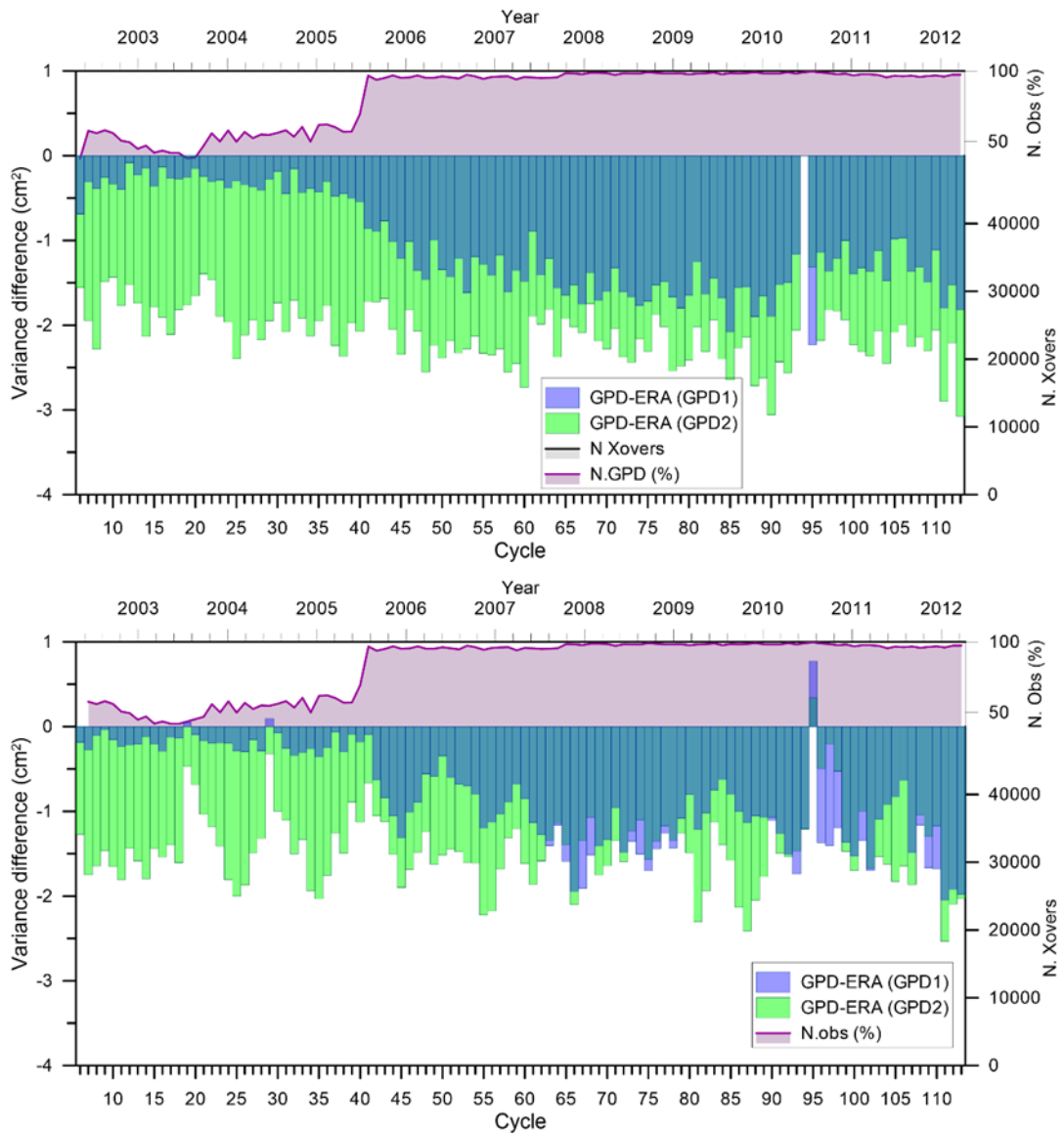


**Figure 7.27** Top panel: Variance differences at crossovers for each Envisat cycle, between GPD1 (no Envisat MWR used) and ERA Interim and between GPD2 (with Envisat MWR) and ERA Interim. Bottom panel: SLA variance differences for each Envisat cycle, between GPD1 (no Envisat MWR used) and ERA Interim and between GPD2 (with Envisat MWR) and ERA Interim.

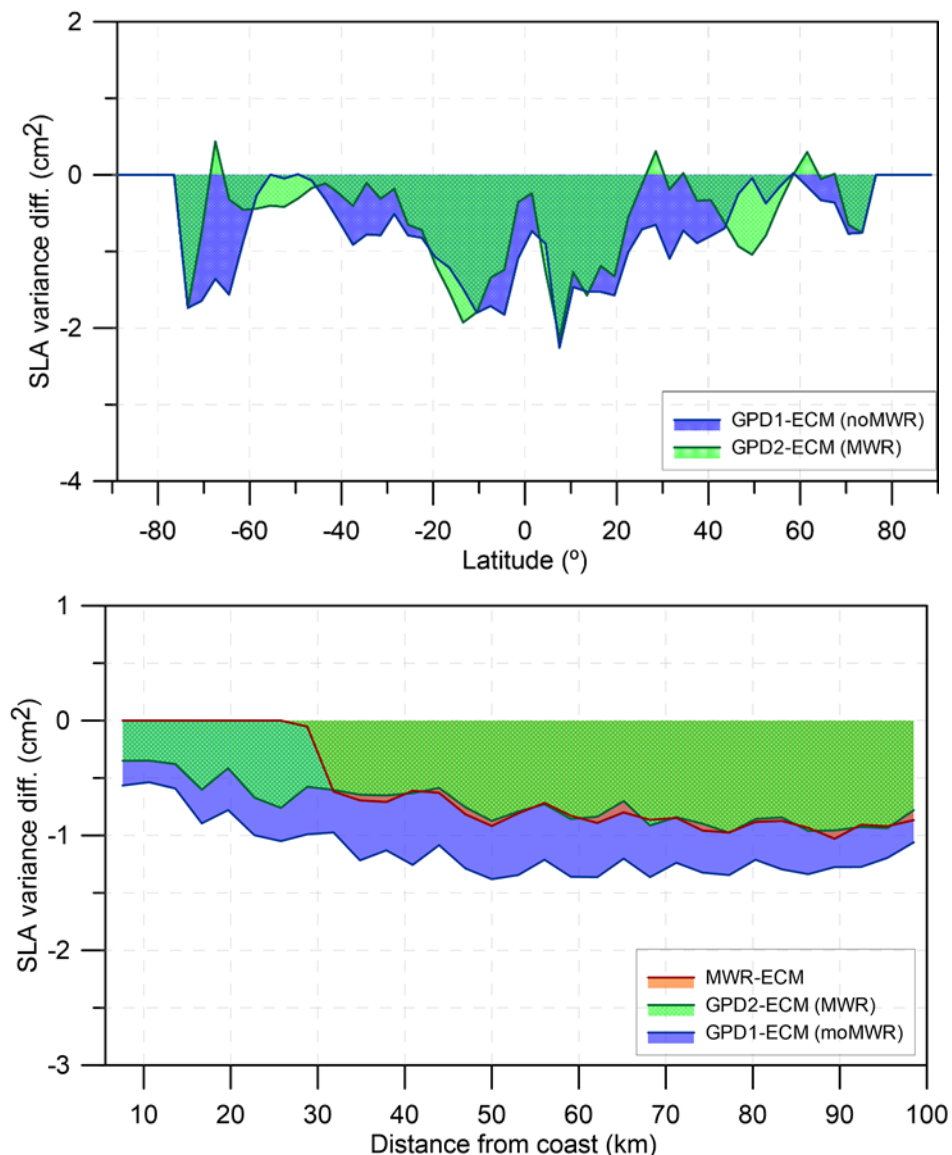


**Figure 7.28** Top panel: SLA variance differences function of latitude between GPD1 (no S3A MWR used) and ECMWF and between GPD2 (with S3A MWR) and ECMWF, over the period of S3A cycles 01 to 26, using all points. Bottom panel: SLA variance differences versus distance from coast for datasets computed using the WTC from MWR and ECMWF, GPD1 and ECMWF and GPD2 and ECMWF, over the period of S3A cycles 01 to 26. In the first case, only valid MWR points were selected while in the last two cases all points with valid SLA were used.

The S3A products used in this study also include the composite WTC. Although EUMETSAT (2017) indicates that this correction is not calibrated yet, a first assessment is also included here. Figure 7.29 depicts some representative examples of S3A passes where this WTC is compared against those from ECMWF, the S3A MWR, and GPD1. Figure 7.30 presents the set of passes with invalid Composite WTC for S3A cycle 06, showing that the correction is not available for 24% of the points.

The examination of the composite correction present on the analysed S3A products shows that the implementation of this WTC still has serious problems, depicted in Figure 7.29. Moreover, the correction is not present in a large percentage of points, e.g., 24% of the points with valid SLA for cycle 06. Like the GPD+ WTC, the composite WTC aims at generating a continuous correction, valid

everywhere, including the coastal zones and high latitudes. Also, similar to the GPD2 type of correction described in this paper, it also preserves the valid MWR values. The main difference between GPD+ and the composite WTC is that, on every invalid point, the former retrieves a new estimate by data combination of all available observations, while the latter uses the model values, adjusted to the closest valid MWR points. This requires robust criteria to detect valid/invalid MWR values, otherwise the model will be adjusted to spurious MWR observations, resulting in large biases or straight lines as shown in the same figure. Similar behaviour has been observed, though in only a few occurrences, in the composite correction present in the Archiving, Validation and Interpretation of Satellite Oceanographic data (AVISO) Corrected Sea Surface Heights (CORSSH) products of TOPEX/Poseidon (Fernandes et al, 2015). Due to potential implementation problems and the fact that GPD+ uses observations while the composite is solely based on model values, it has been shown that the GPD+ type of WTC is a significant improvement with respect to the composite WTC, particularly in the coastal zone.

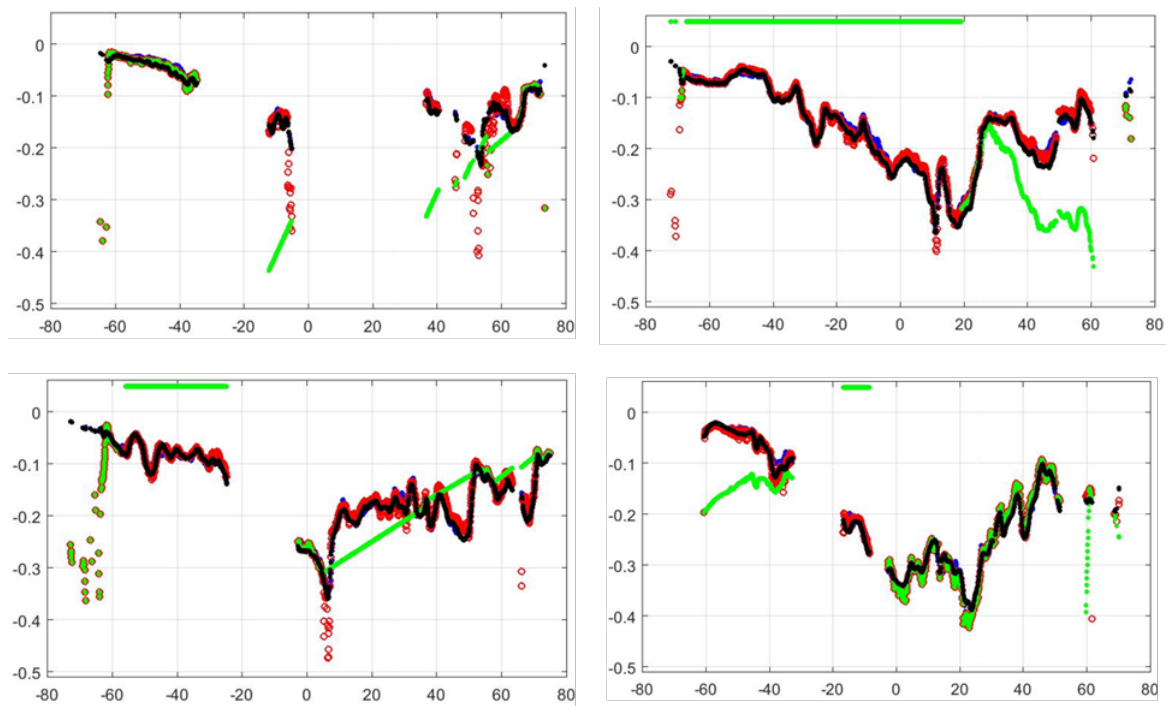


**Figure 7.29** From top to bottom and left to right: WTC (in m) for S3A cycle 06 passes 485, 553, 646 and 660, function of latitude. Shown WTC are: ECMWF (blue), MWR (red), GPD1 (black) and Composite (green).

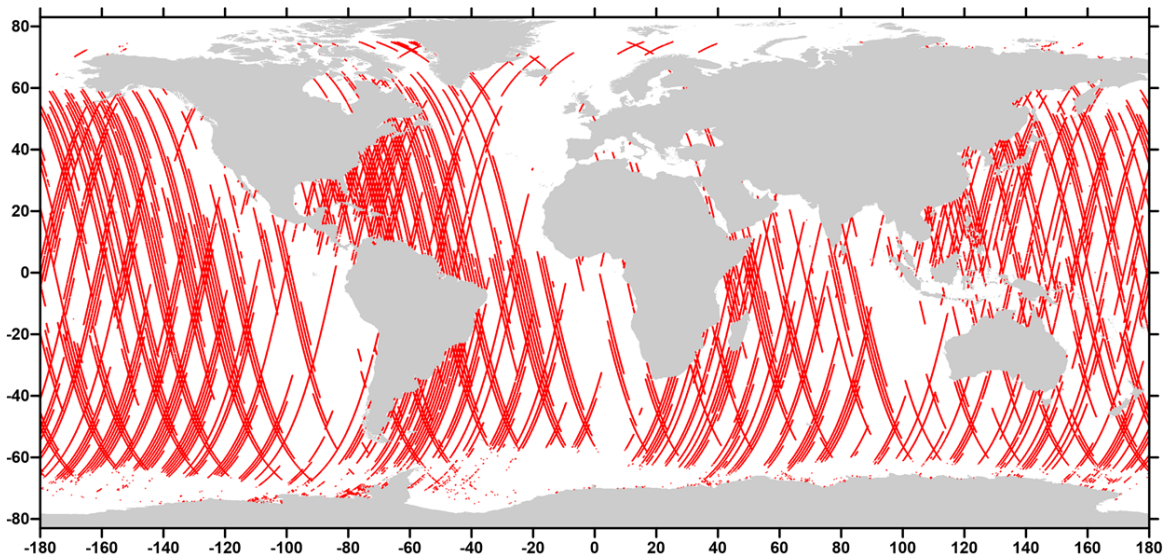


**Figure 7.30 Points with Composite WTC out of limits for S3A cycle 06 (24% of the points with valid SLA).**

#### 7.3.2.4 Comparison with GNSS

Zenith total delays (ZTD) from a network of 60 stations with a good global coverage have been used in this analysis. The details of this computation are given in Vieira et al. (2019), with only the main features being outlined here. These stations have been chosen to cover the various regions of the world with different WTC variability conditions (Figure 7.31) and to ensure that all zenith wet delays (ZWD) have been obtained using the same computation parameters, thus ensuring their long-term stability. All stations are located near the coast, at distances less than 100 km from the coast, and with an orthometric height <1000 m. The second condition aims at reducing the errors due to the height dependence of the WTC.

The GNSS provides accurate (4 - 6 mm) values of the ZTD, the sum of the dry and wet components of the tropospheric delay, at station height, while the quantity of interest in this study is the zenith wet delay (ZWD), symmetric with respect to the WTC, at sea (zero height) level. The latter is obtained from the ZTD at station level by subtracting the dry correction or zenith hydrostatic delay (ZHD) derived from the ECMWF sea-level pressure (SLP) field using the modified Saastamoinen model (Davis et al., 1985). ZHD and ZWD fields are further reduced to sea level using the expression by Kouba (2008), with modifications introduced by Fernandes et al. (2013b).

Using ZHD computed from ECMWF model fields according to Fernandes et al. (2013b), the ZWD can be determined from the GNSS-derived ZTD with an accuracy greater than 1 cm.

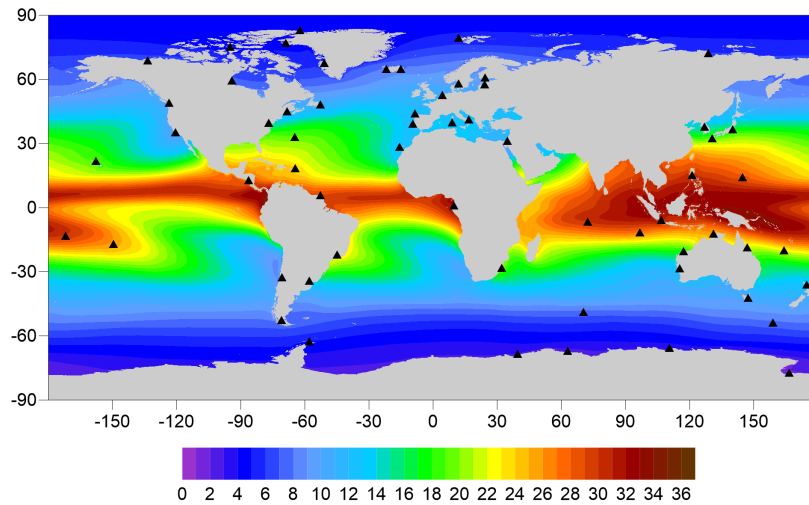


**Figure 7.31** Location of a set of 60 GNSS stations used in this study (adapted from Vieira et al. (2019)). The background map represents the RMS of wet path delay (WPD) in cm.

Figure 7.32 shows the non-collocated comparison with the WTC derived at 60 GNSS stations, as described above. In the comparisons with S3A MWR, only valid MWR observations, except those related with the criterion for land contamination, have been selected. This means that the observations flagged as invalid due to all other error sources (ice and rain contamination and outliers) have been removed. In the comparisons with GPD+ all points have been used. For each epoch of the S3A measurement, a WTC from each GNSS station is linearly interpolated in time. Then, the WTC differences from all stations are binned in classes of distance from coast and the corresponding RMSs are computed.

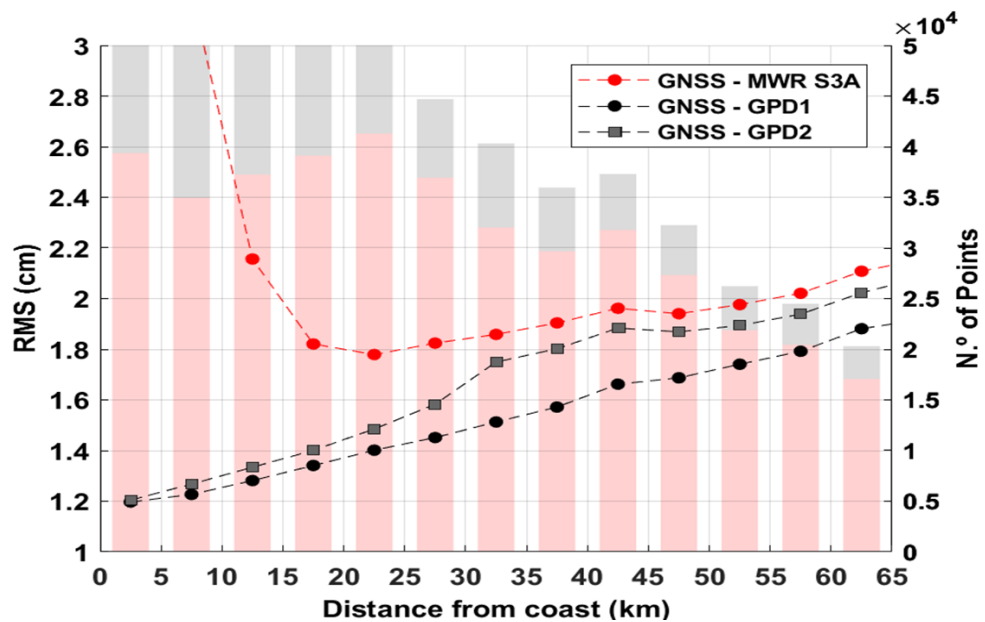


**Figure 7.32** RMS of differences between WTC from GNSS and WTC from S3A MWR (red), from GPD1 (back dots) and from GPD2 (grey squares) at coastal stations (Baseline 2.27, cycles 1 to 26). Land contamination occurs in the MWR up to 20-25 km from coast.

As the GNSS stations are over land and the MWR measurement points are over the ocean, the distance from coast is also directly related with the distance between the points under comparison. Therefore, the RMS of the differences between the GNSS-derived WTC and WTC from either the S3A MWR or GPD+ generally increase with the distance from coast, reaching a minimum at the maximum distance at which land contamination occurs in the MWR observations. Differences between the WTC computed at GNSS stations and derived from S3A MWR (or GPD+) are expected to increase as the distance to the GNSS station increases, as both measurements start to become decorrelated.

The RMS of the differences between the WTC from GNSS and the WTC (or the corresponding WPD) from S3A MWR shows that contamination is observed up to 20–25 km, in line with instrument specifications, the RMS of differences at these distances being about 1.8 cm. On the other hand, no land contamination is observed in the RMS of differences with respect to both GPD+WTC, being always smaller than those with respect to the MWR by about 0.3 cm, reaching 1.2 cm near the coast. This stresses the need for robust criteria to remove the land-contaminated MWR observations and the important role of solutions such as GPD+ in providing valid WTC in the coastal regions.

### 7.3.3 Summary of results

From this study the following main conclusions can be withdrawn:

- The comparisons of the S3A MWR with other MWR (GMI and J3) indicate good overall agreement between all sensors.
- The WPD scale factors of S3A with respect to other MWR are close to 1: 1.00 for GMI and 1.01 for J3. The absolute biases are less than 1 cm: 0.1 cm for GMI and 0.8 cm for J3.
- The RMS of differences with respect to other sensors are of 0.94 cm (GMI) and 1.3 cm (J3).
- A stable temporal evolution of the S3A MWR-derived WTC can be observed. A strong periodic signal is found in the differences with respect to GMI due to the orbit configurations of the respective spacecrafts.
- Strong ice and land contaminations are observed in the S3A MWR observations, in line with the expected behaviour of a dual-frequency MWR. This makes the establishment of validation criteria for the MWR observations difficult, but unavoidable and indispensable, particularly at the high latitudes.
- Comparison with GNSS shows land contamination in the S3A MWR up to 20-25 km from the coast. The same is not observed in any of the analysed GPD+ WTC.
- The GPD2 WTC (includes S3A MWR) shows a small reduction in SLA variance at crossovers with respect to GPD1 (no S3A MWR), however this reduction in SLA variance is not observed when analysing along-track variance differences. The later result was not previously expected and has not been observed before for the analysed missions, thus indicating that the S3A MWR-derived WTC can still be improved.
- The composite correction present in the products is not suitable for use. The average percentage of points with invalid Composite WTC is 23%.
- This study shows that GPD+ WTC would be an added value for Sentinel-3A products.

# 8 Summary of the Performance of the SCOOP Second Test Data Set and WTC

## 8.1 Summary of Results

The earlier sections of this document have provided the details of a comprehensive assessment of the performance of the SCOOP Second Test Data Set and Wet Troposphere Correction. The main results are summarised below:

### 8.1.1 Results from Open Ocean and Coastal Zone Validation by CLS

#### *SCOOP RDSAR Test Data Set*

- Comparison of the SCOOP RDSAR TDS and the CNES CPP PLRM showed differences below 2cm in Sea Level Anomaly
- Residual errors were believed to be correlated to mispointing. The RDSAR processing uses attitude measurements from the products as inputs to the processing, but are estimated in the CNES CPP PLRM product through its MLE4 re-tracker
- The RDSAR SWH exhibit significant biases, believed to be a consequence of a lack of correction for the PTR width.
- Sigma0 shows a bias of 0.2 dB, dependant on SWH, and possibly correlated with mispointing angle.
- The SCOOP RDSAR data set demonstrated an improved noise performance, but higher correlated errors degrading the SLA content at scales below 100km.

#### *SCOOP SAR Mode Test Data Set*

For Sea Surface Height / Sea Level Anomaly

- The innovative SARM method improves the content of the LRM datasets for wavelengths below 100 km.
- When compared to the nominal Sentinel-3 processing, no improvement in the detection of small-scale oceanic structures was observed, since neither the sea level noise level nor the long ocean wave correlated errors have been reduced. In fact the sea level spectrum has slightly more energy for scales from 2 to 10 km due to an overlap between consecutive measurements (resulting from the application of the Hamming function).

For Significant Wave Height

- Results showed that the innovative SARM provides much-enhanced measurement precision than the nominal processing (a reduction > 35% at 2 m SWH). However, a significant bias was seen, especially at low SWH, which it was thought would be addressed by applying an appropriate correction for the PTR width.

#### *GPD+ Wet Troposphere Correction*

- Results showed that the GPD+ approach leads to a significant improvement in the accuracy of the Cryosat-2 SSH and SLA.
- The GPD+ WTC reduces the sea level anomaly variance with respect to the ECMWF operational model correction from both along-track analysis and cross-overs by ~2 cm<sup>2</sup> (particularly effective in low latitude areas). This approach is also of particular relevance to coastal regions where a reduction of the SLA variance is observed.

## 8.1.2 Results from isardSAT Validation of the SAR Mode Test Data Set

### *Sea Surface Height*

- The global scale analysis over the two sets of regions shows consistency between the SSH of the Test-2 and Test-1 data.
- No dependency on the radial velocity was found on the SSH differences between Test-2 and Test-1 data.
- Very similar noise performance is obtained for both Test-2 and Test-1 data, with a slight improvement on the higher SWH that can be related to the intra-burst Hamming application

### *Significant Wave Height*

- A small dependency in the SWH differences between Test-2 and Test-1 data sets as a function of the SWH was observed. This could be related to the PTR setting: Test-1 used an variable PTR empirically tuned for the retracker implementation in GPOD (LUT), while Test-2 used the isardSAT in-house retracker exploiting a fixed PTR setting; in-situ measurements would be required to fine tune and calibrate the PTR settings.
- A improvement in noise performance of around 10 cm was observed throughout the SWH dynamic range (1 to 8-m): Part of this improvement is believed to be related to the combined setting of intra-burst Hamming and zero-padding, and part to the better stability of the retracker, suspected to be associated to the way that the SWH initial seeding is implemented (based on a sliding window of previous estimates).

### *Sigma0:*

- Global scale analysis over the two sets of regions shows consistency between the Sigma0 of Test-2 and Test-1 data, where a small dependency (below 0.1 dB) as a function of radial velocity is observed on the Pacific regions. This can be linked specifically to some related orbit height dependency as shown by CLS analysis (as such dependency was also observed when comparing Test-1 or GPOD data against CPP data).
- Similar noise performance are obtained for both data sets (Phase-1 and Phase-2), with a slight improvement for the Test-2 data.

## 8.1.3 Results from the Coastal Validation by SKYMAT / SatOC

- In terms of the noise of Uncorrected Sea Surface Height (USSH) on approaching the coast, the performance of the Phase1 and Phase 2 SAR mode Test data sets was similar, with a median value of “noise” (measured as the differences between successive values of USSH) of less than 5cm to within 3km of the coast. A filter only including data with a waveform misfit value of greater than 3 was applied. No dependence of USSH performance on Significant Wave Height (SWH) was found.
- The application of the misfit < 3 filter significantly reduces the data available within 10km of the coast
- A bias in the SWH measurements between the Phase 1 and Phase 2 Test Data sets, for SWH less than 1.6 m was observed. This result was consistent with the other validation studies in SCOOP.
- An investigation into any dependency on performance with the angle of arrival with respect to the coastline found no increase in noise, but did find a greater loss of data for measurements along tracks arriving at angles of 30° or less with respect to the coastline.

## 8.1.4 Results from the Validation by the University of Bonn

### Phase 1 Test Data Set

- For Sea Level Anomaly, the SAR mode performs better than RDSAR, in terms of lower noise, and better agreement with reference data sets (models and tide gauge data)
- The SAMOSA+ retracker has been shown to provide better performance (in terms of lower noise) at the coast than SAMOSA2 (for Sea Level Anomaly) (see also Fenoglio et al., 2019, Figure 3).
- The SCOOP Phase 1 RDSAR product showed a greater data loss at the coast than the TUDaBo RDSAR product. This was attributed to the better performance of the TALES retracker in the TUDaBo product, than the MLE retracker applied to the SCOOP RDSAR product. Therefore a coastal retracker, such as TALES, is recommended.

### Phase 2 Test Data Set

- In general, the University of Bonn analyses showed that the phase 1 (GPOD) test data set performed better than the Phase 2 (isardSAT) test data set, though both showed a good agreement with in-situ data. It should be noted though that the two data sets are not directly comparable, due to differences in modelling the PTR width (as discussed above).
- Application of the Hamming window improved performance more than the application of zero-padding.
- The experimental “masked” coastal data set was not seen to perform significantly differently to the “non-masked” Phase 2 test data set.
- No significant differences were seen between the Phase 1 and Phase 2 RDSAR test data sets.

## 8.1.5 Results from the Performance Assessment of Sea State Impact on SSH by Noveltis

### *SAR sea surface height noise:*

- A general improvement was noticed from Phase 1 to Phase 2 processing, with lower noise and variability in the Phase 2 dataset (except in the first kilometre offshore) and more data retrieved whatever the distance to the coast.

### *Sea state impact on the SAR sea surface height estimates:*

- The investigation of the SAR SSH absolute bias estimates against the in situ SWH measurements at Harvest shows the clear dependency of the bias variability with the significant wave heights.

### *SAR significant wave heights accuracy:*

- An improvement of 10 cm is observed in the Phase 2 dataset SWH, compared to the Phase 1 dataset. This is consistent with the observations of the other validation groups in other regions.

### *SAR “coastal” processing:*

- The comparison between along-track SSH processed with the classical Phase 2 SAR processing and with an experimental coastal SAR processing shows some degradations at the coasts in the SSH estimates and in the correlation between the waveforms and the retracking model in the case of the coastal SAR processing, in Harvest.

*RDSAR sea surface height noise:*

- The Phase 1 and Phase 2 MLE3 RDSAR processing give similar results in terms of SSH. The along-track noise of the RDSAR data is globally 50% higher than the noise of the SAR datasets.
- The SSHA (anomaly) parameter in the Phase 1 dataset shows an unexpected loss of data close to the coasts, which is corrected in the Phase 2 dataset.
- The Phase 2 MLE4 RDSAR SSH retrievals are generally noisier than for the MLE3 dataset and a slight loss of data in the first 10 km offshore. However, the comparison with the in situ significant wave heights at Harvest shows an improvement with the MLE4 dataset, compared to the MLE3 dataset.

## 8.1.6 Results from the Validation of the Wet Troposphere Correction by U Porto

### Results for CryoSat

- The results for the project ROI confirm the global results obtained in CP40, i.e., GPD+ is an improvement with respect to the ECMWF baseline model.

### Results for Sentinel-3A

- The comparisons of the S3A MWR with other MWR (GMI and J3) indicate good overall agreement between all sensors.
- The WPD scale factors of S3A with respect to other MWR are close to 1: 1.00 for GMI and 1.01 for J3. The absolute biases are less than 1 cm: 0.1 cm for GMI and 0.8 cm for J3.
- The RMS of differences with respect to other sensors are of 0.94 cm (GMI) and 1.3 cm (J3).
- A stable temporal evolution of the S3A MWR-derived WTC can be observed. A strong periodic signal is found in the differences with respect to GMI due to the orbit configurations of the respective spacecrafts.
- Strong ice and land contaminations are observed in the S3A MWR observations, in line with the expected behaviour of a dual-frequency MWR. This makes the establishment of validation criteria for the MWR observations difficult, but unavoidable and indispensable, particularly at the high latitudes.
- Comparison with GNSS shows land contamination in the S3A MWR up to 20-25 km from the coast. The same is not observed in any of the analysed GPD+ WTC.
- The GPD2 WTC (includes S3A MWR) shows a small reduction in SLA variance at crossovers with respect to GPD1 (no S3A MWR), however this reduction in SLA variance is not observed when analysing along-track variance differences. The later result was not previously expected and has not been observed before for any of the analysed missions, thus indicating that the S3A MWR-derived WTC can still be improved.
- The composite correction present in the S3A products is not suitable for use. The average percentage of points with invalid Composite WTC is 23%.
- This study shows that GPD+ WTC would be an added value for Sentinel-3A products, providing a continuous and consistent correction, valid over all surface types.

## 8.2 Outstanding Issues

### *RDSAR*

- Further validation of RDSAR is recommended under a wider range of mis-pointing angles and radial velocities. There seems to be a problem with the CryoSat attitude information.
- A correction for the PTR width should be included in the RDSAR processing.

### *SAR Mode Processing*

- Further analyses should be performed at global scale (using Sentinel-3 data) to confirm results over a wider range of conditions. Such analyses should pay close attention to any sea level changes in the spectrum. The key issue and challenge for new SARM processing in the open ocean is to enhance the altimeter capability in accessing finer scale structures in order to improve our understanding of oceanic (sub)mesoscale processes.
- Application of the Hamming windowing appears to increase the bias in SWH at low wave heights

### *GPD+ Wet Troposphere Correction*

- An assessment of the GPD+ performance over polar regions was not possible due to the limited geographical coverage of the test data set.

## 8.3 Recommendations

### *RDSAR*

- Further work is needed to better understand and correct the long wavelength errors in the RDSAR product. These issues need to be addressed to ensure better continuity with conventional altimetry missions, and ultimately make this processing of interest for the Sentinel-3 mission.
- Coastal retracers should be applied for coastal data sets as they have been demonstrated to improve performance.
- Further tests on the performance of an MLE4 retracker on the RDSAR product should be carried out.

### *SAR Mode*

- On the basis of the assessment results, showing substantial reduction of SWH noise and almost matching SLA performance (with CNES CPP), the use of the innovative SARM processing for Sentinel-3 mission is recommended to improve ocean altimetry products for end-users (more likely in coastal areas).
- CLS recommend further analysis to identify the specific algorithms that provided the SWH noise improvement and to explain the underlying physical principle underlying the improvement. This would help to fully convince the altimeter community of the benefit of this processing.
- isardSAT recommends in situ measurements be used to fine tune and calibrate the PTR settings within the SAR mode processing.
- The increase in the SSH bias variability for large wave conditions highlights the fact that an appropriate SSB correction dedicated to the SAR SSH is needed to compute accurate SSH.

- Further investigations are required to understand why performance degradations were observed in the “experimental coastal” data set prepared by isardSAT.
- Further studies should be carried out into the development of coastal re-trackers for SAR mode echoes.

#### GPD+ Wet Troposphere Correction

- The GPD+ correction clearly outperforms the ECMWF operational model-derived correction in both open ocean and coastal areas. This improved solution is of particular interest for altimetry missions which do not possess on-board microwave radiometer. For the Sentinel-3 mission embarking an MWR sensor, such a solution is of interest whenever MWR measurements are considered invalid, but could also be used as independent data for assessing the on-board MWR derived WTC (using a version of the correction solely based on third party data).
- Along track discontinuities of a few mm height were observed, without however adverse impact on the SLA accuracy. In case of occurrence of higher discontinuities, a strategy to better handle such discontinuities should be envisaged.
- The composite correction present in the products is not suitable for use. The average percentage of points with invalid Composite WTC is 23%.
- The GPD+ WTC would be an added value for Sentinel-3A products.

## 9 List of Acronyms

ALES	Adaptive Leading Edge Subwaveform retracker
AMR	Advanced Microwave Radiometer
AVISO	Altimetry information website ( <a href="https://www.aviso.altimetry.fr/en/home.html">https://www.aviso.altimetry.fr/en/home.html</a> )
BSH	German Federal Maritime and Hydrographic Agency
CCI	Climate Change Initiative (ESA programme)
CLS	Collecte Localisation Satellite
CNES	Centre National d'Études Spatiales
CORSSH	Corrected Sea Surface Height
CP40	CryoSat Plus For Ocean
CPP	CNES CryoSat-2 Prototype Processing
CS-2	CryoSat-2
CSCM	Cold Sky Calibration Manoeuvres
DComb	Data Combination – U Porto technique for generating Wet Troposphere Correction
DPM	Detailed Processing Model
DTU	Technical University of Denmark
ECMWF	European Centre for Medium-Range Weather Forecasts
ERA	ECMWF ReAnalysis Model
ESA	European Space Agency
FBR	“Full Bit Rate” CryoSat-2 product which includes multi-looked echoes at 20Hz
FTDS	First Test Data Set
GMI	Global Precipitation Measurement Microwave Imager
GNSS	Global Navigation Satellite System
GPD	GNSS derived Path Delay
GPOD	Grid Processing On Demand ( <a href="https://gpod.eo.esa.int">https://gpod.eo.esa.int</a> )
GPM	Global Precipitation Measurement
HAMM	Hamming Window
HS, HS0, HS1, HS2, HS3	Significant wave height of different components of the wave spectrum
IFREMER	Institut Francais de recherché pour L'Exploitation de la mer
IPF	Instrument Processing Facility

IOWAGA	Integrated Ocean Waves for Geophysical and Other Application: 3 year programme
J2	Jason-2: Radar Altimeter satellite mission, part of the JASON series
LRM	Low Rate Mode.
LUT	Look Up Table
MLE	Maximum Likelihood Estimator
MSS	Mean Sea Surface
MWR	Microwave Radiometer
NOC	National Oceanography Centre
NTC	Non Time Critical
PDGS	Payload Data Ground Segment
PLRM	Pseudo Low Resolution Mode
PVP	Product Validation Plan
PVR	Product Validation Report
PTR	Point Target Response
RADS	Radar Altimeter Database System (provided and managed by TU Delft)
RDSAR	ReDuced SAR processing. Processing to produce LRM equivalent product from SAR mode altimeter data.
RMS	Root Mean Square
ROI	Region(s) of Interest
RSS	Remote Sensing Systems
SAMOSAS	Theoretically derived, physically based, SAR altimeter Echo Waveform model.
SAR(M)	Synthetic Aperture Radar (Mode)
SCOOP	SAR Altimetry Coastal and Open Ocean Performance
SEOM	Scientific Exploitation of Operational Missions (element of ESA Earth Observation Envelope Programme 4)
Sigma <sub>0</sub> , $\sigma_0$	Surface radar backscatter at nadir incidence
SI-MWR	Scanning Imaging Microwave Radiometers
SLA	Sea Level Anomaly
SL-CCI	Sea Level – Climate Change Initiative
SNR	Signal to Noise Ratio
SoW	Statement of Work
SSH	Sea Surface Height
SSM/I(S)	Special Sensor Microwave Imager (Sonder)

---

Std (STDD)	Standard Deviation
SWH	Significant Wave Height
S3	Sentinel-3
S3 GPP	Sentinel-3 Ground Prototype Processor
TALES	TU-Darmstadt Adaptive Leading Edge Sub-waveform retracker
TCWV	Total Column Water Vapour
TDS	Test Data Set
TuDaBo	TU-Darmstadt Bonn RDSAR/SAR processing
USSH	Uncorrected Sea Surface Height (i.e. altitude minus range)
WPD	Wet Path Delay
WTC	Wet Troposphere Correction
ZHD	Zenith Hydrostatic Delay
ZWD	Zenith Wet Delay
ZTD	Zenith Total Delay
ZP2	Zero Padding in Range 2